

NORTHWESTERN UNIVERSITY

Nanostructures in Catalysis:
Au/TiO₂ for the Oxidation of CO at Low Temperature and Confinement Effect in Siloxane
Nanocages

A DISSERTATION

SUBMITTED TO THE GRADUATE SCHOOL IN PARTIAL FULFILLMENT OF THE
REQUIREMENTS

for the degree

DOCTOR OF PHILOSOPHY

Field of Chemical Engineering

By

Juan D. Henao

EVANSTON, ILLINOIS

December 2007

ABSTRACT

Nanostructures in Catalysis:
Au/TiO₂ for the Oxidation of CO at Low Temperature and Confinement Effect in Siloxane
Nanocages

Juan D. Henao

Two subjects are the focus of this dissertation: Au/TiO₂ catalyst used for oxidation of CO at low temperature and siloxane nanocages, a novel material (~2nm) recently developed in our group.

While bulk gold is chemically inert, gold supported as nanoparticles is remarkably active for the oxidation of carbon monoxide at low temperature. The reaction has been intensively studied in the last years; however, the origin of this unusual activity is not yet fully understood. In particular, the nature of active site and the reaction mechanism have not been clearly identified. In this work, a combination of *in-situ* XANES, EXAFS and FTIR with microreactor studies are used to develop a structure-activity relationship by monitoring the structural changes during the activation of an inactive catalyst. In addition, the reaction pathway is investigated by identifying the surface species directly involved in the reaction and quantifying their transformation rates under transient and steady-state conditions. It is demonstrated that metallic nanosized gold is a necessary component of the active site. Its role is to activate CO, which is subsequently oxidized at the catalytic centers. Information on the nature of the catalytic centers is obtained through the identification of adsorbed hydroxycarbonyl species, via a combination of

in-situ FTIR, $^{18}\text{O}_2$ isotopic labeling and mass spectrometry. All together, this study suggests that nanosized gold provides the necessary unsaturated sites where CO is activated.

Key properties of the novel siloxane nanocages, including its protonation response to variations in the external pH, are investigated using Au^{3+} as a probe. The binding of Au^{3+} to the amine groups inside the nanocage is studied by a combination of XANES, EXAFS, UV-VIS and cyclic voltammetry. A remarkable reduction of five pH units on the Brønsted basicity of propylamine groups within the nanocage, consequence of their nano-confinement, occurs. When the amine groups inside the nanocage are in excess with respect to gold, they act as a chelating ligand. In addition, all the Au^{3+} inside the nanocage are chemically bound to the amine groups, for all amine/gold ratios.

To my wife, Rosa María

ACKNOWLEDGEMENTS

I would like to thank my research advisors, Professor Harold H. Kung and Professor Mayfair C. Kung. I was fortunate to have two knowledgeable advisors who always encouraged and supported me. Their constant search for the highest quality has always been instructive and inspirational.

I want to thank the members of my thesis committee, Professor Randall Snurr, Professor Peter Stair and Professor Luis Amaral, for their appropriate comments and suggestions.

I also want to acknowledge the scientific staff at the Advance Photon Source at Argonne National laboratory, for their assistance during our multiple long runs at the DND-CAT. Particularly, thanks to Dr. Qing Ma and Dr. Denis Keane for their patience and support. I am very grateful to Dr. Jeff Miller of BP Amoco for his instruction on the analysis and interpretation of EXAFS data and for very helpful discussions. I would like to acknowledge my coworkers in the gold project, Dr. Jeff Yang and Dr. Tiziana Caputo; we had many inspiring “gold meetings” and discussions. Their contribution was essential to this work. I am very thankful to my coworker in the first part of the nanocage project, Dr. Young-Woong Suh. I learned much from him and enjoyed our discussions; his expertise was fundamental for the completion of this work. I want to thank other members of the Kung’s group: Sean Oxford, Michael Missaghi, Christopher Downing, Dr. Jung-Kyoo Lee and Hiu Ying Law for their assistance during all these years and for many interesting conversations. I am grateful to Dana Sauter for reading and providing me feedback on part of this dissertation. I want to acknowledge the Mirkin and the

Hupp laboratories of Chemistry Department at Northwestern, for letting us use the dynamic light scattering and cyclic voltammetry instruments.

I am truly indebted to Professor Wolfgang M. H. Sachtler. His support and friendship made an enormous difference for me during my time at Northwestern.

Finally, I want to thank my wife for her patience and support.

Financial support for this work was provided by the Northwestern University Institute of Environmental Catalysis funded by the Department of Energy (Grant No. DE-FG02-03ER15457). I also want to acknowledge support by Northwestern University through a Henderson Fellowship. The DND-CAT is supported by E. I. DuPont de Nemours & Co., Dow Chemical Co., the National Science Foundation (Grant No. DMR-9304725), and the State of Illinois through the Department of Commerce and the Board of Higher Education (Grant No. IBHE HECA NWU 96). The APS was supported by the U. S. Department of Energy, Office of Energy under Contract No. W-31-102-Eng-38.

TABLE OF CONTENTS

	Page
ABSTRACT	2
DEDICATION	4
ACKNOWLEDGEMENTS	5
TABLE OF CONTENTS	7
LIST OF FIGURES	11
LIST OF SCHEMES	16
LIST OF TABLES	18
CHAPTER	
1 INTRODUCTION	
1.1 Motivation/Objective	19
1.2 Oxidation of CO catalyzed by supported gold	21
1.2.1 Oxidation state of gold at the active site	22
1.2.2 Reaction mechanism	23
1.3 Examples of properties exhibited by nanoconfined structures	26
1.4 Summary	28
2 EXPERIMENTAL	
2.1 Oxidation of CO on Au/TiO ₂	31
2.2 Characterization of Au/TiO ₂	33
2.2.1 Chemical analysis	33
2.2.2 In-situ XANES/EXAFS	34
2.2.3 Controlled reduction using H ₂ pulses	37
2.2.4 Mass spectrometry	38
2.2.5 <i>In-situ</i> FTIR spectroscopy	40
2.2.6 ¹⁸ O isotopic labeling	41
2.3 Characterization of siloxane nanocages	42

CHAPTER	8
	Page
2.3.1 ^1H , ^{13}C and ^{29}Si NMR	42
2.3.2 Dynamic Light Scattering	43
2.3.3 Titration of amine groups	45
2.3.4 Cyclic Voltammetry	47
2.3.5 XANES/EXAFS in the liquid phase	51
2.3.6 UV-VIS spectroscopy	51
3 ACTIVATION OF Au/TiO ₂ CATALYST FOR LOW TEMPERATURE OXIDATION OF CO	
3.1 Synopsis	52
3.2 Introduction	52
3.3 Experimental Section	54
3.3.1 Catalyst Preparation	54
3.3.2. H ₂ and CO Pulse Reduction	54
3.3.3 Catalytic Activity for CO Oxidation	55
3.3.4 X-ray Absorption Spectroscopy (XAS)	55
3.3.5 Transmission Electron Microscopy (TEM) and XPS	57
3.3.6 Microcalorimetry	57
3.3.7 <i>In-Situ</i> Infrared Spectroscopy	57
3.4 Results	60
3.4.1 H ₂ and CO Pulse Reduction	60
3.4.2 Microcalorimetry	63
3.4.3 XPS	63
3.4.4 XAS	66
3.4.5 TEM	72
3.4.6 CO Oxidation at 195 K	72
3.4.7 Infrared Spectroscopy	75
3.5 Discussion	78
3.6 Conclusions	81

4	<i>IN-SITU</i> TRANSIENT FTIR AND XANES STUDIES OF THE EVOLUTION OF SURFACE SPECIES IN CO OXIDATION ON Au/TiO ₂	
4.1	Synopsis	83
4.2	Introduction	83
4.3	Experimental	85
4.3.1	Catalyst Preparation	85
4.3.2	<i>In-Situ</i> FTIR Spectroscopy.	86
4.3.3	CO Adsorption.	86
4.3.4	Oxidation of Adsorbed CO.	87
4.3.5	Isotopic Exchange.	88
4.3.6	<i>In-Situ</i> XANES.	88
4.4	Results	91
4.4.1	CO Adsorption.	91
4.4.2	Reaction of Adsorbed CO.	94
4.4.3	Isotope Labeling Experiments.	103
4.4.4	In Situ XANES Measurements.	106
4.5	Discussion	106
4.6	Conclusions	113
5	SYNTHESIS AND CHARACTERIZATION OF SILOXANE NANOCAGES	
5.1	Synopsis	114
5.2	Synthesis and purification of silicon surfactant	115
5.2.1	Synthesis of surfactant	115
5.2.2	Purification of the surfactant	115
5.3	Preparation of protected nanocages	120
5.4	Generation of nanocage with internal amine groups by carbamate deprotection	127

CHAPTER	10
	Page
5.5 Characterization and purification of siloxane nanocages	129
5.5.1 Quantification of internal amine functionalities	129
5.5.2 Dialysis	129
5.6 Summary	131
6 NANOCONFINEMENT EFFECT ON THE BINDING OF GOLD BY PRIMARY AMINE INSIDE SILOXANE NANOCAGES	
6.1 Synopsis	132
6.2 Introduction	133
6.3 Experimental	134
6.3.1 Synthesis of amine-functionalized nanocages	134
6.3.2 Cyclic Voltammetry	134
6.3.3 XANES and EXAFS data acquisition and analysis	135
6.3.4 Solvolysis of HAuCl_4	136
6.3.5 Reactions of Au^{3+} and the nanocage at various pH	137
6.3.6 DN titration by Au^{3+}	139
6.3.7 Reaction of Au^{3+} and DN at various $\text{R-NH}_2/\text{Au}$ ratios	139
6.4 Results	139
6.4.1 Solvolysis of HAuCl_4	139
6.4.2 Reactions of Au^{3+} and DN at various pH	148
6.4.3. Reaction of Au^{3+} and DN at various $\text{R-NH}_2/\text{Au}$ ratios.	158
6.5. Discussion	162
6.6 Conclusions	172
7 SUMMARY, CONCLUSIONS AND RECOMMENDATIONS FOR FUTURE WORK	
7.1 Summary and conclusions	174
7.2 Recommendations for future work	177
REFERENCES	180

LIST OF FIGURES

FIGURE		Page
3.1	H ₂ consumption at 298 K as a function of pulse sequence; 100 mg of a 7 wt % Au/TiO ₂ catalyst.	58
3.2	CO consumption at 273 K as a function of pulse sequence for 12 mg of a 4 wt % Au/TiO ₂ catalyst.	59
3.3	H ₂ consumption and heat evolved in calorimetry experiment as a function of pulse sequence.	61
3.4	Au (4f) binding energy of Au/TiO ₂ catalyst: (a) as-prepared sample, (b) sample fully reduced by H ₂ pulses, (c) sample reduced by H ₂ pulses to ca. 50% and (d) reference Au/TiO ₂ catalyst (calcined) distributed by WGC.	62
3.5	XANES spectra as a function of H ₂ pulse sequence.	64
3.6	Percentage of Au ³⁺ reduced by each H ₂ pulse as a function of pulse sequence in the XAS experiment.	65
3.7	Magnitude of the Fourier transformed $k^2-\chi$ function in R-space of Au/TiO ₂ after selected H ₂ pulse. The arrows indicate positions of Au–O and Au–Au scattering at 1.6 and 2.3 Å in R-space.	67
3.8	Au–Au coordination number obtained by fitting the $\chi(k^2)$ function (◆), fraction of Au ³⁺ (×), and Au ⁰ (○) obtained by XANES fit, and corrected Au–Au coordination number (■) obtained by dividing the Au–Au CN by the fraction of Au ⁰ , as a function of H ₂ pulse sequence.	68
3.9	TEM pictures of Au/TiO ₂ that were (top) approximately 50% reduced by H ₂ pulses and (bottom) completely reduced by H ₂ pulses.	70
3.10	CO conversion of Au/TiO ₂ catalyst at 20 min TOS as a function of Au ³⁺ reduced by H ₂ pulse. Reaction conditions: 1% CO, 2.5% O ₂ , balance He, 50 mL/min, 0.1 g catalyst, 195 K.	71
3.11	Infrared spectra of as-prepared Au/TiO ₂ under 10% CO and balance He at 213 K.	73
3.12	CO conversion (a) and the normalized intensities of the composite IR band at 2105 cm ⁻¹ (b) and at 2066 cm ⁻¹ (c) of an as-prepared Au/TiO ₂ catalyst as a function of time-on-stream at about 240 K. Reaction conditions: 1% CO, 2.5% O ₂ , balance He, 11 mL/min, 10 mg of catalyst.	74

FIGURE

Page

- | | | |
|------|--|----|
| 3.13 | Time-on-stream behavior of IR spectra of Au/TiO ₂ under the following reaction conditions at about 240 K: 1% CO, 2.5% O ₂ , balance He, 11 mL/min, 10 mg of catalyst. | 76 |
| 3.14 | Ratio of the area of 2066 cm ⁻¹ bands (<i>A</i> ₁) to the area of 2102 cm ⁻¹ bands (<i>A</i> ₂) as a function of partial pressure of CO. | 77 |
| 4.1 | Mass spectra of breakthrough curves of CO (<i>m/e</i> = 28) for 1% CO flowing through (a) as-prepared catalyst, (b) H ₂ -activated catalyst with no previous exposure to CO, and (c) H ₂ -activated catalyst previously exposed to CO and followed by 30 min of He purging. Experimental conditions: catalyst = 300 mg (4% Au), flow rate = 70 mL/min, <i>T</i> = -60 °C. | 89 |
| 4.2 | (A) Changes in FTIR spectra of activated Au/TiO ₂ that had been exposed to 1% CO as a function of purging time in He at -60 °C. (B) Corresponding changes in the peak intensity. | 90 |
| 4.3 | (A) Changes in the IR peak at around 2100 cm ⁻¹ after switching to a flow of 2.5% O ₂ and (B) corresponding changes in the peak intensity (curve b) and intensity of the adsorbed CO ₂ peak (2340 cm ⁻¹ , curve a). | 92 |
| 4.4 | Evolution of the FTIR spectra of a catalyst after the gas was switched from 1% CO to a mixture 1% CO and 2.5% O ₂ in He. Gas-phase CO has been subtracted from the spectra. Experimental conditions: catalyst = 10 mg, flow rate = 70 mL/min, <i>T</i> = -60 °C. | 93 |
| 4.5 | Evolution of FTIR spectra when an O ₂ -saturated catalyst was exposed to a flow of 1% CO in He. Gas-phase CO has been subtracted from the spectra. Experimental conditions: catalyst = 10 mg, flow rate = 70 mL/min, <i>T</i> = -60 °C. | 95 |
| 4.6 | (A) Time-dependent concentration at the exit of CO (×), O ₂ (♦) and CO ₂ (○) in the reaction of preadsorbed CO with flowing O ₂ . After being purged with He for 1.5 min to remove gas-phase CO, O ₂ was admitted. (B) Expanded plot of part A at around 2 min after switching to O ₂ flow. | 96 |
| 4.7 | CO ₂ generated by reaction of adsorbed CO with O ₂ (●) and adsorbed oxygen with CO (▲), as a function of the purging time in He prior to the admission of O ₂ or CO, respectively. Dashed lines are extrapolation of experimental data to zero purging time. Experimental conditions: catalyst = 300 mg, flow rate = 70 mL/min, <i>T</i> = -60 °C. | 98 |
| 4.8 | (A) Time-dependent concentration of CO (×), O ₂ (♦), and CO ₂ (○) in the reaction of preadsorbed O ₂ with flowing CO. After 1.5 min of He flow to remove gas-phase O ₂ , the gas was switched to CO. (B) Expanded version of part A at about 2 min. | 99 |

FIGURE		13 Page
4.9	Comparison of the CO ₂ evolution profiles for a catalyst pretreated with 1% CO and then exposed to flowing O ₂ (▲), and a catalyst pretreated with 2.5% O ₂ and then exposed to flowing CO (○). Experimental conditions: catalyst used = 300 mg, flow rate = 70 mL/min, <i>T</i> = -60 °C.	101
4.10	(A) Changes in the 1100-1350 cm ⁻¹ region of the IR spectrum with time after switching the gas flowing to a fresh H ₂ -activated catalyst to 1% CO and (B) after a sample previously used for reaction using 1% CO and 2.5% ¹⁸ O ₂ was exposed to 1% CO.	102
4.11	Changes in the IR spectrum (A) after switching to 2.5% ¹⁶ O ₂ , of the sample corresponding to Figure 10A, and (B) after switching to 2.5% ¹⁸ O ₂ , of the sample corresponding to Figure 10B. The reference spectra were those just before O ₂ admission.	104
4.12	Changes in intensities of (A) the 1242 cm ⁻¹ peak after switching to ¹⁶ O ₂ (■) and the corresponding transient appearance of carbon dioxide C ¹⁶ O ₂ (●) and (B) the 1236 cm ⁻¹ peak and the corresponding transient appearance of C ¹⁶ O ¹⁶ O (○), C ¹⁶ O ¹⁸ O (●), and C ¹⁸ O ¹⁸ O (×) after switching to ¹⁸ O ₂ .	105
4.13	Figure 4.13. Changes in the in situ XANES spectra of a fully reduced Au/TiO ₂ catalyst that was equilibrated with 1% CO, during purging with (A) He or (B) 2.5% O ₂ . The insets are the entire XANES spectra. Experimental conditions: catalyst = 100 mg, flow rate = 100 mL/min, <i>T</i> = -65 °C.	107
5.1	Proton NMR of (a) an as-prepared surfactant containing an equivalent amount of (Et) ₃ NH ⁺ Cl ⁻ and (b) a surfactant purified by elution through a silica gel bed, using a mixture of hexanes/ethyl acetate (5/1). Spectra acquired at RT in CDCl ₃ at 499.5 MHz.	118
5.2	DLS data corresponding to various stages during the preparation of siloxane nanocages. (a) micelles generated by dissolution of silicon surfactant in anhydrous ethanol, (b) 12 h after treatment of the micelles with 20% pH=1 solution in ethanol, (c) after dilution with ethanol followed by H ₂ O/ethanol (80/20) and (d) after cross-linking and capping with (MeO) ₂ (Me) ₂ Si and (MeO)(Me) ₃ Si, respectively. Since the observed scattering intensity is proportional to the sixth power of the diameter, particles bigger than 10 nm represent less than 0.05% of the population in solution.	121
5.3	¹ H-NMR acquired at different stages during the preparation of protected nanocages in CD ₃ OD. (a) Micelles generated by dissolution of silicon surfactant in CD ₃ OD, (b) 1 h after addition of acidic D ₂ O (pH=1) in CD ₃ OD (20% D ₂ O), (c) after dilution with CD ₃ OD followed by D ₂ O/CD ₃ OD (80/20), (d) after cross-linking with (MeO) ₂ (Me) ₂ Si, (e) after capping with (MeO)(Me) ₃ Si and (f) after evaporation at -5 °C to remove excess cross-linking and capping agents. EA is residual ethyl acetate. Spectra acquired at RT at 499.5 MHz.	122

FIGURE		Page
5.4	DLS of nanocage after deprotection with TMSI. Data acquired in methanol at RT. Since the observed scattering intensity is proportional to the sixth power of the diameter, particles bigger than 10 nm correspond to less than 0.05% of the population in solution.	128
5.5	Comparison of the UV-VIS spectra for the deprotected nanocage before and after dialysis. Both samples contain equivalent amounts of nanocage, as established by the ninhydrin test.	130
6.1	(A) Au XANES for AuCl_4^- in anhydrous methanol at (—) pH=2.9, (···) pH=6.0 and (---) pH=7.6. (B) Corresponding distribution of gold into different species in solution. $[\text{Au}^{3+}] = 430 \mu\text{M}$, $\text{Cl}^-/\text{Au}^{3+} = 1070$.	138
6.2	(A) Magnitude and imaginary component of the Fourier transformed EXAFS (k^2 , $\Delta k = 3.37\text{--}12.3 \text{ \AA}^{-1}$) for AuCl_4^- in anhydrous methanol at (—, —) pH=2.9, (···) pH=6.0 and (---, ---) pH=7.6. Peak positions are uncorrected for phase-shift. (B) Comparison between XANES- and EXAFS-derived Au-Cl coordination numbers. $[\text{Au}^{3+}] = 430 \mu\text{M}$, $\text{Cl}^-/\text{Au}^{3+} = 1070$.	141
6.3	Hydrolysis of AuCl_4^- as a function of pH. Data collected from independent solutions 5h after preparation. The reported pH for each sample was measured right after the spectrum was acquired. $[\text{Au}^{3+}] = 72 \mu\text{M}$, $\text{Cl}^-/\text{Au}^{3+} = 1070$.	143
6.4	Overall Au-Cl coordination number against molar absorptivity at 227 nm for solutions of AuCl_4^- at two different concentrations in three different solvents. Molar absorptivities were all determined by UV-VIS, 5h (water) and 90 min (anhydrous methanol) after preparation. Au-Cl CN for the aqueous systems was calculated using equilibrium constants for reactions (6.1-6.6). For the 426 μM solution in methanol, it was determined using EXAFS. The solutions of 72 μM in methanol and methanol/water were used to test the validity of the relationship (see text for details). In all cases $\text{Cl}^-/\text{Au}^{3+} = 1070$.	147
6.5	(A) UV-VIS spectra of Au^{3+}/DN and $\text{Au}^{3+}/\text{APMBTSS}$ solutions in anhydrous methanol illustrating the difference in pH required to cause a comparable drop in the LMCT band at 227 nm after 10 min of reaction. (B-D) Overall Au-Cl CN vs pH at different reaction times, determined from UV-VIS and Figure 6.4. The reaction times are 10 min (B), 90 min (C) and 48 h (D). $[\text{Au}^{3+}] = 72 \mu\text{M}$, $\text{R-NH}_2/\text{Au}^{3+} = 1.0$, $\text{Cl}^-/\text{Au}^{3+} = 4$ for all solutions.	150
6.6	(A) Magnitude of the Fourier transformed EXAFS (k^2 , $\Delta k = 3.37\text{--}11.6 \text{ \AA}^{-1}$) for (---) AuCl_4^- at pH=3.7, (···) $\text{Au}^{3+}/\text{APMBTSS}$ at pH=4.7 and (—) Au^{3+}/DN at pH=4.0. Peak positions are uncorrected for phase-shift. (B) Au-N coordination number determined by EXAFS. Data collected at $\text{Cl}^-/\text{Au}^{3+} = 4$: (\blacktriangle) Au-Cl CN for AuCl_4^- control solutions, (\blacklozenge) Au^{3+}/DN and (\bullet) $\text{Au}^{3+}/\text{APMBTSS}$. Collected at $\text{Cl}^-/\text{Au}^{3+} = 1070$: (\diamond) Au^{3+}/DN and (\circ) $\text{Au}^{3+}/\text{APMBTSS}$. In all cases the solvent was anhydrous methanol. All solutions were analyzed after 90 min of reaction. Other conditions: $[\text{Au}^{3+}] = 430 \mu\text{M}$, $\text{R-NH}_2/\text{Au}^{3+} = 1.0$.	154

FIGURE

Page

- 6.7 (A) Cyclic voltammograms of Au^{3+}/DN solutions at various pH. (B) Time evolution of the cathodic current (**a+d**) as a function of time at (\blacktriangle) pH=4.6, (\bullet) pH=7.1 and (\blacksquare , \blacklozenge) pH=7.4. Two controls are included: (\diamond) AuCl_4^- and (Δ) Au^{3+}/PN , both at pH=7.4. Reactions carried out in methanol (0.1% water) at 500 rpm. $[\text{Au}^{3+}] = 42 \mu\text{M}$, $\text{R-NH}_2/\text{Au}^{3+} = 1.0$. Scan rate = 0.1 V/s. Reference electrode: Ag/AgCl. Supporting electrolyte: 0.10 M NaClO_4 . 156
- 6.8 (A) Absorbance at 227nm after 6 and 90 min of reaction for independent solutions of Au^{3+}/DN , with different amine/gold ratios. (B) Drop in Au-Cl coordination numbers determined from (A) with the help of Figure 6.4. Data acquired at pH=4.9 in anhydrous methanol. $[\text{Au}^{3+}] = 72 \mu\text{M}$, $\text{Cl}^-/\text{Au}^{3+} = 4$. 159
- 6.9 (A) Magnitude of the Fourier transformed EXAFS (k^2 , $\Delta k = 3.37\text{--}11.6 \text{ \AA}^{-1}$) at different amine/gold ratios for Au^{3+}/DN . (---) AuCl_4^- ($\text{R-NH}_2/\text{Au}^{3+} = 0$), (---) $\text{R-NH}_2/\text{Au}^{3+} = 1.1$ and (—) $\text{R-NH}_2/\text{Au}^{3+} = 4.3$. Peak positions are uncorrected for phase-shift. (B) Au-N coordination number determined by EXAFS. Data collected for Au^{3+}/DN : (\blacksquare) $\text{R-NH}_2/\text{Au}^{3+} = 2.1$ and (\blacktriangle) $\text{R-NH}_2/\text{Au}^{3+} = 4.3$. Data collected for $\text{Au}^{3+}/\text{APMBTSS}$: (\circ) $\text{R-NH}_2/\text{Au}^{3+} = 3.0$ and (Δ) $\text{R-NH}_2/\text{Au}^{3+} = 4.1$. AuCl_4^- control: (\bullet) Au-Cl CN. In all cases the solvent was anhydrous methanol. All solutions were analyzed after 90 min of reaction. $[\text{Au}^{3+}] = 430 \mu\text{M}$, $\text{Cl}^-/\text{Au}^{3+} = 4.0$. 161
- 6.10 Decrease in Au-Cl coordination number of AuCl_4^- in solution with DN or APMBTSS. Data derived from Figure 6.5. Au^{3+}/DN after (\blacklozenge) 10 min, (\bullet) 90 min and (\blacktriangle) 48 hours of reaction. $\text{Au}^{3+}/\text{APMBTSS}$ after (\diamond) 10 min and (\circ) 90 min of reaction. The solvent was anhydrous methanol. $[\text{Au}^{3+}] = 72 \mu\text{M}$, $\text{Cl}^-/\text{Au}^{3+} = 4.0$. 164
- 6.11 Anodic current generated during the oxidative (positive-going) scan of cyclic voltammetry experiments for $\text{AuCl}_4^-/\text{DN}$ solutions with $\text{Au}^{3+}/\text{R-NH}_2 = 0\text{--}1.93$. Each data point was obtained after 90 min of reaction of a fixed amount of nanocage containing 42 μM of primary amine (as determined by the ninhydrin test^{25,26} described in Chapter 2) and the proper amount of Au^{3+} . The reaction was carried out in methanol/water (4.4 % H_2O) at 500 rpm and pH=7.4. Scan rate: 0.1 V/s. Reference electrode: Ag/AgCl. Supporting electrolyte: 0.11 M NaCl. 168

LIST OF SCHEMES

SCHEME	Page
1.1	Proposed mechanism of reaction for the oxidation of CO on a supported gold Catalyst. 24
2.1	Reaction system used to test catalytic activity for oxidation of CO with Au/TiO ₂ . 32
2.2	XAS set-up used to carry out experiments in the transmission mode. A diagram of the <i>in-situ</i> cell is provided. 35
2.3	XAS set-up used to carry out experiments in the fluorescence mode. A diagram of the <i>in-situ</i> cell is provided. 36
2.4	System used to reduce as-prepared Au/TiO ₂ loaded into the <i>in-situ</i> XAS cell. This arrangement allows switching between H ₂ pulses and a reaction mixture. 38
2.5	Reaction system used to perform the mass spectrometry experiments. 39
2.6	<i>In-situ</i> FTIR system detailing the cell used to study the kinetics of surface species on the catalyst 41
2.7	System used on the study of ¹⁸ O isotopic exchange with surface species on Au/TiO ₂ catalyst. 42
2.8	Ninhydrin reaction used in the titration of propylamine functionalities tethered to the interior of siloxane nanocages. 46
5.1	Synthesis of the silicon surfactant used to prepare siloxane nanocages. As HCl is generated by the reaction, TEA in solution traps it forming a quaternary salt. 116
5.2	Purification of silicon surfactant contaminated with traces of (Et) ₃ NH ⁺ Cl ⁻ by thin layer chromatography. The fourth plate shows that elution of the impure surfactant through a bed of silica gel, completely removes the quaternary salt. 117
5.3	Silicon surfactant self-assembly in ethanol, into 2 ± 0.3 nm micelles. The carbamate groups at the interior are used to generate primary amine groups in subsequent steps. 120
5.4	Representation of the hydrolysis and condensation processes occurring by addition of acidic alcohol to a solution of micelles. As observed, only partial condensation of head groups occurs. 123

		17
SCHEME		Page
5.5	Cross-linking and condensation occurring after slow addition of $\text{Me}_2\text{Si}(\text{OMe})_2$ and $\text{Me}_3\text{Si}(\text{OMe})$ to a solution micelles with fully hydrolyzed and partially condensed head groups.	124
5.6	Reaction of protected nanocage with TMSI generates propylamine functionalities at the interior of the nanocage.	126
6.1	Model of the deprotected nanocage (DN) highlighting its porous wall and interior propylamine functionalities. The structure of the primary amine APMBTSS used as a reference in this work is also included.	152
6.2	Binding of Au^{3+} inside DN as the amine/gold ratio increases.	170

LIST OF TABLES

TABLE		Page
3.1	Fraction of Au^{3+} and Au^0 Determined by XANES and Parameters of EXAFS Characterization.	69
4.1	Quantities of various species on Au/TiO_2 .	108
6.1	EXAFS fit parameters for AuCl_4^- solutions in anhydrous methanol (k^2 , $\Delta k=3.37\text{-}12.3 \text{ \AA}^{-1}$; $430 \mu\text{M Au}^{3+}$, $\text{Cl}^-/\text{Au}^{3+}=1070$).	142
6.2	Molar absorptivity ε experimentally determined for aqueous solutions of AuCl_4^- and the corresponding overall Au-Cl CN as given by Eq. (6.7). Entries in columns 4-7 represent each of the terms in Eq. (6.7), which were determined by solving the equilibrium expressions for reactions (6.1-6.6) using reported values of the hydrolysis constants. ²⁸⁻³³ $[\text{Au}^{3+}]=72 \mu\text{M}$, $\text{Cl}^-/\text{Au}^{3+}=1070$.	145
6.3	EXAFS fit parameters for Au^{3+}/DN and $\text{Au}^{3+}/\text{APMBTSS}$ solutions in anhydrous methanol (k^2 , $\Delta k=3.37\text{-}11.6 \text{ \AA}^{-1}$; $430 \mu\text{M Au}^{3+}$).	155
6.4	Conditional formation constants of gold-amine complexes formed by reaction of HAuCl_4 and APMBTSS (90 min) or DN (90 min and 48 h). Data calculated from the experimental results presented in Figure 6.10, using Eq. (6.12). The last column was determined using Eq. (6.14).	167

CHAPTER 1

INTRODUCTION

1.1 Motivation/Objective

This work has been motivated in part by the desire to gain a better understanding of the properties of nanosized gold that make it an unusual catalyst for the oxidation of CO at low temperature. It was also prompted by the wish to explore the chemical properties and possible applications of a novel nanocage developed in our laboratory three years ago.

Since it was discovered that gold nanoparticles are very active for the oxidation of CO at temperatures as low as $-70\text{ }^{\circ}\text{C}$ almost 20 years ago,¹ much research has been devoted to the understanding of the origin of this remarkable activity. With time, it has been found that supported gold also catalyzes other reactions of commercial importance, including vapor phase epoxidation of propylene with H_2 and O_2 ,²⁻⁴ hydrochlorination,⁵ selective hydrogenation,⁶⁻⁹ selective oxidation of CO,¹⁰ water-gas shift,^{11,12} selective oxidation of hydrocarbons,¹³⁻¹⁶ and selective reduction of NO by hydrocarbons.¹⁷ For these reactions, certain gold catalysts appear to provide not only high activity but also a remarkable selectivity. Most published research on catalysis by supported gold has centered on the oxidation of CO. This reaction is not only practically relevant to well known applications, but more importantly, its understanding will facilitate the comprehension of fundamental aspects of more complicated reactions of selective oxidation. One of the major issues not yet resolved in the gold-catalyzed oxidation of CO, is the oxidation state of gold in the active catalysts.¹⁸ Some authors report that the active site consists of cationic gold,^{12,19} others claim that an ensemble of zero-valent and cationic gold is

required,²⁰⁻²² while some authors argue that the active site consists of electron-rich Au.²³ The lack of consensus is, in part, due to differences in preparation and post-treatment conditions of the catalyst and the absence of in-situ characterizations relevant to the catalyst in its steady-state. Closely related to the issue of the nature of the oxidation state, is that of the reaction mechanism, which is not yet fully understood. The first part of this work has been devoted to the understanding of these two interrelated aspects of the oxidation of CO by supported gold, focusing on the case of Au/TiO₂.

The nanocages which are the main subject of the second part of this project, were developed in an attempt to control the nature and localization of active sites in a well defined nanostructure.²⁴ Such a structure could allow fine control of catalytic activity and selectivity, for instance, by tuning the proximity among active sites,²⁵⁻²⁷ changing the nature of a fraction of the active sites or by modification of the environment around those sites.²⁸⁻³¹ There are a lot of examples in nature in which such changes lead to significant changes in catalytic performance.³²⁻³⁴ By active sites, it is meant chemical groups that are capable of performing catalysis, alone or in cooperation with other functionalities, as well as groups that engage in binding with transition metals. In the research reported here, these active sites are primary amine groups located inside the nanocage, which is a hollow structure with spherical symmetry and a diameter of about 2.3 nm. The nanocages consist of a siloxane shell, one atomic layer thick, with pores allowing diffusion of molecules. These pores also prevent bulky molecules from entering the nanocage, giving the material size selectivity properties. One key question is particularly intriguing: does the confinement of the amine groups inside the nanocage modify their chemical properties as compared to unconstrained amines? The question is of high relevance when the potential of this novel material is considered, both as a catalyst and as a nano-reactor. Therefore,

the second part of this work focused on establishing whether confinement induced any changes, specifically in the Brønsted basicity of the amines.

The first part of this work, which is related to the gold-catalyzed oxidation of CO, has two objectives: (1) to construct a relationship between catalytic activity and gold structure, as a means to identify the oxidation state of gold in an active catalyst. (2) to measure the rates of reaction of adsorbed species relevant to the reaction under steady state conditions, as a means to enhance the understanding the reaction mechanism.

The objective of the second part of this work, which focuses on the study of the properties of the siloxane nanocages, is to determine if the confinement of amine inside the nanocage induces changes on their Brønsted basicity, as compared to the same amines in solution.

In order to provide a framework for the discussion in the subsequent chapters, a short introduction to the two topics studied in this dissertation is given below.

1.2 Oxidation of CO catalyzed by supported gold

Four major unresolved issues in the understanding of the oxidation of CO by supported gold are:¹⁸ (i) the role of the support on the activity of the catalyst, (ii) the oxidation state of gold necessary for high catalytic activity, (iii) the effect of the moisture in the reaction feed on the catalytic activity and (iv) the causes of the high activity of small gold particles and for the strong dependence on particle size and morphology. There are several reviews discussing some or all of these issues.^{18,22,35-37} Since this work focuses only on the determination of the oxidation state required for high activity and some aspects of the reaction mechanism, a brief overview of these two subjects is provided.

1.2.1 Oxidation state of gold at the active site

It has been proposed by several researchers that zerovalent gold is required for high catalytic activity. For instance, as early as 1993 Haruta et al.³⁸ indicated that catalysts containing metallic nanoparticles generated by calcination at 400 °C of materials prepared by co-precipitation or deposition precipitation on TiO₂, α -Fe₂O₃, Co₃O₄ and Al₂O₃, were highly active. However, they stressed that the sole presence of metallic gold was not enough for high activity; instead, the metallic nanoparticles had to be firmly attached to the support by epitaxial contact, dislocations or contact with an amorphous layer. More recently, Zanella et al.³⁹ reported the activity of Au/TiO₂ catalyst prepared by deposition-precipitation as a function of the preparation method and calcination temperature between 100 and 400 °C; in their study, they found that the catalytic activity increased with the percentage of metallic gold, being maximum for the catalyst calcined at 200 °C. Their XANES characterization indicated that the catalysts exclusively contained metallic gold. Similarly, several other authors have suggested that the active center for oxidation of CO requires metallic gold;⁴⁰⁻⁴² although they didn't present any evidence supporting the existence of cationic gold species, they do not disregard the possibility that those species could exist in very small concentration (below detection limit). Theoretical studies exist which try to explain why the experimentally observed gold nanoparticles are active for CO oxidation. DFT calculations performed on model Au(111) surfaces indicated that adsorption of CO and O on step sites was significantly stronger than the adsorption on the (111) terraces;⁴³ strain due to mismatch at the gold-support interface generated similar results. Based on these calculations, the authors reasoned that the unusual catalytic activity of highly-dispersed Au particles is in part due to the high density of step sites as the gold nanoparticles become smaller. A decrease in the size also increased the density of strains resulting on more adsorption sites. Later, the same authors

reported calculations for the adsorption of O_2 on model surfaces of gold.⁴⁴ They found that no adsorption took place on Au(111); however some adsorption was predicted to occur on a stretched Au(111) surface or a Au(211) surface, both stretched and unstretched. Once again, their calculations suggested that the highly dispersed gold nanoparticles used in the oxidation of CO contain a high density of steps and tensile strain sites that substantially facilitate the activation of O_2 on the nanoparticles.

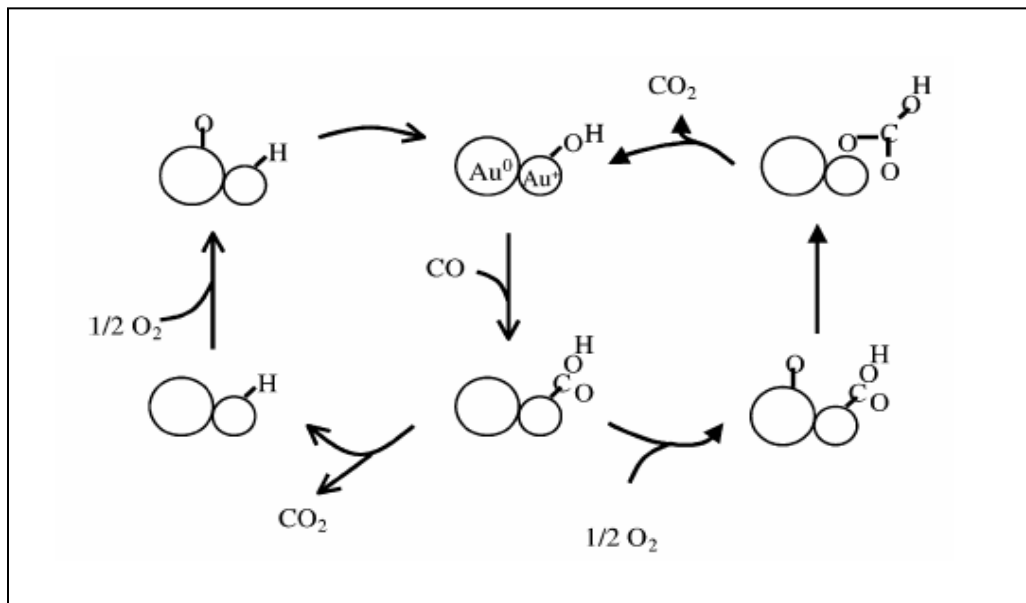
There are also observations pointing to the role of cationic gold as the active species in the oxidation of CO at low temperature. Using a catalysis prepared by coprecipitation of $HAuCl_4$, $Fe(NO_3)_3 \cdot 9H_2O$ and Na_2CO_3 , Hutchings et al.^{45,46} observed that samples calcined in air at 400 °C exhibit very low catalytic activity, despite the fact that they consist of Au metal particles (on crystalline hematite platelets) of 3-5 nm. On the contrary, samples dried at 120 °C, containing non-crystalline $AuOOH \cdot xH_2O$ with poorly crystallized ferrihydrite $Fe_3HO_8 \cdot 4H_2O$ were found to be highly active, suggesting the role of gold oxyhydroxide (Au^{3+}) as an active phase for CO oxidation. Other investigators have associated high catalytic activity to the presence of cationic gold for samples prepared by deposition precipitation on TiO_2 , Al_2O_3 and Fe_2O_3 .⁴⁷ By a combination of XAS and XPS, they established that a phase transition from $Au(OH)_3$ to Au_2O_3 to metallic gold occurred with increasing calcinations temperature. This transformation paralleled a decrease in catalytic activity. As a result, they concluded that the oxidized gold species were more active than metallic gold for this reaction.

1.2.2 Reaction mechanism

It was suggested by Bond and Thompson²² that the active site responsible for CO oxidation consisted of an ensemble of $Au(OH)_3$ and metallic gold, with the ionic gold species

Scheme 1.1

Proposed mechanism of reaction for the oxidation of CO on a supported gold catalyst (after Costello et al.²¹)



acting as a “glue” between the metallic particle and the support. A similar model was later supported by the observations of Costello et al. during deactivation and regeneration of a highly active Au/Al₂O₃ catalyst.²¹ In these experiments, a rapid loss of activity with time on stream occurred, which could be prevented if hydrogen or water vapor was present in the feed. Deactivation was reversible, as a deactivated catalyst could be regenerated at room temperature with a flow containing either hydrogen or water vapor. When the catalyst was treated above 100 °C in a dry atmosphere, deactivation took place. Based on these findings, these researchers postulated that a hydroxyl groups, presumably associated with a Au⁺ cation was a main component of the active site. Cationic gold was presumably stabilized at defects sites on the alumina surface. They tried to selectively poison these sites with chloride ions and found that a Cl/Au ratio < 10⁻³ suppressed catalytic activity by a factor > 10, which suggests that the density

of active sites is very low.⁴⁸ Further evidence supporting the key role of hydroxyl groups as a component of the active site, came from the study of a deuterium isotope effect in the reaction using a feed with H₂ and H₂O.²⁰ Consistently with all these observations, they proposed a reaction mechanism in which the active site consists of an ensemble of Au⁺–OH[–] sites in close contact with the metallic nanoparticles and the support, as illustrated in Scheme 1.1.²¹ The oxidation of CO was proposed to proceed via the insertion of CO into the Au⁺–OH[–] bond to form a hydroxycarbonyl, which is oxidized to a bicarbonate. Decarboxylation of the bicarbonate completes the reaction cycle. The model postulates that oxidation of the hydroxycarbonyl is carried out by an oxygen atom formed by dissociative adsorption on the gold nanoparticle. This reaction model excludes the participation superoxide ions.^{38,49-52}

In the model proposed by Bond and Thompson, the reaction proceeds via a different pathway.²² First, CO is adsorbed on metallic gold (Au⁰–CO), while a hydroxyl ion migrates from the support to the Au⁰/Au³⁺ boundary binding the cation and generating an anion vacancy (Au²⁺–OH). This OH[–] group subsequently reacts with adsorbed CO forming a carboxylate group attached to Au²⁺ (Au²⁺–COOH) which leaves Au⁰ surface free for subsequent adsorption. Activation of oxygen occurs on the support through the formation of superoxide ions (O₂[–]–□_s). Reaction of the superoxide with one carboxylate releases Au²⁺, CO₂ and the intermediate HO₂[–]–□_s which in turn attacks another carboxylate generating Au²⁺, CO₂ and 2OH[–]. The hydroxyl ions return to the support with the consequent reoxidation of Au²⁺ to Au³⁺, closing the catalytic cycle.

Haruta also postulated a model for the reaction in which the perimeter interface plays an important role.⁵³ Based on a study of the activation energy for the reaction on Au/TiO₂, he suggested three different pathways operating at different temperature ranges. According to his

model, below 200K the reaction occurs at step, edge, and corner sites on the Au particles, with apparent activation energies of zero kJ/mol. Activation of CO and O₂ is presumed to take place at these sites on the gold nanoparticles. There is no reaction on the support or at the perimeter interface between Au⁰ and TiO₂ because those sites are covered with carbonate species generated by the reaction. Between 200 and 300K, the reaction proceeds at the perimeter interface, which are partly covered with carbonate species. The coverage of species changes with temperature giving place to an apparent activation energy of 30 kJ/mol. Above 300K, the reaction proceeds at the perimeter interfaces, between CO activated on the gold nanoparticles and O₂ adsorbed on the support. In this case the reaction occurs much faster with an apparent activation energy of zero kJ/mol.

1.3 Examples of properties exhibited by nanoconfined structures

As observed on several biological systems, confinement at the nanoscale induces unusual physical and chemical properties. The most obvious effect of confinement is that of enhanced local concentration, which is partially responsible for the enormous reaction rates observed on enzymes.³²⁻³⁴ Although for these systems the acidic and basic groups performing catalysis are weak compared to hydrogen or hydroxide ions, their proximity to the substrates in the active sites on enzyme-substrate complexes allow them to react very fast. The enhanced local concentration is a consequence of the very high packing at the active center of the enzymes. Typical packing densities of liquids are 0.5 and those of solids are greater than 0.6; near the surface of a protein the packing density may be about 0.60-0.65; deep in the interior it ranges between 0.70-0.85.³² But there is one more advantage besides the high effective concentration of

active groups relative to the substrate; the closeness of active site and substrate eliminates the requirement of a bimolecular collision, which makes the reaction entropically favored.³²

Variations in chemical properties also arise from changes in the microenvironment around active groups. For instance, large pK_a shifts for buried acidic and basic residues of enzymes have been observed by structural deformations occurring during reaction or by folding/unfolding.^{32-34,54} For lysozyme and of staphylococcal nuclease, pK_a shifts of up to 4.7 units are common.⁵⁵ Smaller pK_a shifts have also been reported for Calbindin⁵⁶ and Elastin polymers.⁵⁷ These variations are usually rationalized in terms of electrostatic interactions between the hydrolysable groups^{54,56,58-61} or as of hydrophobic interactions with the microenvironment.^{55,57,61-67} This hydrophobic interaction arises from a repulsive free energy of interaction between the hydration shells of hydrophobic and polar groups when they are sufficiently close to each other.^{57,61-63} pK_a shifts are not restricted to proteins but have also been induced in synthetic peptides with carboxyl side chains by chain stretching (mechanical stretching).⁶⁸ Stretching increases the mean distance between charges, releasing charge-charge repulsion with the consequent discharge of protons into the medium.⁶⁸ However, the proton dissociation is modulated by an increment in the hydrophobic interaction, due to exposure of hydrophobic residues, as the chain is strained.⁶⁸ Marked changes in chemical properties result from other variations near the active sites. For instance, it has been observed that the polar environment around Asp102 in trypsin can be altered by replacement of the adjacent aminoacid Ser214 with Lys and Glu, with minor structural changes around catalytic center.⁶⁹ This disruption however, results in strong depletion of the catalytic activity of the this protease, where the modified structures exhibit 1% and 44% of the original activity, respectively.⁶⁹

Early evidence of pK_a shifts exists for polyelectrolyte solutions, indicating that the values were dependent on external conditions like the degree of neutralization and ionic strength.^{70,71} PAMAM dendrimers also exhibit interesting properties as a result of nano-confinement. Studies of Cu^{2+} binding to such dendrimers using EPR reveal that the protonation tendency of the amines strongly depend upon their location in the structure; as a result, the distribution of copper in the dendrimer is highly dependent on the bulk pH.⁷²⁻⁷³ At low pH the peripheral amines are protonated but only partial protonation occurs at the interior; since protons compete with Cu^{2+} for the binding sites, the metal cations are localized towards the interior of the structure. As pH increases, binding of copper also takes place at the dendrimer's external layers.⁷²⁻⁷³ It has been demonstrated that the internal tertiary amines of hydroxyl-terminated dendrimers have a $pK_a=6.3$, which is 1-2 pH units lower than expected for a single amine in solution; it is believed that the hydrophobic microenvironment within the dendrimer is responsible for this difference.⁷⁴ Contrarily, the peripheral amines in the amine-terminated dendrimers are protonated at the same pH as primary amines in solution ($pK_a=9.23$), because the microenvironment around them is more hydrophilic.⁷⁴⁻⁷⁵

1.4 Summary

This dissertation comprises two parts. In the first part (Chapters 3 and 4), two related aspects of the catalytic oxidation of CO at low temperature over Au/TiO₂ are considered: (i) the oxidation state required for high activity and (ii) the reaction mechanism, through the identification and quantification of surface species relevant to the reaction. The second part reports the synthesis of siloxane nanocages (Chapter 5) and studies the response of the primary amine groups inside those nanocages to protonation, as a result of variations in the external pH

(Chapter 6). The dissertation starts with a detailed presentation in Chapter 2, of the main experimental techniques used throughout this research. Chapter 3 focuses on the development of a relationship between catalytic activity and the oxidation state of gold on the Au/TiO₂ catalyst, for the oxidation of CO at sub-ambient temperatures. This was done via a combination of in-situ techniques that permitted to probe the structure of the catalyst while it was activated in a controlled manner. Chapter 4 goes into the details of the role of metallic gold and the identification of adsorbed species relevant to the reaction. Here in-situ XANES and FTIR, mass spectrometry and isotopic labeling were used in combination to provide a description of the main changes occurring on the catalyst while the reaction was taking place under steady-state and transient conditions. Chapter 5 centers on the synthesis and characterization of siloxane nanocages of 2 nm, which contain propylamine groups tethered to the interior. ¹H-NMR together with Dynamic Light Scattering (DLS) was used to characterize the different steps during the synthesis of the material. Quantification of the amine groups at the nanocages' interior was done by titration with ninhydrin to generate a chromophore that was easily determined by UV-VIS spectroscopy. The use of techniques like flash chromatography and dialysis in the purification of different reactants and products is also discussed. Chapter 6 concentrates on the study of the chemical properties of the amine groups at the interior of the nanocages. Using binding of Au³⁺ to the amine groups as a probe, the effect of the bulk pH on the protonation of the amine groups has been established by means of XANES, EXAFS, UV-VIS and cyclic voltammetry. Ultimately, these results reveal the existence of a confinement effect at the nanoscale that confers unusual properties to this novel material (the nanocage), both as a catalyst and as a nanoreactor where the controlled synthesis of some other materials of interest in catalysis and medicine could be carried out. The dissertation ends with Chapter 7, in which the main accomplishments of this

research are summarized. Some recommendations for future work in order to build a more comprehensive picture of the reaction mechanism for the oxidation of CO on supported gold as well as a discussion on some exciting opportunities offered by the novel nanocage, are also included.

This dissertation offers some answers to key questions on the oxidation of CO on supported gold, related to the nature of the active site and the reaction mechanism. It also illustrates the surge of unusual properties due to confinement at the nanoscale. As a whole, it contributes some important results to the dynamic area of catalysis by gold and lays the foundations for future studies on the use of the siloxane nanocages for catalytic applications and the controlled synthesis of advanced materials.

CHAPTER 2

EXPERIMENTAL

2.1 Oxidation of CO on Au/TiO₂

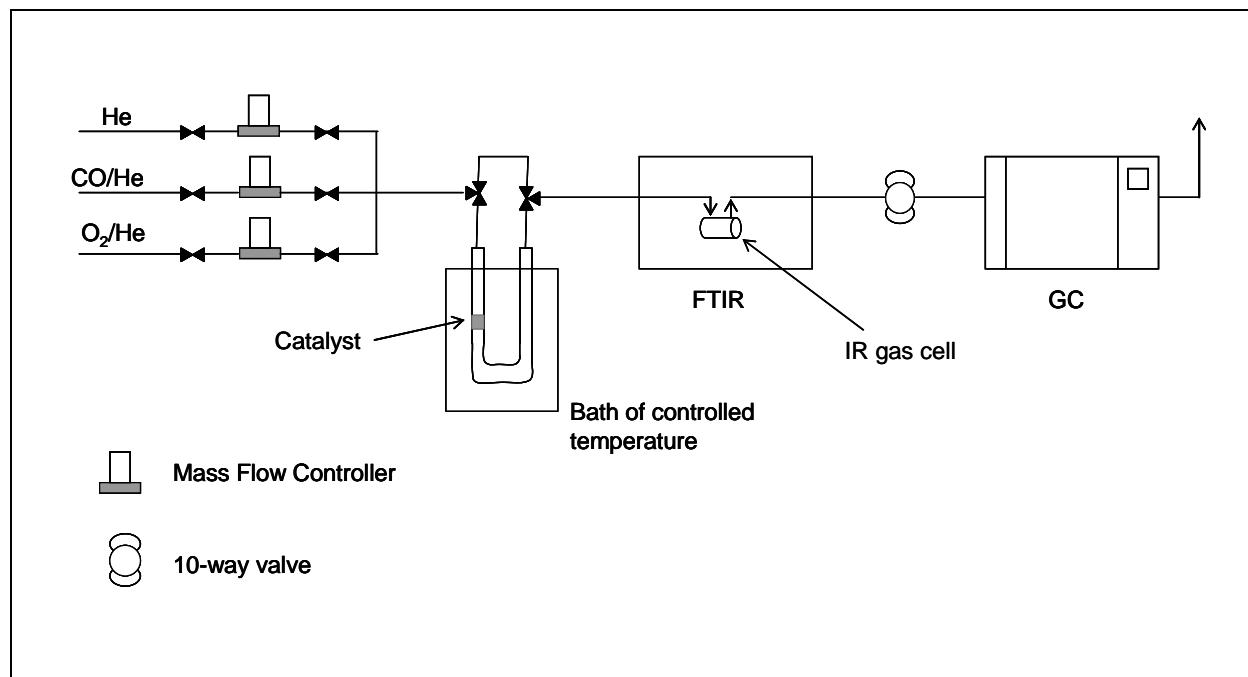
Catalytic activity measurements were performed using 100 mg of powdered catalyst, supported between two acid-washed glass wool slugs inside a U-shaped quartz microreactor (ID=5mm). The reaction was conducted at different temperatures ranging from -77 °C to 20 °C. Below 0 °C, temperature was controlled by immersing the reactor into an isopropanol/dry-ice bath, whose temperature was controlled to ± 2 °C by adjusting the amount of dry ice in the bath. At 0 °C, temperature was controlled with a water/ice bath; at 20 °C, the reactor was submerged into a water bath. The reaction mixture consisted of 1% CO, 2.5% O₂ and balance He, supplied at near atmospheric pressure. Depending on the reaction temperature, the total flow rate was adjusted to 30-200 mL/min with mass flow controllers (Brooks 5850C), in order to achieve approximately 80% CO conversion. Scheme 2.1 illustrates the reaction system employed. The gases leaving the reactor were analyzed by Fourier Transform Infrared Spectroscopy (FTIR), gas chromatography (GC) or an FTIR/GC arrangement in series.

A Perkin Elmer GX2000 FTIR spectrometer equipped with a mercury cadmium telluride (MCT) detector, was used to quantify gas phase CO. The gases were passed through a 35 mL cylindrical glass cell with CaF₂ windows, located inside the FTIR in a compartment purged with dry N₂ to minimize background moisture.

A HP 5890 Series II gas chromatograph furnished with a molecular sieve 13X and a Haysep Q packed column was used. Separation of O₂ and CO was performed in the 13X column, whereas CO₂ was separated with the Haysep Q column, both at 100 °C. Quantification

Scheme 2.1

Reaction system used to test catalytic activity for oxidation of CO with Au/TiO₂.



was carried out by two thermal conductivity detectors (TCD) at the end of each column, using He as carrier/reference gas.

The tandem arrangement used the GC described above, downstream of a Nicolet Nexus 670 FTIR spectrometer equipped with a MCT detector. Once again, the gasses passed through a 35 mL glass cell inside a chamber purged with dry N₂, where they were analyzed.

The FTIR data were acquired every 40 seconds, as an average of 5 scans at a resolution of 0.5 cm⁻¹. The conversion of CO was calculated based on the changes in the intensity of the rotational band at 2147 cm⁻¹, since this band followed Beer's law in the concentration range studied. At the start of the experiment, the initial concentration of CO with correspondent absorbance A_o , was determined. At time zero the mixture was passed through the catalyst bed

and the intensity of the 2147 cm^{-1} band was recorded as a function of time. The conversion of CO was calculated as follows:

$$X_{CO} = \frac{A_0 - A}{A_0} \times 100$$

where A represents the absorbance at 2147 cm^{-1} at any given time. Calculations based on changes on the CO_2 bands were inaccurate, due to random changes in the concentration of this gas outside the glass cell, inside the FTIR chamber.

Similarly, calibration values for CO and O_2 were determined by GC, bypassing the reactor at the beginning of the experiment. Then, the reaction mixture was allowed to flow through the catalyst bed and subsequently into the GC. The area of the peaks corresponding to CO, O_2 and CO_2 were recorded as a function of time. The conversion of CO was calculated from the change in the CO peak area. The O_2 and CO_2 peaks were used to verify the mass balances. Both the carbon and oxygen mass balances were satisfied within 5%.

2.2 Characterization of Au/TiO₂

2.2.1 Chemical analysis

The gold loading of the catalysts was determined by X-ray Fluorescence (XRF) or by Inductively Coupled Plasma Atomic Emission Spectrometry (ICP-AES). The XRF analysis was performed using a Bruker S4 Explorer XRF analyzer. A calibration curve was obtained using five TiO_2 samples impregnated with increasing amounts of gold, by addition of diluted solutions prepared from an Au ICP standard. Standards and samples were analyzed as 100 mg pellets, in He atmosphere. For ICP analysis, 40 mg of catalyst was mixed with 1 mL of a HF/HNO_3 solution (3/1 ratio) and subsequently diluted to 50 mL. Before analysis, samples were first

allowed to digest for 12 h and then filtered to remove undissolved TiO_2 . Calibration samples were prepared by dilution of an Au ICP standard solution (Aldrich).

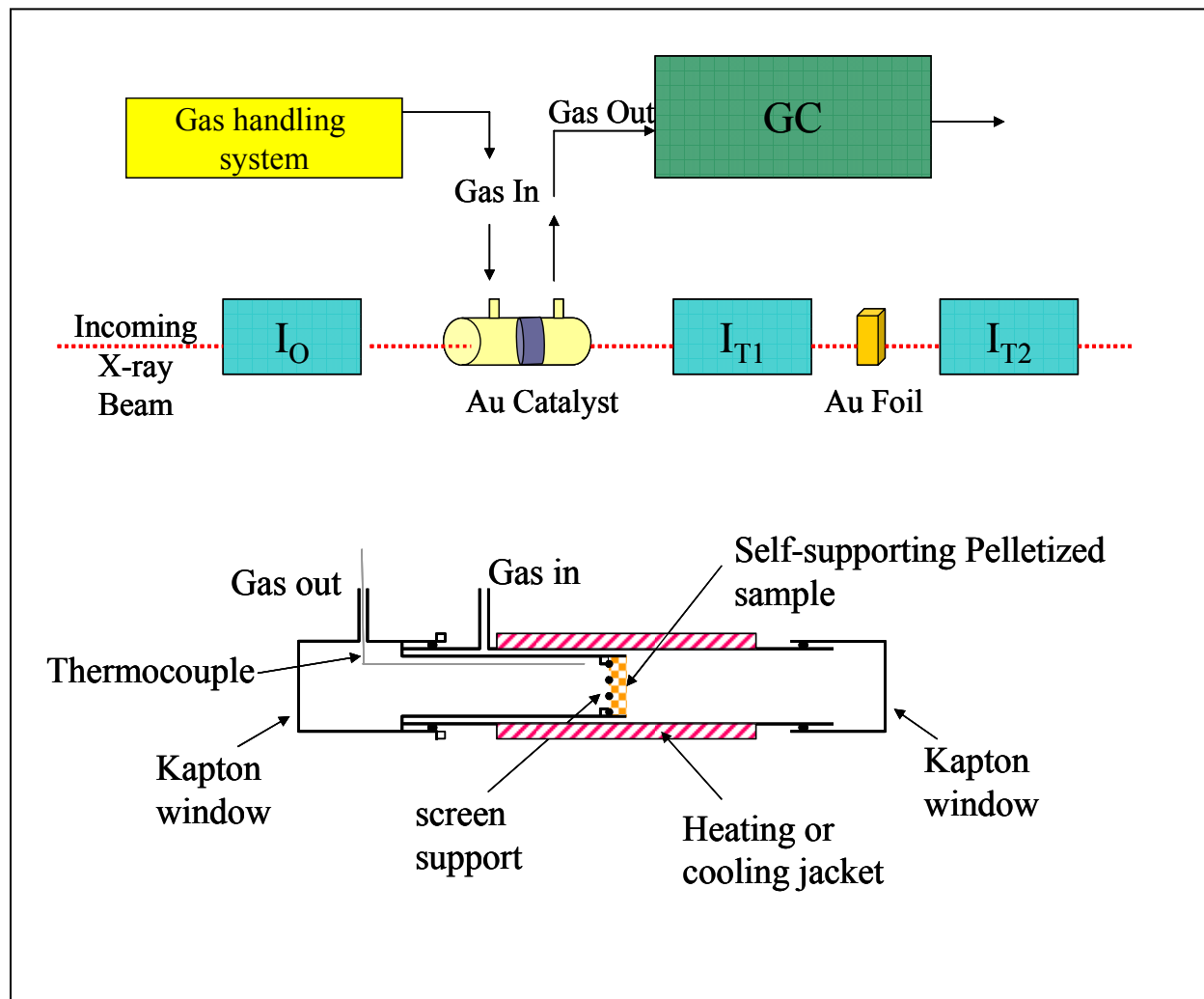
2.2.2 In-situ XANES/EXAFS

X-ray Absorption Spectroscopy (XAS) experiments were performed at the bending magnet beamline 5-BMD of the DuPont-Northwestern-Dow Collaborative Access Team (DND-CAT) at the Advanced Photon Source (APS) at Argonne National Laboratory. The beamline was equipped with a Si(111) double crystal monochromator, which was detuned to $\sim 70\%$ of the maximum intensity to minimize interference by harmonics. Samples were analyzed both in the transmission and the fluorescence mode. The experimental set-up used in each mode is illustrated in Schemes 2.2 and 2.3. In the transmission mode, three ionization chambers arranged in series were used to measure the intensity of the incident radiation (I_0), the radiation after the sample (I_1) and after a gold foil reference (I_2). Chambers 1 and 3 were filled with a mixture of He and Ar to achieve 15% absorption; chamber 2 was filled with a mixture of N_2 and Ar, giving place to absorption of 70% of the signal. In the fluorescence mode, a 13-element solid state detector oriented at 45° with respect to the sample was used. Signals from the 13 independent detectors were averaged before data analysis.

The transmission cell used in the *in-situ* XAS experiments, consisted of two concentric cylinders, the interior one having only half the length of the exterior. Typically, 100 mg of sample were pressed to a self supporting pellet that was placed at the end of the inner cylinder, between two nylon grids (see Scheme 2.2). X-ray transparent Kapton film was used to seal both ends of the cell. Gas entered the cell via the outer cylinder and was forced to flow through the sample into the inner cylinder before exiting. In order to perform experiments at subambient

Scheme 2.2

XAS set-up used to carry out experiments in the transmission mode. A diagram of the *in-situ* cell is provided (after J. H. Yang¹).

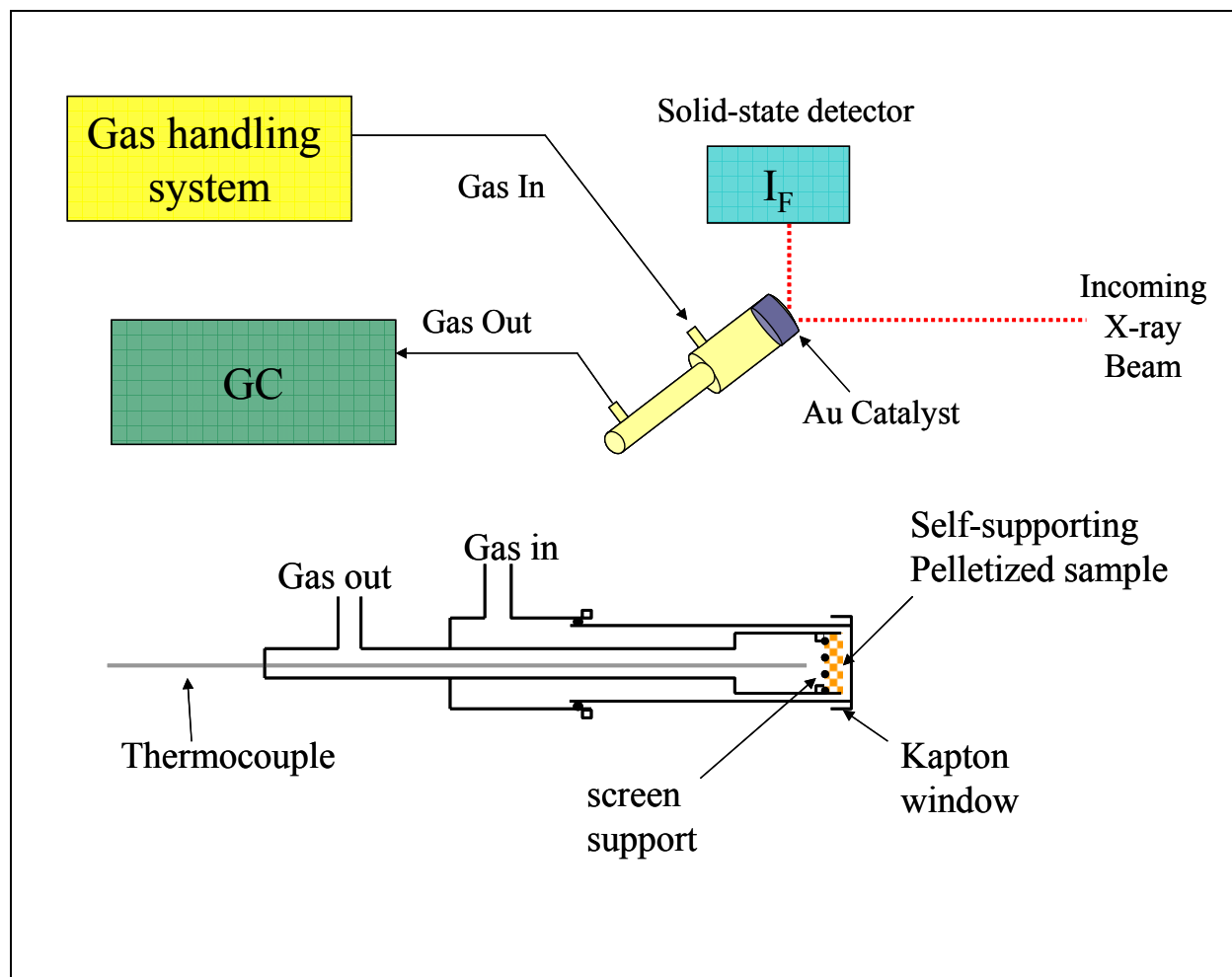


temperatures, the cell was placed inside a copper housing that was cooled with an ethanol/dry ice mixture; this configuration allowed to control temperature to ± 2 °C in the range from 0 to -77 °C. Temperature was monitored with a thermocouple located inside the cell, next to the sample pellet.

The fluorescence *in-situ* cell consisted of two concentric cylinders, arranged in a way that permitted the catalyst to be located at one of the ends of the cell (Scheme 2.3). 100 mg of sample

Scheme 2.3

XAS set-up used to carry out experiments in the fluorescence mode. A diagram of the *in-situ* cell is provided (after J. H. Yang¹).



was loaded as a pellet (Diam=1.59 cm) in a small compartment located at the end of the inner cylinder. When the cell was assembled, the tip of the inner cylinder containing the sample coincided with the end of the outer cylinder exposed to the X-rays. There, the outer cylinder was sealed with a Kapton film. Similarly to the transmission cell, gas entered via the outer cylinder and was forced to flow through the sample prior to exiting the cell. The temperature was monitored by a thermocouple located inside the inner cylinder, in close proximity to the catalyst.

Subambient temperatures were achieved by placing the cell in the copper block previously described.

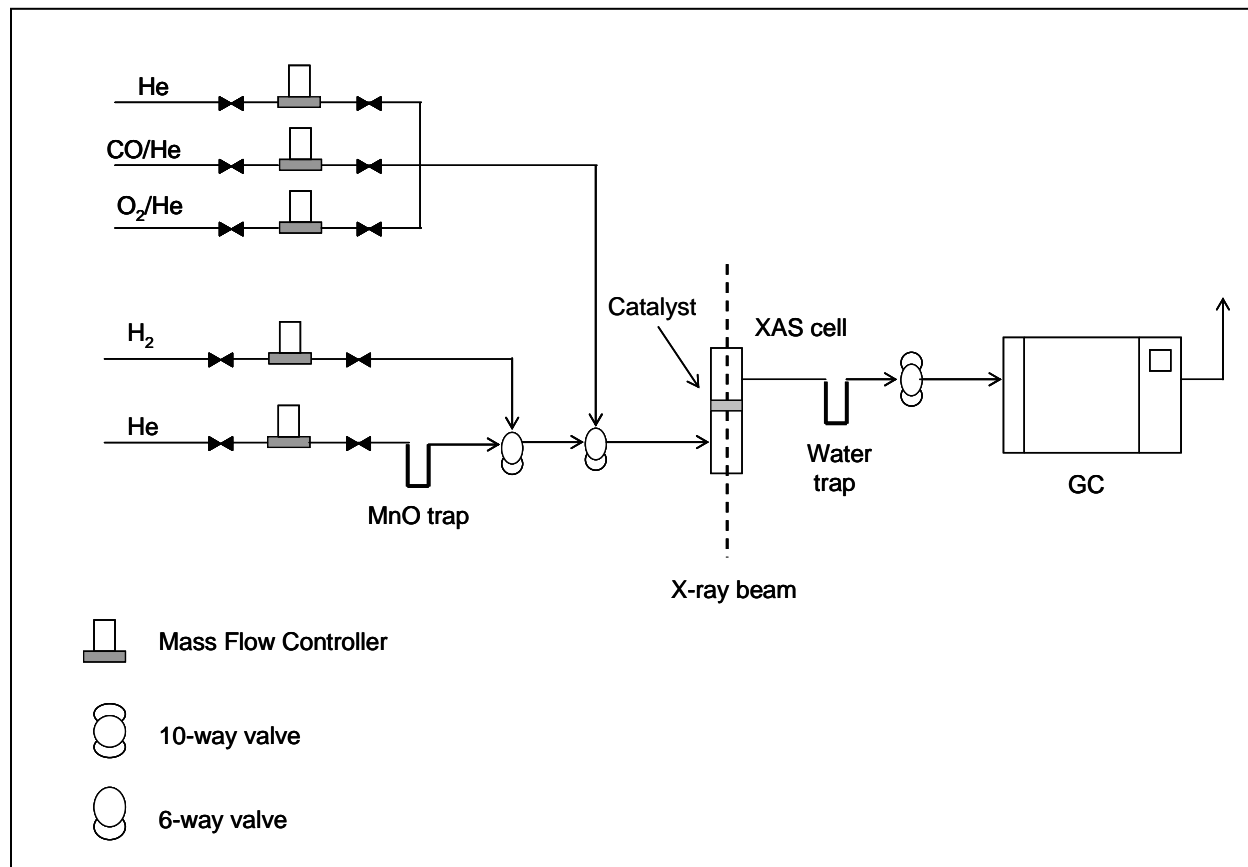
Control experiments indicated that bypass through both cells was minimum. A gas delivering system similar to the one described in section 2.1 was used to test the activity of the catalyst while its structure was probed by EXAFS/XANES. 1% CO and 2.5% O₂ in He were typically used, at a total flow rate that depended on the reaction temperature. The flow and composition of the reaction mixture were controlled by mass flow controllers. A GC (HP 6890) equipped with a 13X molecular sieve packed column and a TCD detector, was used to quantify changes in the concentration of CO in the gas leaving the in-situ cell.

2.2.3 Controlled reduction using H₂ pulses

Controlled reduction of as-prepared Au/TiO₂, which contained only cationic gold (Au³⁺), was performed by repeatedly pulsing 1mL of H₂ through the sample inside the *in-situ* XAS cell, at room temperature. The experiments were performed under oxygen-free conditions (~ 10 ppm O₂), which was attained by placing a MnO trap immediately before the He mass flow controller. H₂ (Matheson 99.999%) was carried out to the sample by He, using a 6-way valve with a 1-mL loop. The water produced by as gold was reduced, was trapped in a cold trap located downstream the in-situ cell. The amount of H₂ consumed was determined by a TCD detector mounted in an HP 6890 gas chromatograph. In some instances, H₂ pulses were alternated with a CO/O₂ mixture through the catalyst; this was achieved by coupling the reaction system described above (section 2.1) with the H₂ pulse system, as depicted in Scheme 2.4.

Scheme 2.4

System used to reduce as-prepared Au/TiO₂ loaded into the *in-situ* XAS cell. This arrangement allows switching between H₂ pulses and a reaction mixture.



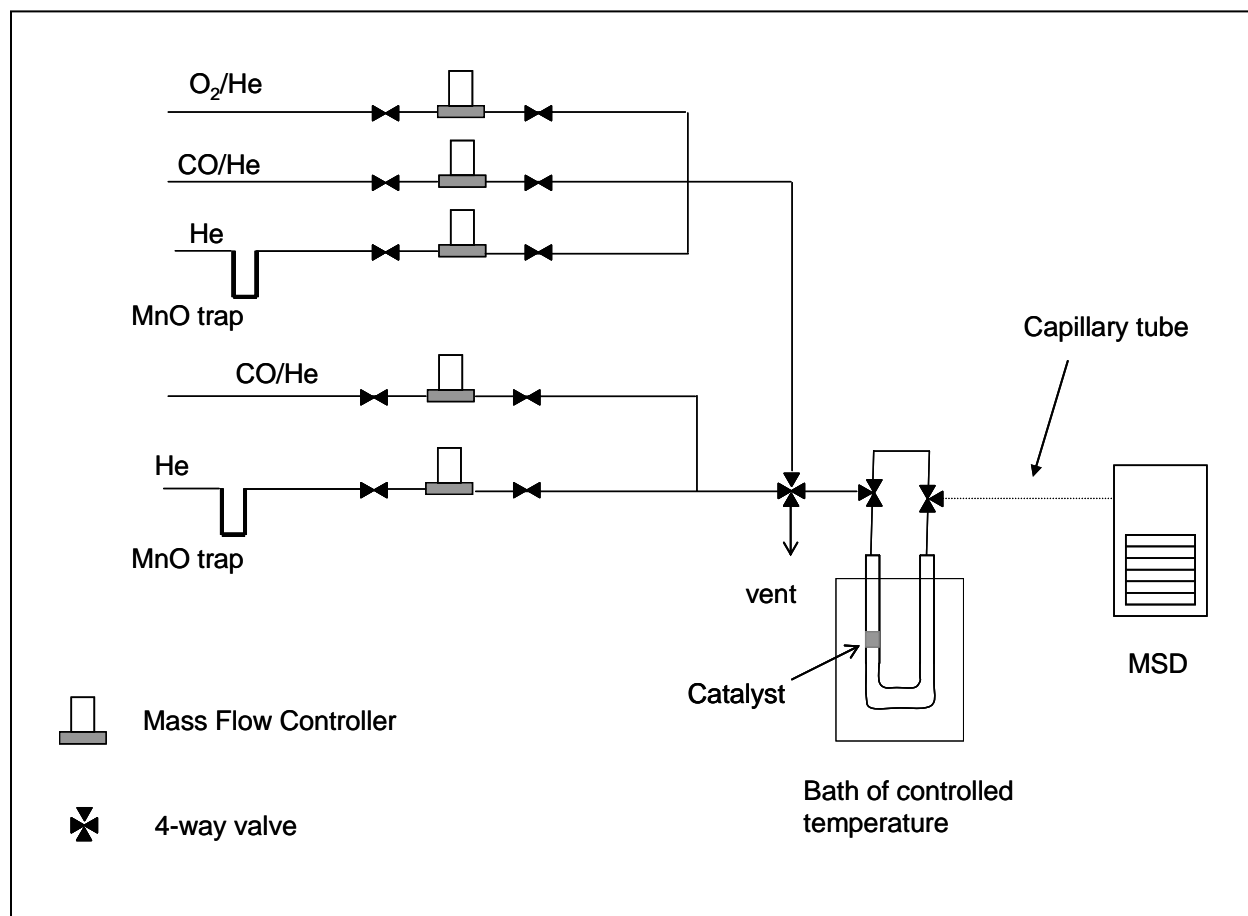
2.2.4 Mass spectrometry

Mass spectrometry was used to quantify the amount of CO adsorbed by a completely reduced Au/TiO₂ sample. It was also employed to follow the changes in the composition of the reactor effluent, as the catalyst was exposed to CO and O₂ under transient conditions. The experiments were carried out with the sample loaded in the powder form into a fused silica U-tube microreactor. Temperature was controlled by placing the reactor in an isopropanol/dry ice bath at -60 ± 1 °C. A 5973 HP Mass Selective Detector (MSD) was employed in the

identification and quantification of the different components in the reaction mixtures. The MSD detector was directly connected to the reactor effluent by a deactivated fused silica capillary tube (ID=0.05mm, L=1 m). Switching between different gases was attained with a four-way valve located right before the reactor inlet. The total flow of the gases in both sides of the four-way valve, were kept equal to eliminate any artifacts on the observed changes in the gas composition during the transients. The tubing length between the 4-way valve and reactor inlet as well as the reactor exit and the MSD, was minimized in order to reduce the response time in the MS. Scheme 2.5 illustrates the system layout.

Scheme 2.5

Reaction system used to perform the mass spectrometry experiments.



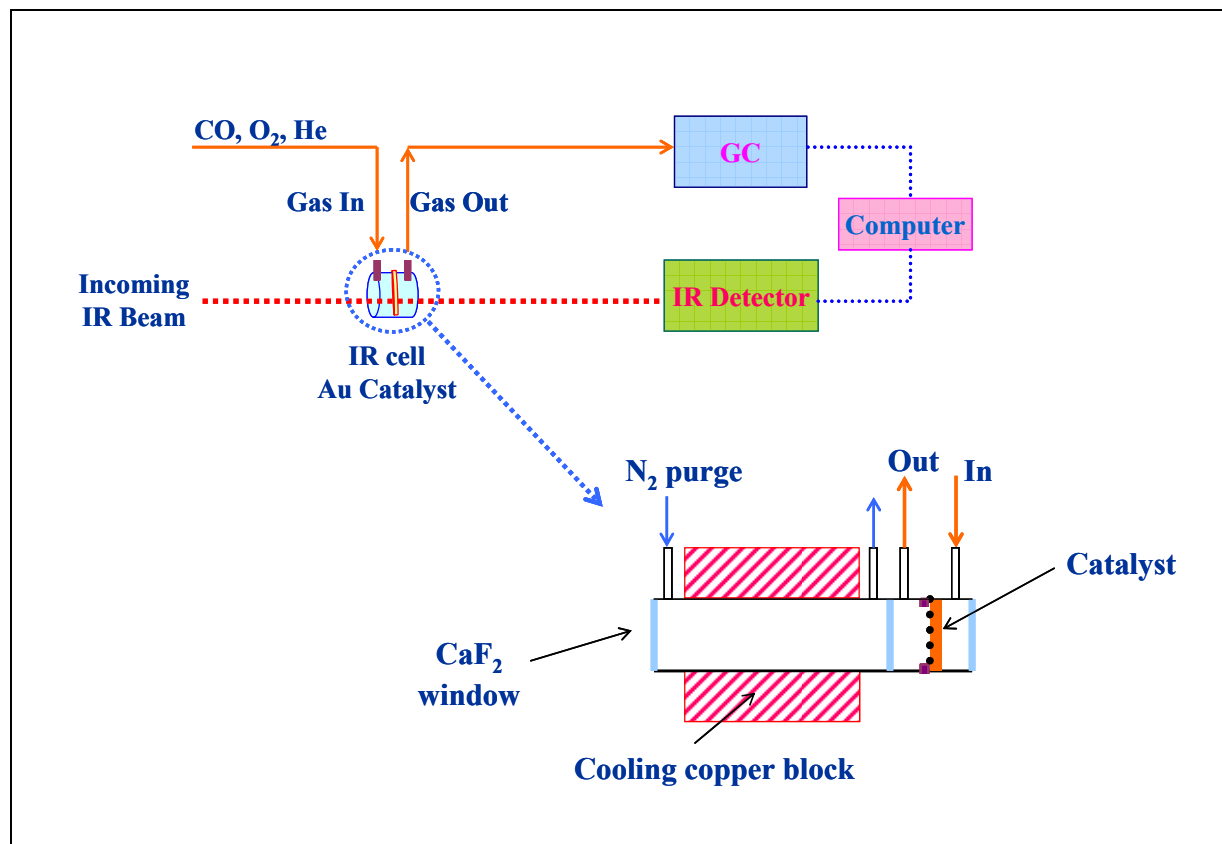
2.2.5 *In-situ* FTIR spectroscopy

A stainless steel cylindrical cell (L=2 cm, I.D.=2 cm) fitted with CaF₂ windows was used to carry out the experiments. Samples were loaded into the cell as self-supporting wafers of 20 mg; this amount of sample provided a good compromise between mechanical strength and IR transparency. The sample was placed on a tungsten mesh and further secured by a stainless steel ring, in order to prevent any movement as the cell was horizontally positioned. Control experiments demonstrated that negligible by-pass occurred when the sample was loaded in this manner. The cell was fixed to one side of a larger stainless steel tube furnished with a CaF₂ window at the other end (see Scheme 2.6). This configuration allowed attachment of the cell to a copper block that was used to cool it down to as low as -70 °C. Cooling was attained by addition of a mixture of isopropanol/dry ice (or dry ice/liquid nitrogen) to a compartment in the copper block; this allowed temperature to be controlled within 2 °C of the target value. The reaction mixture was pre-cooled in a coil at the interior of the copper block, before entering the IR cell. A sub-mini thermocouple assembly (Omega) located immediately downstream the catalyst was used to monitor the reaction temperature.

The ensemble cell-copper block was properly aligned in the analysis chamber of a Nicolet Nexus 670 FTIR spectrometer equipped with an MCT detector. The chamber was purged with 2 L/min of dry nitrogen in order to prevent freezing of water at the CaF₂ windows. The *in-situ* FTIR system was coupled to a gas handling system similar to the one described in Scheme 2.5, allowing the simultaneous study of the dynamic of surface species and catalytic activity. In this case, the gas stream exiting the IR cell was directed to a HP 6890 gas chromatograph.

Scheme 2.6

In-situ FTIR system detailing the cell used to study the kinetics of surface species on the catalyst.

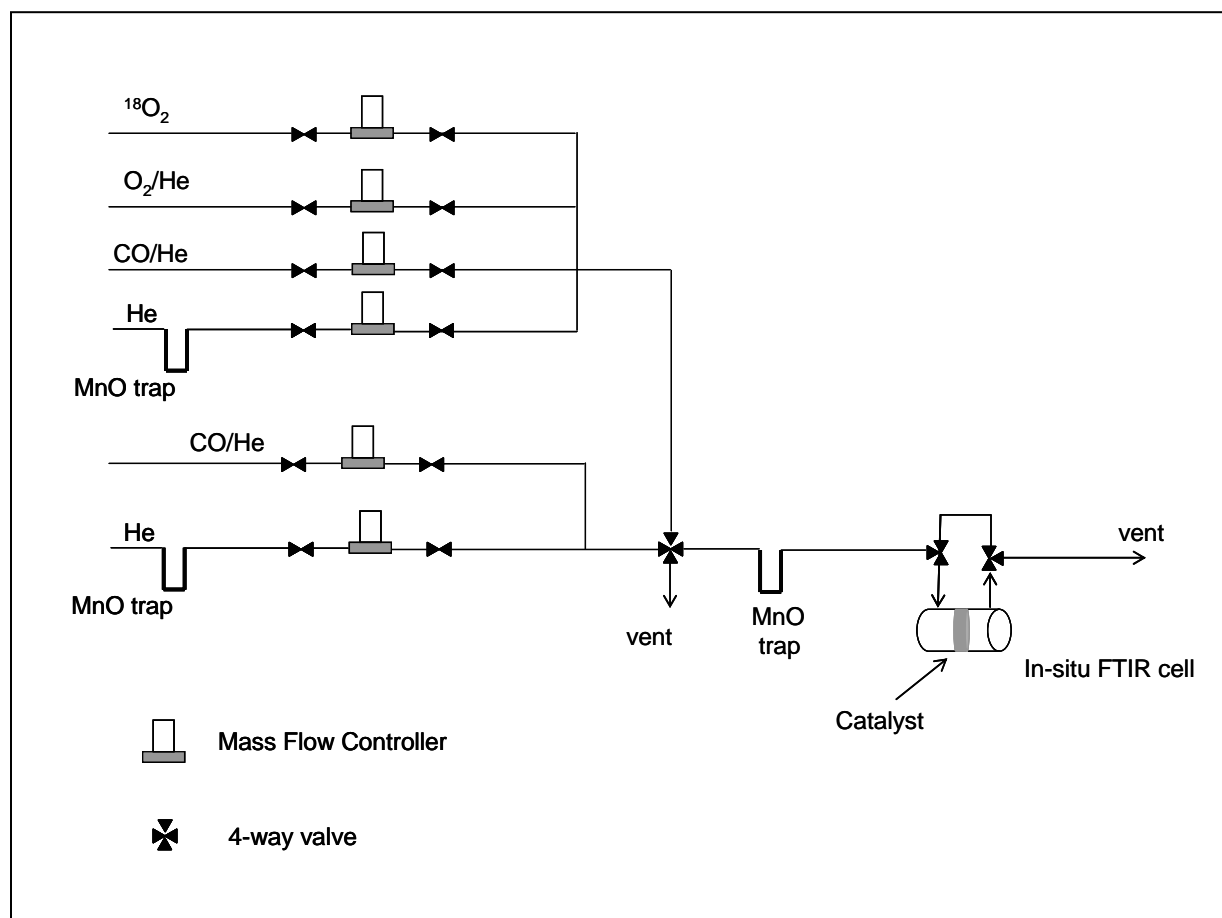


2.2.6 ¹⁸O isotopic labeling

The system shown in Scheme 2.7 was used to study the isotopic exchange of ¹⁸O₂ in the gas phase with oxygen atoms belonging to species adsorbed on Au/TiO₂ catalyst. It was composed of a gas delivery system coupled to the *in-situ* FTIR system described above. The gas delivery system easily allowed the switching between He, CO/He, O₂/He, CO/O₂/He, ¹⁸O₂ and CO/ ¹⁸O₂/He. As established by control experiments, this configuration permitted operation at oxygen levels below 10 ppm when an oxygen-free gas was required.

Scheme 2.7

System used on the study of ^{18}O isotopic exchange with surface species on Au/TiO₂ catalyst.



2.3 Characterization of siloxane nanocages

2.3.1 ^1H , ^{13}C and ^{29}Si NMR

NMR experiments were performed in the liquid phase, using Varian INOVA 400 and INOVA 500 spectrometers. Proton NMR was collected at 400.6 MHz and 499.5 MHz on the INOVA 400 and INOVA 500 instruments, respectively. Depending on the sample, the delay time was varied between 1 and 20 s allowing proper quantification. ^{13}C NMR was obtained at 100.7 and 125.6 MHz in the INOVA 400 and INOVA 500 spectrometers, using standard pulse sequences. Similarly, ^{29}Si NMR was acquired at 79.6 MHz in the INOVA 400 instrument using a

standard pulse sequence. Either TMS or the residual protons in the deuterated solvents were used as internal standards when studying chemical reactions and to reference the peaks. Chemical shifts are reported as ppm values with respect to TMS.

2.3.2 Dynamic Light Scattering

As described in Chapter 5, the synthesis of siloxane nanocages starts with the generation of micelles in ethanol. These micelles are then chemically modified in several stages to produce the nanocages. The size of the particles in solution, all the way from the micelles to the nanocages, was measured by Dynamic Light Scattering (DLS). DLS is a technique used to determine the size of particles in a liquid, by measuring their Brownian motion.² Brownian motion arises from the random collisions between the particles and the solvent surrounding them. An important feature of this motion is that small particles move faster than bigger particles.³ A relationship between the size of the particle and its diffusivity in solution is given by the Stokes-Einstein equation:⁴

$$D_i = \frac{kT}{6\pi\eta_o r_i} \quad (2.1)$$

where D_i is the diffusion coefficient of the particles, k is the Boltzmann constant, η_o the viscosity of the medium and r_i the hydrodynamic radius of the particles. Equation (2.1) strictly holds for highly diluted solutions of hard spheres with $r_o > r_i$;³ however, it can be used to obtain fairly good representations of many real systems under more general conditions.^{4,5}

In a DLS experiment the solution containing the particles of unknown size is illuminated with a laser, generating a time dependent scattering pattern that is analyzed with a digital correlator. The correlator measures the fluctuations in scattering intensity at a given point, in

terms of the degree of similarity between two signals over a period of time. If the signal intensity at a time t is compared with itself, a perfect correlation is obtained, since both signals are identical. However, if the signal at time t is compared to a signal at a much later time $t+\Delta t$, no correlation will exist since the particles are moving randomly. Therefore, an autocorrelation function of the intensity of the signal $I(t)$ has been defined, where a perfect correlation is reported as 1 and no correlation is reported as 0.^{4,6}

$$G_2(\tau) = \langle I(0) I(\tau) \rangle = \lim_{\tau \rightarrow \infty} \frac{1}{T} \int_0^\tau I(t) I(t + \tau) dt \quad (2.2)$$

where the scattering intensity at time zero is compared with that at a delayed time in the order of microseconds to milliseconds. Equation (2.2) is usually converted to a correlation function of the scattered electric field, as discussed elsewhere.⁴⁻⁶ It is the combination of equation (2.1) and the transformed version of equation (2.2) that allows the determination of the size of the particles in solution. Commercial software exists that is used to extract the decay rates for a number of size ranges from the experimental autocorrelation function, to generate a size distribution for the particles in solution.^{2,4-6}

The DLS results reported in this work were obtained with a Zetasizer Nano ZS instrument (Malvern Instruments Ltd.), capable of determining particle size in the range from 0.6 nm to 6 μm . This instrument was equipped with a 633 nm red laser and an attenuator located between the laser source and the sample, in order to optimize the intensity of the scattered light reaching the detector. Adjustment of the attenuator was automatically done by the instrument software. Data collection was performed by backscatter detection, with the detector located at 173° from the sample. This arrangement minimized multiple-scattering and interference by dust. In most cases, the samples were analyzed in polystyrene disposable cuvettes ($10 \times 10 \times 48$ mm,

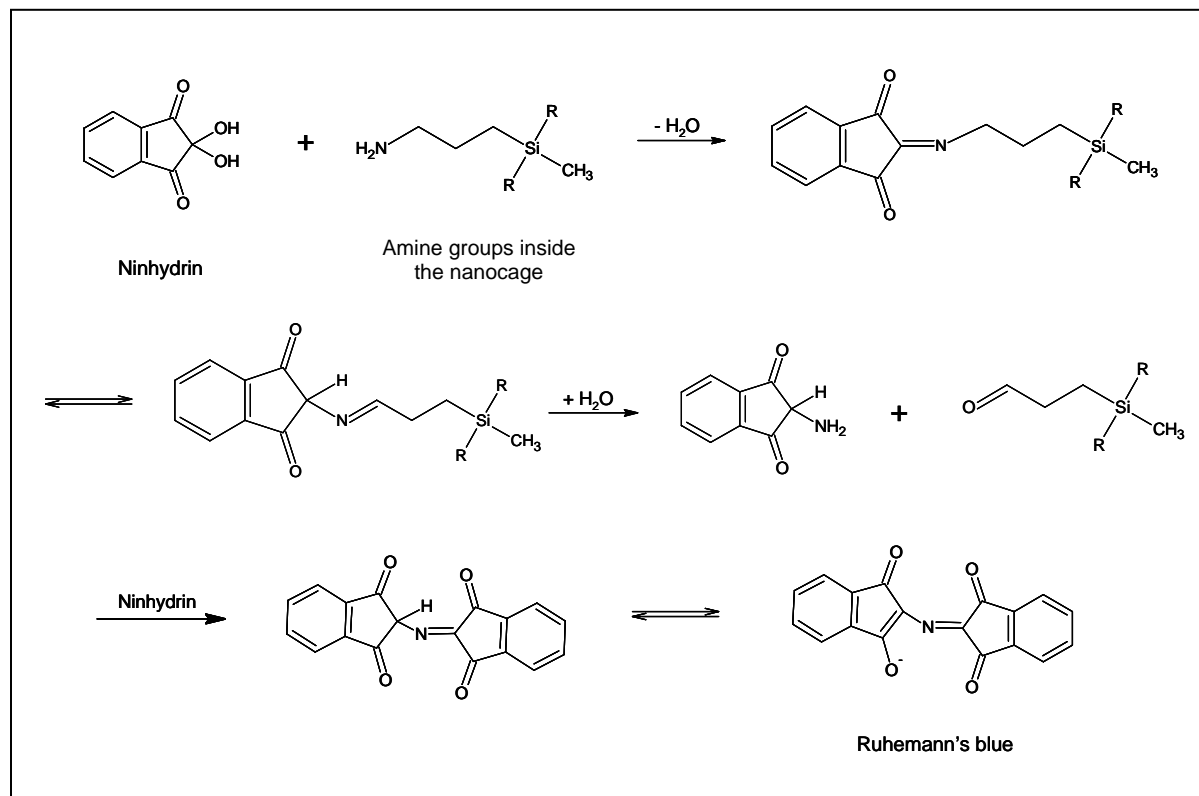
Sarstedt); however, for solutions in chloroform, a quartz cuvette ($10 \times 10 \times 48$ mm, Malvern Instruments Ltd.) was employed. For each sample, 3-7 measurements were acquired; each measurement was the average of 7-10 scans. Data processing was carried out with the commercial software provided by Malvern Instruments Ltd.²

2.3.3 Titration of amine groups

Quantification of primary amine groups tethered to the interior of the nanocage is required in order to understand the chemical properties of the nanocage (see Chapter 6). It also generates additional information on some of the physical properties of this material (see Chapter 5). Quantification was carried out by the Ninhydrin Reaction, commonly used to monitor completeness of amino acid coupling in Solid Phase Peptide Synthesis and Solid Phase Organic Synthesis.⁷ The reaction is illustrated in Scheme 2.8. As observed, there is a one-to-one correlation between the reacted primary amine and the formed chromophore (Ruhemann's blue), which is detected and quantified by UV-VIS spectroscopy at 573 nm. The Ninhydrin Reaction works in several solvents, including methanol, ethanol, chloroform and dichloromethane. In this work, the reaction was carried out in chloroform at 120 °C. Three stock solutions were required to perform the test. Stock solution 1 was prepared by addition of 40 g of phenol (Aldrich, 99.5%) to 10 mL of ethanol (Aldrich, 200 proof). Stock solution 2 was prepared in two steps; first 69 mg of KCN (Aldrich, 98%) were added to 105 mL of DDI water. Then, 2 mL of this solution (KCN/H₂O) were mixed with 98 mL of pyridine (Aldrich, 99%). Stock solution 3 was prepared by addition of 2.5 g of ninhydrin (Riedel-de Haën, 99%) to 50 mL of ethanol (Aldrich, 200 proof). All three solutions were stored in a dessicator; the ninhydrin solution was also wrapped in aluminum foil to protect it from light.

Scheme 2.8

Ninhydrin reaction used in the titration of propylamine functionalities tethered to the interior of siloxane nanocages.⁷



In a typical experiment, 0.5 mL of nanocage were mixed with 0.75 mL of a 6 mM solution of triethylamine in a 10 mL vial and allowed to react for 45 min at 100 rpm. TEA was used to neutralize any residual HI remaining after carbamate deprotection (see Chapter 5), as it interferes with the ninhydrin reaction. Subsequently, the solvent was evaporated under vacuum at RT, leaving mainly the nanocage along with some residual triethylamine (TEA) and TEAH⁺I⁻. Control experiments indicated that neither TEA nor its hydroiodic salt give a positive ninhydrin test; therefore, their presence in the solution did not contribute to the formation of the chromophore. The solid remaining after evaporation was re-dissolved in 2 mL of chloroform; then 3 drops of each stock solution were added to the vial. The solution was stirred at 100 rpm

for 5 min in the absence of light. This was achieved by wrapping the vial in aluminum foil.

Following, the wrapped vial was brought into a silicon oil bath at 120 °C for 90 seconds, where the formation of the chromophore took place. Caution must be exercised in this step, as excessive heating will cause an explosion of the vial due to the high pressure developed in its interior. It was established that heating in properly sealed vials did not cause any significant loss of solvent, as the mass of the sample before and after the reaction was the same. After cooling down, part of the solution was transferred to a UV-VIS cuvette and its spectrum was measured in a Spectronic Genesis 2 instrument (Spectronic). The intensity of the band at 573 nm was then compared against a calibration curve, obtained as just described, with 3-aminopropyl-methylbis(trimethyl-siloxy)silane instead of the nanocage. 3-aminopropyl-methylbis(trimethyl-siloxy)silane (APMBTSS) constituted a good reference to compare the nanocage with, due to their local similarity around the propylamine groups (see Chapters 5 and 6). The use of the calibration curve allowed the determination of the total concentration of amine groups due to the nanocage in solution. Since ninhydrin undergoes slow degradation under storage, losing its titration power, a calibration curve using APMBTSS was required every time that the nanocage was analyzed. Additional control experiments performed with the nanocage right before carbamate deprotection (Chapter 5) as well as several secondary amines generated negative results. Thus, only the primary amine groups generated after deprotection were quantified.

2.3.4 Cyclic Voltammetry

Cyclic voltammetry is an electrochemical technique in which the potential of a stationary working electrode in an unstirred solution, is linearly scanned with time from a potential where no electrode reaction occurs (E_0) to a potential where reduction or oxidation of the substance of

interest takes place (E_1).⁸⁻¹¹ Half the experiment consists of sweeping the potential between E_0 and E_1 . In the other half the scan direction is reversed. The potential E_1 where the scan direction is reversed is known as the switching potential. A scan towards negative potential is known as a forward scan. Usually, the reactions occurring at the working electrode during the forward scan are reversed during the backward scan. However, this does not hold for irreversible reactions where the intermediates or products generated during the first half of the cycle are transformed into different species. The potential of the working electrode is defined with respect to a reference electrode, usually a saturated calomel electrode (SCE) or a silver/silver chloride electrode (Ag/AgCl). Generally, one or more electrode reactions occur in the potential region scanned, generating current responses (Faradaic currents) that are plotted as a function of the applied potential. This current-potential curve is called a voltammogram. Due to its nature, a cyclic voltammogram provides information on the electronic properties of the species undergoing redox reactions at the working electrode, which can be used to study reaction pathways, free radical reactions, oxidation/reduction properties of metals in complexes, identification of complexes containing different ligands, transport properties and many other processes.⁸⁻¹¹

As mentioned, the Faradaic current is a direct measurement of the rate of the electrochemical reaction occurring at the working electrode. It depends mostly on the rate of mass transport from the bulk solution to the electrode and the rate of electronic transfer from the species in solution to the electrode and vice versa (charge transfer).⁸ Mass transfer can occur by a combination of diffusion, migration of ions under the electric field imposed by the electrodes and convection, as described (in one dimension) by the Nernst-Planck equation:¹²

$$J(x, t) = -D \frac{\partial C(x, t)}{\partial x} - \frac{zF}{RT} DC(x, t) \frac{\partial \phi(x, t)}{\partial x} + C(x, t) v_x(x, t) \quad (2.3)$$

where J is the flux ($\text{mol cm}^{-2} \text{s}^{-1}$), D is the diffusion coefficient ($\text{cm}^2 \text{s}^{-1}$), C is the concentration (mol cm^{-3}), z is the number of electrons transferred, F is the Faraday constant, ϕ is the electrostatic potential and v_x is the hydrodynamic velocity.

The cyclic voltammetry experiment is performed under conditions in which the main contribution to the mass transport is due to diffusion. That is achieved by running the experiments under unstirred conditions (which eliminates most of the convective transport), in the presence of a 100-fold excess (or more) of an inert salt (supporting electrolyte). The role of the salt is to dissipate the electric field of the polarized electrode over all the ions in solution and not just the electroactive material. This cuts the migration component in equation (2.3) by about 99%. Under these conditions, the current flowing through the working electrode is given by:

$$i(t) = nFAD \left. \frac{\partial C(x, t)}{\partial x} \right|_{x=0} \quad (2.4)$$

where n is the number of electrons transferred at the working electrode, F is the Faraday constant and A is the electrode area. Equation (2.4) can also be expressed as:^{8,12}

$$i(t) = \frac{nFAD^{1/2}C}{\pi^{1/2}t^{1/2}} \quad (2.5)$$

which is known as the Cottrell equation. Cottrell equation is widely used to interpret cyclic voltammetry results and is valid only under conditions in which diffusion dominates over the other mass transfer mechanisms. Equation (2.5) indicates that the diffusional layer around the working electrode expands in a way in which the diffusional gradient decreases with the inverse

of the square root of time. From this equation, a related expression has been developed, which correlates the Faradaic current with the scan rate, known as the Randles-Sevcik's equation:^{8,9}

$$i(t) = (2.69 \times 10^{-5}) n^{3/2} A D^{1/2} C v^{1/2} \quad (2.6)$$

where v is the rate at which the working electrode is scanned, in V/s.

Equation (2.6) can be used, for instance, to calculate the diffusivity of the active material when the electrochemical reaction is known (defined n), since all the other parameters can be adjusted before the experiment. In this work, the equation was used to measure changes in the concentration of cationic gold in solution, by monitoring the variations in the corresponding Faradaic current. The experimental set up used consisted of a glass cylindrical cell (I.D.=1 cm, 10 mL) containing the solution of interest, the working electrode, reference electrode and a counter electrode. The role of the counter electrode was to provide the current required to sustain the electrolysis at the working electrode. This arrangement avoided large currents through the reference electrode, which could change its potential. A polypropylene cap was used to seal the cell and to maintain the electrodes at fixed positions in the cell. A stirring bar was used to homogenize the solution prior to data collection, when multiple scans were acquired. Data were collected with a CHI 900 Electrochemical Scanning Microscope (CH Instruments Inc.), using a glassy carbon working electrode (CH Instruments Inc., Diam.=3mm) and a Ag/AgCl reference electrode. The counter electrode was a platinum wire (Aldrich, 99.9%). All samples were purged with N_2 before carrying out a measurement, in order to remove dissolved oxygen. 0.1 M NaCl or $NaClO_4$ were used as supporting electrolytes in methanol/water (4.4% H_2O) and methanol (0.1% H_2O), respectively. In all the experiments, the working electrode was scanned at 0.1V/s.

2.3.5 XANES/EXAFS in the liquid phase

X-ray absorption spectroscopy (XAS) experiments were conducted in liquid phase in order to study changes on the first neighbors of Au^{3+} in solution, induced by variations in pH and interaction with siloxane nanocages. The same instrumentation used to study Au/TiO_2 , was used in this case (section 2.2.2); however the sample was loaded into a polypropylene cylinder (Diam.=11 mm, 1 mL), that was subsequently sealed with Parafilm M (Alcan, Inc.). Due to the low concentration of Au^{3+} in the samples (about 430 μM), the measurements were carried out in the fluorescence mode, with the flat surface generated by the Parafilm facing the beam at an angle of 45° with both the beam and the detector. Once again, the analysis of data was performed as described in section 2.2.2.

2.3.6 UV-VIS spectroscopy

UV-VIS analysis of gold solutions was used to complement cyclic voltammetry and XAS characterization. Here again, the analysis focused on the changes in the nature of the ligands of Au^{3+} induced by variations on pH and interactions with the nanocage. The data was acquired using a Spectronic Genesis 2 instrument (Spectronic). For solutions of high concentration of gold (430 μM), a quartz micro-cuvette with a 1 mm path length ($1 \times 10 \times 48$ mm) was used; for solutions with less than 80 μM of gold, a standard quartz cuvette with a 10 mm path length ($10 \times 10 \times 48$ mm) was employed. Before any experiments were conducted, the linearity of the signal in the concentration range of interest, at the desired wavelengths (Beer-Lambert's law), was established.

CHAPTER 3

ACTIVATION OF Au/TiO₂ CATALYST FOR LOW TEMPERATURE OXIDATION OF CO

3.1 Synopsis

Changes in a Au/TiO₂ catalyst during the activation process from an as-prepared state, consisting of supported AuO_x(OH)_{4-2x}⁻ species, were monitored with X-ray absorption spectroscopy and FTIR spectroscopy, complemented with XPS, microcalorimetry, and TEM characterization. When the catalyst was activated with H₂ pulses at 298 K, there was an induction period when little changes were detected. This was followed by a period of increasing rate of reduction of Au³⁺ to Au⁰, before the reduction rate decreased until the sample was fully reduced. A similar trend in the activation process was observed if CO pulses at 273 K or a steady flow of CO at about 240 K was used to activate the sample. With both activation procedures, the CO oxidation activity of the catalyst at 195 K increased with the degree of reduction up to 70% reduction, and decreased slightly beyond 80% reduction. The results were consistent with metallic Au being necessary for catalytic activity.

3.2 Introduction

Although bulk gold has historically been regarded as chemically inert, highly active catalysts of gold on metal oxides have been reported in recent years for various reactions,¹⁻³ including remarkable activity for low-temperature CO oxidation. In particular, Au/TiO₂ exhibits CO oxidation activity at temperatures as low as 90 K.⁴ The intense effort expanded on the elucidation of the origin of the high activity and factors that influence it⁵⁻¹⁰ has led to different models of the Au active site. However, as yet there are no overarching conclusions to account for

all the observations. Metallic Au has been proposed to be the active site, with some proponents advocating that the highest activity occurred when two layers of Au atoms are deposited on a TiO₂ surface.^{11,12} Others report that Au cations in the absence of metallic Au atoms also exhibit catalytic activity.^{13,14} Another model portrays the active site as an ensemble of metallic Au clusters with Au cations at the perimeters of such clusters.^{3,15} Although there is yet no direct

evidence in support of this latter model, it was shown that metallic Au alone is insufficient for high catalytic activity.^{16,17} The most common method to prepare a highly active Au/TiO₂ catalyst is by deposition-precipitation, in which most likely a $[\text{AuO}_x(\text{OH})_{4-2x}]_n^-$ species is deposited on the support.¹⁸ In the earlier studies, the sample would be activated by calcination in air at 200-400 °C. More recent reports indicated that more active catalysts can be obtained by activation in other gases and/or at lower temperatures.^{19,20} For example, Schumacher et al. reported that H₂ treatment at 200 °C yielded catalysts that were significantly more active than the calcined ones.²⁰

We observed that H₂ reduction at 298 K is also an effective activation method. The CO oxidation activity of a catalyst activated with this procedure was 0.29 mol of CO (mol Au min)⁻¹ at 195 K in a feed of 1% CO, 2.5% O₂, and balance He. This rate was more than 3 times higher than that of the calcined Au/TiO₂ catalyst distributed by the World Gold Council (Lot No. 02-4, 1.5 wt %, 3.8 nm Au particle diameter) under the same conditions, which was 0.08 mol CO (mol Au min)⁻¹. Since it is possible to reduce a catalyst with H₂ pulses at room temperature, thereby controlling the degree of reduction, we may be able to monitor the relationship among the average Au oxidation state, Au metal cluster size, and catalytic activity during the activation process. Alternatively, we could also perform reduction with CO at subambient temperatures for comparison. Here we report the investigation using these two activation methods.

3.3 Experimental Section

3.3.1 Catalyst Preparation

The Au/TiO₂ catalyst was prepared by deposition-precipitation with HAuCl₄ (Aldrich, 99.999%) as the precursor and microrutile as the support (Sachtleben, approximately 200 m² g⁻¹). The HAuCl₄ solution (0.014 M) was neutralized slowly with vigorous stirring to pH 7 at 70 °C with a NaOH solution and mixed with a TiO₂ suspension that was kept at 35 °C. The resulting mixture was maintained at pH 7 at 35 °C for an hour. The mixture was filtered, and the solid was washed twice with room temperature deionized water and then once with 70 °C water. The solid was suction filtered and dried at room temperature. The resulting sample is referred to as the as-prepared sample. The Au content was determined by X-ray fluorescence (XRF) to be 7.0 wt %. This sample was used for all experiments except the CO pulse reduction at 273 K. A 4 wt % sample prepared similarly was used there.

3.3.2. H₂ and CO Pulse Reduction

In a typical experiment for H₂ reduction, 0.1 g of as-prepared Au/TiO₂ sample was placed in a fused silica, U-tube microreactor, supported between two layers of acid-washed quartz wool. The reactor was purged with Ar (Matheson, 99.999%) at a flow rate of 50 cm³ min⁻¹. Any O₂ impurity in the Ar stream was removed with a MnO trap located immediately downstream of the mass flow controller. Hydrogen reduction was accomplished by injecting 0.5 cm³ pulses of pure H₂ (Matheson, 99.999%) into the Ar stream. A molecular sieve trap was located downstream of the reactor to remove any water that might be produced during reduction. The consumption of H₂ was determined with a TCD detector in a HP 5890 gas chromatograph. For pulse reduction during X-ray absorption measurements, a pulse system similar to the one above was used

together with a flow-through sample cell for XAS and a N_2 flow of $100 \text{ cm}^3 \text{ min}^{-1}$. The pulse size was ca. 0.6 cm^3 pure H_2 . CO pulse reduction at 273 K was conducted also in a U-tube microreactor, using 0.012 g of a 4 wt % Au/ TiO_2 . After purging the reactor with $100 \text{ cm}^3 \text{ min}^{-1}$ of high purity He that was further purified with a reduced MnO_2 trap to remove O_2 , 0.5 cm^3 pulses of 10% CO in He were passed over the catalyst, and the consumption of CO was monitored by a TCD detector.

3.3.3 Catalytic Activity for CO Oxidation

When desired, CO oxidation at 195 K was also conducted during H_2 pulse reduction in the U-tube microreactor. After reducing a catalyst by a certain number of pulses, the catalyst was first cooled to 195 K using an acetone-dry ice bath while in an Ar gas flow. Then, the gas was switched to the reactant gas flow (1% CO, 2.5% O_2 and balance He, $50 \text{ cm}^3 \text{ min}^{-1}$) by a switching valve. The CO concentration in the effluent was continuously monitored by IR spectroscopy with a gas cell. After CO oxidation, the catalyst bed was purged with Ar for approximately 15 min at 195 K to remove CO and O_2 before warming up to room temperature for subsequent H_2 pulse reduction. This step is critical because we have shown previously that as-prepared Au/ TiO_2 catalyst can be rapidly reduced by the reaction mixture at room temperature.²¹

3.3.4 X-ray Absorption Spectroscopy (XAS)

XAS experiments were carried out at the bending magnet Beamline 5-BMD of the Dupont-Northwestern-Dow Collaborative Access team at the Advanced Photon Source at Argonne National Laboratory in Argonne, IL.¹⁹ Higher harmonics in the X-ray beam were

minimized by detuning the Si(111) monochromator by about 15% at the Au LIII edge (11.919 keV). The spectra were collected in the transmission mode with use of a flow-through sample cell with Kapton windows. The cell consisted of two concentric cylinders with the inner cylinder only about half the length of the outer cylinder. Gas entered via the outer cylinder, swept through the region between the two cylinders, then passed through the inner cylinder before exiting the sample cell. Because of rather extensive backmixing of the gases, it took about 3 min for a complete (>99.5%) sweep of the gas in the cell. About 0.15 g of sample was used to make a self-supporting pellet that was sandwiched between two nylon grids and placed at the end of the inner cylinder, near the center of the sample cell. All XAS data were collected during N₂ purge at room temperature and the XAS measurement typically took 10-25 min depending on the type of scan. We have determined that the XAS measurements did not cause any detectable change in a sample, if the sample had not been previously reduced or reduced only slightly (<5%), i.e., consecutive scans showed no detectable differences. However, if the sample had been previously reduced by 5% or more, then the X-ray beam induced further reduction of the sample, as evidenced by a decrease in the near edge intensity in the consecutive XANES spectrum. Both the XANES and EXAFS data were analyzed by using standard procedures with the WINXAS97 software. Phase shifts, backscattering amplitudes, and XANES references were obtained from reference compounds: Au₂O₃ for Au³⁺-O, and Au foil for Au⁰ and Au-Au. The XANES fits of the normalized spectra were made by a linear combination of experimental standards. The EXAFS coordination parameters were obtained by a least-squares fit in the *k*- and *r*-space of the isolated multiple-shell, *k*²-weighted Fourier transform data.

3.3.5 Transmission Electron Microscopy (TEM) and XPS

TEM examination of Au/TiO₂ samples was performed with a Hitachi HF-2000 TEM with a field emission gun at 200 keV. XPS of the catalysts was conducted in a Perkin-Elmer/PHI XPS system with Al K α radiation (1486.6 eV), using a dual-anode X-ray source with spherical electron energy analyzer. The powder samples were mounted onto the sample holders with carbon tape. They were then placed in the outer chamber of the spectrometer and pumped to vacuum overnight. The spectra were collected with an anode voltage of 15 kV and an emission current of 20 mA. Different energy regions were scanned to obtain separate spectra for carbon, oxygen, titanium, and gold. The 1s binding energy for carbon, 284.7 eV, was used to correct for the shift in energy for all components due to electrostatic charging of the samples.

3.3.6 Microcalorimetry

Calorimetric measurements were performed with 0.1 g of catalyst in a Microscal flow microcalorimeter. At room temperature, 0.66 cm³ of pure H₂ in a N₂ carrier gas flow of 1 cm³ min⁻¹ was pulsed through the catalyst and the H₂ consumption and heat evolved after each pulse were measured.

3.3.7 *In-Situ* Infrared Spectroscopy

Infrared spectroscopy (IR) was conducted in a stainless steel IR cell fitted with CaF₂ windows at subambient temperatures in a Nicolet Nexus 670 FTIR spectrometer. To achieve the desired temperature, the IR cell was brought into contact with a copper housing containing a liquid nitrogen and dry ice mixture. A self-supporting pellet was made by pressing 10 mg of as-prepared sample mixed with an equal amount of anatase. A thermocouple, placed near the pellet,

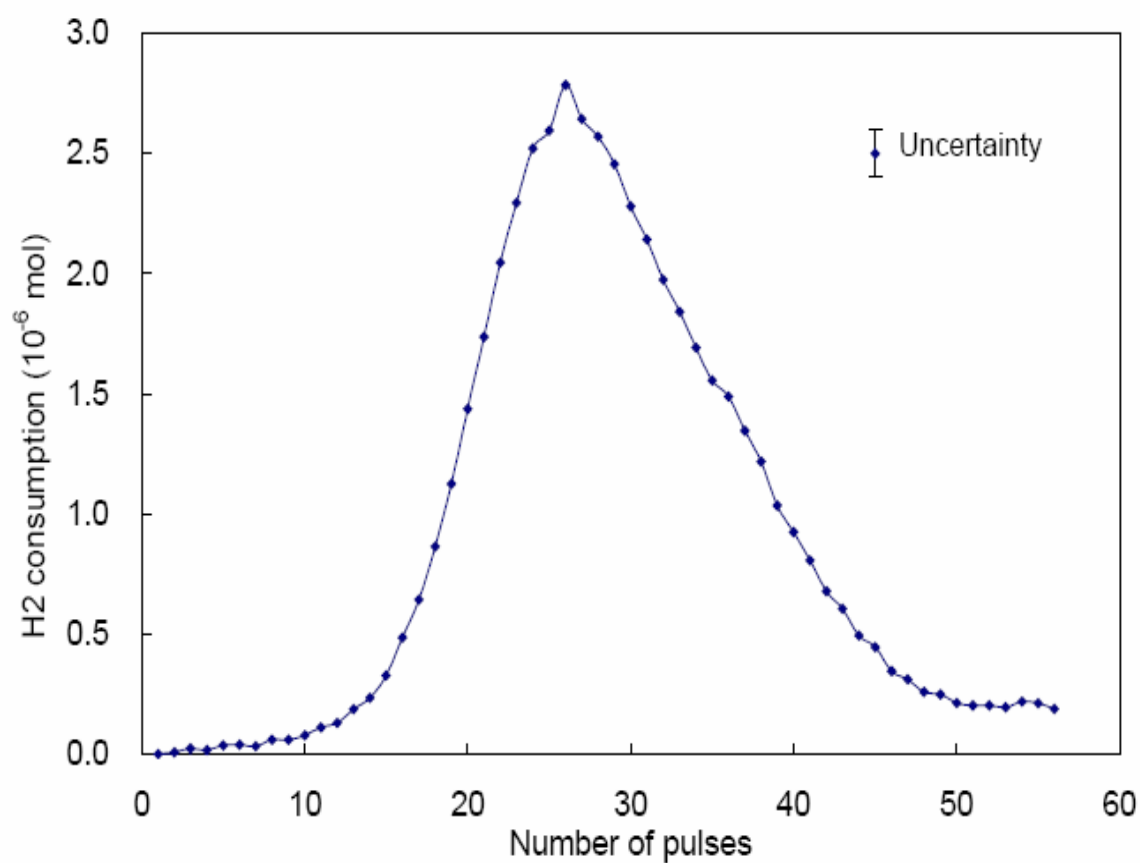


Figure 3.1. H₂ consumption at 298 K as a function of pulse sequence; 100 mg of a 7 wt % Au/TiO₂ catalyst.

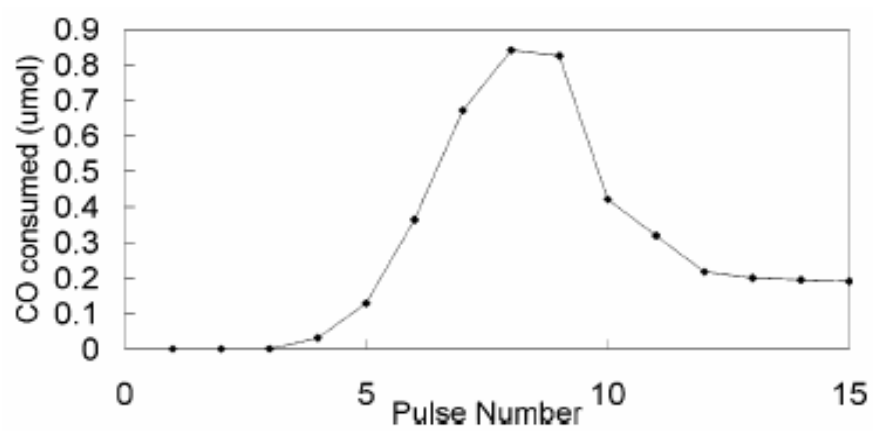


Figure 3.2. CO consumption at 273 K as a function of pulse sequence for 12 mg of a 4 wt % Au/TiO₂ catalyst.

recorded the temperature of the gas immediately after passing through the pellet. The volume of the IR cell was about 6 cm³. Thus, the gas in the cell could be changed reasonably rapidly with a gas flow of 11 cm³ min⁻¹. Reaction with this cell was conducted with 1% CO, 2.5% O₂, and the balance He. The effluent gas of the IR cell was analyzed with a HP 6890 gas chromatograph. The spectra presented are referenced to the sample in He at the same temperature, with contributions from gaseous CO removed.

3.4 Results

3.4.1 H₂ and CO Pulse Reduction

The amounts of H₂ consumed in each pulse in a microreactor experiment are plotted in Figure 3.1 as a function of the pulse sequence. Within uncertainty (± 0.1 $\mu\text{mol H}_2$), there was no consumption of H₂ in the first 10 pulses. Following this initial induction period, the consumption of H₂ slowly increased in the next 5 pulses, and accelerated after that, reaching a maximum at pulse 26. H₂ consumption in subsequent pulses decreased gradually, and approached a steady-state value equivalent to about 0.2 μmol of H₂ after pulse 50. The total amount of Au³⁺ that was reduced by the H₂ pulses in the experiment was determined from the area under the curve up to pulse 58 in Figure 3.1, and found to be 6.8 Au wt %, which was in good agreement with the 7.0 Au wt % determined by XRF. Figure 3.2 shows the CO consumption per pulse at 273 K as a function of the pulse sequence. The CO consumption showed a similar trend as for H₂ consumption. There was little uptake in the first few pulses before significant consumption commenced.

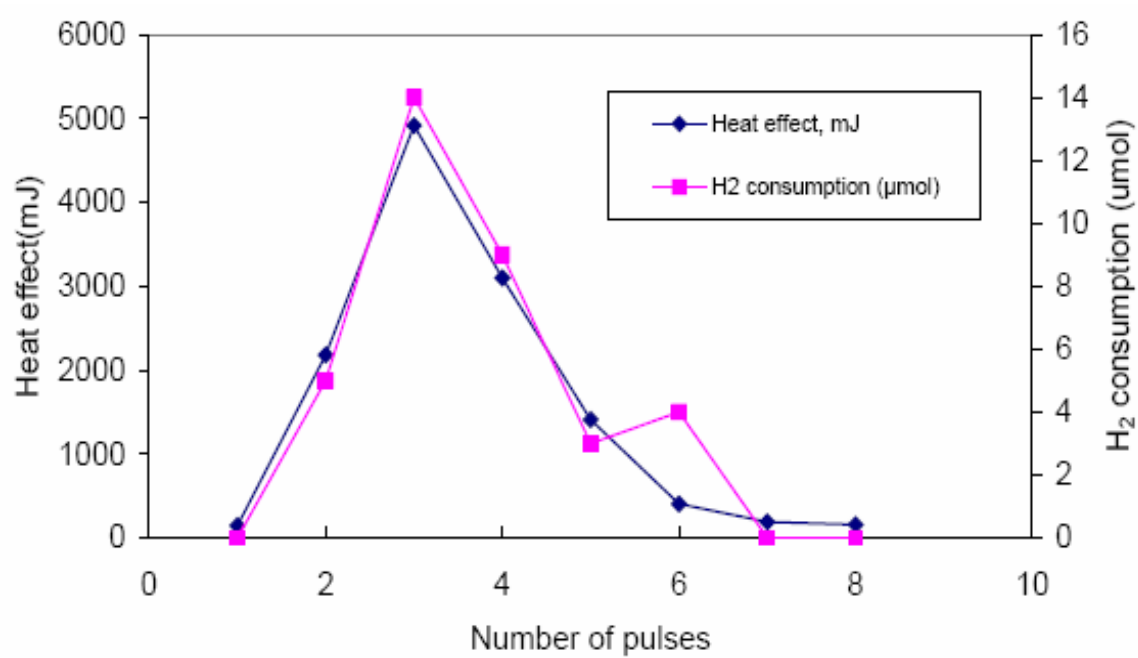


Figure 3.3. H₂ consumption and heat evolved in calorimetry experiment as a function of pulse sequence.

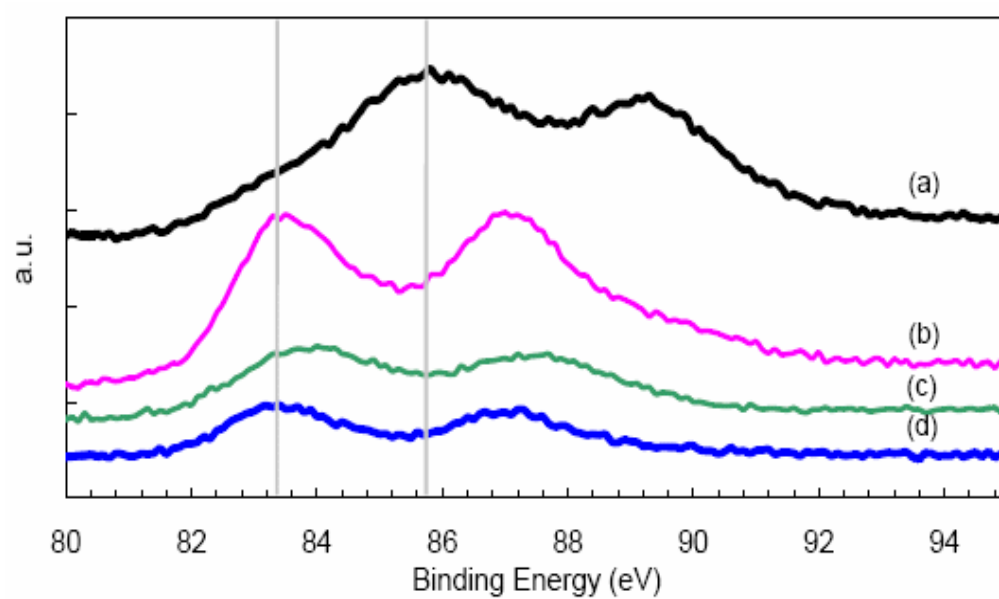


Figure 3.4. Au (4f) binding energy of Au/TiO₂ catalyst: (a) as-prepared sample, (b) sample fully reduced by H₂ pulses, (c) sample reduced by H₂ pulses to ca. 50% and (d) reference Au/TiO₂ catalyst (calcined) distributed by WGC.

3.4.2 Microcalorimetry

The H₂ consumption in the calorimetry experiment followed a similar trend when H₂ pulses were passed through the catalyst, as shown in Figure 3.3. The first H₂ pulse did not yield measurable H₂ consumption while the second pulse showed a significant increase in H₂ consumption, which eventually reached a maximum at the third pulse. The heat evolved from the reduction of the catalyst had an almost identical trend as the H₂ consumption. The integral heat per mole of H₂ consumed was calculated to be 400 ± 62 kJ/mol. This high value was consistent with reduction of Au³⁺ instead of adsorption of H₂. For reference, the heat of formation of water at room temperature is -285.8 kJ/mol.

3.4.3 XPS

The oxidation state of Au on the surface of a sample that had been reduced by H₂ pulse to ca. 50% was determined with XPS. The sample was removed from the microreactor after 26 H₂ pulses. Figure 3.4 shows the spectrum obtained, together with those of an as-prepared and a completely reduced sample. In all samples, the characteristic doublets of Au 4f_{7/2} and 4f_{5/2} peaks were observed. The two peaks for the as-prepared catalyst were at 85.8 and 89.1 eV, which are similar to those reported on Au³⁺ compounds,⁹ while those of the fully reduced catalyst were at 83.2 and 87.0 eV. The latter agree very well with those of the reference Au/TiO₂ catalyst distributed by the World Gold Council (WGC). For the 50% reduced sample, the two peaks were broader, and the maxima appeared intermediate between the other two samples, which is in agreement with the expectation that a mixture of Au oxidation states was present. The oxidation state of the 50% reduced sample was independently determined by XAS measurement (data not

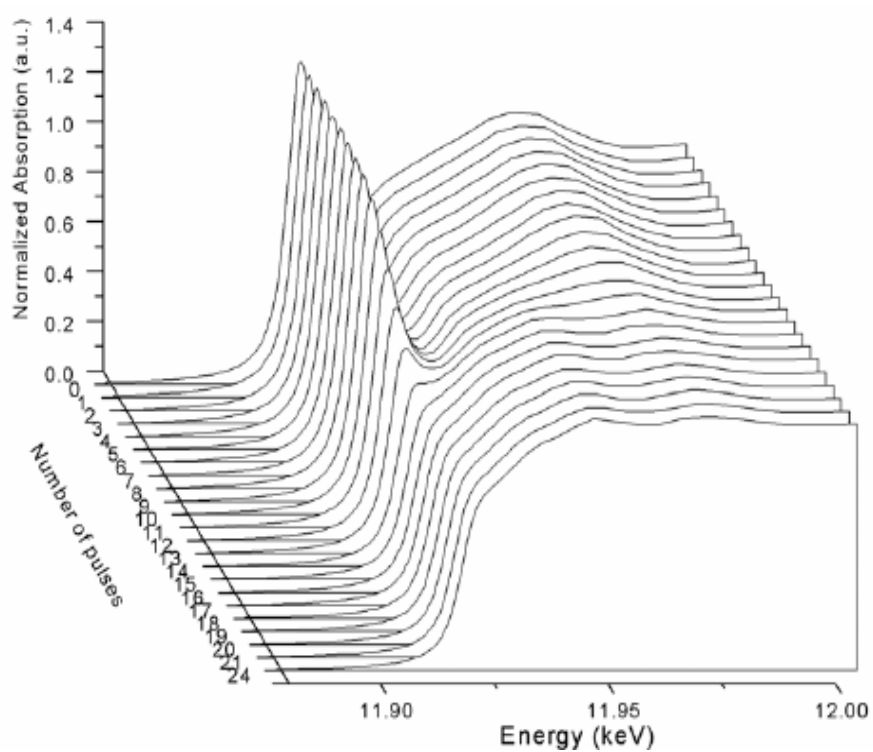


Figure 3.5. XANES spectra as a function of H_2 pulse sequence.

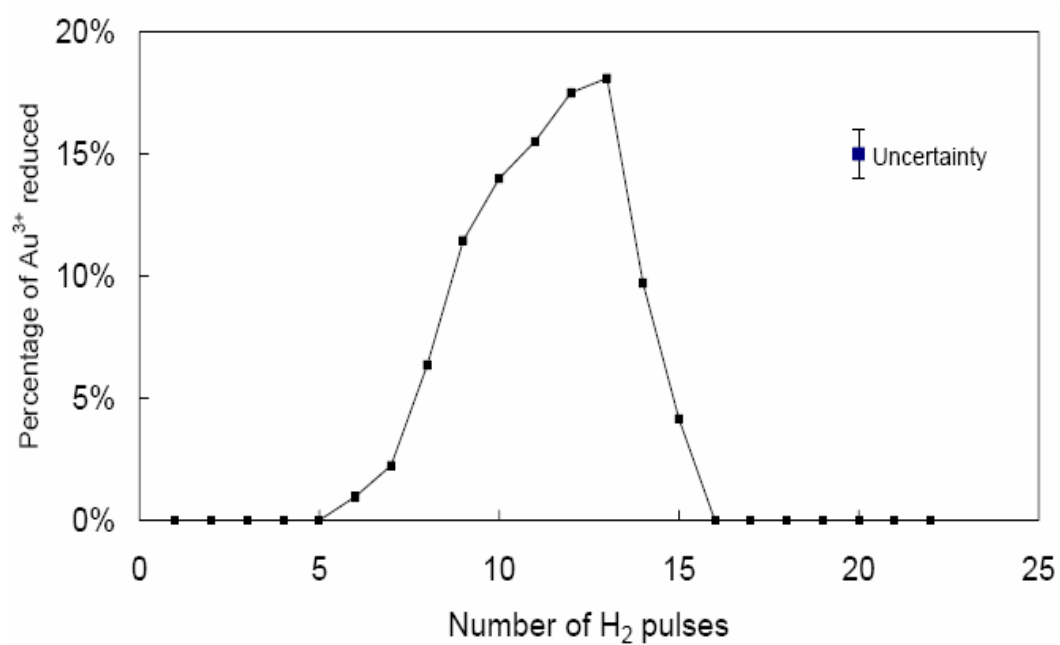


Figure 3.6. Percentage of Au^{3+} reduced by each H_2 pulse as a function of pulse sequence in the XAS experiment.

shown). With use of a linear combination of Au^{3+} and Au^0 XANES spectra, the percentage of Au^{3+} reduced was determined to be 55%.

3.4.4 XAS

The reduction of Au^{3+} species by H_2 pulses at 295 K was also monitored by XAS. Figure 3.5 shows the XAS spectra as a function of pulse sequence. The spectrum of the as-prepared sample showed an intense white line at the Au L_{III} edge, typical of supported Au^{3+} species.¹⁹ Within experimental uncertainties, the intensity of the white line remained unchanged for the first 5 pulses, and began to decrease afterward, indicating detectable reduction of Au^{3+} to Au^0 . By using a linear combination of XANES spectra of Au^{3+} and Au^0 reference compounds, the percentage of Au^{3+} and Au^0 in the sample was determined. The decrease in the percentage of Au^{3+} after each pulse is shown in Figure 3.6. The curve in Figure 3.6 showed a similar trend as Figure 3.1: an induction period followed by increasingly faster and then decreasing reduction rate.

EXAFS analysis was carried out on this set of spectra. Figure 3.7 shows the magnitude of the Fourier transformed, k^2 -weighted χ function of selected EXAFS spectra in R -space. The positions corresponding to Au-O and Au-Au scatterings are indicated by arrows. The magnitude of transform due to the Au-O scattering barely decreased from pulse 1 to pulse 5, and then much more rapidly, particularly between pulse 8 and 14. After pulse 15, there was little Au-O scattering. In contrast, there was little Au-Au scattering until pulse 9. The Au-Au scattering then increased, reaching a maximum value at pulse 16. At this point, assuming hemispherical particles, the coordination number (CN) of about 6 at pulse 16 corresponded to a particle of about 1.0 nm in diameter.²²

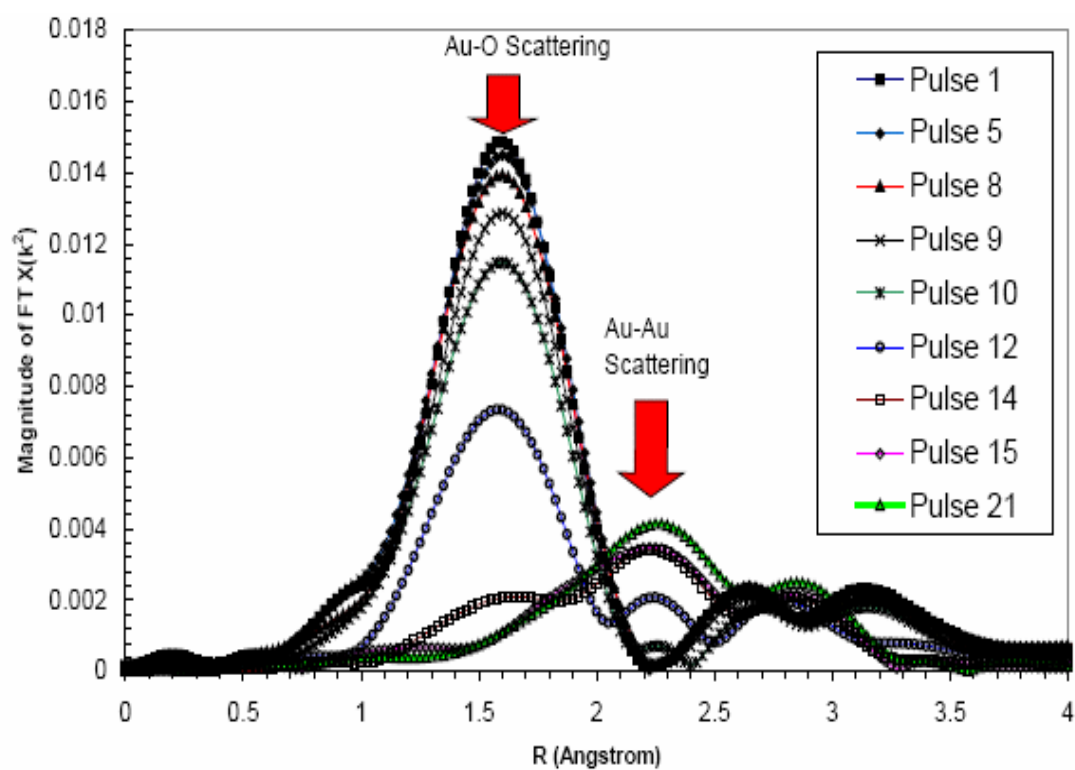


Figure 3.7. Magnitude of the Fourier transformed $k^2-\chi$ function in R-space of Au/TiO₂ after selected H₂ pulse. The arrows indicate positions of Au–O and Au–Au scattering at 1.6 and 2.3 Å in R-space.

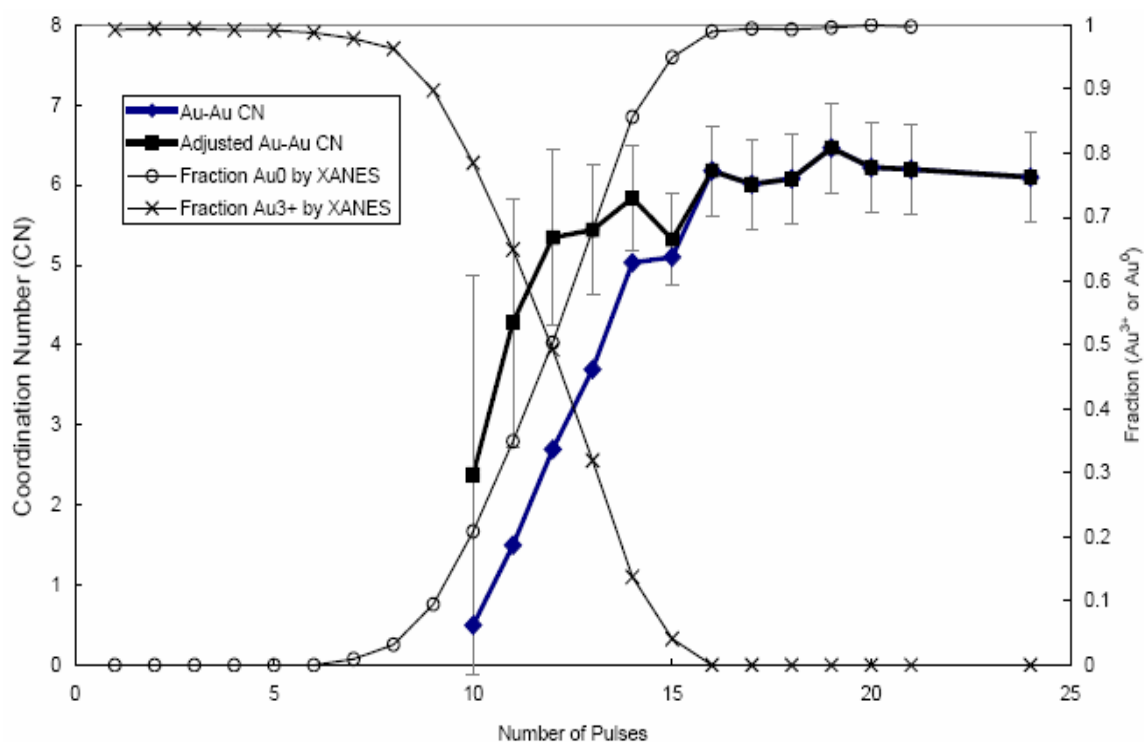


Figure 3.8. Au-Au coordination number obtained by fitting the $\chi(k^2)$ function (♦), fraction of Au^{3+} (×), and Au^0 (○) obtained by XANES fit, and corrected Au-Au coordination number (■) obtained by dividing the Au-Au CN by the fraction of Au^0 , as a function of H_2 pulse sequence.

The change in the Au-Au coordination number with pulse sequence is plotted in Figure 3.8, along with the fractions of Au^{3+} and Au^0 as determined by XANES. Since the Au-Au coordination arises from metallic Au clusters only, it is necessary to correct the magnitude of the Fourier transform by the fraction of metallic Au in the sample in order to obtain the accurate value for the metal clusters. If we assume that Au^{3+} and Au^0 exist in separate phases, then the corrected Au-Au CN in the metallic portion of the sample can be estimated by dividing the CN by the fraction of metallic Au.²³ These corrected values are plotted also in Figure 3.8. Except for pulses 9 and 10, where the uncertainties were large because of the small amounts of Au^0 and low Fourier transform magnitudes, the corrected Au-Au CN was around 6 ± 0.5 , possibly increasing from 5.5 to 6 with increasing extent of reduction. This suggests that the Au particles rapidly attained an average size of about 1.0 nm once they are formed, and grew slowly to about 1.5 nm when the sample was fully reduced. XAS parameters of selected pulses are shown in Table 3.1.

Table 3.1. Fraction of Au^{3+} and Au^0 Determined by XANES and Parameters of EXAFS Characterization.^a

pulse	XANES		EXAFS					
	$\text{Au}^{3+}\text{-O}$ fraction	Au^0 fraction	scatter	CN	R, Å	DWF ($\times 10^{-3}$)	E_0	corrected Au-Au CN
0	1.0	0	Au-O	4.0	2.04	-0.9	0.7	
10	0.79	0.21	Au-O	3.8	2.04	1.0	1.0	
			Au-Au	0.5	2.74	3.0	-6.0	2.4
13	0.32	0.68	Au-O	1.6	2.04	-2.2	0.5	
			Au-Au	3.7	2.74	3.0	-6.0	5.4
16	0	1.0	Au-Au	6.2	2.75	3.4	-6.4	6.2
24	0	1.0	Au-Au	6.1	2.76	3.0	-5.9	6.1

^a First shell coordination number (CN), bond distance (R), Debye-Waller factor (DWF) and inner potential correction (E_0). Corrected Au-Au CN obtained by division of the Au-Au CN by the fraction of Au^0 .

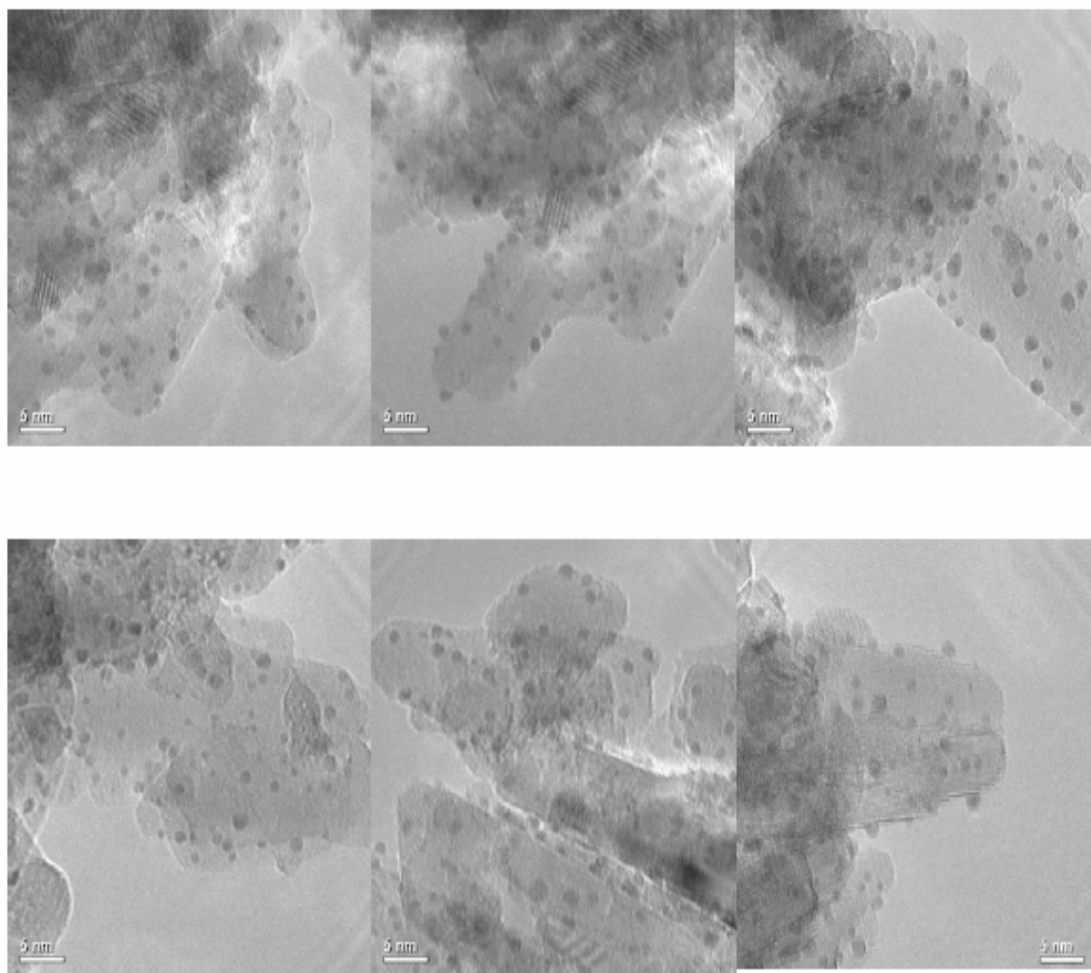


Figure 3.9. TEM pictures of Au/TiO₂ that were (top) approximately 50% reduced by H₂ pulses and (bottom) completely reduced by H₂ pulses.

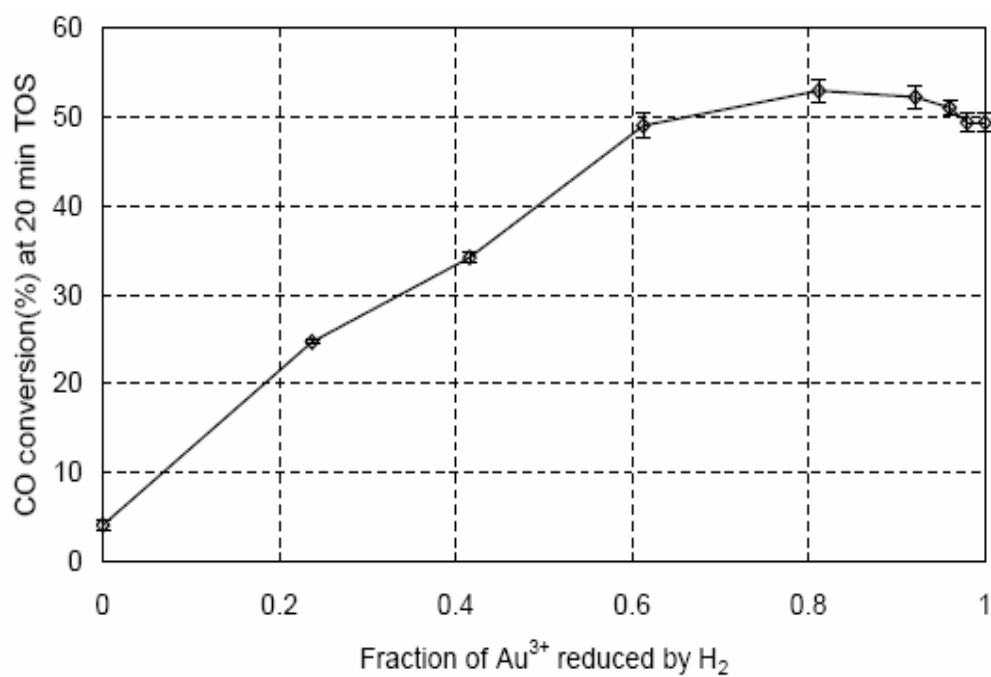


Figure 3.10. CO conversion of Au/TiO₂ catalyst at 20 min TOS as a function of Au³⁺ reduced by H₂ pulse. Reaction conditions: 1% CO, 2.5% O₂, balance He, 50 mL/min, 0.1 g catalyst, 195 K.

The Au–Au bond distance was 2.75 Å for particles with Au–Au CN of 6.0, which is shorter than the 2.88 Å for bulk Au. The shortening of Au–Au bond distance with smaller CN has been reported recently by Schwartz et al. for Au on titania-based supports²⁴ and on alumina as well.²³

3.4.5 TEM

TEM pictures of a Au/TiO₂ sample that was approximately 50% reduced and one that was completely reduced are shown in Figure 3.9. Metallic Au particles in the range 1 to 3 nm are readily observable, but particles smaller than 1 nm could not be distinguished by this instrument. From the limited regions of the samples examined, no significant difference in the size distributions of the two samples could be observed.

3.4.6 CO Oxidation at 195 K

Due to the rapid reduction of Au cations in Au/TiO₂ at room temperature in a CO oxidation reaction mixture,²¹ even in the presence of excess O₂, it is necessary to measure the catalytic activity at 195 K to avoid rapid change of the sample. At this low temperature, we have determined by XAS that the degree of reduction of a sample changed little before and after the catalytic test. Thus, it is possible to measure the CO oxidation activity for samples reduced to different degrees by H₂ pulses. In all cases, the activity declined by about 33% of its initial value with time on-stream before reaching a pseudo-steady-state after 20 min. This pseudo-steady activity versus the degree of reduction was plotted in Figure 3.10. It increased roughly linearly with the degree of reduction until the catalyst was about 70% reduced (calculated from the H₂ consumption), reached a maximum at about 80% reduction, and remained constant or slightly

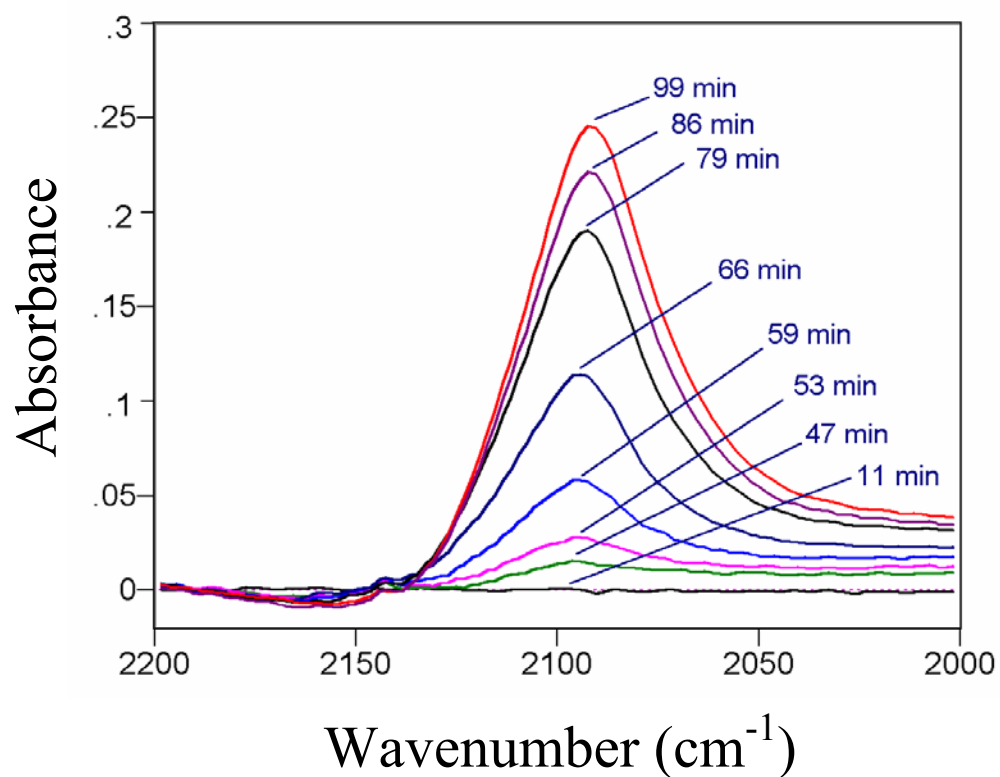


Figure 3.11. Infrared spectra of as-prepared Au/TiO₂ under 10% CO and balance He at 213 K.

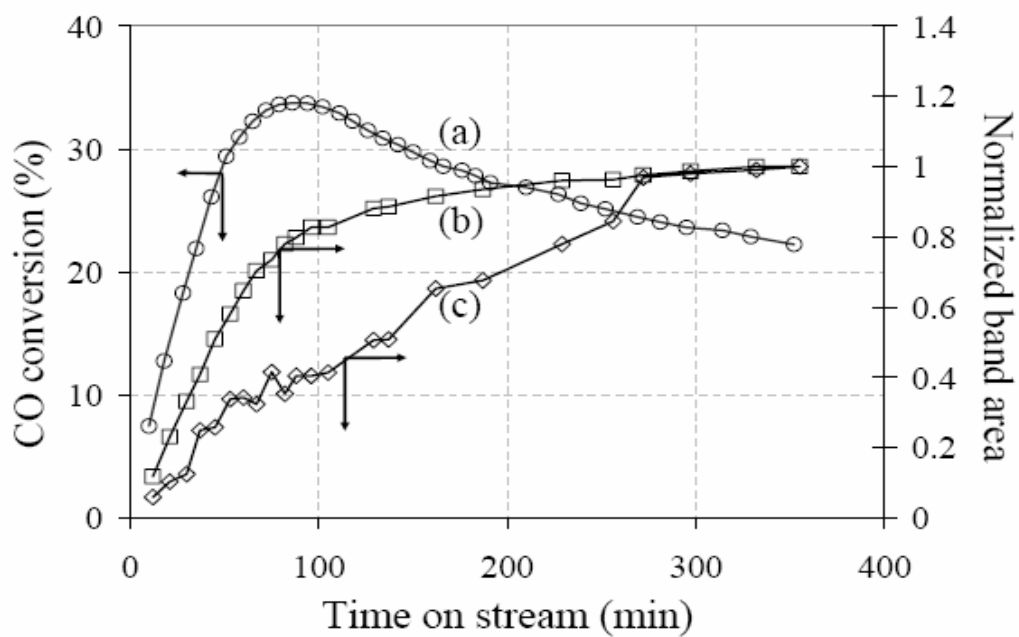


Figure 3.12. CO conversion (a) and the normalized intensities of the composite IR band at 2105 cm^{-1} (b) and at 2066 cm^{-1} (c) of an as-prepared Au/TiO₂ catalyst as a function of time-on-stream at about 240 K. Reaction conditions: 1% CO, 2.5% O₂, balance He, 11 mL/min, 10 mg of catalyst.

declined upon further reduction. The activity for the fully reduced sample corresponded to $0.29 \text{ mol of CO (mol Au}\cdot\text{min)}^{-1}$.

3.4.7 Infrared Spectroscopy

Activation of the as-prepared catalyst by CO was studied at 213 K. The degree of reduction can be inferred from the intensity of the IR band around 2100 cm^{-1} . A band at this frequency is characteristic of CO adsorbed on metallic Au and its frequency is coverage dependent.⁶ At $213 \pm 7 \text{ K}$, the rate of reduction of Au^{3+} in the as-prepared sample was very slow under a reaction feed of CO and O_2 , and no adsorbed CO band at around 2100 cm^{-1} was observed after 65 min on stream. No reaction product was detected either. However, when a gas flow of 10% CO in He ($30 \text{ cm}^3 \text{ min}^{-1}$) was used, reduction occurred as indicated by the appearance of this IR band, as shown in Figure 3.11. The intensity of the IR band was very small even after 47 min on stream but subsequently increased rapidly. The band was rather broad and asymmetric, suggesting that it was a composite band.

When another as-prepared catalyst (2.8 Au wt %) was activated at $240 \pm 7 \text{ K}$ with a reaction feed of CO and O_2 , oxidation activity appeared immediately, which increased together with an increase in the area of the IR band at around 2100 cm^{-1} up to 95 min on stream, as shown in Figures 3.12 and 3.13. A group of bands between 2300 and 2400 cm^{-1} also appeared, which were due to gas phase and adsorbed CO_2 . The broad band at $\sim 2100 \text{ cm}^{-1}$ could be deconvoluted into three peaks with peak maxima centered at 2115, 2102, and 2066 cm^{-1} . They increased at approximately the same rate. Beyond 95 min, the CO conversion decreased slightly. At the same time, the total area of the 2100 cm^{-1} composite band increased slightly, while the 2115 and 2102

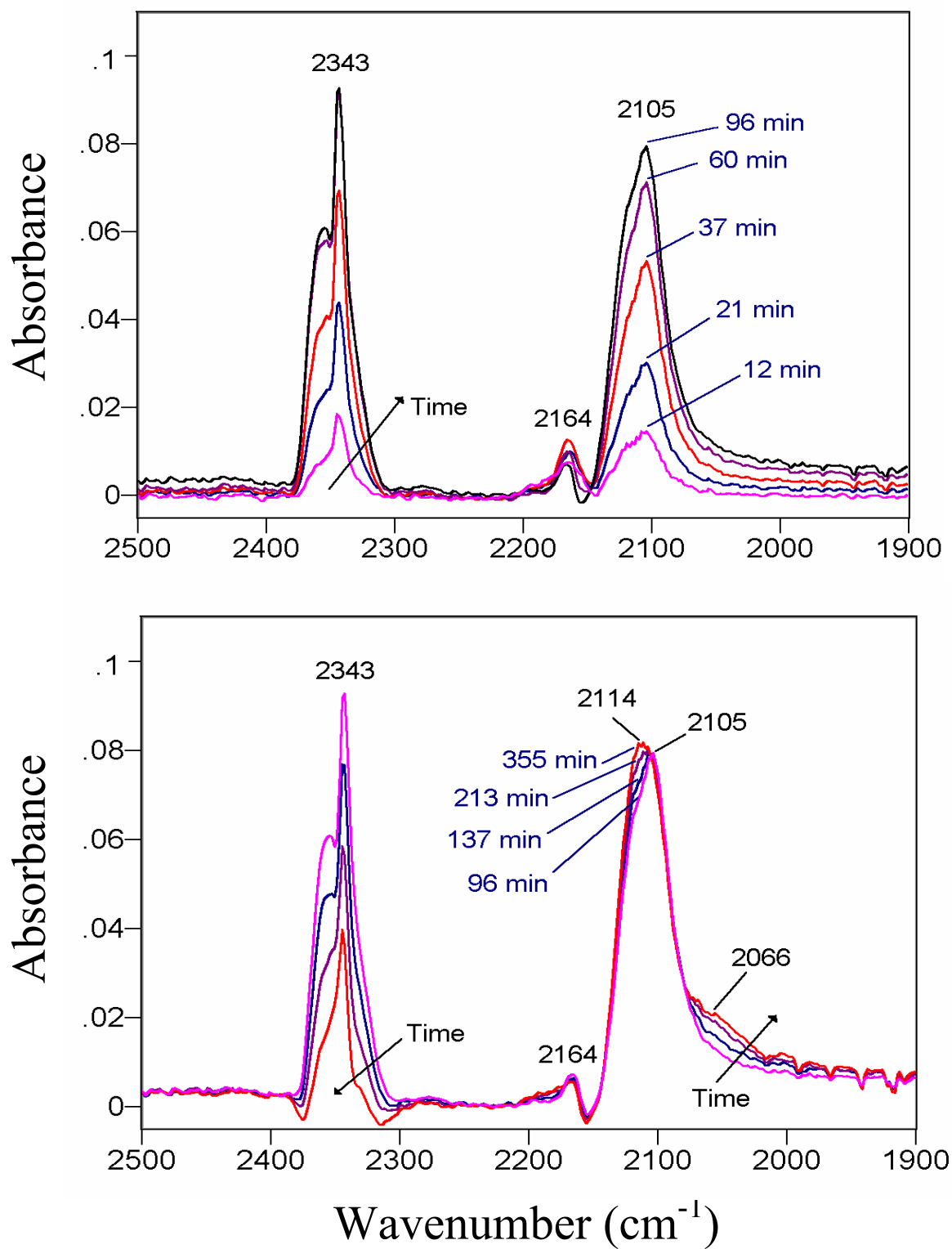


Figure 3.13. Time-on-stream behavior of IR spectra of Au/TiO₂ under the following reaction conditions at about 240 K: 1% CO, 2.5% O₂, balance He, 11 mL/min, 10 mg of catalyst.

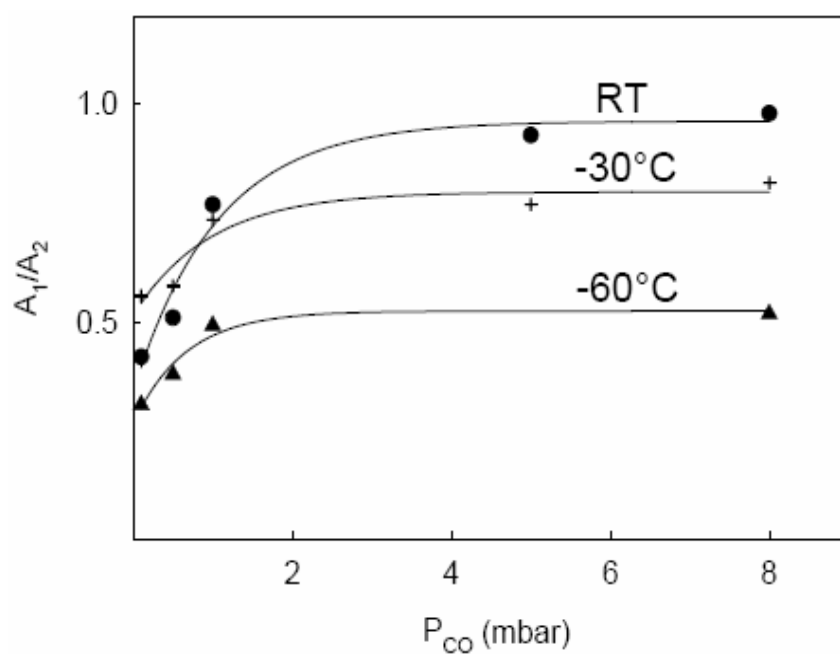


Figure 3.14. Ratio of the area of 2066 cm^{-1} bands (A_1) to the area of 2102 cm^{-1} bands (A_2) as a function of partial pressure of CO.

cm^{-1} bands remained roughly constant. In separate experiments where we activated the as-prepared sample with H_2 at room temperature and kept the sample from exposure to O_2 , CO adsorption generated only bands at 2102 and 2066 cm^{-1} . The latter band intensity has a much stronger dependence on the CO pressure than the former one, as can be seen in Figure 3.14. Finally, the small band at 2164 cm^{-1} did not correlate with the activation process, and its presence varied from sample to sample.

3.5 Discussion

At the pH and Au precursor concentration used in the preparation of the catalyst here, Au exists as $\text{Au}(\text{OH})_4^-$ in solution.²³ This species and its partially dehydroxylated forms are present in our as-prepared sample, as both H_2 consumption in the reduction experiment and XANES suggest that Au exists as Au^{3+} . Exposure of an as-prepared sample to H_2 at room temperature reduces the Au cations. Results from the H_2 pulse consumption, XAS, and microcalorimetry are all consistent with the reduction process. By measuring the catalytic activity on samples reduced to different extents (Figure 3.10), it can be concluded that the conversion of $\text{AuO}_x(\text{OH})_{4-2x}^-$ to metallic Au is necessary for activity.

The same conclusion applies to activation by CO. The appearance of catalytic activity at about 240 K is accompanied by the formation of the 2100 cm^{-1} composite IR band. In the presence of O_2 , this composite band is composed of three bands at 2115, 2102, and 2066 cm^{-1} . If the sample is reduced by H_2 , CO adsorption only generates the 2102 and 2066 cm^{-1} bands. Thus, the 2115 cm^{-1} band is due to CO on Au that is associated with adsorbed oxygen, consistent with the observation by Boccuzzi et al.⁶ The 2102 cm^{-1} has been assigned to CO adsorbed on metallic Au particles.⁶ The assignment for the 2066 cm^{-1} band is not definitive. Boccuzzi et al.²⁵

suggested that it may be the symmetric stretching mode of a $\text{Au}(\text{CO})_2$ species based on the similarity of the frequency to that species isolated in a matrix.²⁶ The authors cautioned that the intense asymmetric stretching band observed in the matrix isolation study was completely absent on the supported Au catalyst. Our result, which shows that this band exhibits a stronger dependence on the CO pressure than the 2102 cm^{-1} band, is consistent with the dicarbonyl assignment.

At near room temperature, reduction of Au^{3+} species by H_2 or CO pulses is relatively slow initially, and there is no detectable reduction in the first couple of pulses (Figures 3.1 and 3.2). In a flow containing CO, the rate of reduction is very slow at 195 K. In fact, it is slower than CO adsorption on metallic Au since a partially reduced sample can be used to catalyze CO oxidation for minutes without being further reduced by the reaction mixture. The initial reduction rate is higher at 213 K, but is still slow as an induction period is clearly observed for an as-prepared sample (Figure 3.11). The initial reduction rate increases with increasing temperature (Figures 3.12 and 3.13), and becomes very rapid at room temperature.²¹ Reduction by CO probably involves first associative adsorption on a Au^{3+} ion and then it is reduced either by removing an oxygen ligand as CO_2 or by reaction with a OH group to form a hydroxycarbonyl or a formate which then decomposes to CO_2 . In the literature, an IR band at 2164 cm^{-1} is assigned to CO adsorbed on cationic Au^{3+} or Ti^{4+} ions.²⁷ This band was observed in some of our samples, but its presence could not be correlated with the extent of reduction of the sample. Associative adsorption of CO would require displacement of another ligand from the Au cation, such as water, and its rate is expected to depend on temperature and partial pressure of CO. In contrast to CO, activation by H_2 likely requires dissociative adsorption, which does not occur easily on a cation.

The induction period in the reduction of an as-prepared sample can be explained by two effects. First, adsorption and activation of the reductant (hydrogen or CO) on metallic Au are much more facile than on ionic Au. Second, Au cation species are mobile and move to metallic Au clusters where they are reduced readily by activated reductant. Thus, the initial rate of reduction is very low when the Au is ionic. The rate is substantially enhanced when the sample is partially reduced because facile activation of H₂ or CO becomes possible by the presence of metallic Au. Rapid reduction continues until eventually, the rate is limited by the availability of Au cations. It should be mentioned that instead of migration of cationic Au species, migration of metallic Au clusters or Au atoms would have the same effect.

Growth of the Au clusters is determined by the rate of formation of nucleation sites as well as the availability of AuO_x(OH)_{4-2x}⁻ species in the immediate vicinity of these nucleation sites. Both TEM and EXAFS results indicate that the metallic Au clusters grew rapidly to 1-3 nm in size. There were very few larger particles. Although the techniques we used could not exclude the existence of much smaller Au clusters, results of a preliminary investigation using the high-resolution, Z-contrast technique in TEM that is capable of detecting isolated Au atoms, conducted by courtesy of Dr. Steven Pennycook, on selected regions of a fully reduced sample were consistent with the results reported here; that is, few isolated Au atoms or very small clusters were detected.

In the EXAFS analyses of the coordination numbers, we assumed separate phases of Au³⁺ and Au⁰. This implied that reduction of Au³⁺ did not proceed via the core-shell model: a shell of Au⁰ covering a core of Au³⁺. This is consistent with the XPS results which showed about equal quantities of Au³⁺ and Au⁰ in the 50% reduced sample (Figure 3.4). For the core-shell model, one would expect a much higher intensity of Au⁰ peaks than Au³⁺ peaks. FTIR results discussed

earlier also supported this scenario. The intensity of the band for CO adsorbed on metallic Au increased with increasing extent of reduction (Figure 3.11).

In this study, H₂ pulse reduction was conducted using both the U-tube microreactor and the XAS sample cell. The faster reduction in the XAS cell could be due to the longer contact time of the sample with H₂ in the XAS sample cell because of back-mixing of gases and the larger pulse size. Reduction by the X-ray beam may contribute to a small extent. We observed that exposure to the beam, while not affecting an as-prepared sample initially, caused a detectable increase in the extent of reduction in a partially reduced sample. This would shorten the induction period.

In the H₂ pulse activation experiment, the activity of the Au/TiO₂ catalyst for CO oxidation at 195 K increased almost linearly with degree of reduction until about 70% reduction was reached (Figure 3.10). This is consistent with the picture discussed above regarding the rapid formation of small Au metal particles upon reduction. Up to 70% reduction, the major change in the sample is the increase in the number of these small metal particles, and thus the activity. Beyond 80% reduction, the increase in the number of particles is counter-balanced by increase in the particle size and changes in particle morphology, with a net result of a slight decrease in the overall activity. The latter is suggested by changes in the IR spectra. This scenario implies that not all surface metallic Au atoms are active for reaction, and we are investigating this possibility at present.

3.6 Conclusions

A more detailed picture of the activation of a Au/TiO₂ catalyst by H₂ pulse or CO reduction has emerged from this study. The process was found to begin with an induction period

when sites for nucleation and hydrogen activation or CO adsorption, consisting of reduced Au species, are formed that catalyze further reduction of cationic Au species on the support. Eventually, gold particles with an average diameter of 1 to 1.5 nm are obtained. The catalytic activity for CO oxidation at 195 K increases with the extent of reduction of the sample until a maximum activity per gram of Au/TiO₂ samples is obtained at about 80% reduction, which suggests that metallic Au clusters are necessary for activity. Further reduction of the samples results in a slight decrease in catalytic activity, which was observed in both activation processes. In situ IR results suggest that the decrease is not accompanied by a decrease in the total adsorbed CO band intensity, suggesting that it might not be due to agglomeration of Au particles but changes in the Au morphology.

CHAPTER 4

IN-SITU TRANSIENT FTIR AND XANES STUDIES OF THE EVOLUTION OF SURFACE SPECIES IN CO OXIDATION ON Au/TiO₂

4.1 Synopsis

In the previous chapter, it was demonstrated that metallic gold is required for high catalytic activity, however it wasn't clear what the role of the nanoparticles was in the reaction. Elucidating that, at least partially, is one of the main themes of this chapter.

The adsorption of CO and its reaction with oxygen were investigated using a combination of in-situ Fourier transform infrared spectroscopy, step response measurements in a microreactor, ¹⁸O isotopic labeling and X-ray absorption near edge structure spectroscopy. An as-prepared sample in which Au is present as a surface oxyhydroxy complex does not adsorb CO. On an activated sample in which only metallic Au is detected, 0.18 ± 0.03 mol CO/(mol Au) are adsorbed on Au at -60 °C, which shows an IR band at 2090 cm^{-1} . When oxygen is present in the gas phase, this species reacts with a turnover rate of 1.4 ± 0.2 mol CO (mol Au min)⁻¹, which is close to the steady-state turnover rate. In contrast, there is a very small quantity of adsorbed oxygen on Au. A small IR peak at 1242 cm^{-1} appears when an activated sample is exposed to CO. It reacts rapidly with oxygen and is shifted to 1236 cm^{-1} if ¹⁸O is used. It is assigned to the possible intermediate hydroxycarbonyl.

4.2. Introduction

Nanosized Au particles catalyze oxidation of carbon monoxide at temperatures as low as -183 °C.¹⁻³ The catalytic activity is enhanced by the presence of moisture⁴⁻⁹ and depends on the

method of preparation, the support¹⁰ and the presence of impurities (e.g., chloride).¹¹ Different explanations for the exceptional activity of nanostructured gold have been proposed, which include the effect of the thickness of the metal particle on its electronic properties,^{12,13} the high density of defect sites,^{14,15} the existence of sites at the metal-support interface,^{7,8,16-18} Au cations¹⁹ or electron-rich Au.²⁰ In the case of Au supported on TiO₂ prepared by deposition-precipitation from a neutralized chloroauric acid solution, reduction of cationic to metallic Au is required for the catalyst to be active, and, (as shown in Chapter 3), a correlation exists between activity and fraction of metallic gold in the catalyst.²¹

Although there is much discussion on the nature of the active sites, there are far fewer investigations on the reaction mechanism. Most computational investigations of the reaction pathway consider reaction of adsorbed CO with adsorbed oxygen and the manner that adsorbed oxygen is activated.²²⁻²⁵ Experimental studies on gold supported on TiO₂, Fe₂O₃, and nanosize Y₂O₃ and CeO₂²⁶⁻³¹ and computational studies²²⁻²⁴ suggest that O₂ does not dissociate to atomic oxygen on the Au surface. Instead, CO reacts with vicinally coadsorbed molecular oxygen²² or superoxide species at oxygen vacancy sites on the support.³² Hydroxycarbonyl has been proposed as a reaction intermediate,^{5,7,16} but this species has not been detected, although its viability has been suggested based on computational results.³³

There are some in situ spectroscopic investigations of the reaction. On Au/TiO₂, a number of CO adsorbed species have been identified that have different reactivities, and their formation depends on the particular history of the catalyst and the temperature of reaction.^{3,34-38} However, there was no quantitative determination of their surface coverages or reactivities. Results with transient isotope labeling showed that at 296 K on Au/ γ -Al₂O₃ the surface coverage of the intermediate was 4.9%, which increased if water vapor was present in the feed gas.³⁹ The

intrinsic turnover frequency (TOF) was 1.6 s^{-1} , which also increased in the presence of water vapor. In view of the scarcity of information on the reaction mechanism, we have conducted an investigation, primarily using in situ Fourier transform infrared (FTIR) spectroscopy of the adsorbed species relevant to the reaction, and quantified the surface coverage of adsorbed CO and their reactivities. The results contribute to enhance our understanding of the reaction and should be useful for future computational and mechanistic investigations.

4.3. Experimental

4.3.1. Catalyst Preparation

The Au/TiO₂ catalyst was prepared by deposition-precipitation using HAuCl₄ (Aldrich, 99.999%) as the precursor and microrutile as the support (Sachtleben, 150 m²/g). A 0.010 M HAuCl₄ solution, which was vigorously stirred for 1.5 h at pH 7 (by adjusting with NaOH) and 70 °C, was added slowly to a suspension of TiO₂ while maintaining the pH at 7 (by adjusting with diluted nitric acid). The resulting suspension was kept at 35 °C for 2 h with stirring. Then, the solid was suction-filtered and washed repeatedly with deionized distilled water until no chloride could be detected using Quantab (Hach) paper (<28 ppm). The catalyst was dried for 24 h at room temperature and was labeled as-prepared catalyst. X-ray fluorescence (XRF) analysis indicated a loading of 4 wt % of Au with 90 ppm residual chloride. An activated sample was obtained by treating the as-prepared catalyst in 50 mL/min flowing H₂ for 1 h at room temperature.

4.3.2. *In-Situ* FTIR Spectroscopy.

FTIR data were collected at $-60\text{ }^{\circ}\text{C}$ in a Nicolet Nexus 670 FTIR spectrometer equipped with a mercury cadmium telluride (MCT) detector. The IR cell was comprised of a stainless steel cylinder of 6 cm^3 , fitted with CaF_2 windows. Typically, a gas flow of 70 mL/min was used, which corresponded to an average residence time through the cell of $\sim 5\text{ s}$. The catalyst was loaded as a 20 mg wafer ($\phi=1.59\text{ cm}$) covering an opening at the center of the cell by a fine tungsten mesh such that the reaction mixture flowed through the catalyst with minimal bypass. The latter was supported by the fact that results obtained from this reactor agreed with those from the U-tube microreactor. The temperature of reaction was monitored by a thermocouple located at the supporting mesh behind the catalyst. To achieve low temperature, the cell was in thermal contact with a copper housing cooled by liquid nitrogen, and the reaction gases were precooled before entering the cell. The temperature was controlled to within $\pm 2\text{ }^{\circ}\text{C}$. To prevent moisture condensation on the CaF_2 windows, the cell was jacketed in a housing purged with 1.5 L/min of dry N_2 . In situ IR spectra were acquired in the transmission mode with 15 s acquisition time per spectrum and a resolution of 4 cm^{-1} .

4.3.3. CO Adsorption.

The CO adsorption capacity of a sample was determined by monitoring the breakthrough curve of a step input in a $3/8\text{ in. o.d.}$ U-tube fused silica microreactor. Approximately 300 mg of an as-prepared Au/TiO_2 , sandwiched between two slugs of clean quartz wool, was loaded into the microreactor. The sample was cooled to $-60 \pm 1\text{ }^{\circ}\text{C}$ using a 2-propanol/dry ice bath. After the sample was purged with 70 mL/min He that was purified with a MnO trap, the gas was switched to 70 mL/min of 1% CO in He (sometimes also containing 2% Ar for internal calibration) using

a four-way switching valve. The concentration of CO leaving the reactor was monitored by a HP 5973 mass-selective detector at 1 s intervals. An identical CO profile was obtained by repeating the purging and CO exposure cycle. Subsequently, the sample was activated in 50 mL/min flowing hydrogen at 0 °C for 1 h. Afterward, the sample was purged again in He at 25 °C before cooling to -60 °C. At -60 °C, the gas was switched to 1% CO in He (sometimes with 2% Ar), and the exit CO and Ar concentration profiles were recorded. For the second cycle of CO exposure, the sample was first purged in He at -60 °C for 30 min, before starting the CO/Ar/He flow.

4.3.4. Oxidation of Adsorbed CO.

The oxidation of adsorbed CO was studied with both in situ FTIR spectroscopy, in which the evolution of different surface species in the carbonyl region was followed, and microreactor experiments, in which evolution of products was determined by mass spectrometry at 1 s intervals and gas-phase FTIR spectroscopy at 12 s intervals. After an as-prepared sample at 0 °C was activated in flowing H₂ for 60 min, the catalyst was cooled to -60 °C, and the following experimental sequence was followed: He purging (15 min), 1% CO flow (20 min), He purging (20 min), 1% CO flow (20 min), He purging (1.5 min), 2.5% (or other specified concentrations and 2% Ar) O₂ flow (20 min), He purging (1.5 min), and finally 1% CO flow (20 min).

For comparison, steady-state CO oxidation was also conducted. Approximately 100 mg of as-prepared Au/TiO₂ catalyst was loaded into the microreactor, activated at 0 °C in flowing H₂ for 1 h (50 mL/min), purged in He at room temperature for 30 min, cooled to -60 °C, and then exposed to 30 mL/min of a mixture 1% CO and 2.5% O₂ in He. The reaction products were monitored by gas-phase FTIR spectroscopy.

4.3.5. Isotopic Exchange.

$^{18}\text{O}_2$ (Cambridge Isotope Laboratories, 95%) labeling experiments were conducted using in situ FTIR spectroscopy. A 30 mg wafer of as-prepared catalyst was used, and the experiments consisted of the steps below, carried out at $-60\text{ }^\circ\text{C}$ and using a constant flow rate of 50 mL/min: H_2 activation (60 min, $0\text{ }^\circ\text{C}$), He purging (20 min), 1% CO + 2.5% $^{16}\text{O}_2$ flow (20 min), He purging (60 min), 1% CO flow (10 min), He purging (1 min), 2.5% $^{16}\text{O}_2$ flow (10 min), He purging (20 min), 1% CO flow (10 min), 1% CO + 2.5% $^{18}\text{O}_2$ flow (4 min), He purging (60 min), 1% CO flow (20 min), He purging (1 min), and 2.5% $^{18}\text{O}_2$ flow (10 min).

4.3.6. *In-Situ* XANES.

X-ray absorption near edge structure (XANES) experiments at the Au L_{III} edge (11.919 keV) were carried out at the bending magnet beamline 5-BMD of the DuPont-Northwestern-Dow Collaborative Access Team (DND-CAT) at the Advanced Photon Source (APS) at Argonne National Laboratory, following the procedure described previously.²¹ A flow-through sample cell was used, and the exit gas was analyzed by gas chromatography. Because of rather extensive back-mixing of the gases, it took about 3 min for a complete ($>99.5\%$) sweep of the gas in the cell. About 150 mg of sample was used to make a self-supporting pellet that was sandwiched between two nylon grids and placed at the end of the inner cylinder, near the center of the cell. Transient experiments were performed at $-65\text{ }^\circ\text{C}$, and the XANES data were analyzed by standard procedures with the WINXAS97 program. The normalized spectra were fitted with a linear combination of experimental standards for $\text{Au}^{3+}\text{-O}$ (Au_2O_3) and Au-Au (Au foil).

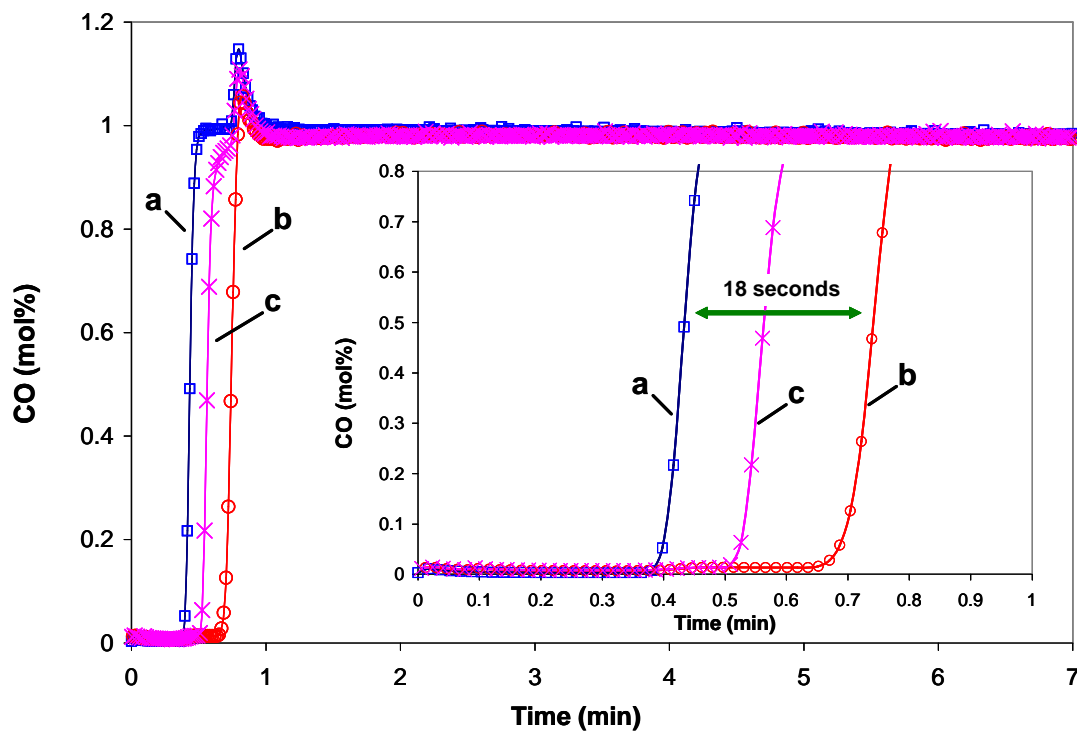


Figure 4.1. Mass spectra of breakthrough curves of CO ($m/e = 28$) for 1% CO flowing through (a) as-prepared catalyst, (b) H_2 -activated catalyst with no previous exposure to CO, and (c) H_2 -activated catalyst previously exposed to CO and followed by 30 min of He purging. Experimental conditions: catalyst = 300 mg (4% Au), flow rate = 70 mL/min, $T = -60\text{ }^\circ\text{C}$.

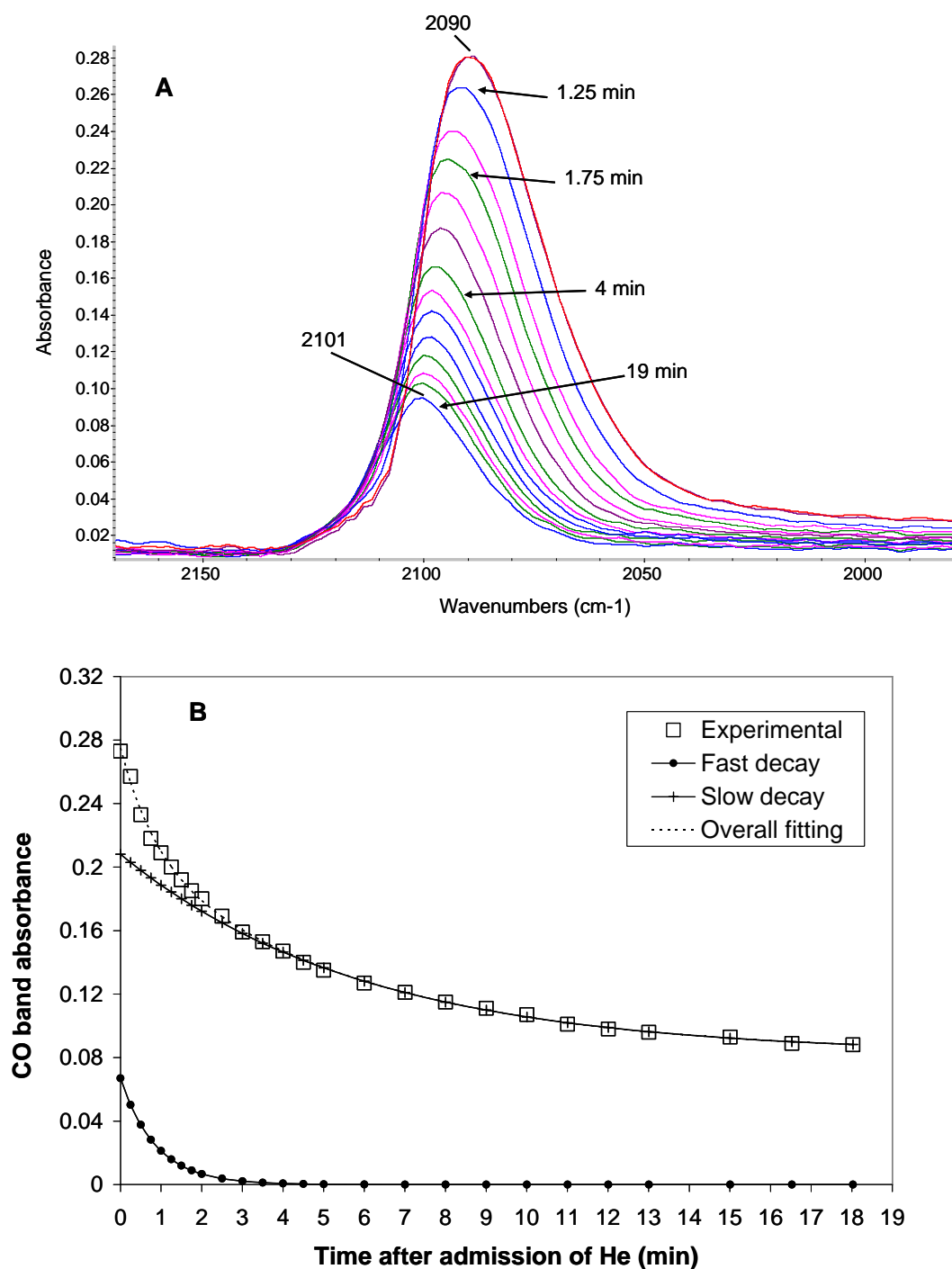


Figure 4.2. (A) Changes in FTIR spectra of activated Au/TiO₂ that had been exposed to 1% CO as a function of purging time in He at -60 °C. (B) Corresponding changes in the peak intensity.

4.4. Results

4.4.1. CO Adsorption.

Preliminary experiments showed that there was no adsorption of CO on an as-prepared sample at $-60\text{ }^{\circ}\text{C}$. There was no detectable adsorbed CO band at around 2100 cm^{-1} in the IR experiments, and the CO breakthrough curve was the same as for Ar in the U-tube microreactor flow experiments (Figure 4.1, curve a).

However, a H_2 pretreated sample adsorbed CO readily, such that the breakthrough curve in the microreactor flow experiment was delayed relative to the breakthrough curve for Ar (Figure 4.1, curve b). From the time difference between these two breakthrough curves, the concentration of CO (1%), and gas flow rate, the quantity of adsorbed CO could be estimated to be $10.6 \pm 2\text{ }\mu\text{mol}$ in this experiment, which corresponded to $0.18 \pm 0.03\text{ mol CO}/(\text{mol Au})$ in the sample. It should be pointed out that the spike at about 0.8 min was an artifact in the mass spectrometer signal due to switching of gases. It appeared for all gases and even in the absence of a sample, and its magnitude was nearly constant. Therefore, it was removed from the data in the analyses.

A similar experiment conducted in the IR cell showed the appearance of an intense asymmetric absorption band at around 2090 cm^{-1} that attained a constant intensity within 60 s and could be deconvoluted into two bands at 2091 and 2066 cm^{-1} . Multiple bands in the $1200\text{--}1700\text{ cm}^{-1}$ carbonate/bicarbonate region also appeared.

Purging in He at $-60\text{ }^{\circ}\text{C}$ removed part of the adsorbed CO rather rapidly, as indicated by the decrease in the intensity of the 2090 cm^{-1} band (Figure 4.2A). At the same time, the peak maximum shifted to 2101 cm^{-1} . The change in the absorbance at the peak maximum with purging time is shown in Figure 4.2B. Assuming a constant absorbance for the species that constituted

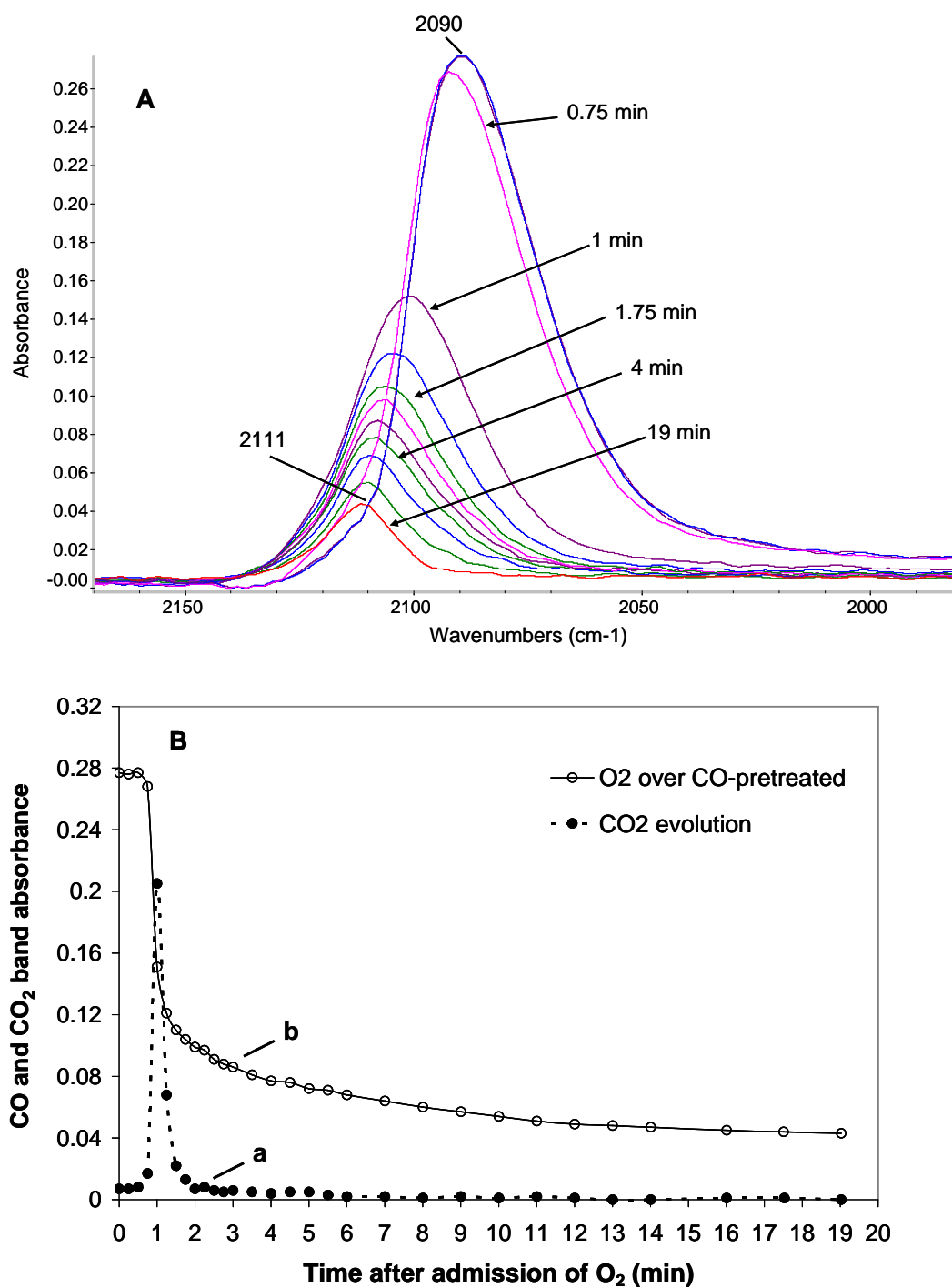


Figure 4.3. (A) Changes in the IR peak at around 2100 cm⁻¹ after switching to a flow of 2.5% O₂ and (B) corresponding changes in the peak intensity (curve b) and intensity of the adsorbed CO₂ peak (2340 cm⁻¹, curve a).

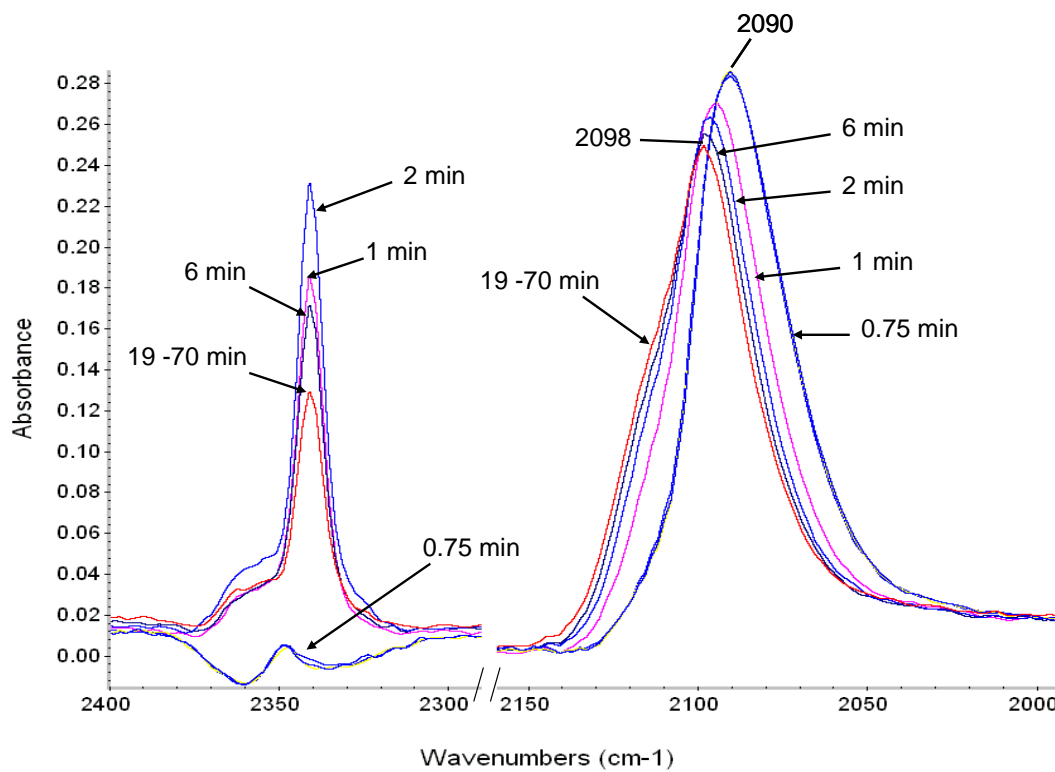


Figure 4.4. Evolution of the FTIR spectra of a catalyst after the gas was switched from 1% CO to a mixture 1% CO and 2.5% O₂ in He. Gas-phase CO has been subtracted from the spectra. Experimental conditions: catalyst = 10 mg, flow rate = 70 mL/min, $T = -60^{\circ}\text{C}$.

this peak, this curve also represented the change in the coverage of adsorbed CO. Thus, about half of the adsorbed CO was desorbed in less than 5 min. The remaining CO was desorbed slowly, and about 25% remained after 40 min. The total desorption curve could be fitted reasonably well with two exponential decay terms with rate constants of 0.168 and 1.15 min⁻¹ for the slow and the fast process, respectively. The corresponding preexponential constants were 0.126 and 0.067, implying a relative coverage of 2:1 for the slow and fast processes. The slow desorption at long times was consistent with results from the microreactor experiments. After 30 min of He purging, ~73 ppm of CO was detected in the exit gas, and the background level measured at the beginning of the experiment was typically 40-76 ppm of CO.

After 30 min of He purging, exposure of the sample to a 1% CO flow again resulted in a breakthrough curve that was delayed but by a shorter time (Figure 4.1, curve c). It was estimated that for this second cycle of exposure the amount of CO adsorbed by the sample was 5.3 ± 1 μ mol (or 0.09 ± 0.02 mol/(mol Au)). Infrared spectroscopy also showed readsorption of CO and the reappearance of the asymmetric 2090 cm⁻¹ band to the same intensity. In fact, we repeated the desorption and readsorption cycle of these CO species three times and obtained similar results. The decrease in the CO uptake in subsequent cycles compared to the first cycle was due to incomplete CO desorption after 30 min of purging. The bands in the carbonate/bicarbonate region also increased, but the change in the second cycle was much less (about 20%) than that for the freshly activated sample.

4.4.2. Reaction of Adsorbed CO.

Figure 4.3A shows the IR spectra of the reaction of adsorbed CO with O₂. A freshly activated sample (that had not been exposed to oxygen previously) was first exposed to 1% CO

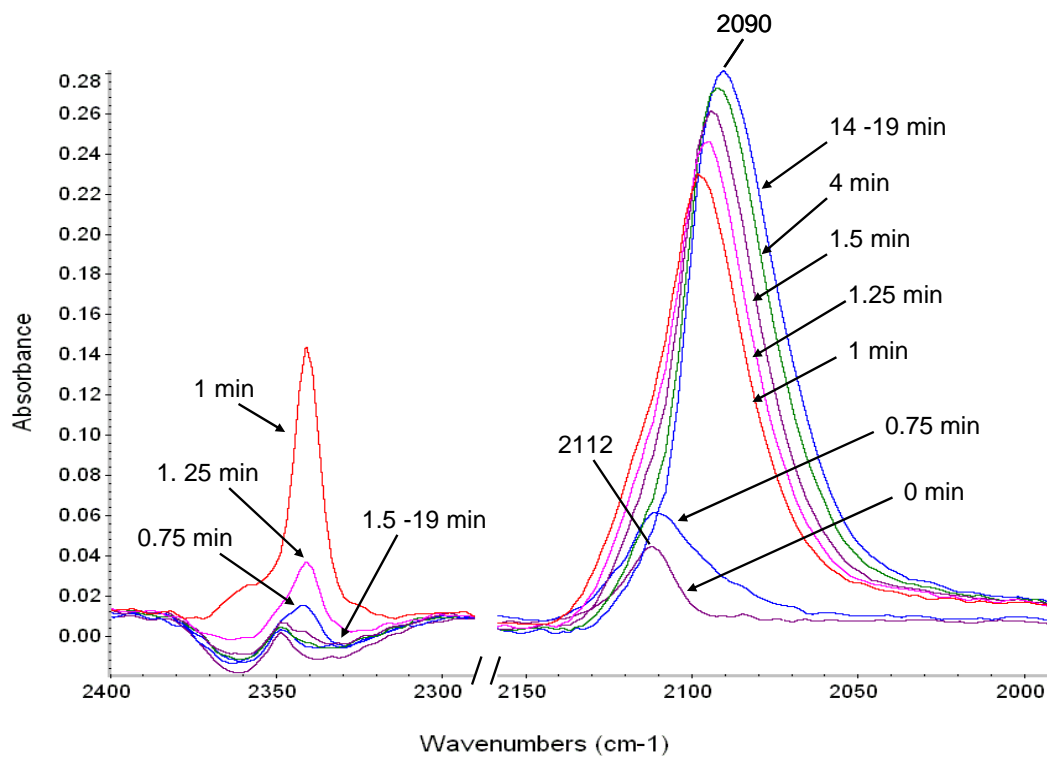


Figure 4.5. Evolution of FTIR spectra when an O₂-saturated catalyst was exposed to a flow of 1% CO in He. Gas-phase CO has been subtracted from the spectra. Experimental conditions: catalyst = 10 mg, flow rate = 70 mL/min, $T = -60\text{ }^{\circ}\text{C}$.

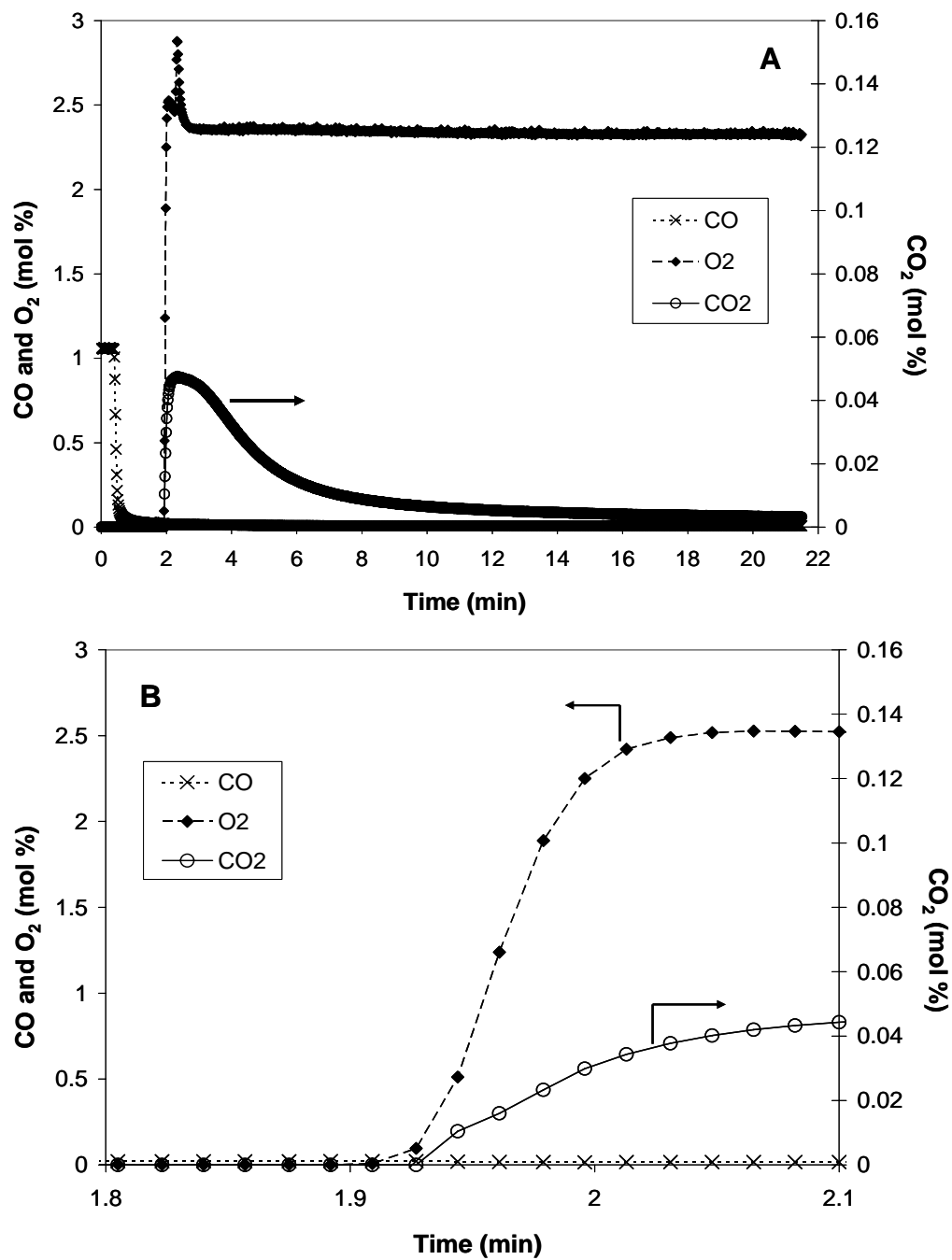


Figure 4.6. (A) Time-dependent concentration at the exit of CO (×), O₂ (♦) and CO₂ (○) in the reaction of preadsorbed CO with flowing O₂. After being purged with He for 1.5 min to remove gas-phase CO, O₂ was admitted. (B) Expanded plot of part A at around 2 min after switching to O₂ flow.

at $-60\text{ }^{\circ}\text{C}$ and then purged with He (see Experimental Section for details). Then, the gas was switched to 2.5% O_2 . The intensity of the 2090 cm^{-1} band decreased very rapidly in the first 1 min, and a new band appeared at 2112 cm^{-1} . The intensity of this new band increased initially and then decreased slowly until it disappeared after 60 min. A band at about 2340 cm^{-1} due to adsorbed CO_2 also appeared. Its intensity increased and then decreased rather rapidly, as shown in Figure 4.3B, curve a. The intensity of the carbonate/bicarbonate bands in the $1200\text{--}1700\text{ cm}^{-1}$ region nearly doubled. Further increase was much more moderate in repeating cycles of CO and O_2 exposures.

The intensity of this carbonate/bicarbonate region could be brought to a nearly steady state by using the sample for catalytic CO oxidation with 1% CO and 2.5% O_2 at $-60\text{ }^{\circ}\text{C}$. In a flow of this reaction mixture, a constant intensity of the overlapping bands at 2112 and 2090 cm^{-1} as well as of the adsorbed CO_2 band at about 2340 cm^{-1} could be obtained beyond about 20 min (Figure 4.4).

A complementary set of experiments to investigate the reaction of adsorbed oxygen with CO was conducted, and the results are shown in Figure 4.5. A sample, after being in flowing 2.5% O_2 at the end of the experiment shown in Figure 4.3 and then purged in He for 1.5 min, was exposed to a flow of 1% CO. The resulting set of IR spectra was almost reverse to those of Figure 4.3. When the CO was admitted to the IR cell, the residual band at 2112 cm^{-1} increased in intensity, and immediately afterward, the band at 2090 cm^{-1} appeared, which became dominant by 1 min. Simultaneously, the band of adsorbed CO_2 at about 2340 cm^{-1} appeared briefly at around 1 min.

The results of these experiments using a microreactor are shown in Figures 4.6 and 4.7. A sample that was exposed to a flow of 1% CO was purged with He for 1.5 min. The mass

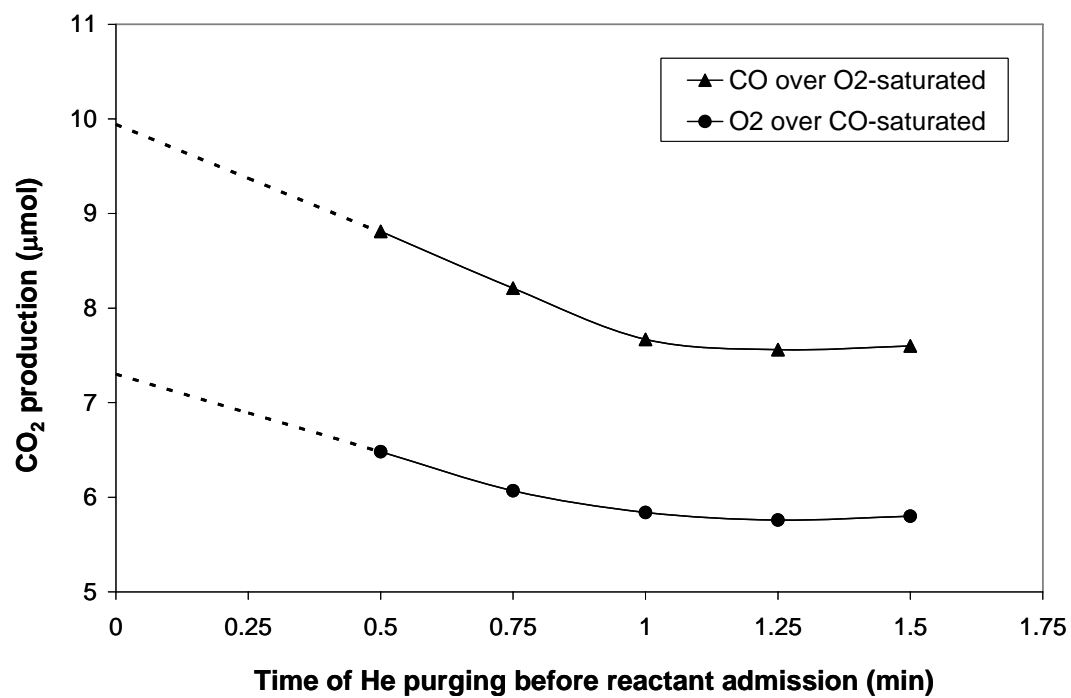


Figure 4.7. CO₂ generated by reaction of adsorbed CO with O₂ (●) and adsorbed oxygen with CO (▲), as a function of the purging time in He prior to the admission of O₂ or CO, respectively. Dashed lines are extrapolation of experimental data to zero purging time. Experimental conditions: catalyst = 300 mg, flow rate = 70 mL/min, $T = -60\text{ }^{\circ}\text{C}$.

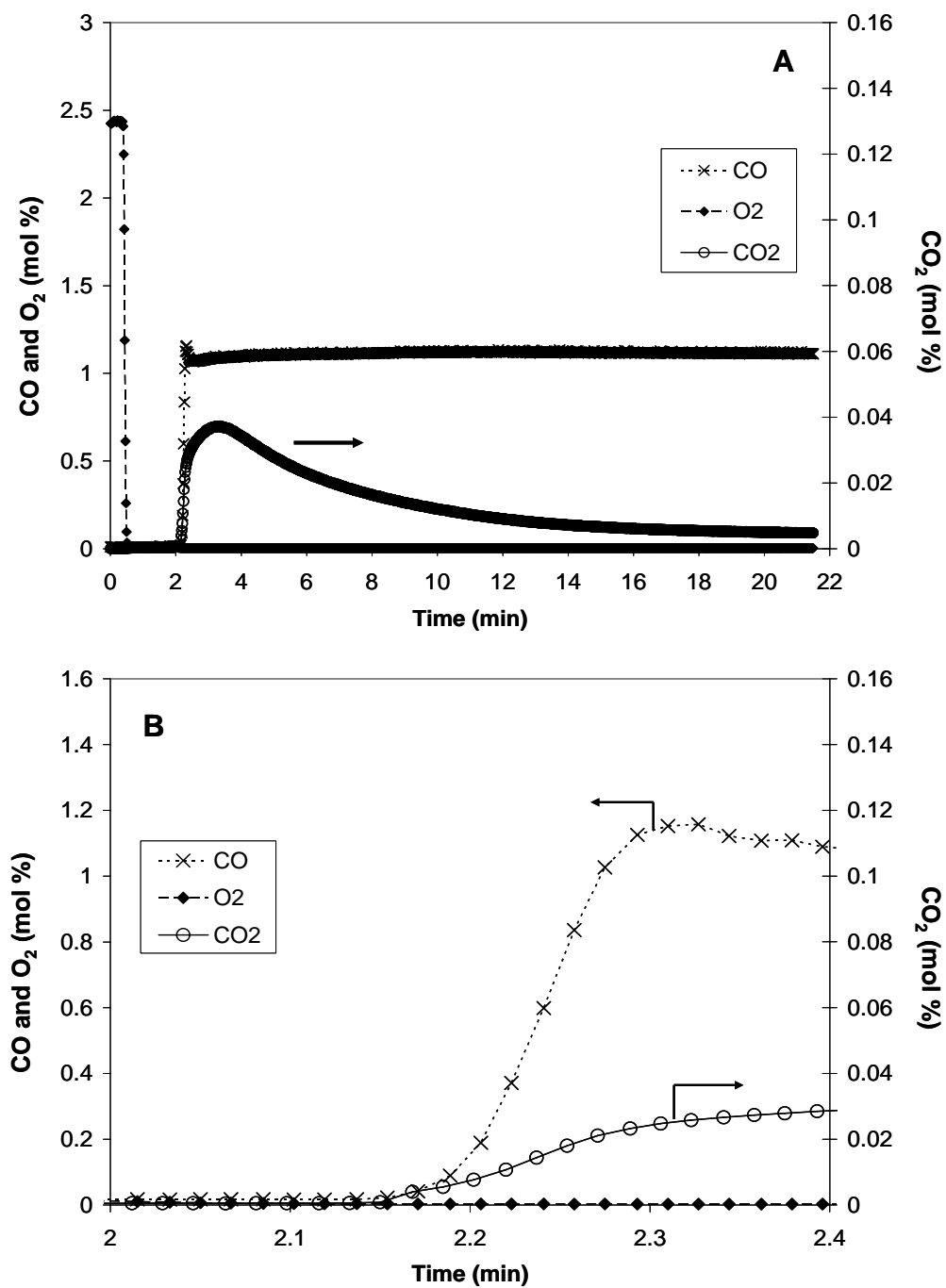


Figure 4. 8. (A) Time-dependent concentration of CO (\times), O₂ (\diamond), and CO₂ (\circ) in the reaction of preadsorbed O₂ with flowing CO. After 1.5 min of He flow to remove gas-phase O₂, the gas was switched to CO. (B) Expanded version of part A at about 2 min.

spectrum CO signal decreased rapidly to the background level within 0.5 min. After being purged, the gas was switched to 2.5% O₂; both CO₂ and oxygen signals appeared simultaneously at the reactor exit (Figure 4.6A). The CO₂ intensity increased rapidly to a maximum in less than 1 min after its first appearance and decreased slowly over the next 8 min. The area under this curve, which corresponded to the amount of CO₂ detected, decreased slowly with increasing He purging time, due to desorption of adsorbed CO. By quantification of the dependence of CO₂ produced with He purging time and extrapolation of the data to zero purging time, an amount of $7.3 \pm 0.7 \mu\text{mol}$ of CO₂ (or $0.12 \pm 0.01 \text{ mol CO}_2/(\text{mol Au})$) was found to be produced from adsorbed CO equilibrated with 1% CO in the gas (Figure 4.7).

The breakthrough curve for O₂ depended on its concentration between 2.5% and 0.1%. It appeared later for lower concentrations, due to the fact that it took longer to supply the same amount of O₂ molecules to react with a certain number of adsorbed CO molecules. Interestingly, the appearance of CO₂ always coincided with the appearance of breakthrough O₂, although the total amount of CO₂ detected remained rather constant. From the delay in the breakthrough curve of the 0.1% O₂ experiment, an estimated $4.6 \pm 0.5 \mu\text{mol}$ of O₂ (or $0.08 \pm 0.01 \text{ mol O}_2/(\text{mol Au})$) was consumed by reaction and adsorption on the catalyst.

After the reaction of adsorbed CO with 30 min of flowing O₂, the sample, now containing adsorbed oxygen and some unreacted adsorbed CO (as indicated by the intensity of the 2112 cm⁻¹ band being 10-15% of total adsorbed CO), was used to examine the reaction of adsorbed oxygen with flowing CO. Thus, after 1.5 min of purging in He, the gas was switched to 1% CO. As shown in Figure 4.8, CO₂ was detected, breaking through at the same time as CO. The CO₂ production rate reached a maximum between 1.5 and 2 min after switching and then decreased slowly. Again, the amount of CO₂ detected decreased slightly with increasing He purging time.

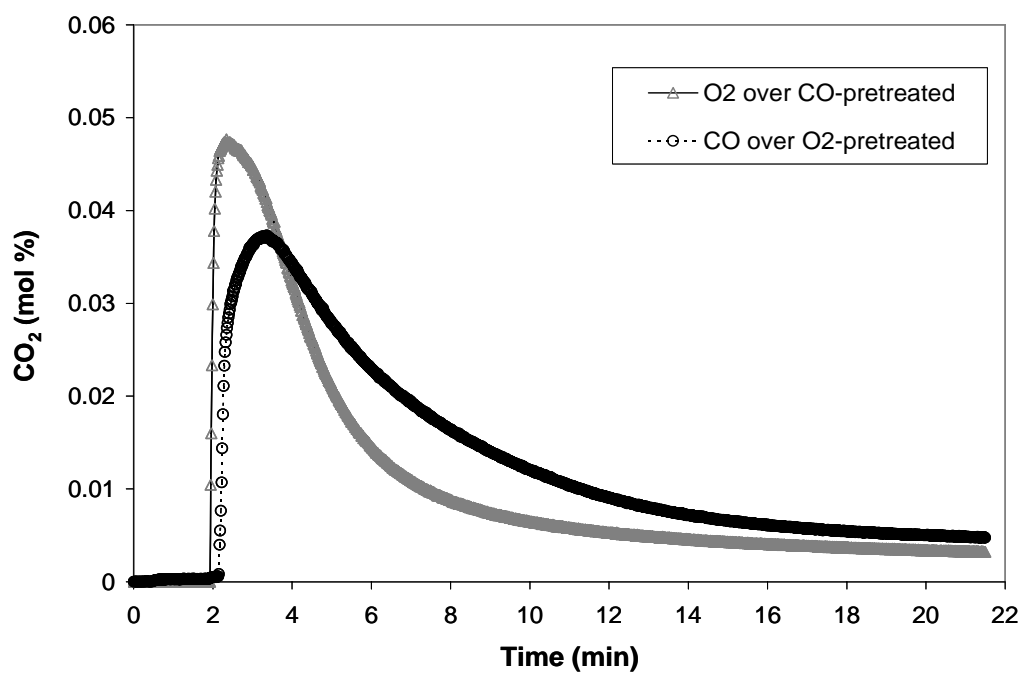


Figure 4.9. Comparison of the CO₂ evolution profiles for a catalyst pretreated with 1% CO and then exposed to flowing O₂ (▲), and a catalyst pretreated with 2.5% O₂ and then exposed to flowing CO (○). Experimental conditions: catalyst used = 300 mg, flow rate = 70 mL/min, $T = -60$ °C.

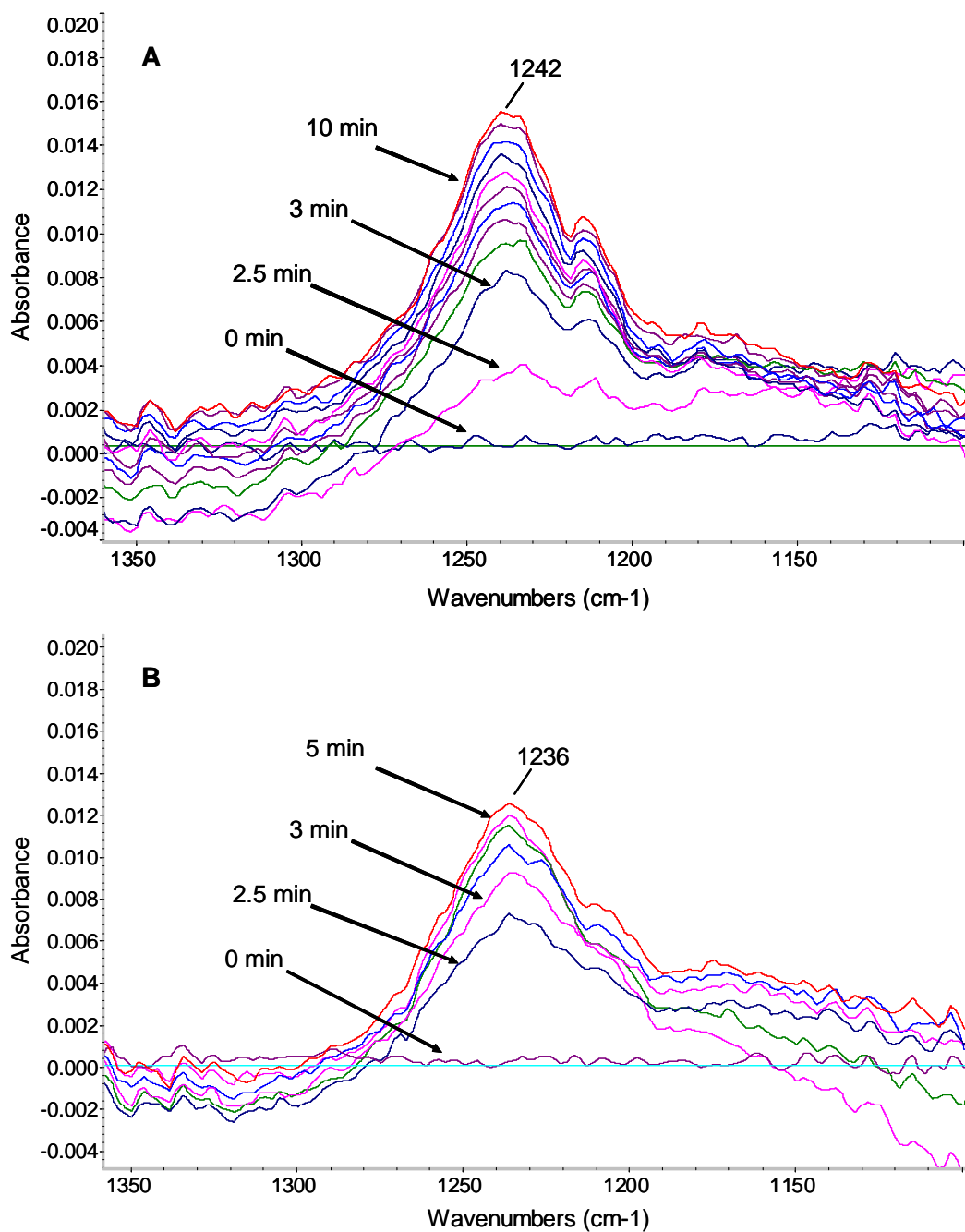


Figure 4.10. (A) Changes in the 1100-1350 cm⁻¹ region of the IR spectrum with time after switching the gas flowing to a fresh H₂-activated catalyst to 1% CO and (B) after a sample previously used for reaction using 1% CO and 2.5% ¹⁸O₂ was exposed to 1% CO.

By extrapolation of the results to zero purging time, a value of $9.9 \pm 1.5 \mu\text{mol}$ of CO_2 ($0.17 \pm 0.02 \text{ mol CO}_2/(\text{mol Au})$) was found to be produced from adsorbed oxygen (Figure 4.7). In addition, from the breakthrough curve of CO, an estimated $9.6 \pm 1 \mu\text{mol}$ of CO ($0.16 \text{ mol CO}/(\text{mol Au})$) was consumed by reaction with adsorbed oxygen and subsequent adsorption on Au within the first minute.

The CO_2 evolution curve from reaction of CO with adsorbed oxygen differed from reaction of oxygen with adsorbed CO, as shown in Figure 4.9. Specifically, the CO_2 was evolved noticeably slower in the former experiment, although a fraction of the CO_2 was evolved rapidly in both cases.

4.4.3. Isotope Labeling Experiments.

Experiments were conducted to detect the possible presence of hydroxycarbonyl, which is expected to exhibit a vibrational band in the $1200\text{-}1300 \text{ cm}^{-1}$ region.³³ An as-prepared sample, freshly activated with H_2 in the IR sample cell, was exposed to a stream of 1% CO at -60°C . Multiple peaks in the $1200\text{-}1700 \text{ cm}^{-1}$ region appeared (not shown). Of particular interest was the appearance of a peak at 1242 cm^{-1} (Figure 4.10A). The intensity of this peak increased with time of exposure to CO before reaching a maximum and decreased slightly upon purging the sample with He. It disappeared rather quickly when the sample was exposed to 2.5% O_2 at -60°C (Figure 4.11A). At the same time, transient production of CO_2 (2345 cm^{-1} peak) was observed. The changes in these peak intensities with time are shown in Figure 4.12A.

This 1242 cm^{-1} peak could not be detected if the sample was at steady state with a reaction mixture (1% CO and 2.5% O_2). An attempt to determine if the species responsible for this peak contains oxygen atoms was made using ^{18}O labeling. The catalyst surface was first

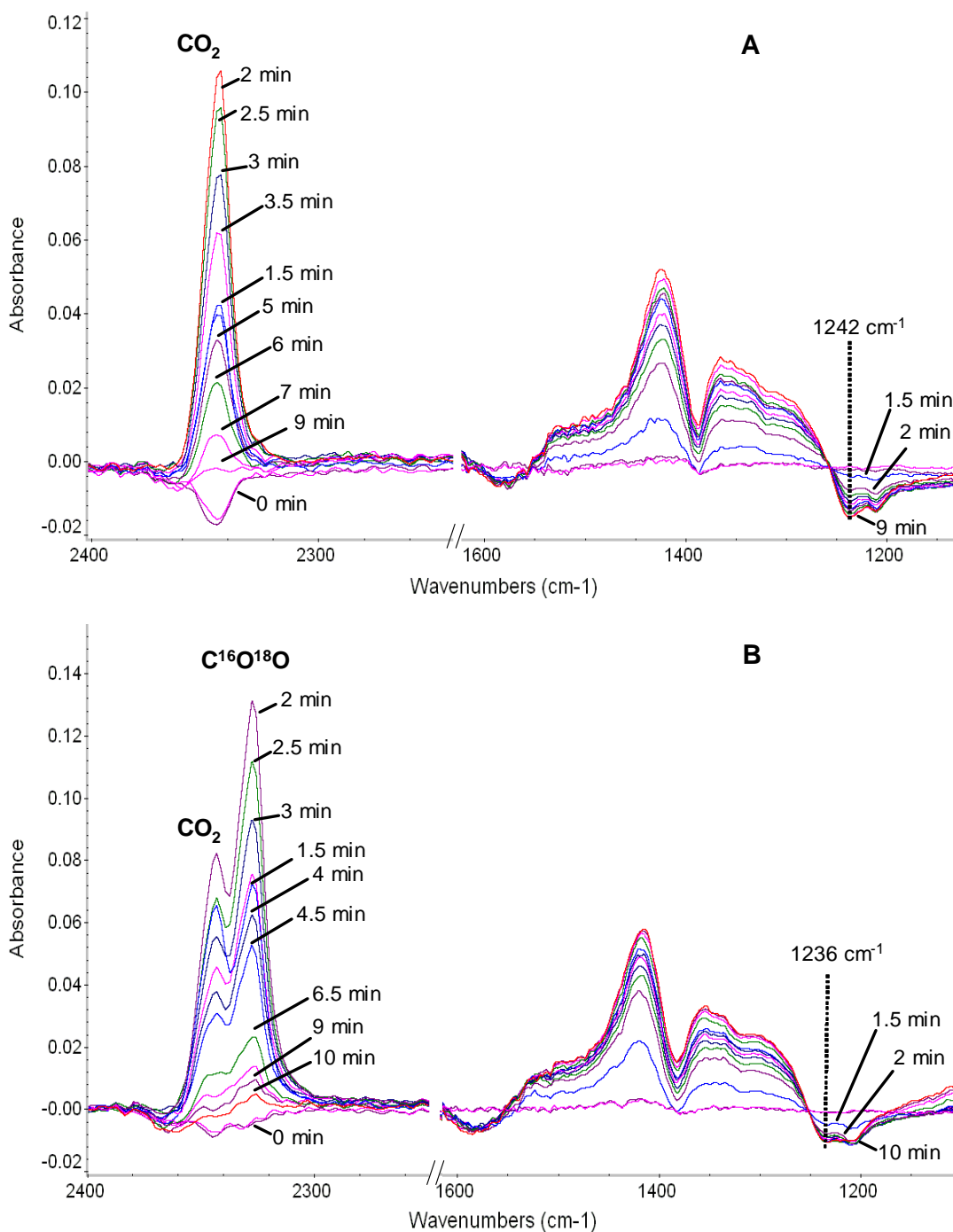


Figure 4.11. Changes in the IR spectrum (A) after switching to 2.5% ¹⁶O₂, of the sample corresponding to Figure 10A, and (B) after switching to 2.5% ¹⁸O₂, of the sample corresponding to Figure 10B. The reference spectra were those just before O₂ admission.

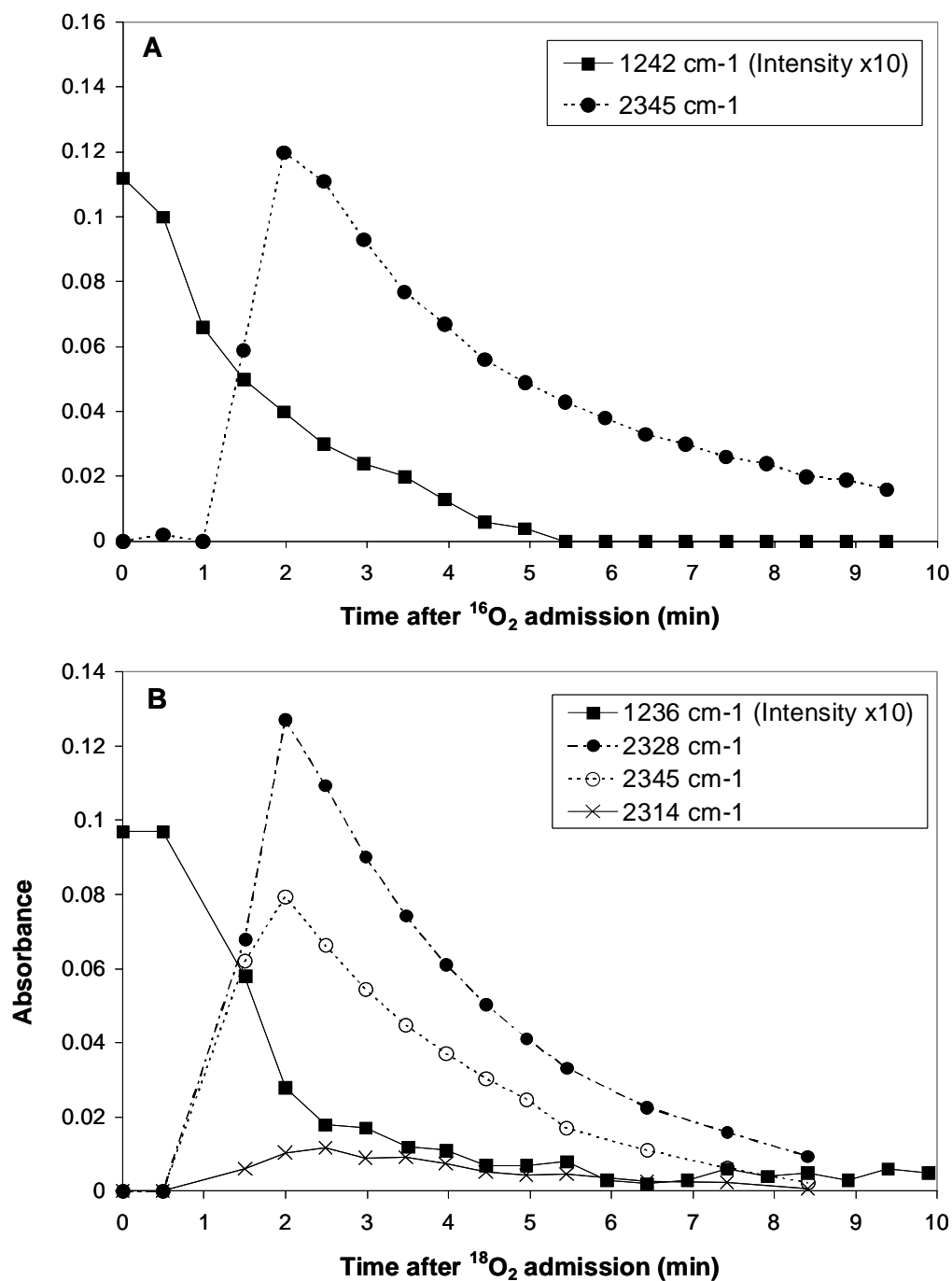


Figure 4.12. Changes in intensities of (A) the 1242 cm⁻¹ peak after switching to ¹⁶O₂ (■) and the corresponding transient appearance of carbon dioxide C¹⁶O₂ (●) and (B) the 1236 cm⁻¹ peak and the corresponding transient appearance of C¹⁶O¹⁶O (○), C¹⁶O¹⁸O (●), and C¹⁸O¹⁸O (×) after switching to ¹⁸O₂.

populated with ^{18}O by running a steady state reaction at $-60\text{ }^{\circ}\text{C}$ using a mixture of 1% CO and 2.5% $^{18}\text{O}_2$ for 4 min. After being purged with He subsequently, the sample was exposed to a flow of 1% CO. A peak at 1236 cm^{-1} appeared instead of the 1242 cm^{-1} peak (Figure 4.10B). This peak also disappeared rather rapidly when the sample was exposed to 2.5% $^{18}\text{O}_2$ (Figure 4.11B). The transient production of CO_2 now consisted of a mixture of C^{16}O_2 (2345 cm^{-1} peak), $\text{C}^{16}\text{O}^{18}\text{O}$ (2328 cm^{-1} peak), and C^{18}O_2 (2314 cm^{-1} peak). The changes in these peak intensities with time are shown in Figure 4.12B.

4.4.4. In Situ XANES Measurements.

The XANES spectrum of a H_2 -activated sample resembled that of metallic Au.²¹ When the sample was exposed to 1% CO, there was a small increase in the edge absorption (Figure 4.13A). The edge absorption decreased slowly by purging in He and returned to the state prior to exposure to CO in about 40 min. If the sample was purged with 2.5% O_2 instead of He, then the decrease in the edge absorption was faster, and the edge absorption returned to the initial state within 13 min (Figure 4.13B). There was no substantial structural change due to treatment in CO or O_2 , compared to He. For instance, the Au-Au coordination numbers determined by extended X-ray absorption fine structure (EXAFS) analysis were (± 0.2) 8.4, 8.6, and 8.9 when the sample was in He, CO, and O_2 , respectively.

4.5. Discussion

The combination of IR spectroscopy and quantitative determination of adsorption and reaction of adsorbed species generated information about the CO oxidation reaction pathway

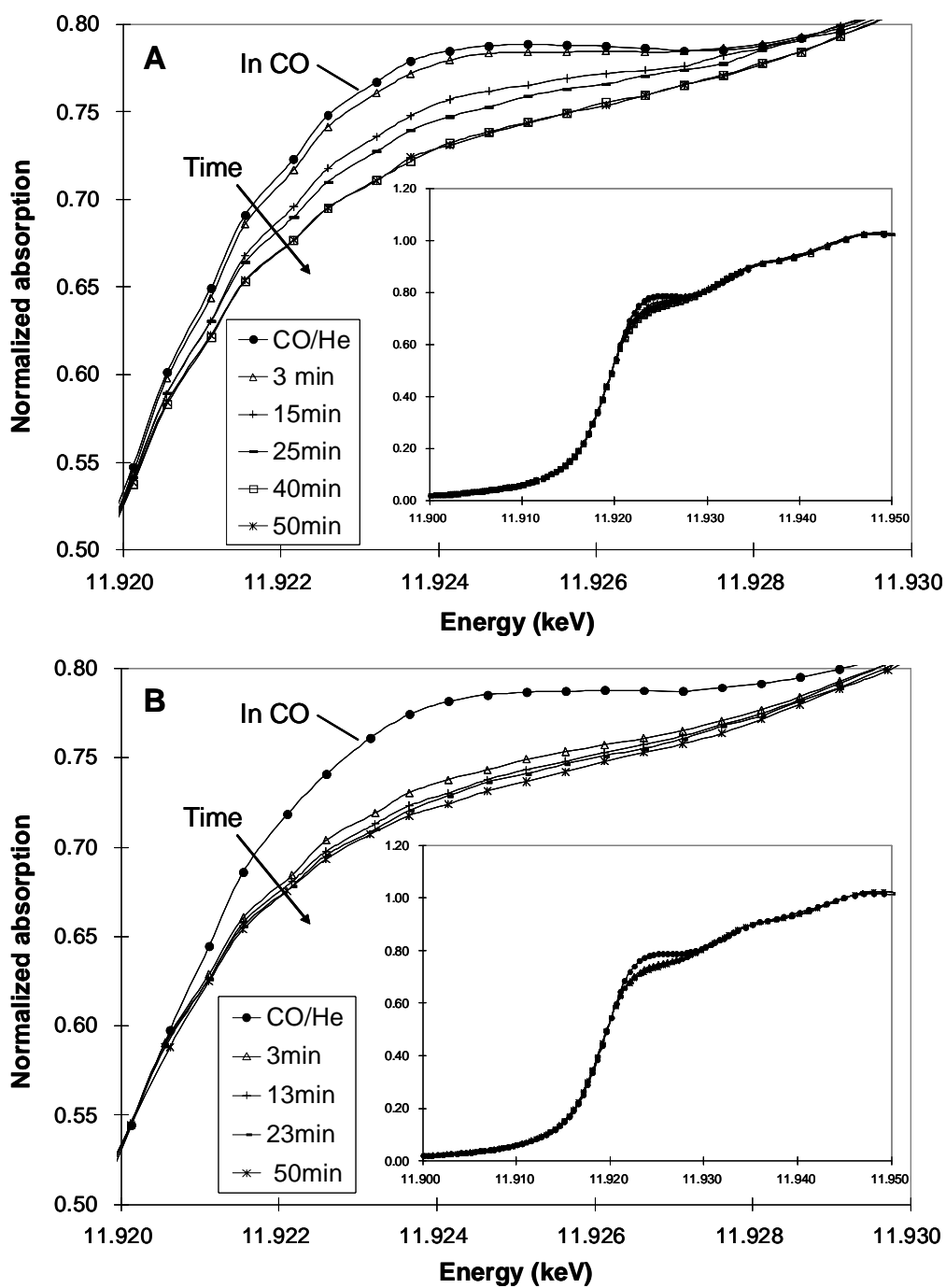


Figure 4.13. Changes in the in situ XANES spectra of a fully reduced Au/TiO₂ catalyst that was equilibrated with 1% CO, during purging with (A) He or (B) 2.5% O₂. The insets are the entire XANES spectra. Experimental conditions: catalyst = 100 mg, flow rate = 100 mL/min, $T = -65$ °C.

over Au/TiO₂ and, specifically, the role of various adsorbed CO species and identification of a possible reaction intermediate signified by the 1242 cm⁻¹ peak.

There was no adsorption of CO on an as-prepared sample, which is consistent with the fact that the Au precursor is present as an oxyhydroxy complex on the support and catalytically inactive. The catalyst can be activated by treatment in H₂ at room temperature to reduce the Au cation to Au⁰,²¹ and the activated sample adsorbs CO readily. Similar to the observations by Boccuzzi et al.,^{2,3,40} at room temperature, the IR peak of the adsorbed CO is asymmetric (Figure 4.2), which might indicate surface heterogeneity. The peak shifts to a higher frequency with decreasing coverage (Figure 4.2A), as was observed by others.^{40,41} In the literature, this has been interpreted as due to decreasing σ -donation from adsorbed CO to the metal on increasing coverage. Results from the microreactor measurements show that about 18% of the Au in the catalyst adsorbs CO (Table 4.1, footnote). Since the average Au particle size is 2 nm,²¹ about 50% of the atoms in the Au particles are exposed. Hence, only 36% of the surface Au adsorbs CO at -60 °C.

Table 4.1. Quantities of various species on Au/TiO₂^a

Species	Quantity (mole/mole Au) ^b		
	2.5% O ₂	0.6% O ₂	0.1% O ₂
CO consumed by reaction with adsorbed O ₂ and subsequent adsorption on Au ^c	0.16 ± 0.01	0.15 ± 0.01	0.14 ± 0.01
O ₂ consumed by reaction with adsorbed CO and subsequent adsorption on catalyst ^c	0.06 ± 0.01	0.06 ± 0.01	0.08 ± 0.01
CO ₂ formed by reaction of CO with adsorbed O ₂	0.13 ± 0.01	0.13 ± 0.01	0.13 ± 0.02
CO ₂ formed by reaction of O ₂ with adsorbed CO	0.12 ± 0.01	0.12 ± 0.01	0.12 ± 0.02

^a In all experiments, 1% CO was used. The amount of CO adsorbed on a clean Au surface (one never exposed to CO or O₂) was 0.18 ± 0.03 mol/(mol Au). ^b Data reported for 2.5% and 0.6% O₂ corresponds to 1.5 min of He purging. For 0.1% O₂, it corresponds to 0.5 min of He purging. ^c From delays in the breakthrough curves.

When this adsorbed CO is exposed to 2.5% O₂, the IR results show that a portion of it reacts rapidly (Figure 4.3A). At the same time, a new peak appears at 2112 cm⁻¹. This new species is rather unreactive and disappears slowly in the flow of oxygen. It has been assigned to an OC–Au^{δ+}–O^{δ-} species.^{3,36} The same species has been proposed to be a very unstable intermediate that decomposes to CO₂ during CO oxidation in the presence of water.⁶ Under our conditions, however, its slow rate of disappearance suggests that it is unimportant in our reaction.

The portion of adsorbed CO that reacts rapidly with O₂ can be estimated by the changes in the 2090 cm⁻¹ peak. Assuming identical extinction coefficients for all adsorbed CO, the change in the surface coverage of CO after O₂ exposure is shown in Figure 4.3B, curve b. After correction for the portion due to desorption using the data in Figure 4.2B and application of the absolute coverage of 0.18 ± 0.03 mol/(mol Au), it is estimated that the adsorbed CO reacts with a turnover rate (TOR) of 1.4 ± 0.2 mol CO (mol Au min)⁻¹ at -60 °C. The steady-state TOR at this temperature, using 1% CO and 2.5% O₂, is 1.2 ± 0.1 mol CO (mol Au min)⁻¹. That these values are similar suggest that the 2090 cm⁻¹ adsorbed CO is responsible for steady-state reactivity. The simultaneous evolution of CO₂ when this species reacts with O₂ further supports this assignment (Figure 4.3B). Under the steady-state reaction conditions, the surface coverage of this species is almost as high as in the adsorption experiment (Figure 4.4), which is consistent with similar TORs obtained in both cases. It is present together with the much less reactive species at 2112 cm⁻¹ (Figure 4.4).

The less reactive, 2112 cm⁻¹ species can also react with oxygen but at a slower rate. The reaction of this species and readsorption of CO₂ on TiO₂ result in CO₂ evolution extending

beyond 20 min (Figure 4.9). When all CO₂ evolved up to 20 min is collected, the total amount, 0.12 mol/(mol Au) (Figure 4.7), approaches the total adsorbed CO (Table 4.1).

After the catalyst has been under flowing oxygen for over 4 min, there is little 2090 cm⁻¹ species left. However, there could be adsorbed oxygen that is catalytically active. When this sample is exposed to flowing CO, transient formation of CO₂ is observed (Figure 4.5), and from the breakthrough curve of CO, a total of 0.14-0.16 mol CO/(mol Au) was consumed by reaction and subsequent adsorption on Au within the first 2 min (Table 4.1). Since about 0.18 ± 0.03 mol/(mol Au) is due to adsorption (or 0.14 ± 0.05 after correcting for the portion of the surface occupied by the remaining 2112 cm⁻¹ species), the result implies that only a small amount of CO reacted with adsorbed oxygen. In other words, there is only a small amount of adsorbed oxygen on the Au.

It should be noted that the entries in the first two rows in Table 4.1 are determined from delays in the breakthrough curves in the microreactor transient experiments. Thus, they represent quantities due to the fast processes (within the first 2-3 min). Quantities due to slower processes are not determined in these experiments.

The much lower surface density of adsorbed oxygen than that of adsorbed CO is consistent with the XANES results (Figure 4.13). In comparison to a clean Au sample, the intensity of the near edge absorption peak is stronger in a 1% CO atmosphere than in 2.5% O₂, when the intensity is indistinguishable from a clean Au sample. The increase in edge intensity by adsorbed CO implies electron transfer from Au to adsorbed CO, consistent with the red shift in the CO stretching frequency compared with that of gas-phase CO.

The small amount of adsorbed oxygen on Au, however, appears to contradict the amount of CO₂ detected. As shown in Table 4.1, 0.13 mol CO₂/(mol Au) is detected when CO passes

over a sample preexposed to 2.5% O₂. If CO₂ can only be formed from adsorbed oxygen on Au (and there is little residual gaseous oxygen in the reactor), then one should expect an amount no more than the difference between the quantity of CO adsorbed and the total CO consumed, i.e., close to the uncertainty of the measurements (about 0.03 mol CO₂/(mol Au)). We believe that the much larger amount of CO₂ detected is because there is an additional slow process in which CO₂ is formed by reaction with another form of adsorbed oxygen. We postulate that there is a small quantity of very active oxygen adsorbed on Au, which reacts with CO with a TOF of the order of 1 min⁻¹. However, there are other reactive oxygen species, possibly adsorbed on TiO₂ near the Au particles, which either can migrate to and react with CO on Au (therefore at a slower observed rate) or react directly but more slowly on the support such that, as mentioned earlier, they cannot be readily detected by the delay in the breakthrough curve. Boccuzzi et al. also postulated another source of oxygen from the support, in addition to that on Au.³⁴ That this oxygen on the support reacts more slowly is indicated by the slower and longer decay curve of the detected CO₂ at the reactor exit (Figure 4.9) when CO reacts with adsorbed oxygen than in the reverse experiment of O₂ reacting with adsorbed CO. This difference also suggests that the slow evolution of CO₂ is not entirely due to readsorption of formed CO₂ on the support. There are suggestions in the literature that oxygen is activated on vacancy sites on the support during steady-state reaction.^{26-28,32} Our results suggest that such oxygen species, though capable of oxidizing CO either directly or after migration to Au, do not contribute much to the steady state reaction rate under our conditions because of their slow reaction rate.

Regarding potential surface reaction intermediates, adsorption of CO also produces a peak at 1242 cm⁻¹, which is shifted to 1236 cm⁻¹ when ¹⁸O was used (Figure 4.10). When the sample is exposed to O₂, this peak disappears rapidly (Figure 4.11), unlike other peaks in this

region also formed at the same time and increasing in intensity, which we assign to carbonate/bicarbonate. In one of the proposed reaction mechanisms in the literature, adsorbed CO is inserted into a surface hydroxyl to form a hydroxycarbonyl. The hydroxycarbonyl is oxidized to bicarbonate, which decomposes rapidly to CO₂ and regenerates the surface hydroxyl.^{7,8} A density functional theory (DFT) calculation of hydroxycarbonyl on Au(110) surfaces indicates that such a species should have a normal vibrational mode δ_{OH} at 1245 cm⁻¹.³³ In addition, theoretical calculations conducted by us using a model molecular species of HO(CO)M (M = heavy element) show a red shift of ~ 5 cm⁻¹ due to isotopic substitution of ¹⁶OH by ¹⁸OH. We observed a shift of 6 cm⁻¹. Thus, we assign the 1242 cm⁻¹ peak to a surface hydroxycarbonyl. In the presence of CO but absence of oxygen, hydroxycarbonyl accumulates on the surface because no oxygen is available to oxidize it. When oxygen is admitted, it is oxidized rapidly, and CO₂ is evolved. If ¹⁸OH populates the surface and insertion of C¹⁶O forms H¹⁸O(C¹⁶O)-M, then oxidation of this species with ¹⁸O would result in a surface bicarbonate HC¹⁸O₂¹⁶O-M in the first reaction cycle. When this bicarbonate decomposes, the expected product would be a mixture of C¹⁸O₂ and C¹⁸O¹⁶O but no C¹⁶O₂. If, for some unknown reasons, the oxygen atoms in the surface bicarbonate or hydroxycarbonyl species scrambled randomly, then the product would be a mixture of C¹⁸O₂, C¹⁸O¹⁶O, and C¹⁶O₂ in a ratio of 4:4:1. We observed less C¹⁸O₂ and much more C¹⁶O₂ than predicted by either of these scenarios. We believe that this is due to rapid isotopic scrambling of the product CO₂ with surface carbonate, which greatly reduces the ¹⁸O content in the observed CO₂.

4.6. Conclusions

The combined results from IR, microreactor, and XANES studies offer a consistent picture regarding the CO oxidation reaction on Au/TiO₂. On this catalyst, the active CO species is adsorbed on metallic Au and exhibits an IR peak at 2090 cm⁻¹. Other adsorbed CO species, such as the species at 2112 cm⁻¹, do not contribute much to the reaction at steady state. While metallic Au adsorbs CO readily, it does not adsorb much oxygen, but the adsorbed oxygen is catalytically very active. There are other adsorbed oxygen species that oxidize CO but only slowly and probably do not contribute much to the steady-state activity. Finally, there is evidence that hydroxycarbonyl is a relevant reaction intermediate for this reaction.

CHAPTER 5

SYNTHESIS AND CHARACTERIZATION OF SILOXANE NANOCAGES

5.1 Synopsis

This chapter presents the work performed to synthesize and characterize siloxane nanocages previously developed in our group.¹ While the main steps used to prepare them paralleled those previously reported,¹ several modifications to the original protocol were implemented in order to facilitate the purification of reactants and products, increase the yield of several chemicals involved in the synthesis, enhance reproducibility and ultimately, reduce the time required to produce clean and fully deprotected nanocages. Siloxane nanocages were prepared in four major steps: (i) self-assembly of silicon surfactant into 2nm micelles, (ii) hydrolysis and condensation of the surfactant's head groups, (iii) cross-linking of unreacted groups at the surface to form a porous shell with spherical symmetry enveloping the surfactant's hydrophobic tails and (iv) deprotection of internal carbamate groups with the subsequent generation of primary amine functionalities at the interior. Since the surfactant used in step (i) is not commercially available, it had to be prepared and purified in advance, as discussed in section 5.2. Steps (i)-(iii) are considered in section 5.3, whereas section 5.4 describes step (iv). Chemical probes, ¹H-NMR and dynamic light scattering (DLS) were used to provide a detailed account of the most important aspects of the synthesis. Other standard techniques such as thin layer chromatography (TLC), column chromatography and dialysis were also employed. The chapter ends with a description of the purification and quantification of the amine groups inside the nanocages.

5.2 Synthesis and purification of silicon surfactant

5.2.1 Synthesis of surfactant

The raw material used to prepare the siloxane nanocages was the silicon surfactant 3-(triethoxysilyl) propyl-cetylcarbamate, containing a hydrolysable head and a carbamate group that can be transformed to a primary amine in subsequent steps (see Scheme 5.1). To prepare the surfactant, 42 mmol of 3-aminopropyltriethoxysilane (Aldrich, 99%) were dissolved in 100 mL of ice-cold anhydrous ether (Aldrich, 99.7%), along with 40 mmol of triethylamine (Acros, 99.7%, 0.06% H₂O) dried with molecular sieve 3A. The mixture was allowed to homogenize for 30 min, before 40 mmol of cetylchloroformate (TCI America, 95%) were added in a dropwise manner at 13 mL/h with a syringe pump. Temperature was kept at 0 °C until all the cetylchloroformate was added; after that, it was raised to RT while the reaction mixture was stirred at 400 rpm. Stirring continued for 5 more hours, in order to bring the reaction to completion. Triethylamine (TEA) was used to trap the HCl generated, which could prematurely hydrolyze the surfactant's head group. A description of both reactions is shown in Scheme 5.1.

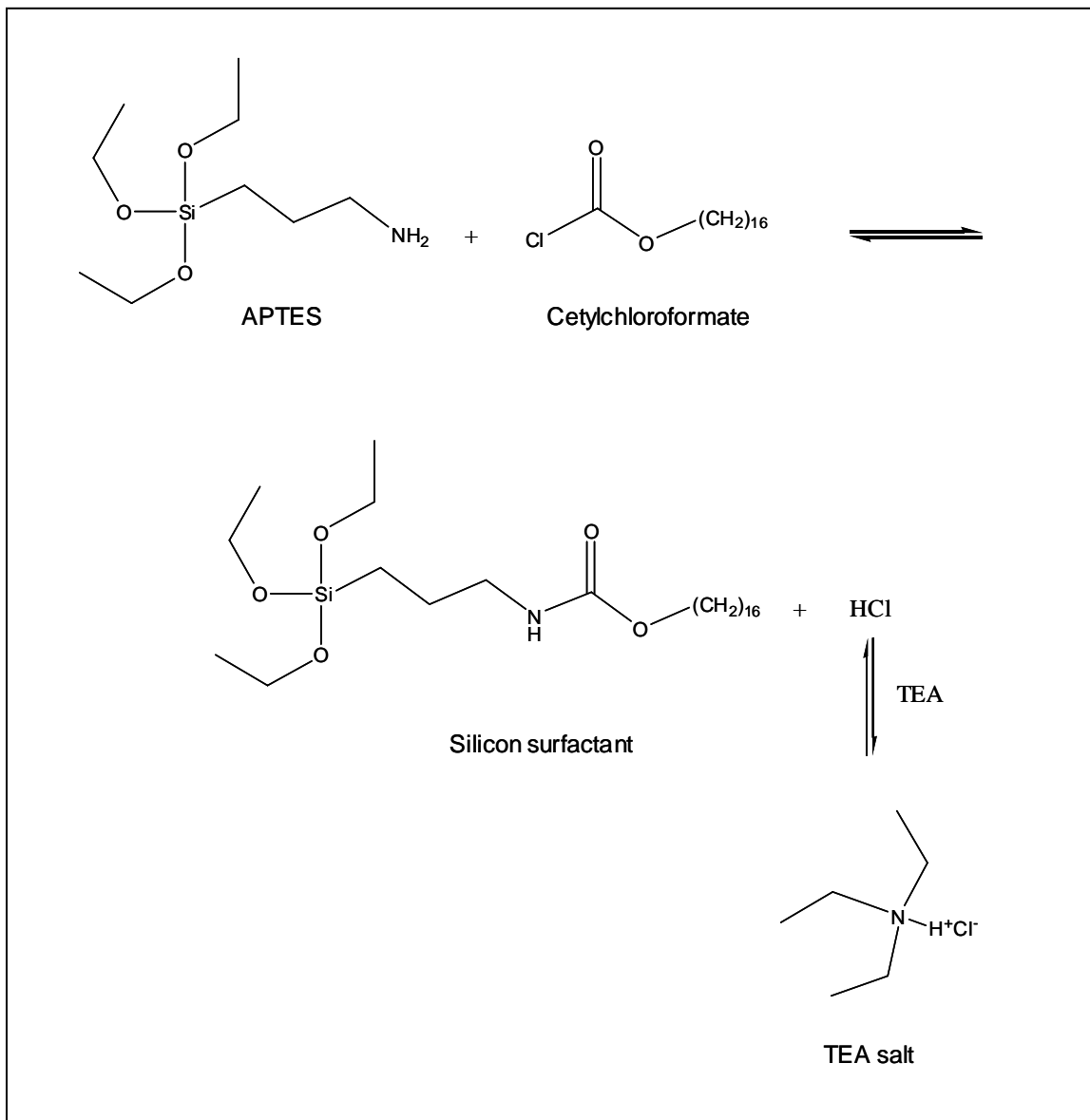
After the reaction finished, the solvent was evaporated under vacuum at RT using a Schlenk line. The solid product containing a mixture of silicon surfactant and the hydrochloric quaternary salt of TEA, was re-suspended in 70 mL of dry hexanes plus 40 mL of dry chloroform; after 30 min of stirring, the solvent was evaporated under vacuum and the dry solid stored under N₂.

5.2.2 Purification of the surfactant

Efforts were made to purify the surfactant by extraction as reported by Suh et al.,¹ performing successive washes with acidic and salty water. According to proton NMR, extraction

Scheme 5.1

Synthesis of the silicon surfactant used to prepare siloxane nanocages. As HCl is generated by the reaction, TEA in solution traps it forming a quaternary salt.

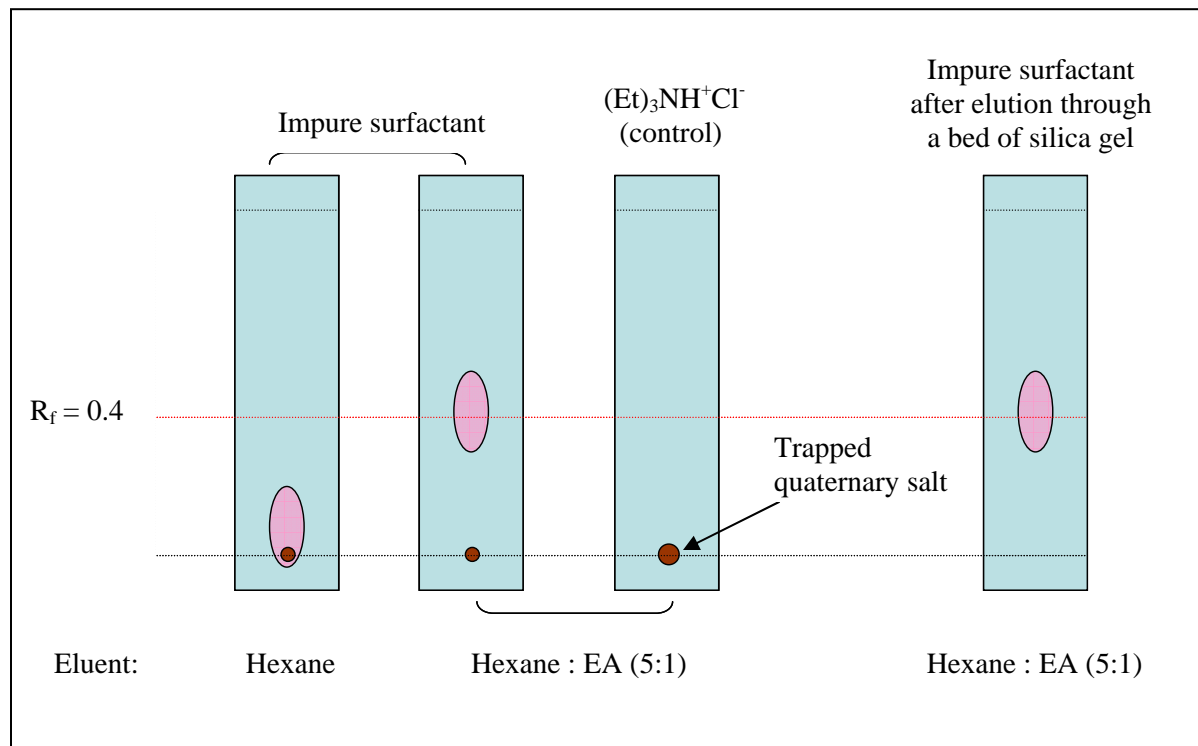


fully removed the quaternary salt, but it also lead to the formation of different hydrolysis sub-product. This resulted in a low quality surfactant, unsuitable for further use. Therefore, in this

work the surfactant was purified in a different way. The impure solid was re-suspended in 150 mL of dry hexanes in order to dissolve only the surfactant. A milky suspension was formed, in which the white quaternary salt $(\text{Et})_3\text{NH}^+\text{Cl}^-$ was insoluble. After stirring for 1.5 h, the suspension was allowed to settle for additional 1.5 h, separating into a white solid and a clear supernatant liquid. The supernatant liquid was transferred to a dry Schlenk flask, using a syringe filter (Anotop, 0.2 μm). Although ^1H -NMR analysis of the material dissolved in the supernatant liquid indicated that it consisted of pure surfactant, thin layer chromatography (TLC) showed that it contained traces of $(\text{Et})_3\text{NH}^+\text{Cl}^-$ (see Scheme 5.2). TLC analysis is highly

Scheme 5.2

Purification of silicon surfactant contaminated with traces of $(\text{Et})_3\text{NH}^+\text{Cl}^-$ by thin layer chromatography. The fourth plate shows that elution of the impure surfactant through a bed of silica gel, completely removes the quaternary salt.



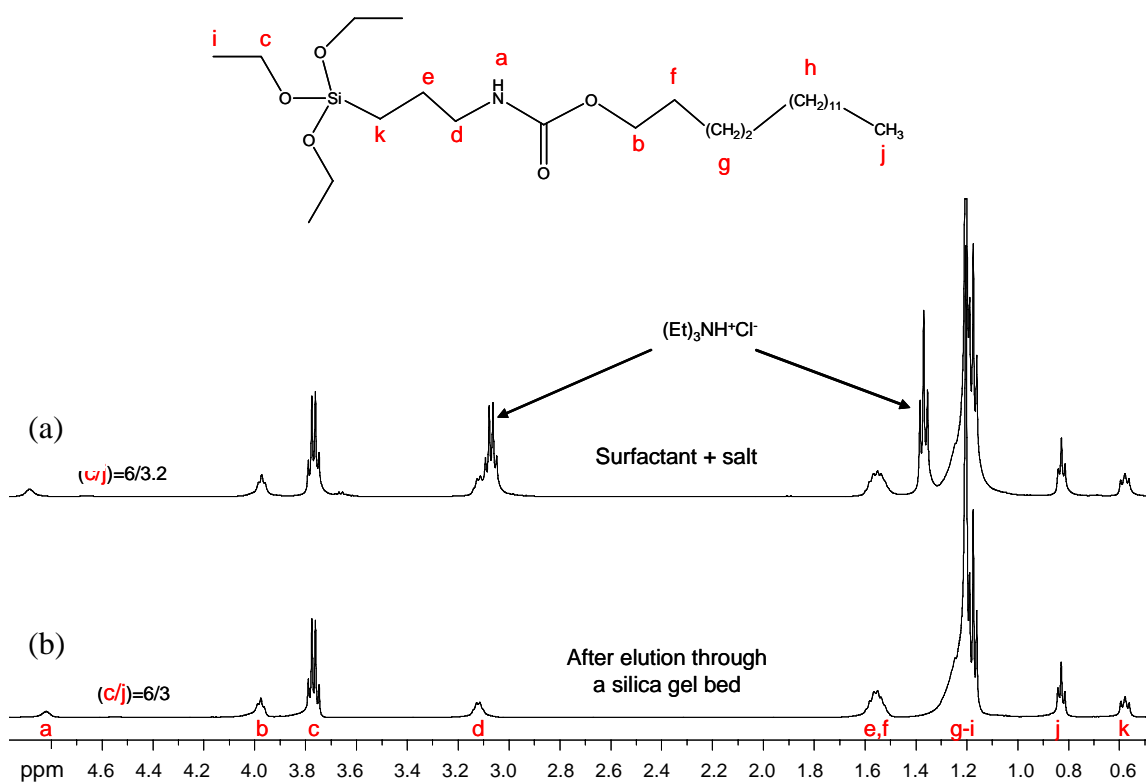


Figure 5.1. Proton NMR of (a) an as-prepared surfactant containing an equivalent amount of (Et)₃NH⁺Cl⁻ and (b) a surfactant purified by elution through a silica gel bed, using a mixture of hexanes/ethyl acetate (5/1). Spectra acquired at RT in CDCl₃ at 499.5 MHz.

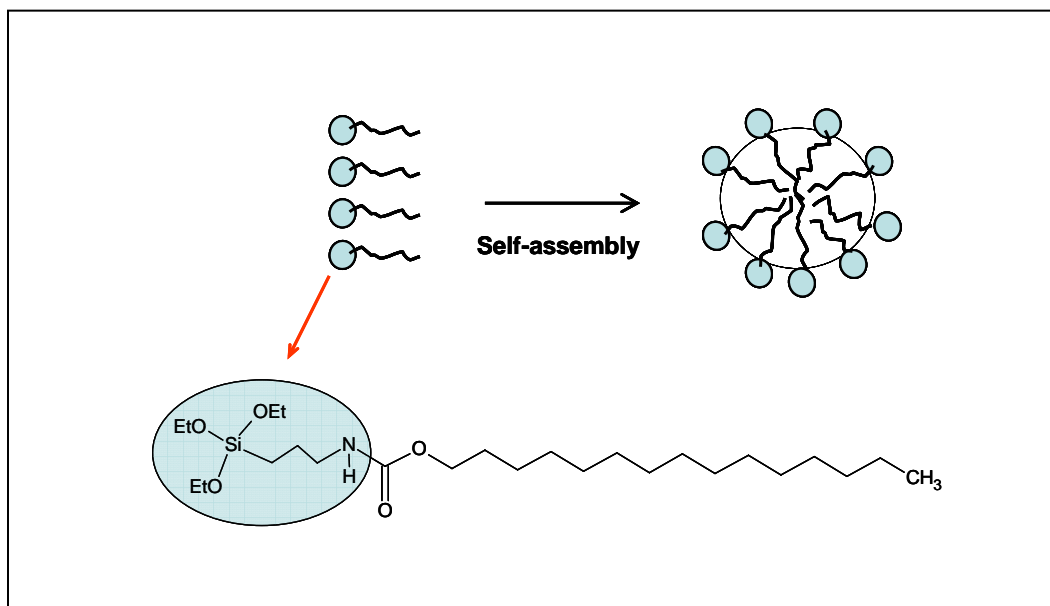
sensitive to amine traces when a ninhydrin/ethanol solution is used to develop the plates; ninhydrin reacts at 200 °C with tertiary amines or their quaternary salts, generating a dark brown product easily detected by eye. Any attempts to prepare the nanocage using the surfactant contaminated traces of salt failed, suggesting that high purity is a necessary condition for successful nanocage synthesis. Exploratory tests using thin layer chromatography (TLC) showed that the surfactant could be completely separated from $(\text{Et})_3\text{NH}^+\text{Cl}^-$ by elution with a mixture of hexanes/ethyl acetate in a 5/1 ratio. Since the surfactant is never in contact with water, there is no formation of hydrolysis sub-products. Scheme 5.2 shows the results obtained in these tests. Implementation of the purification method at a larger scale was carried out using a bed of silica gel (Aldrich, 220-400 mesh, 60 Å) in a filtration funnel. Initially, the silica gel was wetted with the eluent (hexanes/ethyl acetate, 5/1); then the solution containing the impure surfactant was loaded dropwise using a Pasteur pipette. Subsequently, about 20 mL of eluent were carefully added. After that, vacuum was admitted forcing the eluent through the bed, while dragging the pure surfactant from the surface. Then more eluent was added followed by suction to drag the surfactant further towards the bottom. The procedure was repeated until all the surfactant was recovered. As the TLC experiments demonstrate, the elution process removes only the surfactant, leaving the quaternary salt trapped in the silica gel. Since formation of hydrolysis by-products was suppressed, very pure surfactant was easily obtained by this method. Figure 5.1 shows proton NMR spectra of the surfactant before and after purification. The pure surfactant (from now called *silicon surfactant*) was dried under vacuum at RT and stored in nitrogen for further use.

5.3 Preparation of protected nanocages

The synthesis of *protected nanocages* (PN) started with the dissolution of silicon surfactant in 32 mL of ethanol (Aldrich, 200 proof) to form a 5 mM solution. Once in ethanol, the surfactant self-organized into micelles with sizes distributed around 2.3 nm, as indicated by the dynamic light (DLS) results in Figure 5.2(a). Control experiments using colloidal gold with a nominal size of 3.5 nm (Aldrich) as determined by TEM, indicated that the hydrodynamic diameter observed by DLS was about 0.75 the diameter obtained by TEM. Thus, a correction factor of 1/0.75 was applied to the particle size determined by DLS. The micelles formed by the silicon surfactant display two very important features: (i) the hydrolysable head groups are

Scheme 5.3

Silicon surfactant self-assembly in ethanol, into 2 ± 0.3 nm micelles. The carbamate groups at the interior are used to generate primary amine groups in subsequent steps.



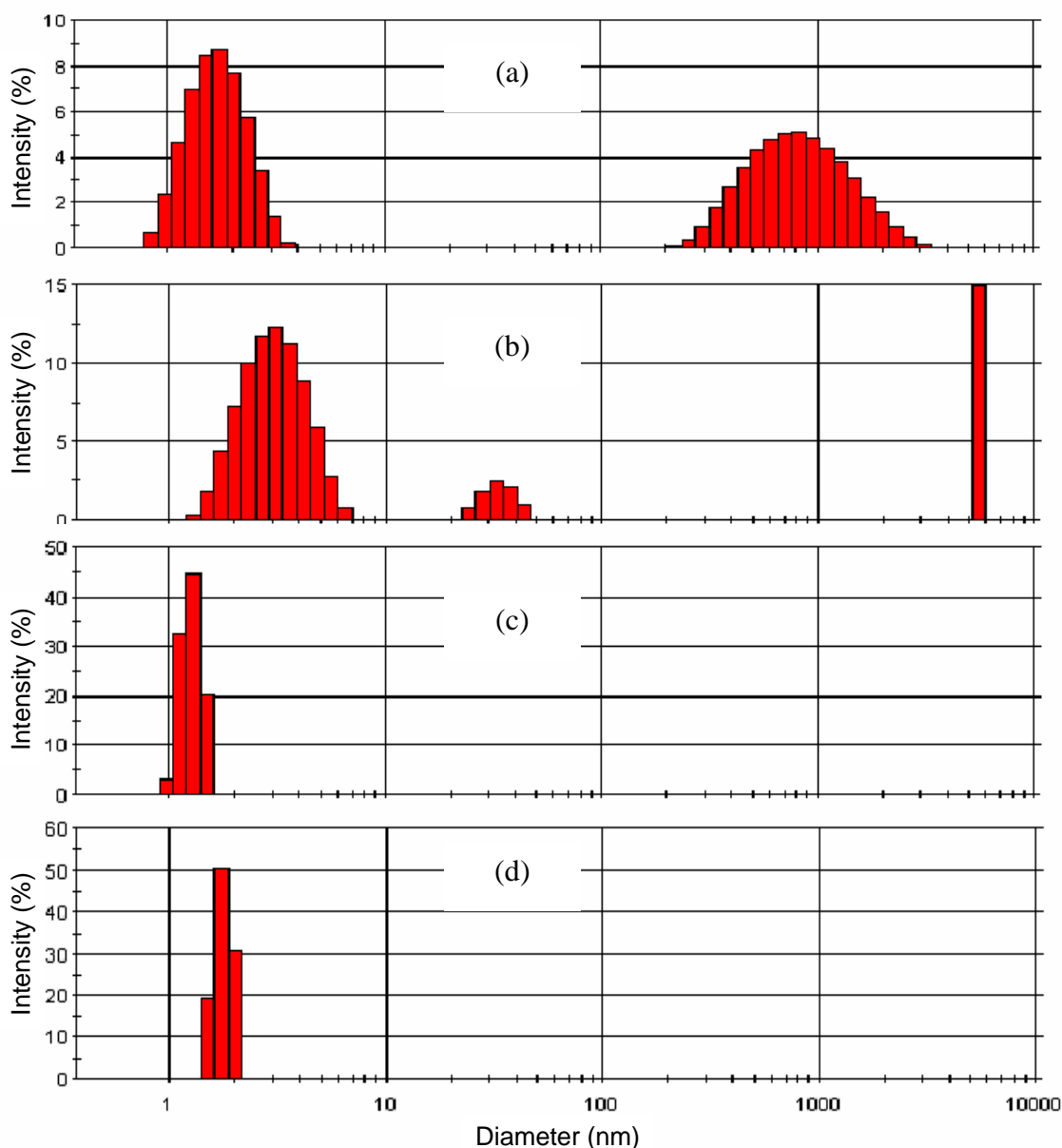


Figure 5.2. DLS data corresponding to various stages during the preparation of siloxane nanocages. (a) micelles generated by dissolution of silicon surfactant in anhydrous ethanol, (b) 12 h after treatment of the micelles with 20% pH=1 solution in ethanol, (c) after dilution with ethanol followed by H₂O/ethanol (80/20) and (d) after cross-linking and capping with (MeO)₂(Me)₂Si and (MeO)(Me)₃Si, respectively. Since the observed scattering intensity is proportional to the sixth power of the diameter, particles bigger than 10 nm represent less than 0.05% of the population in solution.

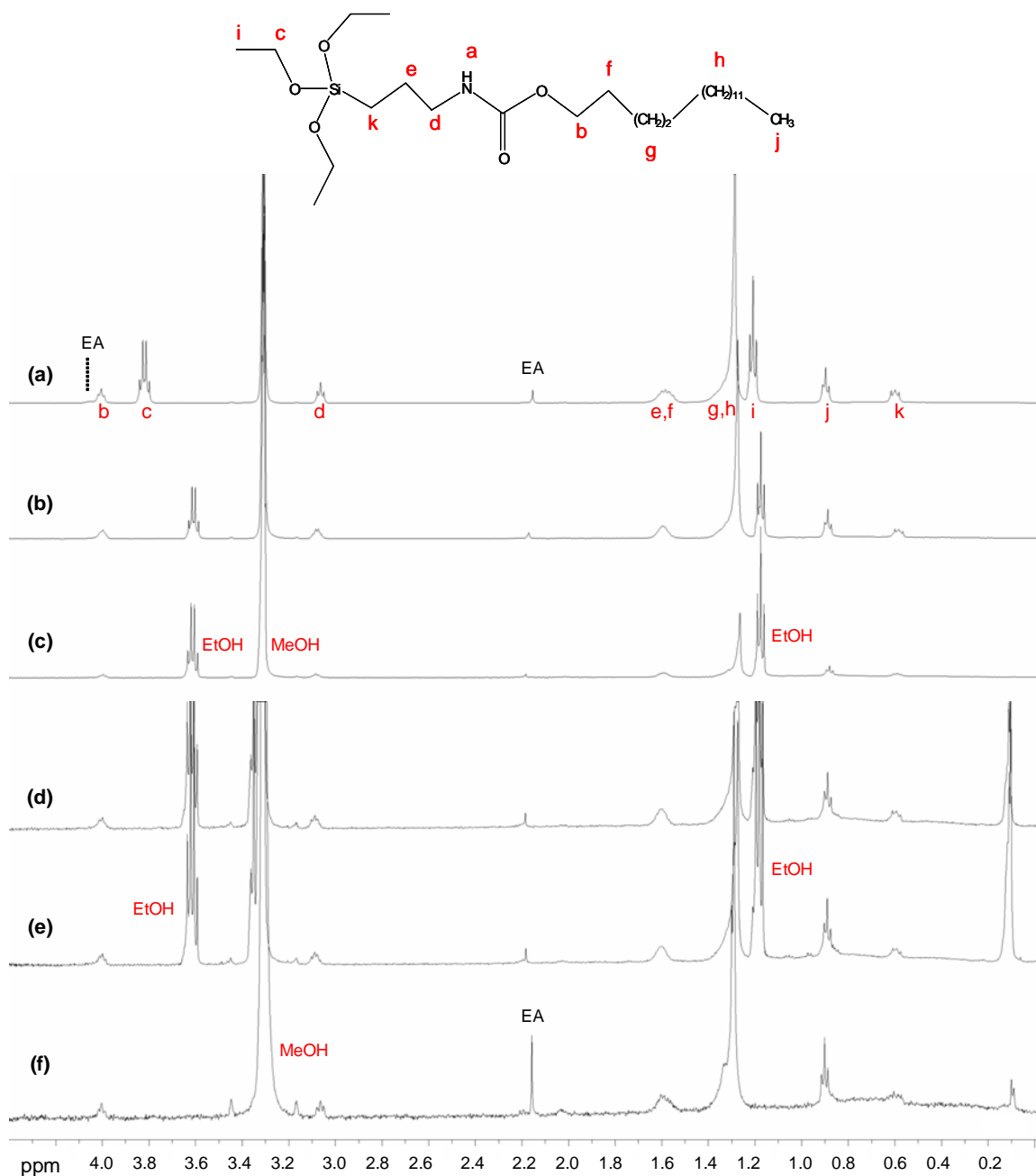


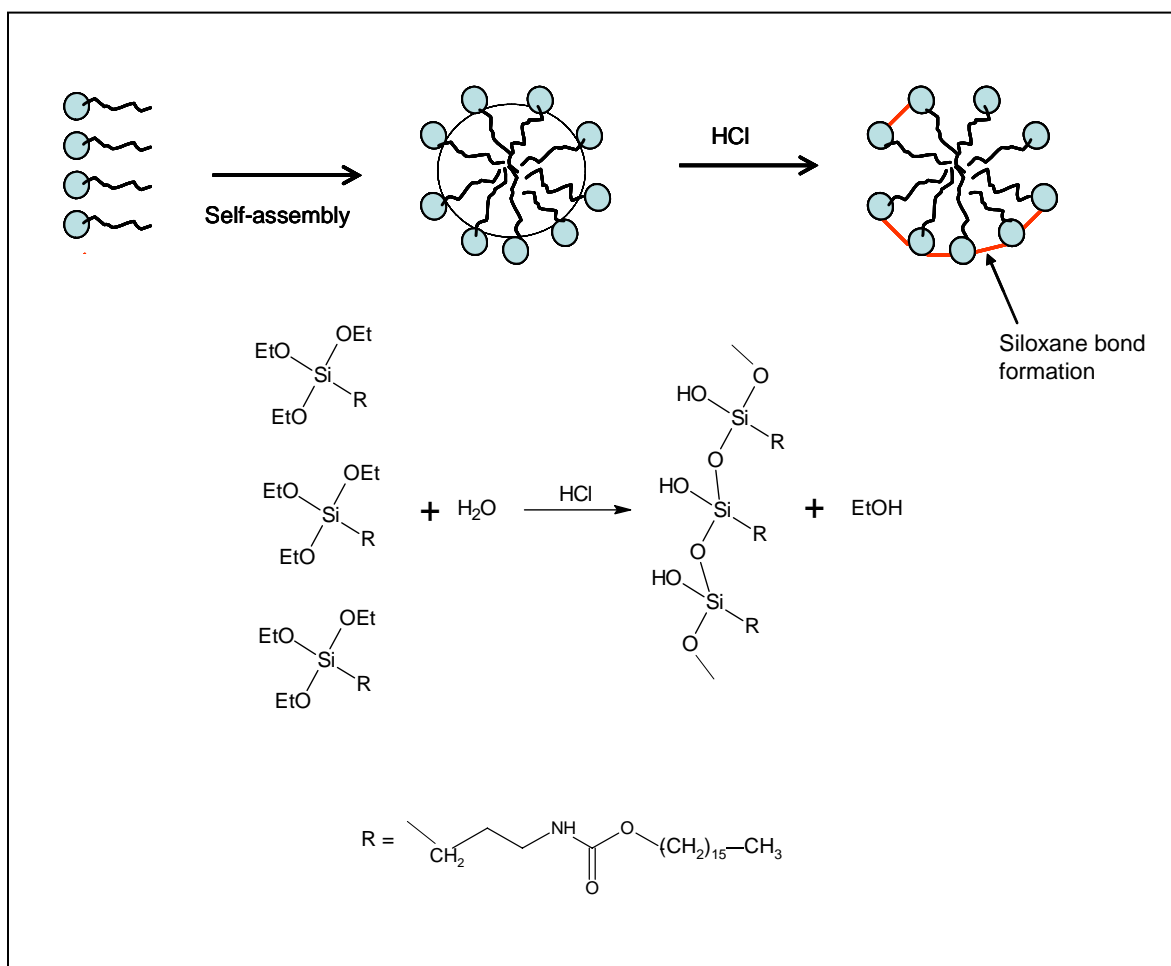
Figure 5.3. ¹H-NMR acquired at different stages during the preparation of protected nanocages in CD₃OD. (a) Micelles generated by dissolution of silicon surfactant in CD₃OD, (b) 1 h after addition of acidic D₂O (pH=1) in CD₃OD (20% D₂O), (c) after dilution with CD₃OD followed by D₂O/CD₃OD (80/20), (d) after cross-linking with (MeO)₂(Me)₂Si, (e) after capping with (MeO)(Me)₃Si and (f) after evaporation at -5 °C to remove excess cross-linking and capping agents. EA is residual ethyl acetate. Spectra acquired at RT at 499.5 MHz.

located at the external surface and (ii) the long hydrophobic tail directs the carbamate group towards the interior (see Scheme 5.3). As it will be discussed later, this carbamate acts as the precursor of amine groups that are located at interior of the nanocage.

Subsequently, the micelles were treated with 32 mL of solution that was 80% ethanol and 20% HCl/H₂O (pH=1), added with a syringe pump at a rate of 10 mL/h. After the addition of the acidic solution ended, the mixture was stirred at 400 rpm for 12 more hours. Addition of the

Scheme 5.4

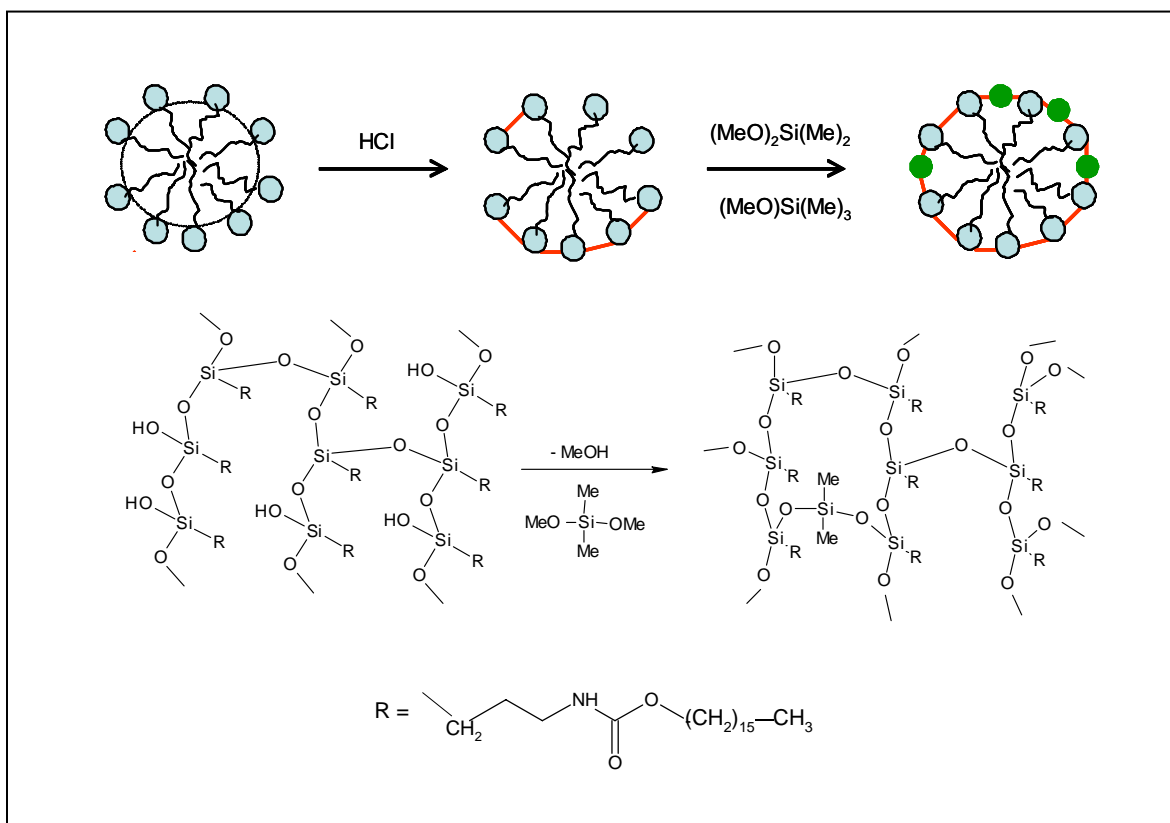
Representation of the hydrolysis and condensation processes occurring by addition of acidic alcohol to a solution of micelles. As observed, only partial condensation of head groups occurs.



acidic alcohol induced hydrolysis of the ethoxy groups at the surfactant's head within one hour, as indicated by the disappearance of the ethoxy peaks and the concomitant formation of ethanol in the $^1\text{H-NMR}$ spectra of the solutions (Figure 5.3 (a) and (b)). During the remaining 11 hours, condensation took place, generating particles with a size distribution centered about 4.1 nm (Figure 5.2(b)). Since condensation generated clusters of a size larger than expected if isolated micelles had condensed ($\sim 2\text{nm}$), based on the size of the surfactant tail, further dilution was carried out in order to break the clusters. This was performed by addition of 32 mL

Scheme 5.5

Cross-linking and condensation occurring after slow addition of $\text{Me}_2\text{Si}(\text{OMe})_2$ and $\text{Me}_3\text{Si}(\text{OMe})$ to a solution micelles with fully hydrolyzed and partially condensed head groups.



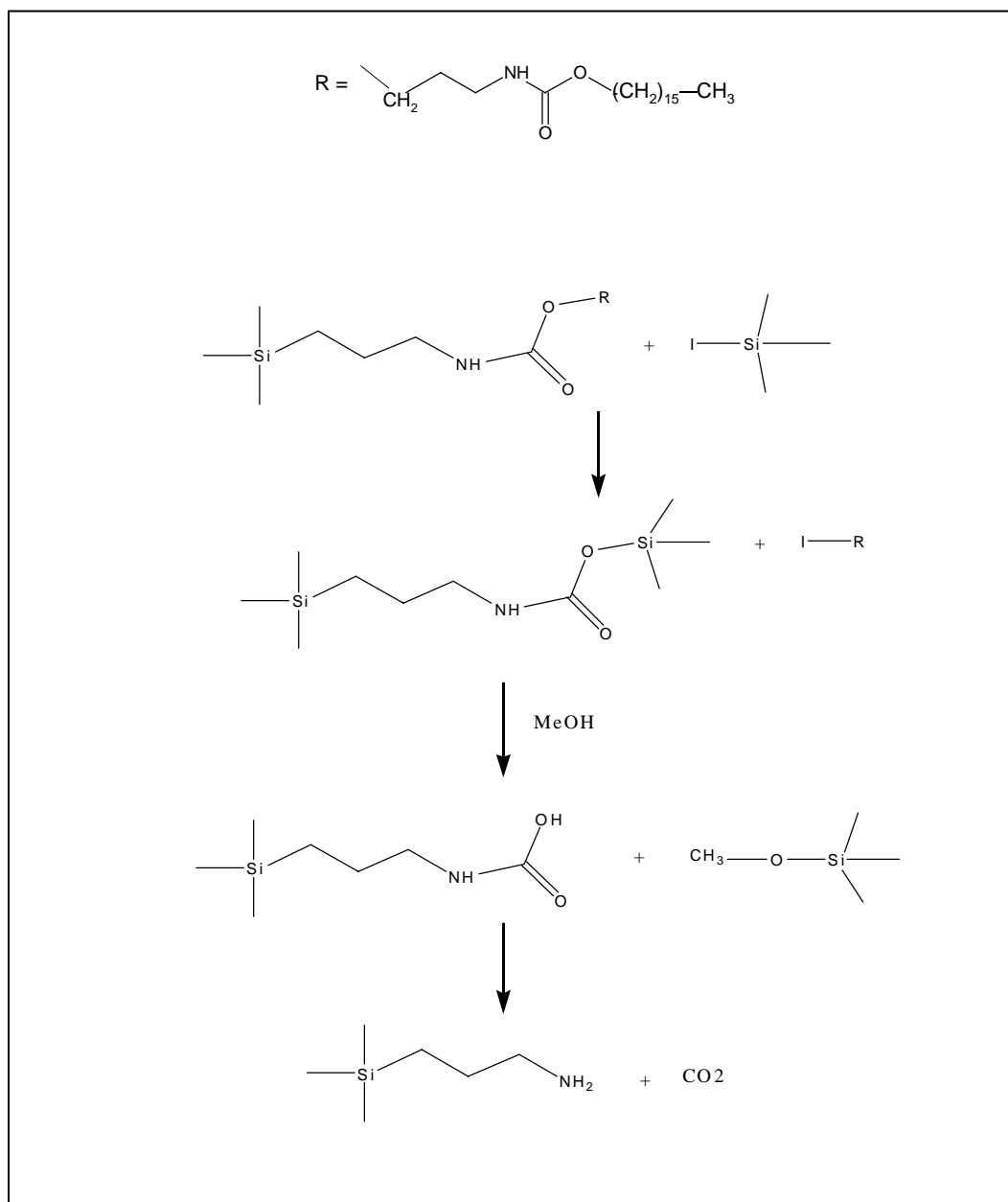
of ethanol with a syringe pump at a rate of 40 mL/h, followed by addition of 32 mL of a solution H₂O/ethanol (80/20) at a rate of 20 mL/h. DLS data collected after dilution, indicated that this treatment effectively broke the bigger clusters, as only particles of about 1.7 ± 0.3 nm were observed (Figures 5.2(c) and 5.3(c)). The fact that the particles are smaller than 2.3 nm, suggest that not all the silanol groups underwent condensation. A representation of the process occurring after the addition of acid, based on the NMR and DLS observations, is shown in Scheme 5.4.

Partial condensation left some silanols unreacted, which were used to fully develop the shell enclosing the hydrophobic tails. This was achieved by addition of 32 mL of a 5mM solution of the cross-linking agent dimethyldimethoxysilane in ethanol, at 2 mL/h, using a syringe pump; slow addition was necessary to keep the reactant highly diluted in order to reduce self condensation. Subsequently, 32 mL of a 5 mM solution of trimethylmethoxysilane in ethanol was added at the same rate (2 mL/h) using a syringe pump, in order to fully cap any possible unreacted silanol remaining. This last step was essential to prevent agglomeration during water removal, prior to carbamate deprotection (see below). Figures 5.2(d) and 5.3(d-e) illustrate the DLS and proton NMR of the material after cross-linking and capping, while Scheme 5.5 illustrates the reactions taking place.

NMR and DLS characterization of the cross-linked and capped material, here referred to as protected nanocage, indicated that it was stable for 6 months, tolerating multiple evaporations and re-suspension in several solvents without agglomeration or disintegration. A typical proton NMR spectrum of the protected nanocage is shown in Figure 5.3(f). The peak at ~ 0.1 ppm represents the methyl groups incorporated by reaction with the cross-linking and capping agents. Its small relative value, suggests that most of the surface silanol groups reacted during

Scheme 5.6

Reaction of protected nanocage with TMSI generates propylamine functionalities at the interior of the nanocage.^{1,2}



condensation. As shown in Fig 5.2(d), the protected nanocage also had a very uniform size of 2.3 ± 0.3 nm. This material constituted the precursor from which the siloxane (hollow) nanocages were generated by chemical breaking of the internal carbamate groups with TMSI.

5.4 Generation of nanocage with internal amine groups by carbamate deprotection

The protected nanocage was treated with trimethylsilyl-iodide (TMSI) to regenerate the propylamine groups converted to carbamate during the synthesis of the surfactant (Scheme 5.6).^{1,2} 20 mL of protected nanocage solution was transferred with a syringe filter (Anotop, 0.2 μ m) to a Schlenk flask and dried under vacuum at -10 °C. Once dry, traces of water were removed by evaporation at 0 °C and then at RT. Water removal is crucial as it reacts with the TMSI required for deprotection. The dry protected nanocage was loaded into a glove box where it was redissolved in 120 mL of anhydrous toluene. To this solution, 22 μ L of trimethylsilyl-chloride were added in order to eliminate traces of water. An addition of 22 μ L of trimethylsilyl-iodide followed, which was done under complete absence of light. The sealed flask was taken out of the glove box and allowed to react for 40 h at 40 °C under darkness. The post-reaction treatment included evaporation of 90% of the solvent under vacuum at RT, followed by addition of 110 mL of dry toluene. This procedure was repeated three more times. Subsequently, the solvent was completely evaporated at 0 °C. Decomposition of the silylcarbamate (Scheme 5.6) was accomplished by addition of 80 mL of dry methanol to the solid left after evaporation. After deprotection, the nanocage was completely soluble in methanol, ethanol or toluene. DLS acquired in methanol indicated that the deprotected nanocage had a hydrodynamic diameter of 2.3 nm (Figure 5.4). The nanocage was partially characterized and purified as described below.

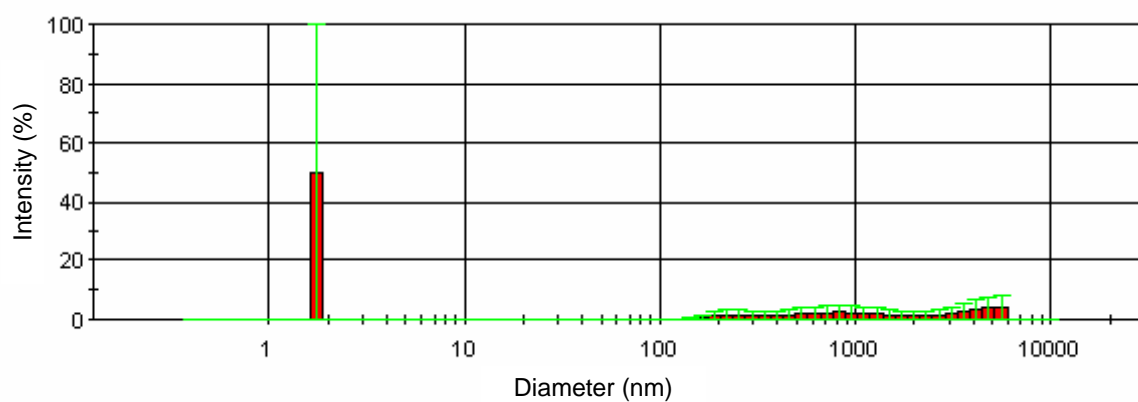


Figure 5.4. DLS of nanocage after deprotection with TMSI. Data acquired in methanol at RT. Since the observed scattering intensity is proportional to the sixth power of the diameter, particles bigger than 10 nm correspond to less than 0.05% of the population in solution.

5.5 Characterization and purification of siloxane nanocages

5.5.1 Quantification of internal amine functionalities

The extent of carbamate deprotection achieved by treatment with TMSI was determined using the ninhydrin reaction, as described in Chapter 2, section 2.3.3. A calibration curve was first developed using the model compound 3-aminopropylmethylbis(trimethyl-siloxy)silane (APMBTSS), due to its similarity to the amine groups inside the nanocage. Then the deprotected nanocage was tested and the concentration of the chromophore generated compared with the calibration curve. Since there was a 1:1 correlation between the concentrations of primary amine and the chromophore generated, quantification was straight forward. It was found that in all cases, the level of deprotection achieved was superior to 95%. For control purposes, a protected nanocage which was not treated with TMSI was also reacted with ninhydrin; in this case, the test gave negative results, as expected for a material containing carbamate groups instead of primary amine. Only the protected nanocage that was exposed to TMSI under the conditions described above contained primary amine groups at its interior.

The deprotection of the internal carbamate groups generated hexadecyliodide chains that were trapped at the nanocages's interior (Scheme 5.6). These residual chains had to be removed before the nanocage could be used.

5.5.2 Dialysis

Purification of the deprotected nanocage by dialysis in methanol very effectively removed the alkyl iodide fragments at its interior, while allowing recovery of more than 50 % of the original nanocage. Other purification techniques were attempted, including sedimentation and centrifugation in chloroform; however, in both cases the recovery was very poor. As

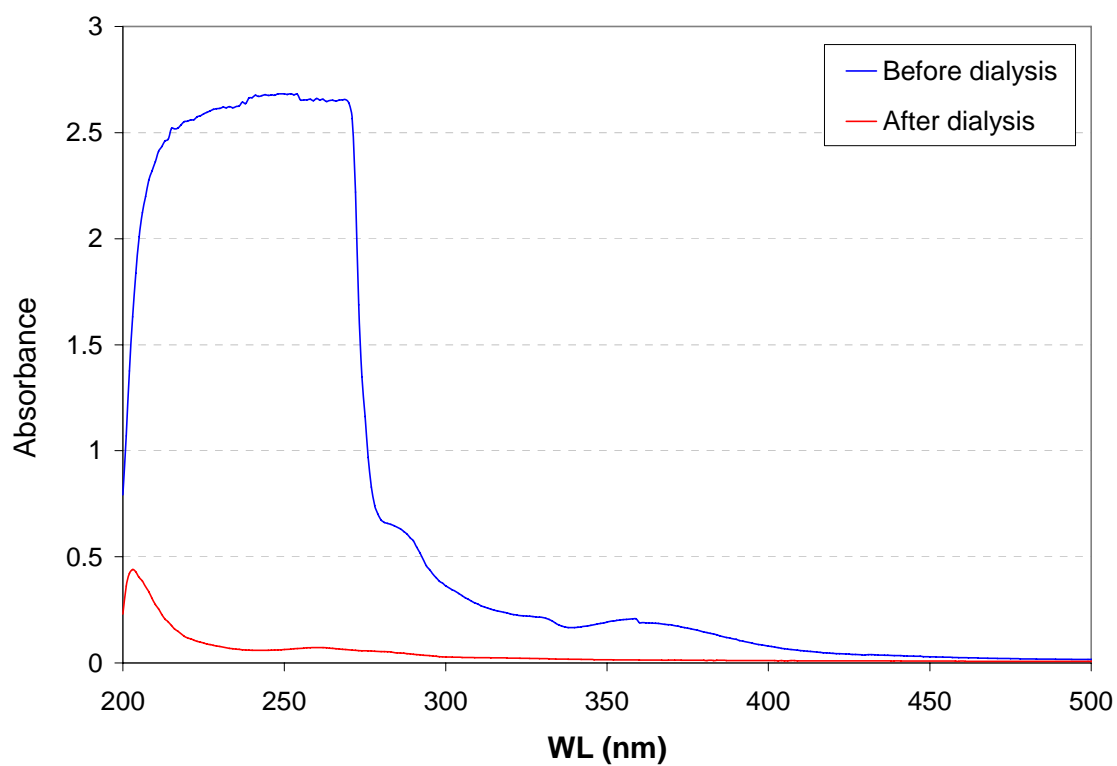


Figure 5.5. Comparison of the UV-VIS spectra for the deprotected nanocage before and after dialysis. Both samples contain equivalent amounts of nanocage, as established by the ninhydrin test.

illustrated by Figure 5.5, a just deprotected nanocage absorbs very strongly in a wide range of the UV-VIS spectrum, consequence the impurities at its interior. These impurities are removed after 4 days of dialysis using a regenerated cellulose membrane (500 Da). For a dialyzed deprotected nanocage, only the absorption due to primary amine is seen in the UV-VIS (Figure 5.5). The ninhydrin reaction was also used to determine the degree of recovery of the deprotected nanocage after dialysis. The results indicated that recovery using a new dialysis membrane was about 50%, but a membrane used twice allowed around 70% recovery.

5.6 Summary

Siloxane nanocages have been synthesized, using a modification of the protocol reported by Suh et al.¹ Initially a silicon surfactant was prepared and purified by elution through silica gel. Then the nanocages were prepared in four steps: (i) self-assembly of silicon surfactant into 2nm micelles, (ii) hydrolysis and condensation of the surfactant's head groups, (iii) cross-linking of unreacted groups at the micelles' surface generating a porous network with spherical symmetry and (iv) deprotection of internal carbamate groups forming primary amine groups at the nanocage's interior. The deprotected nanocages had a hydrodynamic diameter of 2.3 nm; usually more than 95% of the carbamate groups at the nanocages' interior were transformed into primary amine groups by treatment with TMSI.

CHAPTER 6

NANOCONFINEMENT EFFECT ON THE BINDING OF GOLD BY PRIMARY AMINE INSIDE SILOXANE NANOCAGES

6.1 Synopsis

Some key properties of the novel siloxane nanocage described in the previous Chapter, including its protonation response to variations in the external pH, were investigated using Au^{3+} in methanol as a probe. Characterization was carried out following the binding of the gold cation to the amine groups inside the nanocage, by a combination of XANES, EXAFS, UV-VIS and cyclic voltammetry. UV-VIS quantification was performed using the LMCT band at 227 nm characteristic of $\text{Au}(\text{OH})_x\text{Cl}_{4-x}$ species in methanol and water, whose intensity was correlated with the overall Au-Cl coordination number. A remarkable reduction of the Brønsted basicity of propylamine groups within the nanocage, consequence of their nano-confinement, was observed (the protonation constant dropped five orders of magnitude). As a result, the nanocage formed complexes with Au^{3+} at a pH five units lower than an equivalent isolated amine in solution. The stoichiometry of the complex generated was determined by the total amine/gold ratio in solution. When $\text{amine/gold} \leq 1$, only 1:1 complexes formed. For higher ratios, the nanocage acted as a chelating ligand forming multiple Au-N bonds per gold. These observations suggest that propylamine groups tethered to the internal surface of the nanocage possess high flexibility, easily adjusting to the spatial constraints imposed by gold upon multiple binding. Adsorption of Au^{3+} inside the nanocage also occurred under excess chloride (2600-fold with respect to Au^{3+}). It was determined that all the Au^{3+} inside the nanocage was chemically bound the amine groups; therefore, the maximum gold load inside the nanocage corresponds to complete formation of a 1:1 complex.

6.2 Introduction

Designing highly selective and active materials remains one of the main goals of catalytic technology. Engineering such catalysts requires atomic-length-scale control of the composition, structure and location of active sites. It would be desirable to locate those sites at well known positions inside a cavity able to change its configuration to facilitate the access of specific reactants to the active sites and the discharge of the products, as done by enzymes.¹⁻⁴ If in addition, the active sites are highly packed as to permit only certain favorable configurations, then additional advantages in terms of stereoselectivity could be obtained.⁵⁻⁸ Cages exhibiting size/shape selectivity, with immobilized metal cations or metallic nanoparticles as active centers, have been amply used in heterogeneous catalysis.⁹⁻¹⁴ Examples exist of zeolites that have been modified with sulfoxides or metal cations, enabling them to perform asymmetric catalysis.¹⁵ Other materials containing cavities have been developed and used as nanoreactors to synthesize catalytic nanoparticles,¹⁶⁻²⁰ semiconductors²¹⁻²³ and for controlled drug release.²⁴ Similarly, our group has reported the synthesis of 2nm cages, possessing an atom-thick, porous and covalently cross-linked shell.²⁵ These nanocages contain propylamine functional groups affixed to the interior shell surface, which have been shown to have catalytic activity.²⁵ It is our interest to continue exploring the properties of these cages as catalysts, binding centers for metal ions and nanoreactors for the synthesis of metallic and metal oxide clusters. Here we investigate the chemical properties of the internal amines using their complexation with Au^{3+} as a handle. In particular, we report on the effect of confinement at the nanoscale on the Brønsted basicity of the amine groups and the advantages this confers to the nanocage as a ligand. The results complement other properties already reported for the nanocage²⁵ and serve as the starting point for the investigation of its properties as a nanoreactor and catalyst.

6.3 Experimental

6.3.1 Synthesis of amine-functionalized nanocages

Shell cross-linked siloxane nanocages internally functionalized with propylamine groups, were synthesized as described in Chapter 5.²⁵ Initially, (triethoxysilyl)propylcetylcarbamate was dissolved in ethanol (5mM) forming micelles of $\sim 2\text{nm}$. Then, the siloxy headgroups were acid-hydrolyzed and cross-linked in several steps using dimethyl-dimethoxy silane. Unreacted silanols were subsequently capped with trimethyl-methoxy silane. The resulting 2nm globular structures consisted of a cross-linked siloxane shell wrapping propyl-cetylcarbamate tails fixed to the shell wall; this material will be referred to as “*protected nanocage*” (PN). Treatment of PN with iodotrimethylsilane at 40 °C, followed by reaction with methanol at RT promoted the cleavage of 95-100% of internal carbamate groups (see Chapter 5); purification by dialysis in methanol to remove the fragments resulting from carbamate breaking, yielded a cage-like material of $\sim 2\text{nm}$ with propylamine functionalities tethered to the interior walls. This material will be referred to as “*Deprotected nanocage*” (DN) or simply “*nanocage*”. The nanocage is stable in different solvents and exhibits size selectivity allowing only molecules smaller than $\sim 5\text{\AA}$ to diffuse inside.²⁵ Quantification of primary amine functionalities inside the nanocage was performed by the Ninhydrin reaction (Chapter 2).^{25,26}

6.3.2 Cyclic Voltammetry

Data were collected with a CHI 900 Electrochemical Scanning Microscope (CH Instruments Inc.) in a one-compartment cell using a glassy carbon working electrode (diameter=3mm), a platinum wire counter electrode and a Ag/AgCl reference electrode. Before carrying out a measurement, N₂ was flowed through the solution for 10 minutes at a rate of 2

mL/min using a stainless steel needle. NaCl or NaClO₄ (Aldrich, $\geq 98.0\%$) at a concentration of 0.1 M were used as supporting electrolytes in methanol/water (4.4% H₂O) and methanol (0.1% H₂O) solutions, respectively. The working electrode was scanned at 0.1V/s. Additional details on the experimental set-up are provided in Chapter 2.

6.3.3 XANES and EXAFS data acquisition and analysis

X-ray absorption Spectroscopy (XAS) experiments were carried out at the bending magnet Beamline 5-BMD of the Dupont-Northwestern-Dow Collaborative Access Team (DND-CAT) at the Advanced Photon Source at Argonne National laboratory. The Si(111) monochromator was detuned by 30% at the Au L_{III} edge (11919 eV) to minimize harmonics. The spectra were collected in the fluorescence mode, from solutions contained in polyethylene cylindrical cells (diameter=1 cm, volume=1 cm³) sealed with Parafilm M (Alcan, Inc.). The cell's flat surfaces were oriented at 45° with respect to the detector. All XAS data were collected at room temperature, 60-90 min after sample preparation. Each measurement typically took 30-45 min depending on the type of scan. Phase shifts, backscattering amplitudes, and XANES references were obtained experimentally from reference compounds: AuCl₃ (Aldrich, 99.99+%) for Au(III)-Cl, Au(OH)₃ (Aldrich) for Au(III)-O, Pt(NH₃)₄(NO₃)₂ (Aldrich, 99.995%) for Au(III)-N and Au foil for Au⁰ and Au-Au. Both the XANES and EXAFS data were analyzed by standard procedures using the WINXAS97 software.²⁷ Linear combinations of experimental standards were used to fit the XANES portion of normalized spectra. The EXAFS coordination parameters were obtained by a least squares fit in the *r*-space of the isolated nearest neighbor *k*²-weighted Fourier transform. The data were also fit with both *k*¹- and *k*³-weightings in the *r*-space, as well as *k*²-weighting in the *k*-space, with similar results.

6.3.4 Solvolysis of HAuCl_4

X-ray absorption spectroscopy and UV-VIS were used to study the solvolysis of AuCl_4^- species in water and methanol. UV-VIS absorption spectra were recorded on a Spectronic Genesys 2 spectrometer. The optical path length was 1.0 or 0.1 cm and deionized water or methanol was used as reference. UV-VIS data were collected for: (i) twenty samples of 72 μM HAuCl_4 (Aldrich, 99.9% $\text{HAuCl}_4 \cdot 3\text{H}_2\text{O}$) in water in the 2.8-11.6 pH range; (ii) four samples of 426 μM HAuCl_4 in water in the 2.8-11.6 pH range; (iii) four samples of 72 μM HAuCl_4 in methanol/water (3.7% H_2O) in the 3.5-7.6 pH range; (iv) four samples of 72 μM HAuCl_4 in anhydrous methanol (Aldrich, $\text{H}_2\text{O} < 0.002\%$) in the 3.5-7.6 pH range; (v) three samples of 430 μM HAuCl_4 in anhydrous methanol in the 3.5-7.6 pH range. For the set of samples (i-iii), NaCl was added so that the $\text{Cl}^-/\text{Au}^{3+}$ ratio was 1070. For samples (iv-v) the same $\text{Cl}^-/\text{Au}^{3+}$ ratio was achieved by addition of LiCl (Aldrich, anhydrous 99.998%). pH was adjusted using $\text{NaOH}/\text{H}_2\text{O}$ or $\text{NaOH}/\text{methanol}$ solutions; in the later case, NaOH was dried for 1 hour under vacuum at RT prior to preparation of the solution. The reported pH for solutions in methanol corresponds to the measured pH of an equivalent solution in water. pH was determined with an Oakton pHTestr 10 meter regularly calibrated using buffers of pH=4.0, 7.0 and 10. Blank solutions (without gold) of the same pH and Cl^- content as those in (i-v) were prepared and their spectra used to correct for free chloride absorption at low wavelengths.

XAS data were recorded for six samples of 430 μM HAuCl_4 in anhydrous methanol in the 2.9-7.6 pH range, at $\text{Cl}^-/\text{Au}^{3+}=1070$ (by addition of LiCl). Stock solutions of HAuCl_4 , LiCl and NaOH (dried under vacuum) in anhydrous methanol were prepared in a nitrogen atmosphere and stored in a drierite-containing desiccator. HAuCl_4 stock solutions were stored in darkened containers.

6.3.5 Reactions of Au^{3+} and the nanocage at various pH

Typically, a concentrated solution of HAuCl_4 was added to a nanocage/methanol mixture, so that the final ratio $\text{R-NH}_2/\text{Au}^{3+}$ was 1.1. The pH of the solutions was adjusted by addition of HCl /methanol (33.0 mM) or NaOH /methanol (14.0 mM). Reactions were carried out in the absence of light, under stirring at 400-500 rpm.

Reaction of 42 μM HAuCl_4 and the nanocage was investigated by cyclic voltammetry at $\text{pH}=4.6$, 7.1 and 7.4. During the experiment, the current generated by reduction of $\text{Au}(\text{OH})_{4-x}\text{Cl}_x^-$ species in solution was recorded with time. As control, a nanocage-free solution of gold (42 μM $\text{Au}(\text{OH})_{4-x}\text{Cl}_x^-$) and a mixture Au^{3+}/PN equivalent to $\text{Au}^{3+}/\text{nanocage}$, were analyzed at $\text{pH}=7.4$.

UV-VIS spectroscopy was used to follow the reaction of 72 μM HAuCl_4 and DN with time at different pH in the range 3.5-7.6. For comparison, the experiments were repeated replacing DN by 3-aminopropylmethylbis(trimethyl-siloxy)silane (APMBTSS), which provided a less restricted environment for gold binding (Scheme 6.1). In this case, the pH range was extended to 9.8. Control experiments were conducted to measure the progress of AuCl_4^- solvolysis in the absence of DN and APMBTSS.

X-ray absorption spectroscopy was used to study the reaction of 430 μM HAuCl_4 and DN in anhydrous methanol, at $\text{pH}=3.5$ -5.4. Experiments using APMBTSS were also carried out at $\text{pH}=4.7$ -10.9. Data was acquired in the presence ($\text{Cl}^-/\text{Au}^{3+}=1070$) and absence ($\text{Cl}^-/\text{Au}^{3+}=4$) of excess chloride.

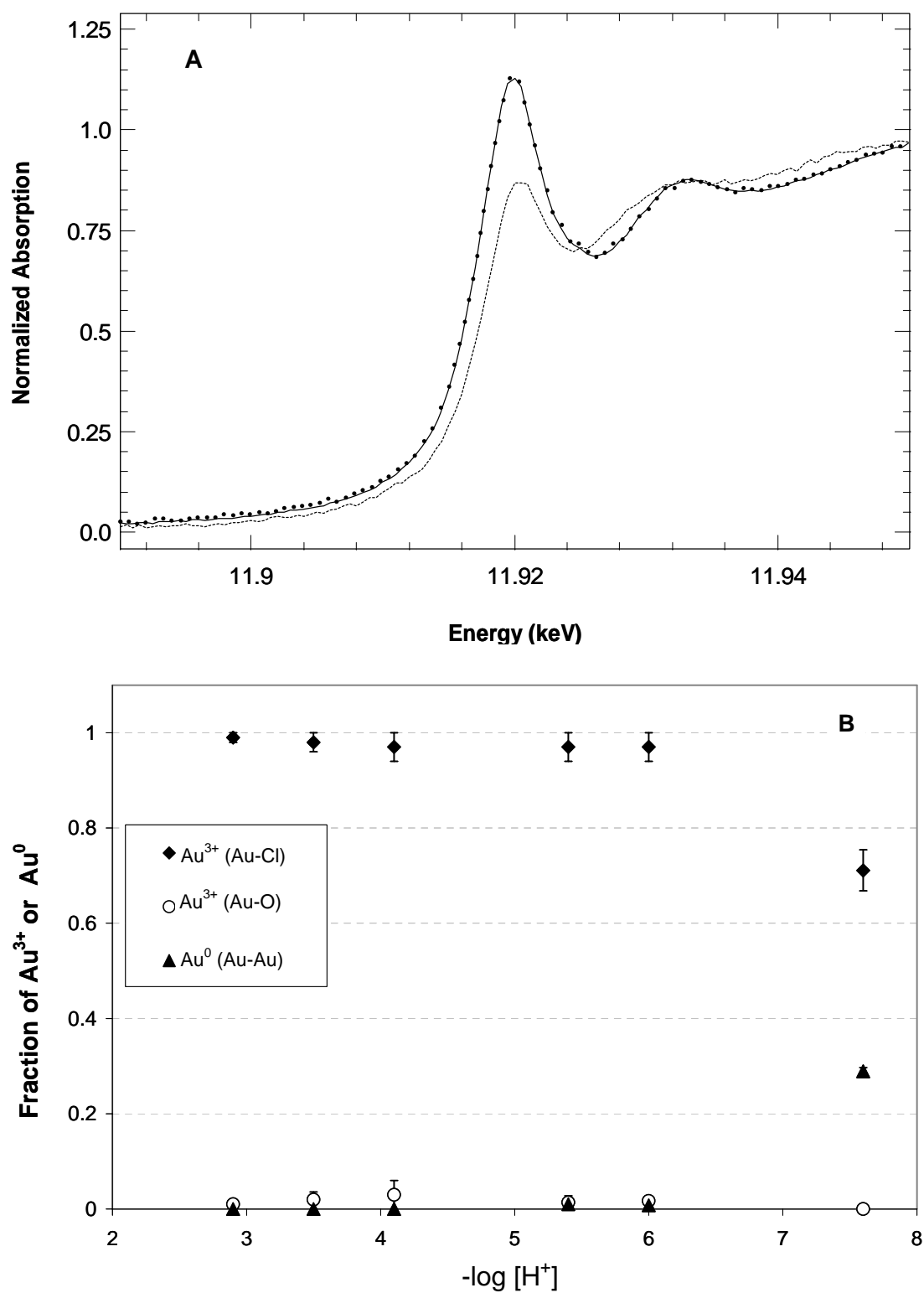


Figure 6.1. (A) Au XANES for AuCl_4^- in anhydrous methanol at (—) pH=2.9, (···) pH=6.0 and (---) pH=7.6. (B) Corresponding distribution of gold into different species in solution. $[\text{Au}^{3+}] = 430 \mu\text{M}$, $\text{Cl}^-/\text{Au}^{3+} = 1070$.

6.3.6 DN titration by Au^{3+}

Ten independent solutions of DN (containing a total of 42 μM of primary amine) and variable amounts of HAuCl_4 were analyzed, covering the range $\text{Au}^{3+}/\text{R-NH}_2=0.0\text{-}1.9$. Cyclic voltammograms were acquired after 90 min of reaction under darkness at 500 rpm and $\text{pH}=7.4$. The supporting electrolyte and solvent were 0.1 M NaCl and methanol/water (4.4% H_2O) respectively.

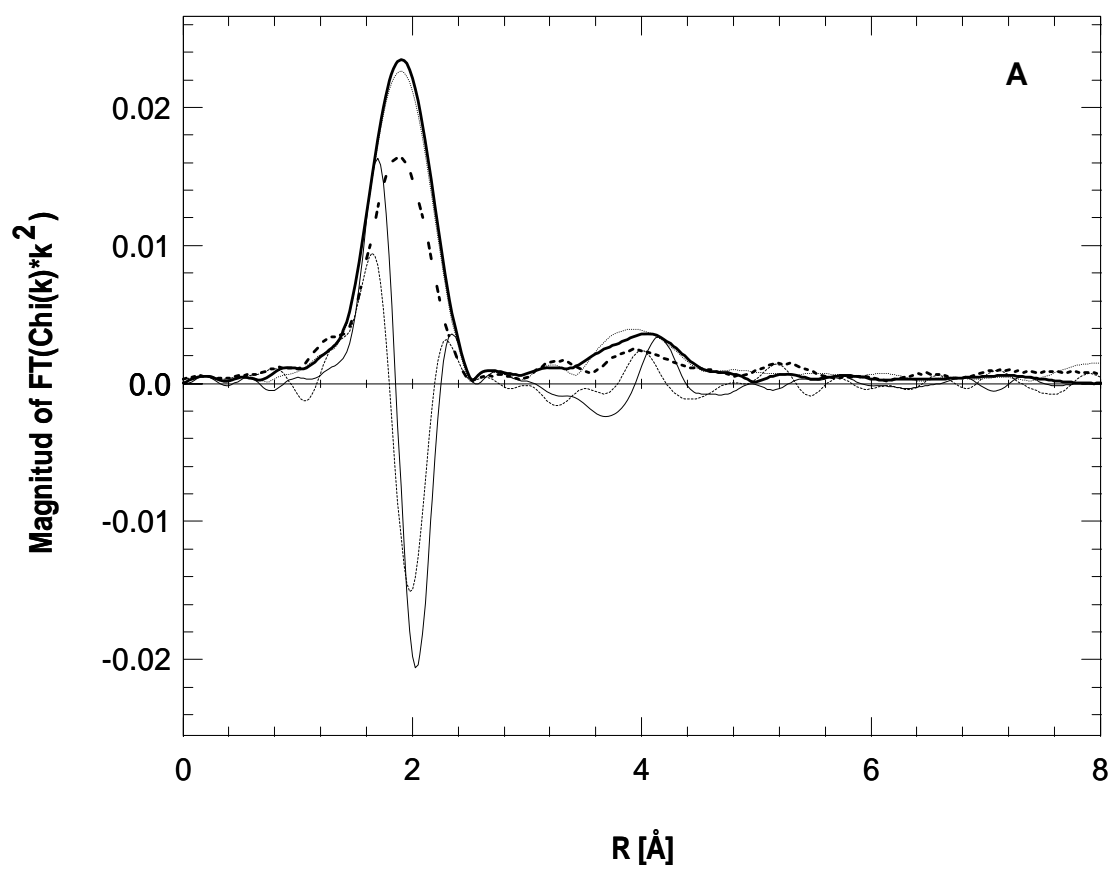
6.3.7 Reaction of Au^{3+} and DN at various $\text{R-NH}_2/\text{Au}$ ratios

Seven solutions of 72 μM HAuCl_4 and variable amounts of DN in methanol spanning the range $(\text{R-NH}_2)/\text{Au}^{3+}=0.0\text{-}4.0$, were studied by UV-VIS spectroscopy, 6 and 90 min after mixing. Reaction took place under darkness at 400 rpm, 25 $^\circ\text{C}$ and $\text{pH}=4.9$. Solutions containing 430 μM HAuCl_4 and variable amounts of DN ($\text{R-NH}_2/\text{Au}^{3+}=2.1$ and 4.3) were characterized by EXAFS at $\text{pH}=4.0\text{-}4.2$. Samples of 430 μM HAuCl_4 and APMBTSS ($\text{R-NH}_2/\text{Au}^{3+}=0.0\text{-}4.1$) were also analyzed. Additionally, a mixture of 430 μM HAuCl_4 and APMBTSS ($\text{R-NH}_2/\text{Au}^{3+}=104$, $\text{Cl}^-/\text{Au}^{3+}=1070$) was also studied.

6.4 Results

6.4.1 Solvolysis of HAuCl_4

$\text{HAuCl}_4 \cdot 3\text{H}_2\text{O}$ was dissolved in anhydrous methanol ($\text{H}_2\text{O} < 0.002\%$) in order to study the solvolysis of the complex at increasing pH (no water added). Figure 6.1A illustrates the XANES spectra of three selected solutions 90 min after pH adjustment. As observed, there was no major difference between the traces at pH 2.9 and 6.0, but a significant reduction in the



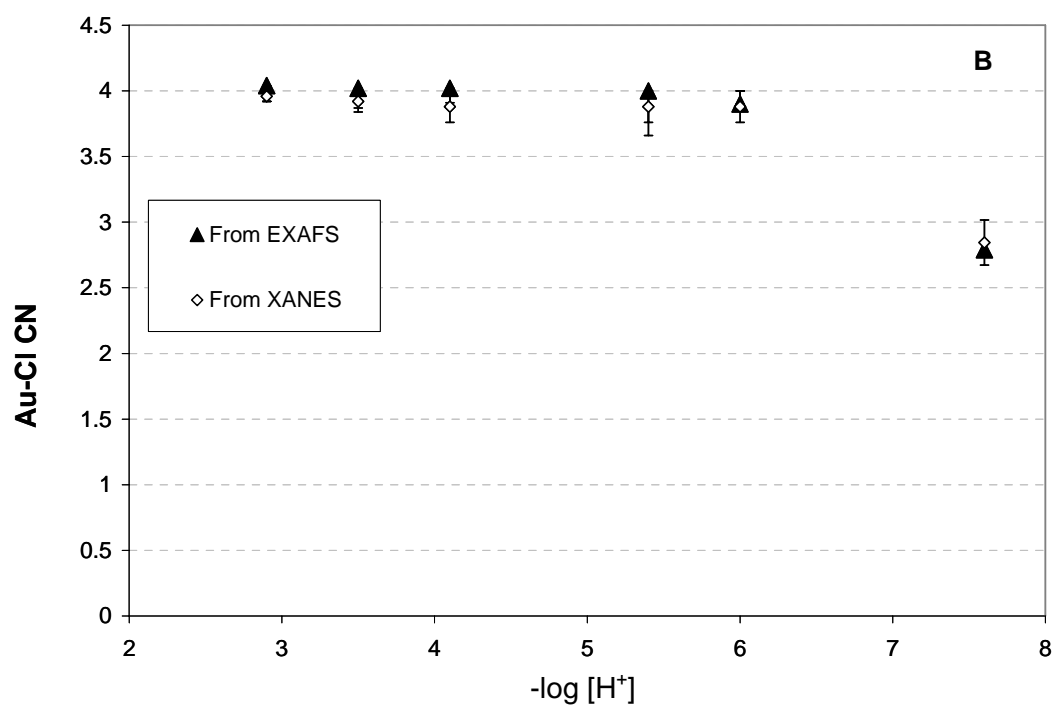


Figure 6.2. (A) Magnitude and imaginary component of the Fourier transformed EXAFS (k^2 , $\Delta k=3.37-12.3 \text{ \AA}^{-1}$) for AuCl_4^- in anhydrous methanol at (—, —) pH=2.9, (···) pH=6.0 and (---, ---) pH=7.6. Peak positions are uncorrected for phase-shift. (B) Comparison between XANES- and EXAFS-derived Au-Cl coordination numbers. $[\text{Au}^{3+}]=430 \text{ }\mu\text{M}$, $\text{Cl}^-/\text{Au}^{3+}=1070$.

intensity at the edge occurred at pH=7.6. XANES fitting considering Au-Cl, Au-O and Au-Au convoluted components, gave the distribution of species in solution showed in Figure 6.1B. Since the feature appearing immediately after the white line (Figure 6.1A) progressively disappears as Au-Cl is replaced for Au-O, it was possible to quantify the fraction of Au-O in the sample. Between pH=2.9 and 6.0, gold was present as Au^{3+} bound to chloride, although a very small fraction of Au-O bonds was detected. At pH=7.6, Au^{3+} was partially reduced to Au^0 under the beam. It is known that increasing pH promotes Cl^- replacement from AuCl_4^- by OH^- .²⁸ Thus, although no $\text{AuCl}_x(\text{OH})_{4-x}$ species were observed, the formation of zerovalent gold at high pH suggests the role of oxygen-containing Au^{3+} as an important precursor for Au^0 . EXAFS results were in line with XANES (Figure 6.2A); when pH increased from 6.0 to 7.6, the magnitude of the Fourier transform for the Au-Cl shell dropped by $\sim 25\%$. On the other hand, the magnitude was fairly constant in the pH=2.9-6.0 range. Since gold existed in solution either as AuCl_4^- or a combination with Au^0 , the Au-Cl coordination number (CN) for each solution was readily determined. These values are compared to Au-Cl coordination numbers derived from EXAFS in Figure 6.2B. Table 6.1 summarizes the EXAFS parameters obtained.

Table 6.1. EXAFS fit parameters for AuCl_4^- solutions in anhydrous methanol (k^2 , $\Delta k=3.37\text{-}12.3 \text{ \AA}^{-1}$; $430 \text{ }\mu\text{M Au}^{3+}$, $\text{Cl}^-/\text{Au}^{3+}=1070$)

pH	XANES CN	Fraction $\text{Au}^{3+}\text{-Cl}$	Fraction $\text{Au}^{3+}\text{-O}$	Fraction Au^0	Scattering path	EXAFS CN	R (\AA) (± 0.01)	DWF ($\times 10^{-3}$)	Eo (eV)
2.9	3.96	0.99	0.01	0	Au-Cl	4.04	2.28	-0.6	0
3.5	3.92	0.98	0.02	0	Au-Cl	4.02	2.27	-0.8	-0.5
4.1	3.88	0.97	0.03	0	Au-Cl	4.02	2.28	-0.8	-0.3
5.4	3.88	0.97	0.02	0	Au-Cl	4.02	2.27	-0.3	-0.4
6.0	3.88	0.97	0.02	0.01	Au-Cl	3.90	2.28	-0.8	0
7.6	2.84	0.71	0	0.29	Au-Cl	2.79	2.27	-0.8	-0.9

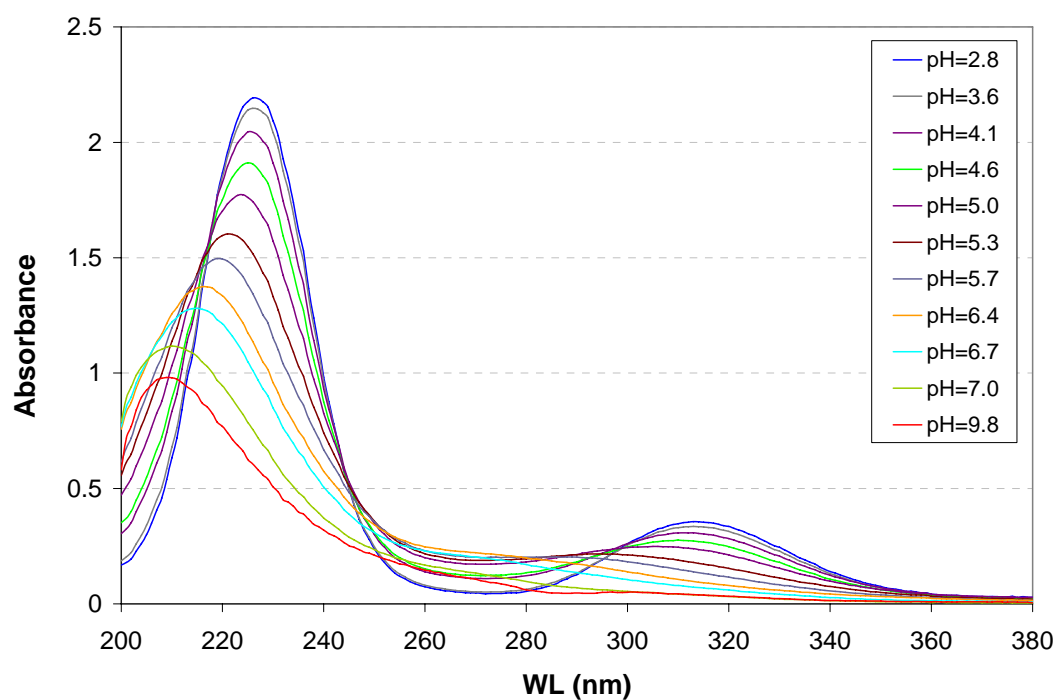
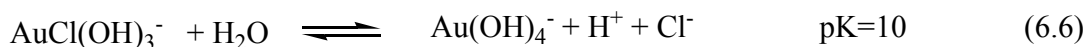
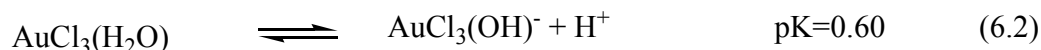
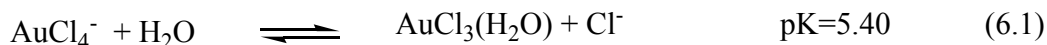


Figure 6.3. Hydrolysis of AuCl_4^- as a function of pH. Data collected from independent solutions 5h after preparation. The reported pH for each sample was measured right after the spectrum was acquired. $[\text{Au}^{3+}] = 72 \mu\text{M}$, $\text{Cl}^-/\text{Au}^{3+} = 1070$.

The hydrolysis of AuCl_4^- was followed via UV-VIS spectroscopy in water, since hydrolysis in this medium is well characterized; the results were used to interpret the absorption spectra of Au^{3+} /DN and Au^{3+} /APMBTSS in methanol. Figure 6.3 shows some selected results, which illustrate the changes as the solution became increasingly basic. Given that each of the samples analyzed contained the same amount of gold and chloride ($72 \mu\text{M AuCl}_4^-$ and $\text{Cl}^-/\text{Au}^{3+}=1070$), the differences among spectra were due only to variations in pH. An estimation of the distribution of species in solution at different pH was attained using reported values of the experimental hydrolysis constants. The following set of reactions were assumed to occur as the pH of the solutions increased:²⁸⁻³³



By solving the equilibrium expressions for reactions (6.1-6.6) along with the mass balances for gold and chloride, the concentrations of the various hydrolyzed Au^{3+} species were obtained. The calculations indicate that at pH=2.8, 99.2% of gold exists as AuCl_4^- , but the percentage decreases very fast with pH, reaching 0.16% at pH=6.7. At pH=5.0 gold splits almost evenly between AuCl_4^- (41.6%) and $\text{AuCl}_3(\text{OH})^-$ (50%); above pH=6.7, gold largely distributes among $\text{AuCl}_2(\text{OH})_2^-$, $\text{AuCl}(\text{OH})_3^-$ and $\text{Au}(\text{OH})_4^-$, being mostly $\text{Au}(\text{OH})_4^-$ (90.6%) at pH=9.9. These

results were utilized to determine the number of Au-Cl bonds per total gold in solution, i.e.

the overall Au-Cl CN, as a function of pH (see last column, Table 6.2):

$$\text{CN} = \sum_{x=1}^4 xF_{\text{AuCl}_x(\text{OH})_{4-x}} \quad (6.7)$$

where $F_{\text{AuCl}_x(\text{OH})_{4-x}}$ is the mole fraction of gold coordinated to x chloride atoms.

Table 6.2. Molar absorptivity ε experimentally determined for aqueous solutions of AuCl_4^- and the corresponding overall Au-Cl CN as given by Eq. (6.7). Entries in columns 4-7 represent each of the terms in Eq. (6.7), which were determined by solving the equilibrium expressions for reactions (6.1-6.6) using reported values of the hydrolysis constants.²⁸⁻³³ $[\text{Au}^{3+}] = 72 \mu\text{M}$, $\text{Cl}^-/\text{Au}^{3+} = 1070$.

pH	Abs (226nm)	$\varepsilon \times 10^4$ ($\text{M}^{-1} \text{cm}^{-1}$)	$xF_{\text{AuCl}_x(\text{OH})_{4-x}}$				Au-Cl CN
			AuCl_4^-	$\text{AuCl}_3(\text{OH})^-$	$\text{AuCl}_2(\text{OH})_2^-$	$\text{AuCl}(\text{OH})_3^-$	
2.8	2.192	3.040	3.97	0.02	0.00	0.00	3.99
3.6	2.147	2.978	3.81	0.14	0.00	0.00	3.95
3.8	2.132	2.957	3.70	0.21	0.01	0.00	3.92
4.1	2.044	2.835	3.45	0.39	0.02	0.00	3.85
4.3	2.038	2.827	3.18	0.57	0.03	0.00	3.78
4.6	1.906	2.644	2.63	0.94	0.06	0.00	3.63
5	1.743	2.417	1.66	1.50	0.17	0.00	3.33
5.3	1.518	2.105	0.97	1.75	0.34	0.00	3.07
5.5	1.422	1.972	0.62	1.75	0.51	0.01	2.88
5.7	1.344	1.864	0.36	1.61	0.71	0.02	2.70
6.4	1.137	1.577	0.03	0.60	1.25	0.17	2.04
6.7	1.012	1.404	0.01	0.28	1.18	0.31	1.78
7	0.756	1.049	0.00	0.11	0.92	0.49	1.53
7.2	0.642	0.890	0.00	0.05	0.72	0.61	1.38
7.4	0.64	0.888	0.00	0.03	0.52	0.71	1.26
9	0.538	0.746	0.00	0.00	0.01	0.45	0.46
9.4	0.578	0.802	0.00	0.00	0.00	0.25	0.25
9.8	0.606	0.840	0.00	0.00	0.00	0.12	0.12
9.9	0.599	0.831	0.00	0.00	0.00	0.09	0.09
11.6	0.51	0.707	0.00	0.00	0.00	0.00	0.00

As seen in Figure 6.3 (trace at pH=2.8), the absorption spectrum of the AuCl_4^- complex in water exhibits two characteristic bands at 227 nm and 313 nm, which are also present at almost the same positions in methanol. The band at 227 nm has been attributed to the $^1\text{A}_{1g} \rightarrow ^1\text{E}_u(\text{a})$ ligand-to-metal charge-transfer transition (LMCT); the one at 313 nm is a double degenerate LMCT band, corresponding to the $^1\text{A}_{1g} \rightarrow ^1\text{A}_{2u} + ^1\text{E}_u(\text{b})$ transition.^{28,34-36} Some authors however, have assigned the band at 313 nm as a LMCT involving only the $^1\text{A}_{2u}$ or the $^1\text{E}_u(\text{b})$ excited state.^{37,38} Both bands shift to higher energies as H_2O or OH^- replace Cl^- from the Au^{3+} inner-coordination sphere. Therefore, as hydrolysis of AuCl_4^- proceeds, the observed absorbance at 227 and 313 nm decreases, while the corresponding bands move to lower wavelengths (Figure 6.3). Given the direct relationship between the number of chloride atoms in the inner-coordination sphere of Au^{3+} and the intensity of the LMCT bands, an attempt was made to correlate these two quantities. The first two columns in Table 6.2 list the pH of the $\text{AuCl}_x(\text{OH})_{4-x}$ solutions studied and the corresponding absorbance at 227 nm. Column 2 was transformed to molar absorptivity ϵ with respect to the total Au^{3+} concentration (column 3), whereas the last column gives the overall Au-Cl CN as determined from the calculated distribution of Au^{3+} in solution, using eq. (6.7). A plot of the overall Au-Cl coordination number against the molar absorptivity at 227 nm derived from this table, is given in Figure 6.4. As observed, the Au-Cl coordination number decreases linearly with the extinction coefficient at 227 nm in the $\Delta\epsilon=0.8\text{-}3.0$ range. Below $\epsilon \sim 0.8$, any further substitution of chloride by hydroxide slightly decreases ϵ , consequence of an overlapping of the band at 227 nm and a hypsochromic-shifted band originally located at 313 nm.

If as suggested by the aqueous solutions, the absorbance at 227 nm is mainly a function of the number of Au-Cl bonds, then the CN vs ϵ correlation should be valid regardless of the

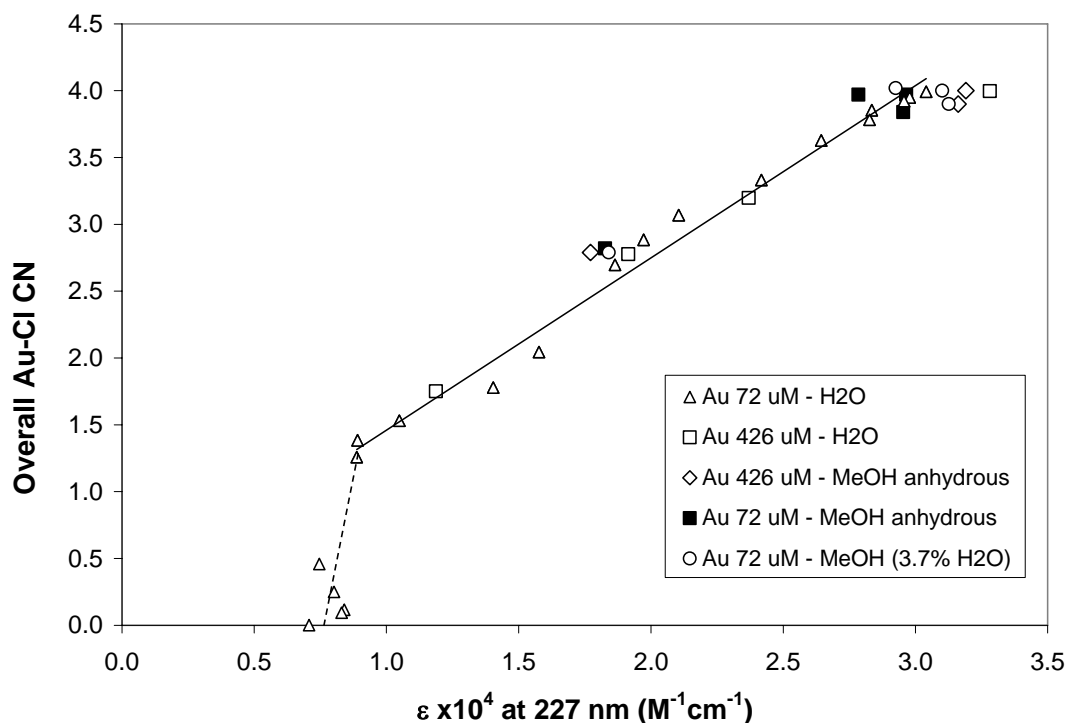
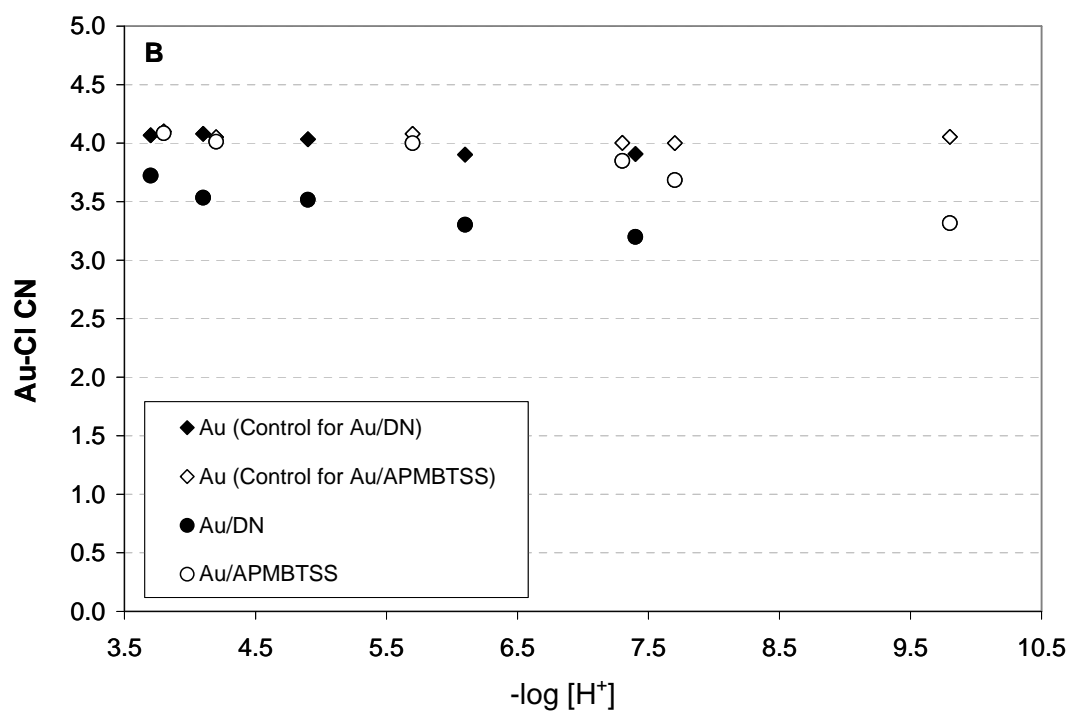
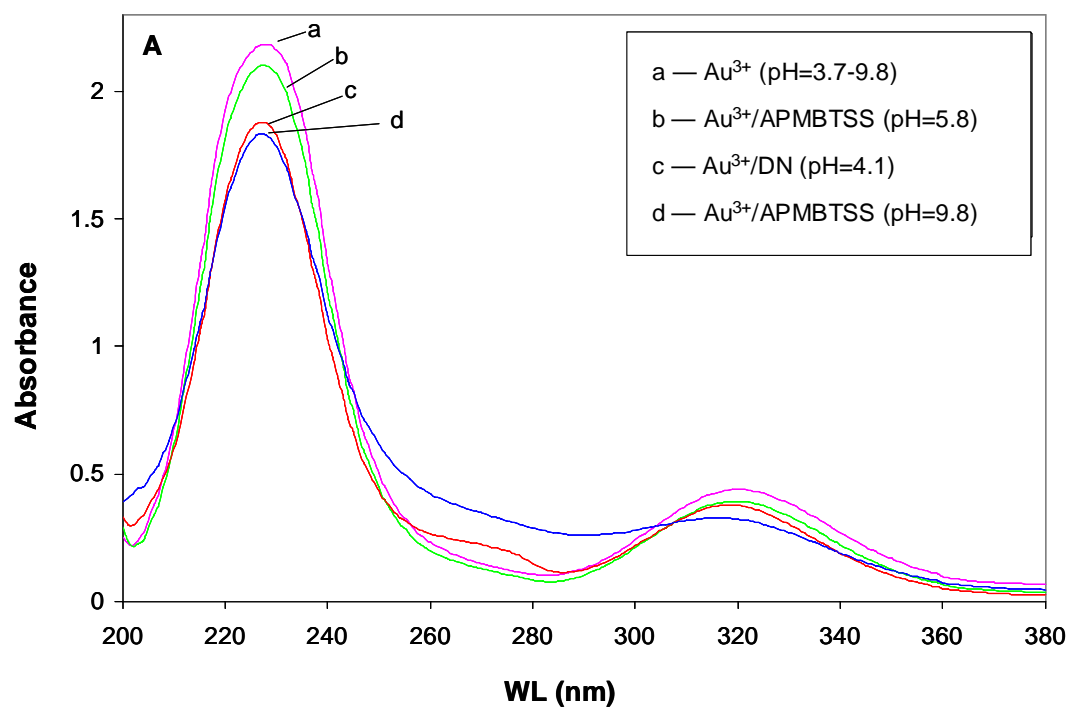


Figure 6.4. Overall Au-Cl coordination number against molar absorptivity at 227 nm for solutions of AuCl_4^- at two different concentrations in three different solvents. Molar absorptivities were all determined by UV-VIS, 5h (water) and 90 min (anhydrous methanol) after preparation. Au-Cl CN for the aqueous systems was calculated using equilibrium constants for reactions (6.1-6.6). For the 426 μM solution in methanol, it was determined using EXAFS. The solutions of 72 μM in methanol and methanol/water were used to test the validity of the relationship (see text for details). In all cases $\text{Cl}^-/\text{Au}^{3+}=1070$.

total concentration of gold and solvent used, although the energy of the LMCT transition could be different for solvents with dissimilar permittivities due to solvatochromism.^{39,40} To test this hypothesis, solvolysis was studied for four additional Au^{3+} solutions in which either the total concentration of gold or the solvent was changed: (i) 426 μM AuCl_4^- in water, (ii) 426 μM AuCl_4^- in anhydrous methanol, (iii) 72 μM AuCl_4^- in anhydrous methanol and (iv) 72 μM AuCl_4^- in methanol/water (3.7% H_2O). In all the solutions the $\text{Cl}^-/\text{Au}^{3+}$ ratio was 1070. The concentrated aqueous solutions (i) (426 μM AuCl_4^-) were analyzed exactly as the lower concentration solutions (72 μM AuCl_4^-) just described. Similarly, UV-VIS spectra were collected for solutions (ii) at pH=5.4, 6.0 and 7.6, and the absorbance at 227 nm converted to molar absorptivity ϵ . Since samples (ii) were prepared exactly as those used for the XANES/EXAFS studies, it was possible to assign an EXAFS-determined overall Au-Cl CN to each of them. A plot showing the CN vs ϵ correlation is included in Figure 6.4. As shown, whether solvolysis happens at low or high gold concentration, in anhydrous methanol or water, there is no significant difference in the relationship between the intensity of the LMCT band and the Au-Cl CN. Thus, it was possible to include samples (iii-iv) in Figure 6.4, using the CNs obtained by EXAFS for samples (ii) and extinction coefficients determined via UV-VIS; as expected, all the experimental points lie on the same curve. This connection between LMCT band intensity and coordination number was used to interpret the UV-VIS spectra of solutions of AuCl_4^- and DN at different pH and amine/gold ratios.

6.4.2 Reactions of Au^{3+} and DN at various pH

Understanding the binding of Au^{3+} to DN involves determining whether the constrained environment at the nanocage interior modified the properties of amine as a ligand, and if so, to



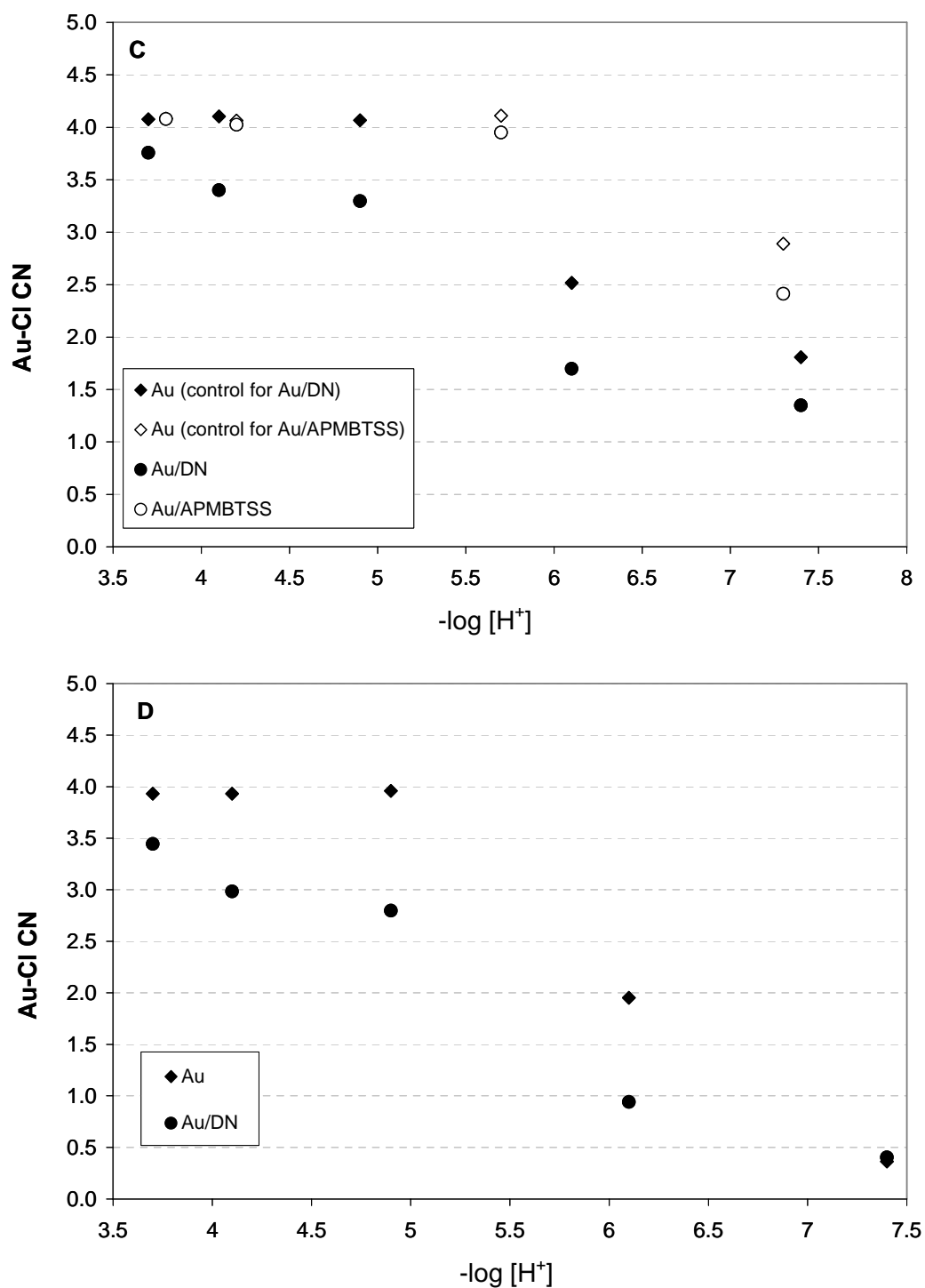


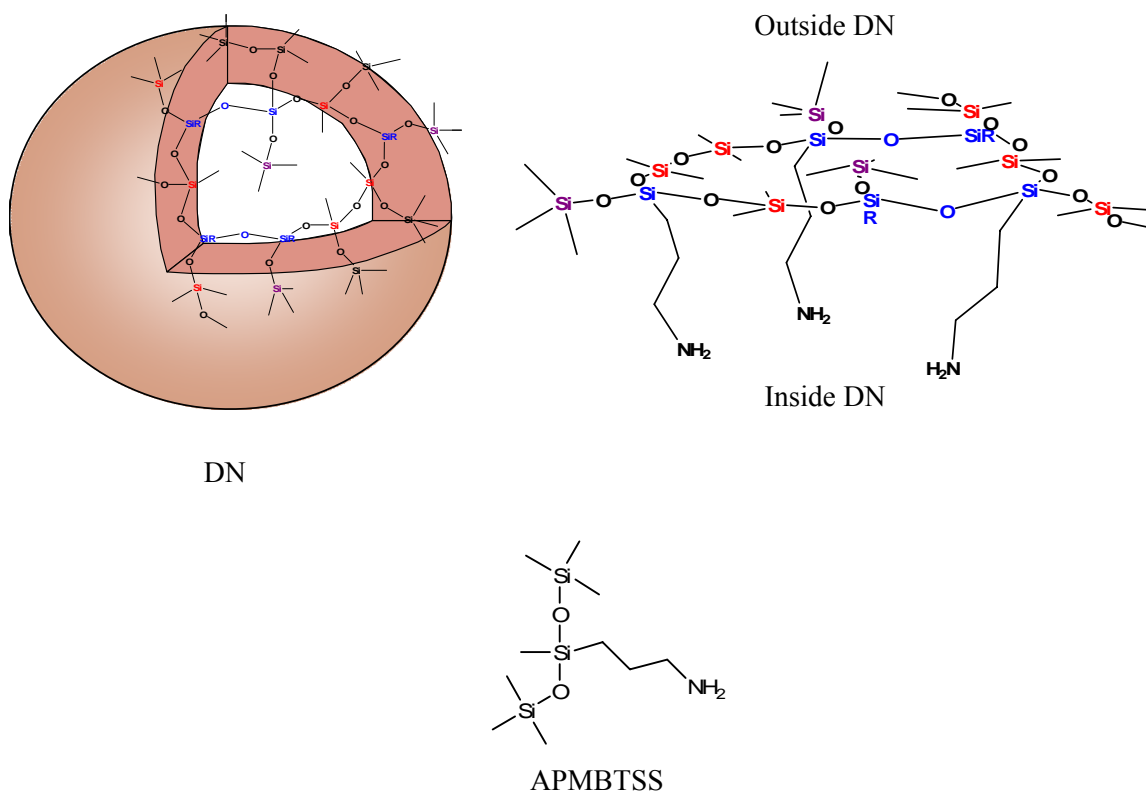
Figure 6.5. (A) UV-VIS spectra of Au^{3+}/DN and $Au^{3+}/APMBTSS$ solutions in anhydrous methanol illustrating the difference in pH required to cause a comparable drop in the LMCT band at 227 nm after 10 min of reaction. (B-D) Overall Au-Cl CN vs pH at different reaction times, determined from UV-VIS and Figure 6.4. The reaction times are 10 min (B), 90 min (C) and 48 h (D). $[Au^{3+}] = 72 \mu M$, $R-NH_2/Au^{3+} = 1.0$, $Cl^-/Au^{3+} = 4$ for all solutions.

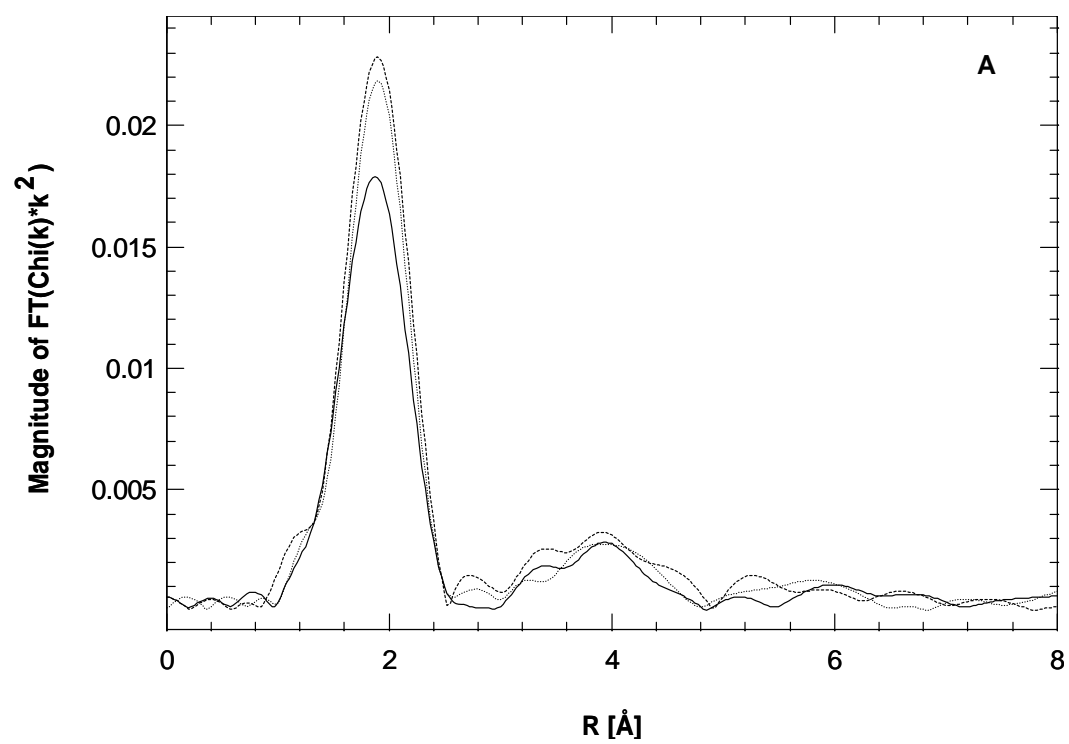
what extent as compared to a similar unconstrained amine in solution. Studying the influence of pH on the adsorption of AuCl_4^- inside DN provided a means to address this question. As previously discussed, ligand exchange of Cl^- in the primary coordination sphere of Au^{3+} by H_2O , MeOH , MeO^- or OH^- lowers the intensity of the CT band at 227 nm.^{41,42} This holds if Cl^- exchanges with amine ligands, since the ionization potential of the nitrogen lone pair is higher than that of chloride.^{35,43} The interest was to promote exchange with nitrogen, as it determines the anchoring of Au^{3+} to the nanocage interior. However, as the pH of solutions of AuCl_4^- , DN and methanol (with traces of water) increased, both R-NH_2 at the interior of DN (Scheme 6.1) and oxygen-containing ligands (H_2O , MeOH , MeO^- or OH^-) could potentially exchange with chloride. Accounting for gold binding to DN required distinguishing between both processes. This was achieved by parallel running a control per sample, which excluded DN but was otherwise similar to the solution under study. Figure 6.5A illustrates some of these results for solutions of Au^{3+} and DN in methanol 10 min after mixing. The difference of absorbance between Au^{3+} and Au^{3+}/DN at a given pH was a consequence of the presence of DN in the second solution. For comparison, mixtures of Au^{3+} and the primary amine APMBTSS (Scheme 6.1) were also analyzed; as the traces suggest, the drop in the intensity of the band at 227 nm caused by addition of DN at pH=4.1 was comparable to the drop generated by an equivalent amount of APMBTSS at pH=9.8. This was a first indication that free amine required a higher pH than constrained amine, to cause a specific decrease in the LMCT band. The pH effect was further explored by UV-VIS at different reaction times; the results are summarized in Figures 6.5B-D in the form of Au-Cl CN vs pH. To make the plots, the spectra (not shown) were used to determine ϵ at 227 nm and Figure 6.4 was employed to calculate a corresponding overall Au-Cl CN. In general, the free amine APMBTSS required higher pH than the primary amine confined

inside DN, to cause the same drop in the LMCT band at any given time. As time progressed the trend was maintained, although the drop in the intensity of the band became more pronounced. Since the controls accounted for exchange with oxygen-containing ligands, the extra drop in the LMCT band is attributed to replacement of Au-Cl by Au-N bonds, and consequently, binding of AuCl_4^- to DN. The possibility of amine-enhanced solvolysis was ruled out by the fact that APMBTSS didn't cause such an effect and by cyclic voltammetry (below).

Scheme 6.1

Model of the deprotected nanocage (DN) highlighting its porous wall and interior propylamine functionalities. The structure of the primary amine APMBTSS used as a reference in this work is also included.





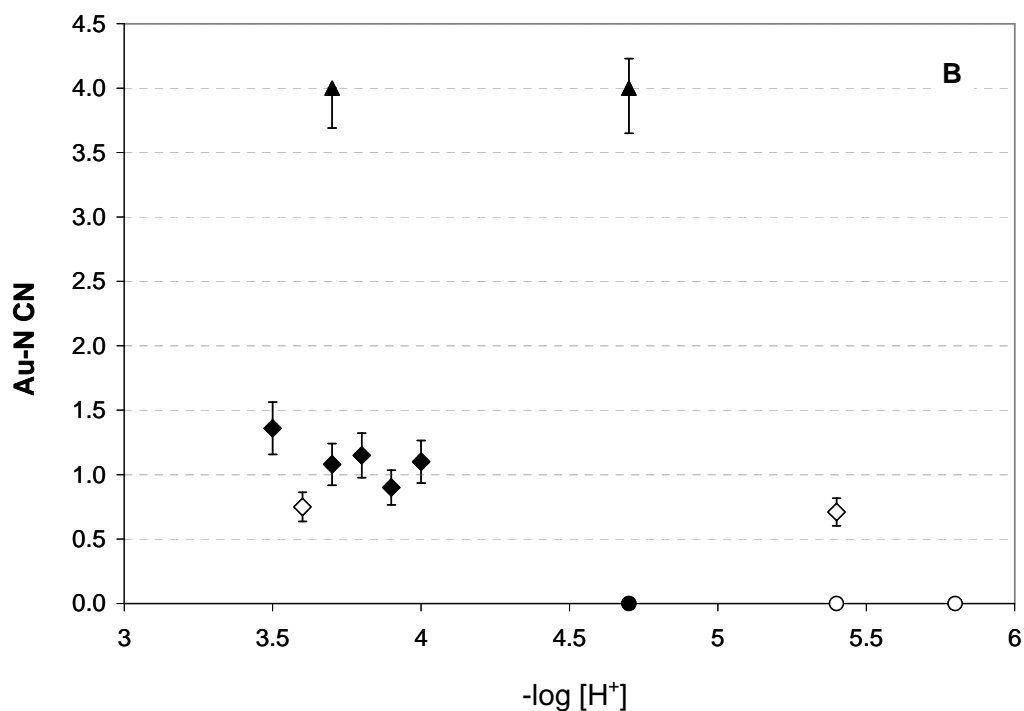


Figure 6.6. (A) Magnitude of the Fourier transformed EXAFS (k^2 , $\Delta k=3.37-11.6 \text{ \AA}^{-1}$) for (---) AuCl_4^- at pH=3.7, (\cdots) Au^{3+} /APMBTSS at pH=4.7 and (—) Au^{3+} /DN at pH=4.0. Peak positions are uncorrected for phase-shift. (B) Au-N coordination number determined by EXAFS. Data collected at $\text{Cl}^-/\text{Au}^{3+}=4$: (▲) Au-Cl CN for AuCl_4^- control solutions, (◆) Au^{3+} /DN and (●) Au^{3+} /APMBTSS. Collected at $\text{Cl}^-/\text{Au}^{3+}=1070$: (◇) Au^{3+} /DN and (○) Au^{3+} /APMBTSS. In all cases the solvent was anhydrous methanol. All solutions were analyzed after 90 min of reaction. Other conditions: $[\text{Au}^{3+}]=430 \text{ }\mu\text{M}$, $\text{R-NH}_2/\text{Au}^{3+}=1.0$.

Table 6.3. EXAFS fit parameters for Au^{3+}/DN and $\text{Au}^{3+}/\text{APMBTSS}$ solutions in anhydrous methanol (k^2 , $\Delta k=3.37\text{-}11.6 \text{ \AA}^{-1}$; $430 \mu\text{M Au}^{3+}$).

pH	R-NH ₂ /Au ³⁺	Cl ⁻ /Au ³⁺	CN (±10%)		R/Å (±0.01)		DWF x 10 ⁻³		Eo (eV)	
			Au-N	Au-Cl	Au-N	Au-Cl	Au-N	Au-Cl	Au-N	Au-Cl
Au ³⁺ /APMBTSS										
3.7	0	4	0	4	0	2.28	0	-0.69		0.7
4.7	1	4	0	4	0	2.28	0	-0.34	0	0.4
10.9	1	4	---	1.45	---	2.28	---	-2.1	---	0.9
6.6	3	4	3.08	0.92	2.05	2.28	-2	-7.2	0.89	-4.7
6.4	4.1	4	2.84	1.16	2.05	2.28	-3.6	-5.5	1.2	-4.5
6.8	4.1	4	3.41	0.59	2.05	2.28	6.2	-10	-4	3.1
7.5	4.1	4	3.63	0.37	2.05	2.28	7.3	-10	-4.9	4.7
5.4	1	1070	---	4.06	---	2.27	---	-0.55	---	-0.3
5.8	1	1070	---	3.83	---	2.26	---	0.67	---	-0.7
10.9	104.3	1070	3.78	0.22	2.07	2.28	4.3	-9.9	-3.4	8.7
Au ³⁺ /DN										
3.5	1.07	4	1.36	2.64	2.05	2.28	-0.34	-4	2.7	-0.2
3.7	1.07	4	1.08	2.92	2.05	2.28	-3.3	-3.4	4.4	-1.2
3.8	1.07	4	1.15	2.85	2.05	2.28	-4	-2.9	5.1	-0.9
3.9	1.06	4	0.9	3.1	2.05	2.28	-7.1	-2.6	6.3	-0.9
4	1.07	4	1.1	2.9	2.05	2.28	-3.5	-1.7	2.7	-1.2
4	2.12	4	1.23	2.77	2.05	2.28	4.3	-2.9	0.7	0.3
4	4.31	4	1.92	2.08	2.05	2.28	-4.8	-5.7	3.6	-2.9
4.2	4.31	4	2.3	1.9	2.05	2.28	-4.2	-7.7	4.2	-4.0
3.6	0.99	1070	0.75	3.25	2.05	2.28	-3.1	-2.5	1	-0.3
5.4	0.99	1070	0.71	3.29	2.05	2.28	-2.3	-2.2	2.9	-0.4

The influence of pH was also studied by XAS on Au^{3+}/DN and $\text{Au}^{3+}/\text{APMBTSS}$ solutions. Since EXAFS can't distinguish Au-O from Au-N scattering, experiments were carried out in anhydrous methanol in order to minimize ligand exchange between chloride and oxygen-containing groups. Additionally, reference solutions of AuCl_4^- (no amine or DN) under the same conditions as the samples of interest, were analyzed; those controls showed no solvolysis of the

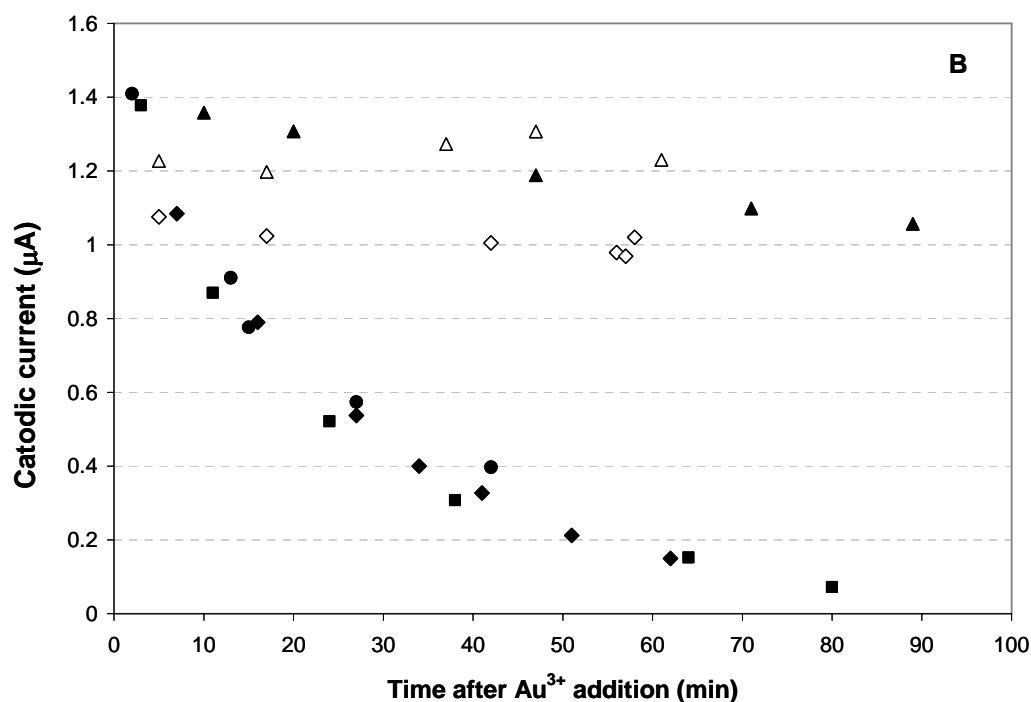
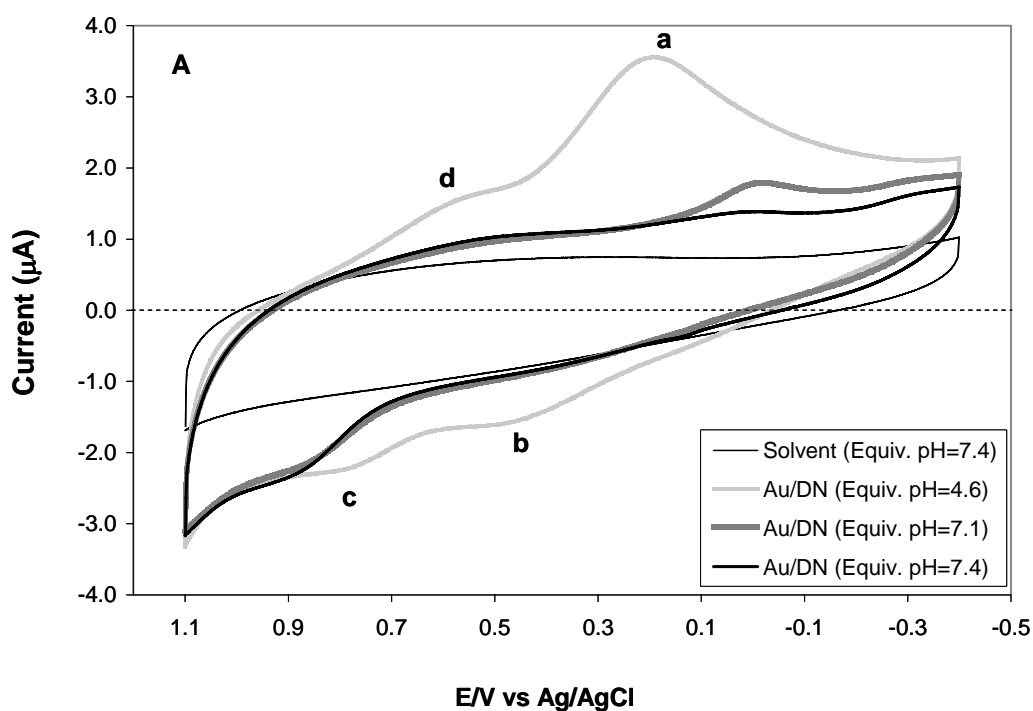
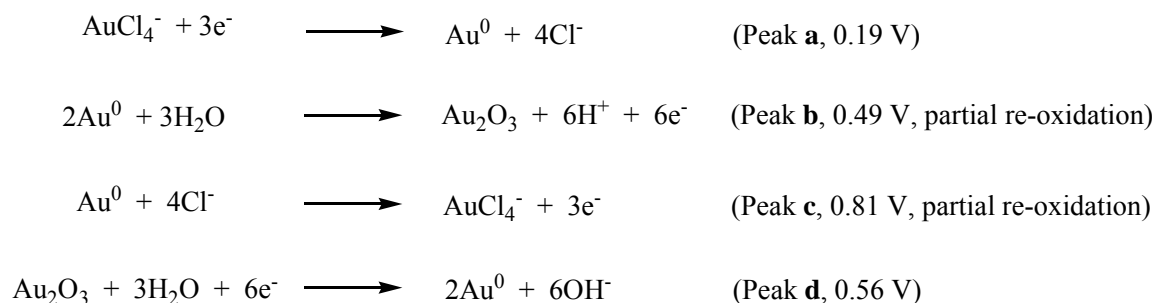


Figure 6.7. (A) Cyclic voltammograms of Au^{3+}/DN solutions at various pH. (B) Time evolution of the cathodic current (**a+d**) as a function of time at (\blacktriangle) pH=4.6, (\bullet) pH=7.1 and (\blacksquare , \blacklozenge) pH=7.4. Two controls are included: (\diamond) AuCl_4^- and (Δ) Au^{3+}/PN , both at pH=7.4. Reactions carried out in methanol (0.1% water) at 500 rpm. $[\text{Au}^{3+}] = 42 \mu\text{M}$, $\text{R-NH}_2/\text{Au}^{3+} = 1.0$. Scan rate = 0.1 V/s. Reference electrode: Ag/AgCl. Supporting electrolyte: 0.10 M NaClO_4 .

gold precursor in the pH range studied. Figure 6.6A compares the magnitude of the Fourier transform of the EXAFS corresponding to AuCl_4^- , $\text{Au}^{3+}/\text{APMBTSS}$ and Au^{3+}/DN at pH=3.7, 4.0 and 4.7 respectively. No significant change was induced upon addition of APMBTSS, contrary to what was observed for DN even at lower pH. Since there was no solvolysis of AuCl_4^- with or without amine (APMBTSS), the changes observed were due solely to the formation of new Au-N bonds. EXAFS fitting led to the Au-N coordination numbers shown in Figure 6.6B and the optimized parameters reported in Table 6.3. As the figure indicates, DN binds gold at a much lower pH than free amine in solution, which is commensurate with the foregoing UV-VIS results.

At lower gold concentration, binding of Au^{3+} to DN appears to occur at higher pH, as suggested by cyclic voltammetry (Figure 6.7). Figure 6.7A compares the cyclic voltamograms for Au^{3+}/DN solutions ($42\ \mu\text{M}\ \text{Au}^{3+}$, amine/gold=1.0) at various pH. For control purposes, data are included for the solvent/electrolyte system; this trace showed no Faradaic currents in the potential range investigated. Data collected for solutions of DN and PN (the precursor of DN which lacks amine functionalities at the interior) also confirmed the absence of Faradaic currents. Therefore, neither the solvent, DN nor PN underwent redox processes between 1.1 and -0.4 V. However, redox products formed once gold was present in solutions. Inspection of the top trace reveals four features due to reduction (a,d) and re-oxidation (b,c) of gold on the electrode's surface.⁴⁴ Similar peaks have been observed for this and other gold complexes.^{28,45,46} In accordance with the literature, we assign peaks (a-d) to these overall reactions:^{28,45,46}



As pH increased, the cathodic current decreased until eventually became close to zero, indicating that there was no gold left in solution to react on the electrode. Two possible explanations are that either Au^{3+} precipitated from solution as pH increased or it was trapped inside DN. Figure 6.7B presents more detailed results, including two control experiments aiming to test whether precipitation occurred. The current generated by gold in Au^{3+} /DN solutions decreased with time, faster at higher pH. Contrarily, a solution of Au^{3+} with no DN, showed no change, even at the highest pH considered, suggesting that in the absence of DN gold remained in solution. A possible precipitation of gold on the external surface of DN, which could limit its diffusion to the electrode, was ruled out after analyzing a solution in which DN had been replaced by an exact amount of PN (Au^{3+} /PN). Once again, the current remained constant with time. Different from DN, PN is not hollow and doesn't contain amine functionalities at the interior. Thus, we interpreted the decrease in the current as a result of Au^{3+} being trapped at the interior of DN.

6.4.3. Reaction of Au^{3+} and DN at various R-NH₂/Au ratios.

The binding of Au^{3+} to DN under various amine/gold ratios at pH=4.9 was evaluated by UV-VIS and EXAFS. The results derived from UV-VIS are given in Figure 6.8, both as

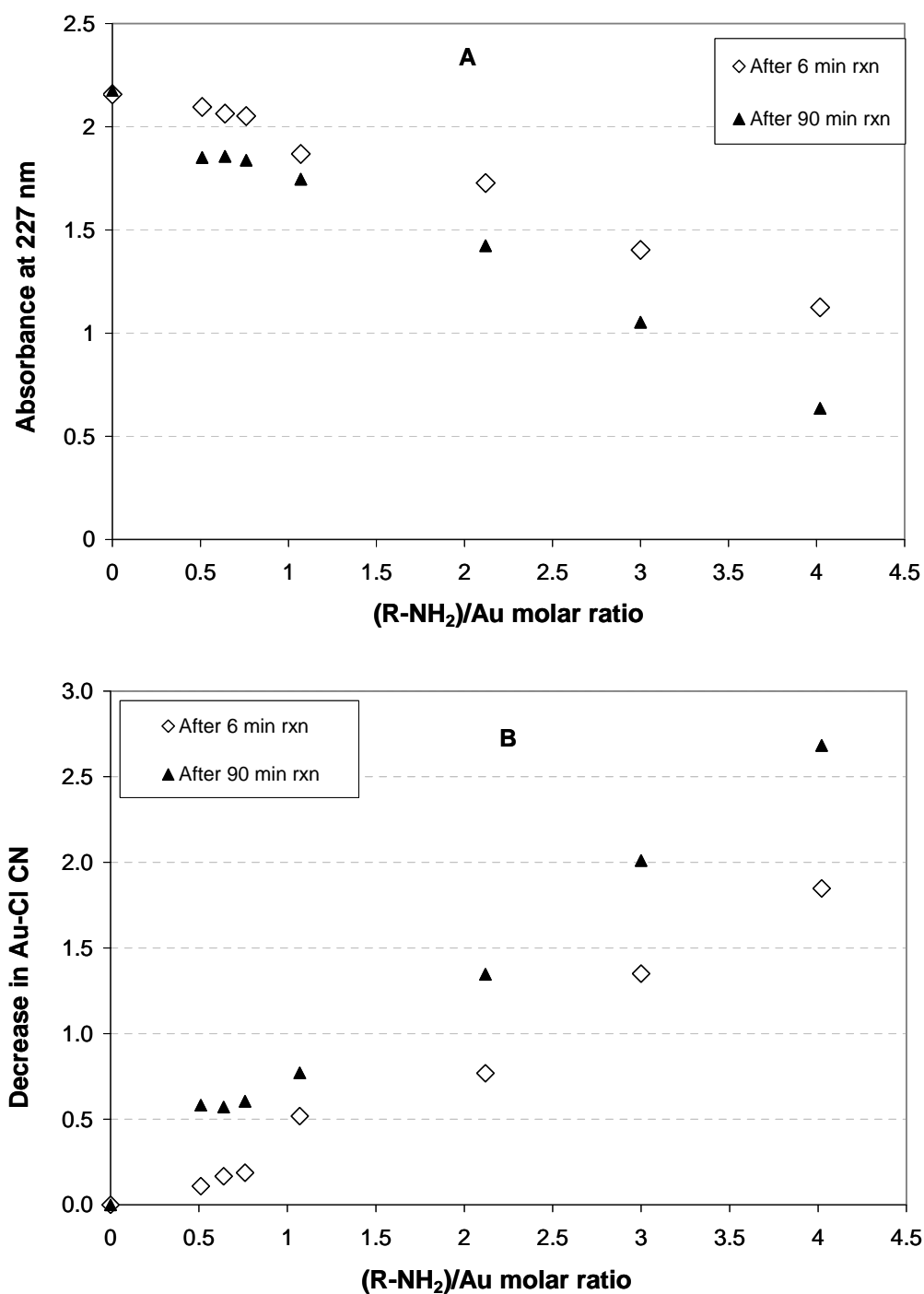
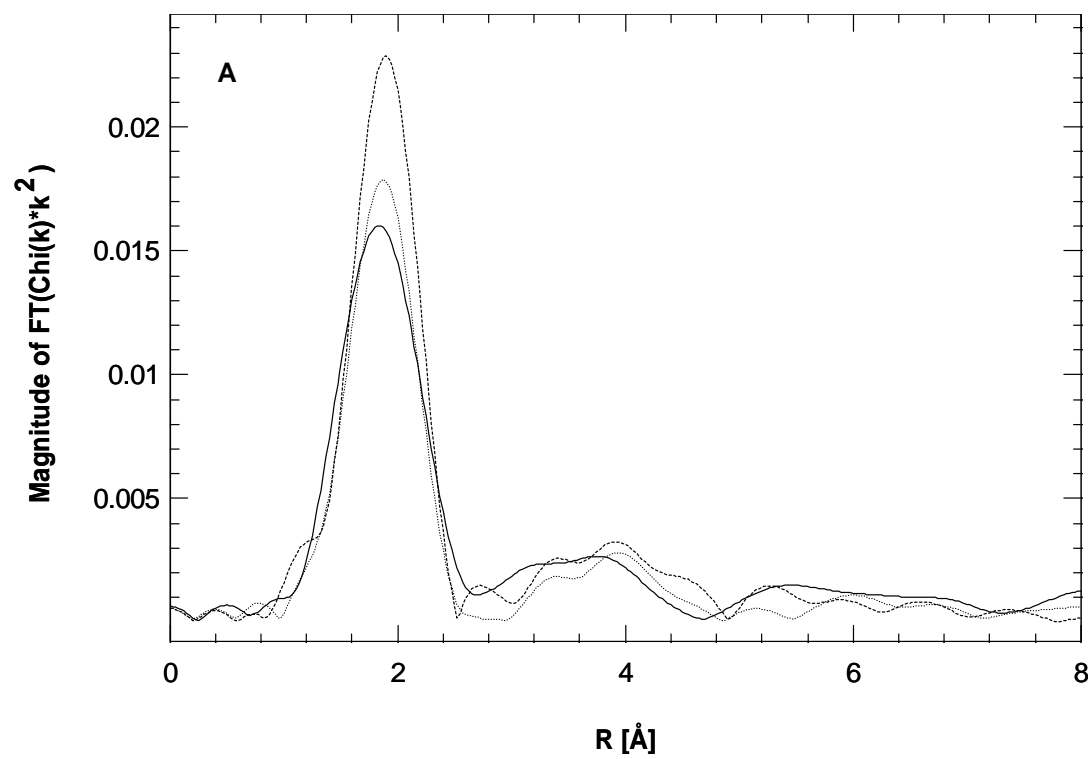


Figure 6.8. (A) Absorbance at 227nm after 6 and 90 min of reaction for independent solutions of Au³⁺/DN, with different amine/gold ratios. (B) Drop in Au-Cl coordination numbers determined from (A) with the help of Figure 6.4. Data acquired at pH=4.9 in anhydrous methanol. [Au³⁺]=72 μ M, Cl⁻/Au³⁺=4.



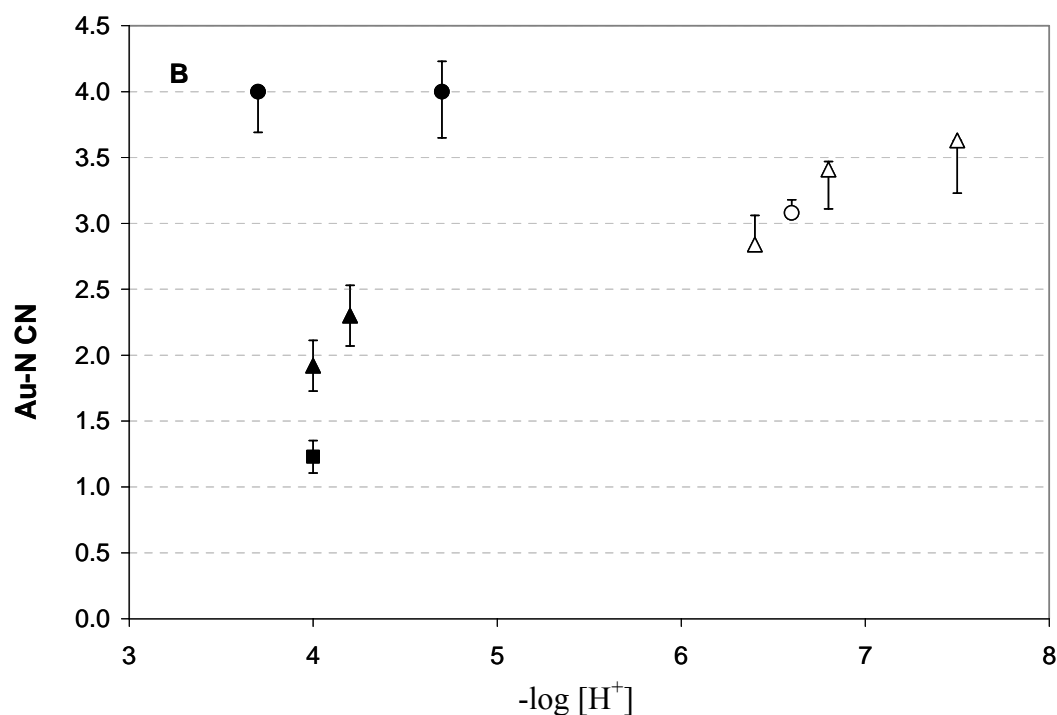


Figure 6.9. (A) Magnitude of the Fourier transformed EXAFS (k^2 , $\Delta k=3.37-11.6 \text{ \AA}^{-1}$) at different amine/gold ratios for Au^{3+}/DN . (---) AuCl_4^- ($\text{R-NH}_2/\text{Au}^{3+}=0$), (...) $\text{R-NH}_2/\text{Au}^{3+}=1.1$ and (—) $\text{R-NH}_2/\text{Au}^{3+}=4.3$. Peak positions are uncorrected for phase-shift. (B) Au-N coordination number determined by EXAFS. Data collected for Au^{3+}/DN : (■) $\text{R-NH}_2/\text{Au}^{3+}=2.1$ and (▲) $\text{R-NH}_2/\text{Au}^{3+}=4.3$. Data collected for $\text{Au}^{3+}/\text{APMBTSS}$: (○) $\text{R-NH}_2/\text{Au}^{3+}=3.0$ and (△) $\text{R-NH}_2/\text{Au}^{3+}=4.1$. AuCl_4^- control: (●) Au-Cl CN. In all cases the solvent was anhydrous methanol. All solutions were analyzed after 90 min of reaction. $[\text{Au}^{3+}]=430 \text{ }\mu\text{M}$, $\text{Cl}^-/\text{Au}^{3+}=4.0$.

absorbance at 227 nm and drop of Au-Cl CN, based on the correlation developed in Figure 6.4. After 6 minutes of reaction, the Au-Cl CN decreased almost linearly with the amine/gold ratio up to a maximum of 1.8. After 90 min and below $R-NH_2/Au^{3+}=0.8$, the drop increased only to 0.5, whereas it became 0.8 at $R-NH_2/Au^{3+}=1$. For higher amine/gold, the Au-Cl CN decreased linearly reaching ~ 2.8 at $R-NH_2/Au^{3+}=4.3$. There was no solvolysis of $AuCl_4^-$ ($R-NH_2/Au^{3+}=0$), even after 48 h (see also Figure 6.5). Thus, the changes observed were exclusively due to the nanocage, more specifically to the formation of Au-N bonds in its interior. Similar results were obtained by EXAFS, as reported in Figure 6.9. The decrease in the magnitude of the FT (Figure 6.9A) points to a progressive ligand exchange with increasing amine/gold ratio. In terms of the Au-N coordination number (Figure 6.9B), there was no significant change when doubling $R-NH_2/Au^{3+}$ from 1.1 to 2.1. Nonetheless, Au-N underwent a two fold increase when $R-NH_2/Au^{3+}$ was raised to 4.3. Figure 6.9B also shows results for a few $Au^{3+}/APMBTSS$ solutions; although binding occurred at $R-NH_2/Au^{3+} > 1.0$, a higher pH was in general required as compared to DN. The EXAFS for $Au^{3+}/APMBTSS$ samples were fitted assuming only Au-Cl and Au-N scatterings; however, due to the high pH it was possible that Au-N and Au-O scatterings were convoluted, so the real Au-N CN might be lower than reported. Evidence for the formation of Au-N bonds came from an easily detectable color change from pale yellow to darker green-brown that followed the mixing of Au^{3+} and APMBTSS. The color change was also observed when DN was used.

6.5. Discussion

UV-VIS in combination with XAS provided a means to determine the extent of solvolysis of $AuCl_4^-$ in nonaqueous solution. Quantification relied on the relationship between

Au-Cl coordination number and the extinction coefficient corresponding to the LMCT band at 227 nm, which appeared invariable in the concentration range 72-430 μM , whether the solvent was water or methanol. In order to employ this relationship to quantify the binding of cationic gold to primary amine, the assumption was made that the outer coordination sphere of gold had no influence on the measured extinction coefficient, i.e. that the relationship was applicable to Au^{3+} , Au^{3+}/DN and $\text{Au}^{3+}/\text{APMBTSS}$ solutions.

There was a significant difference on the binding properties of primary amine tethered to the interior of DN, as compared to the same amine in solution. Below pH 6, only DN forms Au-N bonds (Figures 6.5 and 6.6). Moreover, only single bonds form regardless of the pH, as far as gold and amine are in a 1:1 ratio. In contrast, APMBTSS displaces less than one chloride per gold at pH =7.0-10. Attempts to determine the binding stoichiometry of Au^{3+} and APMBTSS at higher pH were inconclusive owing to very fast exchange of Cl^- by OH^- . A color change from pale yellow (AuCl_4^-) to a dark brown-green occurred when a $\text{Au}^{3+}/\text{APMBTSS}$ solution was brought to pH=11.0, signaling the formation of new Au-N bonds; a similar color change was observed when the amine/gold ratio was raised to 104. The different response of DN to bulk pH as compared to unconstrained amine is better appreciated in Figure 6.10. In less than 48 h, all the Au^{3+} in solution migrates inside DN forming Au-N bonds in a 1: 1 ratio; in fact, about 80% of the reaction takes place within 90 min. DN exhibits a steep increase of Au-N CN from pH=3.8 to 4.3, which levels off at higher pH. Contrarily, APMBTSS binding to Au^{3+} increases monotonically with pH. The 1:1 stoichiometry of the complex formed between Au^{3+} and the amine functionalities inside DN, was also observed at higher (Figure 6.6) and lower (Figure 6.7) gold concentrations. Clearly, APMBTSS achieves a comparable degree of binding to Au^{3+} as DN, 4 to 5 pH units above. A similar pH gap has been reported for PANAM dendrimers, where

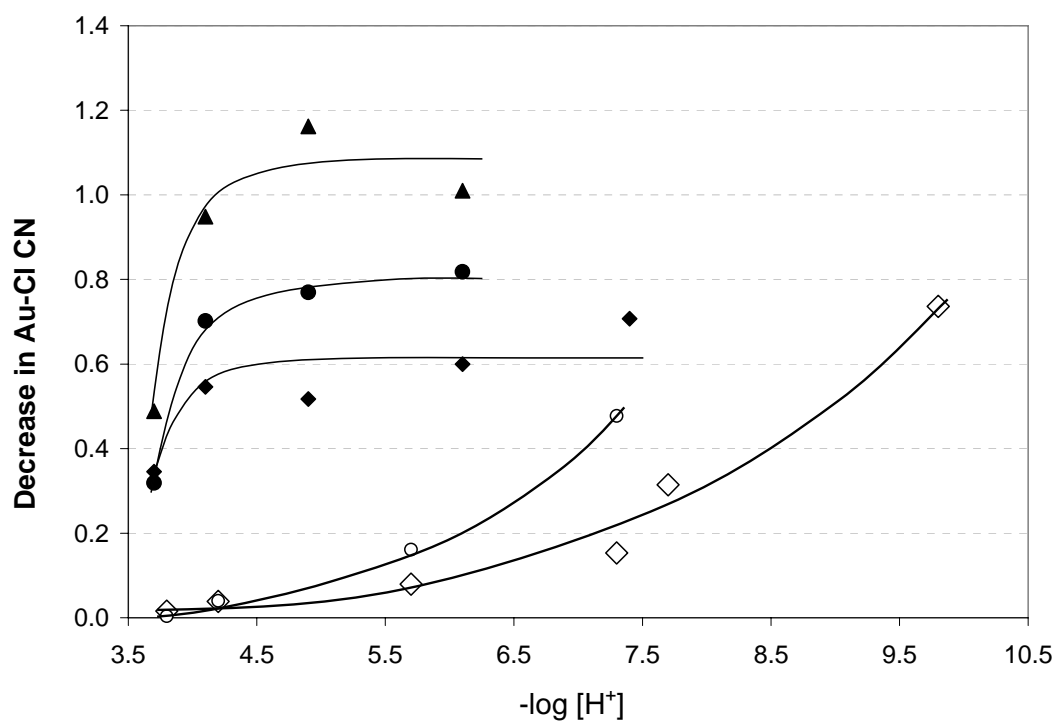
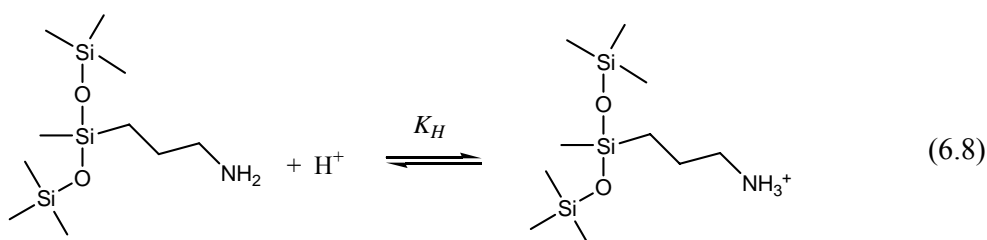


Figure 6.10. Decrease in Au-Cl coordination number of AuCl_4^- in solution with DN or APMBTSS. Data derived from Figure 6.5. Au^{3+}/DN after (◆) 10 min, (●) 90 min and (▲) 48 hours of reaction. $\text{Au}^{3+}/\text{APMBTSS}$ after (◇) 10 min and (○) 90 min of reaction. The solvent was anhydrous methanol. $[\text{Au}^{3+}] = 72 \mu\text{M}$, $\text{Cl}^-/\text{Au}^{3+} = 4.0$.

the constrained tertiary amines appear to be less basic than the peripheral primary amines.⁴⁷⁻

⁵⁰ For DN and APMBTSS, the pH difference can be rationalized in terms of the ability of amine to stabilize protons in an infinite solution as compared to inside a restricted nano-environment.

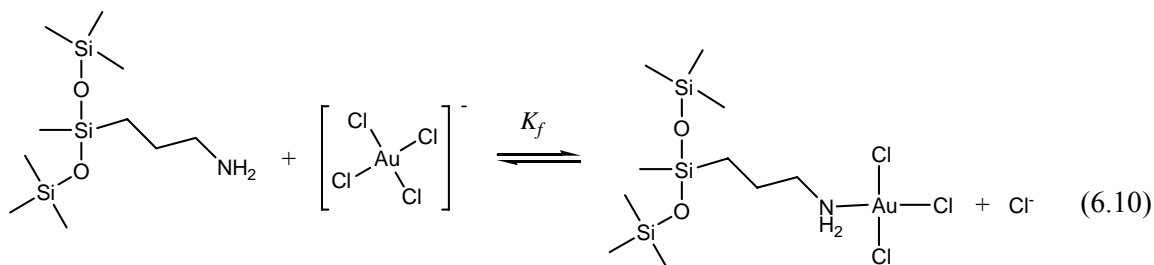
Aliphatic amines have strong affinity for protons, as demonstrated by their high protonation constants.⁵¹ As a result, protons compete with Au^{3+} for the amine groups:



The fraction of proton-free amine is given by:

$$\frac{[R-NH_2]}{(R-NH_2)_t} = \frac{1}{1 + K_H[H^+]} = \alpha \quad (6.9)$$

where $(R-NH_2)_t$ is the total concentration of amine in solution and K_H the amine protonation constant. For instance, if it is assumed that APMBTSS have a similar protonation constant as propylamine ($\log K=10.57$ at zero ionic strength and 25°C),⁵¹⁻⁵⁵ the required pH to have 96% proton-free amine would be 12. The reaction yielding the gold-amine complex:



is characterized by the formation constant:

$$K_f = \frac{(Au_t - [AuCl_4^-])^2}{[R-NH_2][AuCl_4^-]} = \frac{(Au_t - [AuCl_4^-])^2}{\alpha(R-NH_2)_i[AuCl_4^-]} \quad (6.11)$$

where Au_t is the total concentration of Au^{3+} and α is given by Eq. (6.9). Rearranging Eq. (6.11),

a conditional formation constant K_f^* can be defined:

$$K_f^* = \alpha K_f = \frac{(Au_t - [AuCl_4^-])^2}{(R-NH_2)_i[AuCl_4^-]} \quad (6.12)$$

which describes the formation of the gold-amine complex at any particular pH. The calculation of K_f^* is straight forward, using the $[AuCl_4^-]$ determined via UV-VIS or EXAFS. Reactions (6.8) and (6.10) are also valid when APMBTSS is replaced by DN, so equations (6.9), (6.11) and (6.12) can be used to describe the binding. Table 6.4 compares K_f^* for Au^{3+} /DN and Au^{3+} /APMBTSS solutions at various pH.

Table 6.4. Conditional formation constants of gold-amine complexes formed by reaction of HAuCl_4 and APMBTSS (90 min) or DN (90 min and 48 h). Data calculated from the experimental results presented in Figure 6.10, using Eq. (6.12). The last column was determined using Eq. (6.14).

$\text{Au}^{3+}/\text{APMBTSS}$		Au^{3+}/DN			
pH	$\log K_f^*$	pH	$\log K_f^*$		$(K_H)_{\text{DN}}/(K_H)_{\text{APMBTSS}}$
3.8	3.40	3.7	7.42	7.91	2.42×10^{-5}
4.2	5.47	4.1	8.46	9.49	7.59×10^{-5}
5.7	6.74	4.9	8.66	n.a.	n.a.
7.3	7.88	6.1	8.81	n.a.	n.a.

The dissimilar behavior of DN and APMBTSS observed in Figure 6.10 is rationalized in terms of the differences in the protonation constants. Given the similarity of propylamine tethered inside DN and APMBTSS, it is reasonable to expect a similar value of K_f for binding to Au^{3+} in each case. Writing Eq. (6.12) for these two instances, it follows that:

$$\left(\frac{K_f^*}{\alpha} \right)_{\text{DN}} = \left(\frac{K_f^*}{\alpha} \right)_{\text{APMBTSS}} \quad (6.13)$$

which can be expressed in terms of the protonation constants:

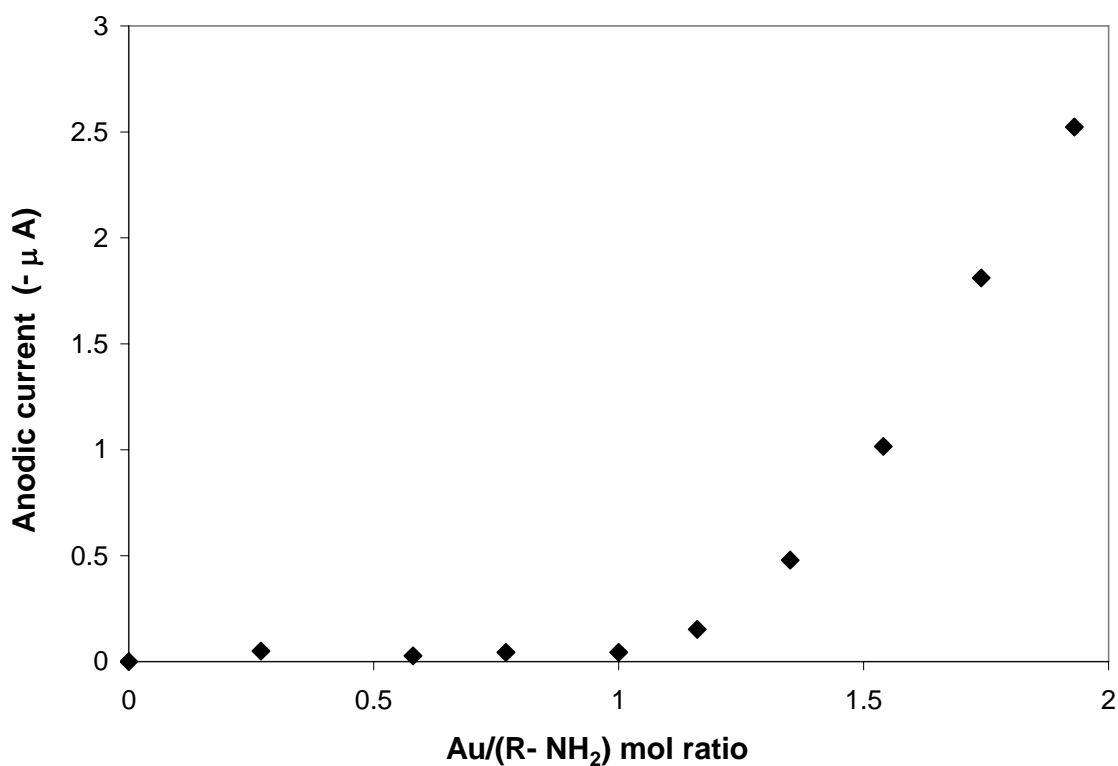


Figure 6.11. Anodic current generated during the oxidative (positive-going) scan of cyclic voltammetry experiments for $\text{AuCl}_4^-/\text{DN}$ solutions with $\text{Au}^{3+}/\text{R-NH}_2=0.1.93$. Each data point was obtained after 90 min of reaction of a fixed amount of nanocage containing 42 μM of primary amine (as determined by the ninhydrin test^{25,26} described in Chapter 2) and the proper amount of Au^{3+} . The reaction was carried out in methanol/water (4.4 % H_2O) at 500 rpm and $\text{pH}=7.4$. Scan rate: 0.1 V/s. Reference electrode: Ag/AgCl. Supporting electrolyte: 0.11 M NaCl.

$$\frac{(K_H)_{DN}}{(K_H)_{APMBTSS}} \approx \frac{(K_f^*)_{APMBTSS}}{(K_f^*)_{DN}} \frac{[H^+]_{APMBTSS}}{[H^+]_{DN}} \quad (6.14)$$

In deriving the equation, the simplification was made that $(1 + K_H[H^+]) \approx K_H[H^+]$ which applies to the pH range considered. Eq. (6.14) reveals that the constraining of propylamine to the nanocage interior, reduces its protonation constant by five orders of magnitude (see Table 6.4); as a result, binding of gold to DN occurs at a significantly lower bulk pH. It should be noted that an overall of ~ 10 propylamine groups are closely packed inside DN.²⁵ Thus, the remarkable drop in K_H suggests that protonation of the amine groups is very unfavorable as it would dramatically increases the energy of the system, consequence of the intense charge repulsion. Electrostatic-induced pK_a shifts arising from similar mechanisms have been observed in polyelectrolytes⁵⁶⁻⁵⁸ and biopolymers.⁵⁹⁻⁶²

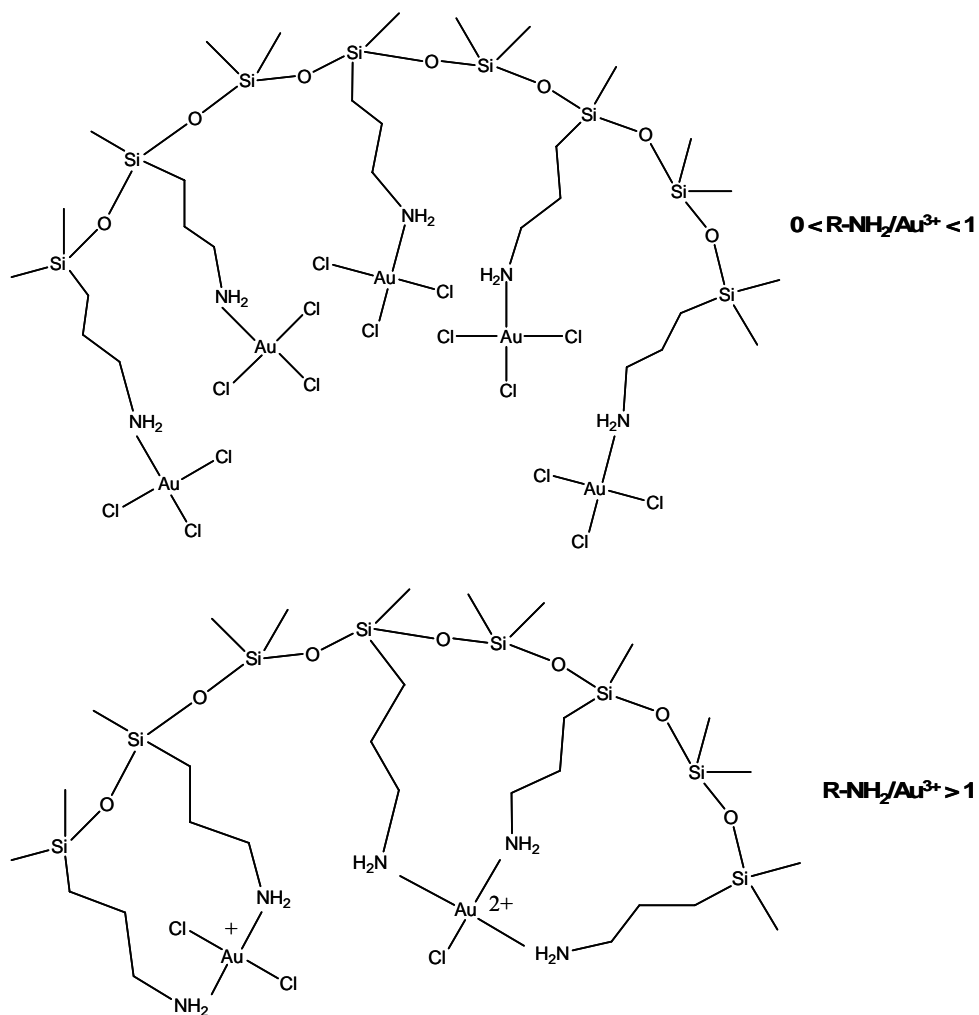
For samples with $R-NH_2/Au^{3+}=1$, the minimum pH necessary to have complete binding of Au^{3+} inside DN appears to shift to higher values, as the total concentration of gold decreases. At 430 μM , complete binding occurs at $pH=3.5$ (Figure 6.6); for 72 μM solutions, it occurs at $pH \sim 4.3$ (Figure 6.10), whereas for 42 μM solutions, the pH lies between 4.6 and 7.1 (Figure 6.7). At present, we don't have a satisfactory explanation for this observation.

It is worth noting that DN forms a complex with $AuCl_4^-$ even under excess of chloride, which tends to favor the unbound state (see Figure 6.6). Figure 6.11 shows the Faradaic current measured in a set of cyclic voltammetry experiments for solutions of 42 μM of amine inside DN and increasing amounts of Au^{3+} (0.11 M NaCl). Regardless of the presence in solution of a 2600-fold excess of chloride, a $\sim 1:1$ binding stoichiometry was observed. The result indicates that only chemically bound gold is present inside the nanocage; no physically trapped gold exists at

its interior. This feature makes the nanocage very attractive as a nanoreactor in the preparation of gold (and other metals) clusters, where fine control of the number of atoms

Scheme 6.2.

Binding of Au^{3+} inside DN as the amine/gold ratio increases.



trapped inside is a requirement. It was observed that in general, the amine/gold ratio in solution determines the binding stoichiometry of the Au^{3+} -DN complexes. When $\text{R-NH}_2/\text{Au}^{3+} = 1$, a 1:1 complex forms. As the ratio increases, so does the number of Au-N bonds up to an overall ~ 2.5 (Figures 6.8 and 6.9), pointing out to the role of DN as a chelating ligand. Scheme 6.2 illustrates this situation. The packing density inside DN for a 1:1 complex is higher than that for complexes with higher amine/gold ratio; this is possible in part due to the neutrality of the complex formed so that no electrostatic repulsions exist. As the amine/gold ratio increases, charged species form; minimum Coulombic repulsion would require the complexes to be as far apart as possible. Besides, the presence of charged species within the cage would in principle alter the $\text{p}K_a$ of the free amine groups. Other factors controlling the binding of gold inside DN are the relative proximity of the amine groups and the orientation of the d-orbitals participating in the formation of the complex; in the end, the formed structures will be the result of the interplay among all these variables. Importantly, the similarities in the Fourier transformed EXAFS in Figures 6A and 9A, suggest minor changes on the local environment around Au^{3+} upon complexation to DN.⁶³⁻⁶⁵ This observation along with the multiple binding characteristics of the nanocage already discussed, suggest that the interior propylamine groups are very flexible and can easily accommodate the spatial requirements imposed by gold, so that it retains its characteristic square planar geometry.

DN offers size selectivity properties combined with a set of densely packed amine groups, which can be exploited for catalytic purposes.²⁵ It also possesses a monolayer-thick wall that allows facile diffusion in and out the cage. The interior amines can be partially used as pro-functional groups to generate materials exhibiting hetero-functionalities, which may be used to enhance its catalytic properties. They could also be used to perform base catalysis in a neutral or

oven slightly acidic medium. Partially loaded Au^{3+} /DN can be used to carry out bi-functional catalysis by gold and amine; in this case, the amine/gold ratio can be manipulated to tune reactivity. This in turn will affect the $\text{p}K_a$ of the amine, which is expected to have a marked influence on reactivity.^{61,62,66-69} Other possible applications include using DN as a nano-reactor to synthesize mono- and bi-metallic nanoparticles, as well as metal oxide nanoclusters.

6.6 Conclusions

The combination of EXAFS, UV-VIS and cyclic voltammetry offers a consistent picture of the adsorption of tetrachloroaurate ions inside shell cross-linked siloxane nanocages (DN), and at the same time, reveals unknown properties of this novel material. Solutions of $\text{Au}(\text{OH})_x\text{Cl}_{4-x}$ in water or methanol exhibit a LMCT band at 227 nm whose intensity correlates with the Au-Cl coordination number, regardless of the total gold concentration. In methanol Au^{3+} diffuses inside DN forming gold-amine complexes of a stoichiometry that depends on the total amine/gold ratio in solution. If amine/gold ≤ 1 , only 1:1 complexes form. If amine is present in excess over gold, DN acts as a chelating ligand forming multiple Au-N bonds per gold. Confining propylamine groups inside DN (2nm), induces a drop of five orders of magnitude on their protonation constant. As a result, DN is capable of binding Au^{3+} at a pH five units lower than an equivalent amine in solution (e.g. APMBTSS). Au^{3+} binding to DN is very favorable even under excess of chloride (2600-fold); thus, when amine/gold=1, a 1:1 complex forms. With or without excess chloride, the maximum amount of Au^{3+} adsorbed by DN is it that generates a 1:1 complex. All the gold inside the nanocage is chemically bound to propylamine; no physically trapped gold was observed. Propylamine groups tethered within DN are very flexible; they re-

accommodate to changing external conditions and other restrictions imposed the relative orientation of the accepting orbitals of Au^{3+} .

CHAPTER 7

SUMMARY, CONCLUSIONS AND RECOMMENDATIONS FOR FUTURE WORK

7.1 Summary and conclusions

The combination of *in-situ* XANES, EXAFS and FTIR offers an effective way to probe Au/TiO₂ catalyst under different conditions, providing insight into the structure and the reaction mechanism. These techniques were jointly used with H₂ pulses and catalytic activity data to construct a relationship between structure and activity. It was determined that:

- Au³⁺ in an as-prepared catalyst, presumably as AuO_x(OH)_{4-2x}⁻ species on microrutile, is inactive for the oxidation of CO at sub-ambient temperatures.
- Catalytic activity increases with the fraction of metallic gold in the catalyst up to about 80% reduction. Above that level, a slight reduction in activity takes place, apparently caused by morphological changes of the gold nanoparticles and deactivation by carbonates.
- Controlled reduction of Au³⁺ with H₂ pulses at room temperature promotes the formation of a fairly narrowly distributed population of gold nanoparticles in the range 1.5-2nm.
- Two well differenced stages are involved in the formation of the nanoparticles: (1) an induction period where nuclei are formed and (2) growth where H₂ consumption is significant.
- Activity is also developed if an *as-prepared* catalyst is exposed to 10% CO at -60 °C or a reaction mixture containing 1%CO and 2.5% O₂ at -33 °C. In this case two IR bands corresponding to CO adsorbed on gold and CO₂ adsorbed on the support, are readily detected.

From these observations, it can be concluded that cationic gold is inactive for the oxidation of CO at low temperature and that an active catalyst requires zero-valent gold.

The same *in-situ* techniques were combined with isotopic labeling to study the rates of formation and disappearance of species on the surface of an active catalyst, under different conditions. It was determined that:

- CO is adsorbed on the step sites of the gold nanoparticles.
- CO adsorbed on the nanoparticles reacts with O₂ at the same rate as the production of CO₂ under steady-state conditions.
- About 18% of the atoms at the surface of nanoparticles participated in the adsorption of CO. Only 60% of these sites are capable of activating CO.
- Activation of CO at the surface of a nanoparticle involves transfer of electrons from gold to CO.
- Either O₂ is not adsorbed on gold or the amount adsorbed is below the detection limits of the techniques used.
- The oxidation of CO occurs via a hydroxycarbonyl Au^δ-COOH intermediate that is very sensitive to oxygen; it can be detected only under oxygen-free conditions.
- As expected for a true reaction intermediate, the disappearance of the hydroxycarbonyl correlates with the formation of CO₂.
- The hydroxycarbonyl undergoes isotopic exchange with ¹⁸O; the products resulting from its decomposition include C¹⁶O¹⁸O and C¹⁸O₂.

From these observations, it is concluded that metallic gold is a necessary component of an active catalyst, because the activation of CO takes place at the surface of the supported nanoparticles. Only 60% of the adsorbed CO is catalytically active. It is likely that the activated CO migrates to

the active sites, where hydroxide groups attached to gold (of an unknown oxidation state) react with it forming a hydroxycarbonyl intermediate that is very sensitive to oxygen. In the presence of oxygen, the hydroxycarbonyl decomposes generating CO₂.

The binding of cationic gold to the amines inside the siloxane nanocages was used as a “handle” to study the response of the system to the external pH, because protonation and binding to gold are mutually exclusive reactions. Once an amine is protonated, its nucleophilic character is lost and no binding to gold takes place. Knowing the conditions where protonation does not occur is crucial to the further applications of this novel material in catalysis and synthesis of advanced materials. UV-VIS combined with XANES, EXAFS and cyclic voltammetry was used to carry out this investigation. It was determined that:

- The intensity of the ligand-to-metal charge transfer band at 227 nm in HAuCl₄ correlates with the Au-Cl coordination number.
- The amines inside a nanocage had a far smaller affinity for protons than a comparable amine in solution. Their protonation constant was five orders of magnitude smaller than that of the same isolated amine.
- The high degree of confinement of the amine groups inside the nanocage is presumably the cause of this remarkable difference. As the number of protonated amines increases, so does the electrostatic repulsion (which is a long range force). Since protonation makes the system unstable, it is an unfavorable process.
- There is another effect that overlaps with the previous one. A high degree of confinement also enhances the local concentration of ions. In solution, it is very common to have a OH⁻ counter-ion to H⁺. If H⁺ diffuses inside the cage and is trapped by an amine, the OH⁻ counter

ion will be in an effective concentration enough to bring the local pH to a value close to pH=14. At this pH, no further protonation of the amines will occur.

- All the gold inside the nanocages was chemically bound to the internal amine groups. This is rationalized by recognizing that the diffusion into the nanocage is entropically unfavored. However, the driving force causing the diffusion is the formation of the Au-N coordination bond, which is highly exothermic. Thus, if in a solution with excess gold the possibility of forming Au-N bonds doesn't exist because, for example, all the internal amines have already been taken, no retention of gold inside the cage will occur.
- When the internal amines are in excess with respect to the gold in the cage, multiple Au-N bonds per gold are formed. This implies that the amines have to accommodate to the spatial restrictions imposed by the orbitals of Au^{3+} in its square planar configuration. This indicates that the internal amines are highly flexible.

From these observations, it is concluded that nanoconfinement is an effective way of generating materials with unusual chemical properties. In the case of the nanocage, the decreased Brønsted basicity could be exploited, for example, to perform catalysis under neutral or slightly acidic conditions.

7.2 Recommendations for future work

Studies on the oxidation of CO at low temperature with supported gold suggest that the fraction of active sites where reaction between an activated form of CO (or an intermediated formed with activated CO) and oxygen occurs, is very small. This limits the number of techniques suitable as a direct probe for such sites. Several attempts have been made to

selectively titrate these sites with a “poison” such as chloride. Recent data exist which support a model of the active site being an ensemble of metallic and a cationic form of gold located at the perimeter with the support.¹ Additional studies appear desirable for the construction of a more comprehensive model of the active sites.

A still poorly understood aspect of the oxidation of CO at low temperature is the nature of the active form of oxygen and the locus of its activation. Activation of oxygen is very important for a complete picture of the mechanism of reaction. It also will be relevant to more complicated oxidation reactions using gold catalyst. Techniques such as Raman and EPR spectroscopy are expected to be useful in the study of this process.

Using samples with gold nanoparticles of different sizes might be helpful to clarify whether small nano-particles are required because of the higher density of active sites associated with them. Since CO oxidation is a structure sensitive reaction, it would be an ideal candidate to probe this hypothesis. However, a method capable of discerning the active sites from the adsorption sites must be utilized. Selective poisoning is a good candidate, but it must be carried out under carefully controlled conditions so that the information obtained is unambiguous. Caution must be also exercised to compare samples that only differ in the size of the gold particles.

Siloxane nanocages appear to offer several opportunities that are worthwhile exploring. First, they exhibit a monolayer-thick wall that allows facile diffusion in and out the cage. They also display size selectivity properties combined with amine functionalities densely packed into a 4 nm³ volume, which can be explored for catalytic purposes. Due to the high confinement, the local concentration of amines with respect to a substrate inside the cage is markedly high. This will favor reactions which kinetics is dependent on the concentration of the amines. The local

confinement of the amines could also be exploited to perform concerted catalysis requiring attack by more than one basic group. Since there is no requirement for a two-body collision in order for the reaction to take place, a rate enhancement could be expected; Aldol condensations are an example of such reactions. The interior amines can be partially used as pro-functional groups to generate materials exhibiting hetero-functionalities, which may be used to enhance its catalytic properties. They could also be used to perform base catalysis in a neutral or even slightly acidic medium. Partially loaded Au^{3+}/DN could be used to carry out bi-functional catalysis by gold and amine; in this case, the amine/gold ratio can be manipulated to tune reactivity. This in turn will affect the $\text{p}K_a$ of the amine, which is expected to have a marked influence on reactivity. Other possible applications include using DN as a nano-reactor to synthesize mono- and bi-metallic nanoparticles, as well as metal oxide nanoclusters.

REFERENCES

Chapter 1

- (1) Harura, M.; Yamada, N.; Kobayashi, T.; Iijima, S. *J. Catal.* **1989**, 115, 301-309.
- (2) Stangland, E. E.; Stavens, K. B.; Delgass, W. N. *J. Catal.* **2000**, 191, 332.
- (3) Qi, C.; Okumura, M.; Akita, T.; Haruta, M. *Appl. Catal. A* **2004**, 263, 19.
- (4) Hayashi, T.; Tanaka, K.; Haruta, M. *J. Catal.* **1998**, 178, 566.
- (5) Nkosi, B.; Adams, M. D.; Coville, N. J.; Hutchings, G. J. *J. Catal.* **1991**, 128, 378.
- (6) Corma, A.; Serna, P. *Science* **2006**, 313, 332.
- (7) Milone, C.; Ingoglia, R.; Schipillitt, L.; Crisafulli, C.; Neri, G.; Galvagno, S. *J. Catal.* **2005**, 236, 80.
- (8) Parvulescu, V. I.; Parvulescu, V.; Endruschat, U.; Filoti, G.; Wagner, F. E.; Kubel, C.; Richards, R. *Chem. Eur. J.* **2006**, 12, 2343.
- (9) Milone, C.; Ingoglia, R.; Tropeano, M. L.; Neri, G.; Galvagno, S. *Chem. Commun.* **2003**, 868.
- (10) Bethke, G. K.; Kung, H. H. *Appl. Catal. A* **2000**, 194, 43.
- (11) Andreeva, I.; Tabakova, T.; Andreev, A. *J. Catal.* **1996**, 158, 354.
- (12) Fu, Q.; Saltsburg, H.; Flytzani-Stephanopoulos, M. *Science* **2003**, 301, 935.
- (13) Prati, L.; Porta, F. *Appl. Catal. A* **2005**, 291, 199.
- (14) Comotti, M.; Della Pina, C.; Falletta, E.; Rossi, M. *J. Catal.* **2006**, 244, 122.
- (15) Enache, D. I.; Edwards, J. K.; Landon, P.; Solsona-Espriu, B.; Carley, A. F.; Herzing, A. A.; Watanabe, M.; Kiely, C. J.; Knight, D. W.; Hutchings, G. J. *Science* **2006**, 311 362.

- (16) Hughes, M. D.; Xu, Y.-J.; Jenkins, P.; McMorn, P. I.; Landon, P.; Enache, D. I.; Carley, A. F.; Attard, G. A.; Hutchings, G. J.; King, F.; Stitt, E. H.; Johnston, P.; Griffin, K.; Kiely, C. J. *Nature* **2005**, 437, 1132.
- (17) Ueda, A.; Oshima, T.; Haruta, M. *Appl. Catal. B* **1997**, 12, 81.
- (18) Kung, M. C.; Davis, R. J.; Kung, H. H. *J. Phys. Chem. C* **2007**, 111, 11767-11775.
- (19) Davis, R. J. *Science* **2003**, 301, 926.
- (20) Costello, C. K.; Yang, J. H.; Law, H. Y.; Wang, Y.; Lin, J.-N.; Marks, L. D.; Kung, M. C.; Kung, H. H. *Appl. Catal., A* **2003**, 243, 15.
- (21) Costello, C. K.; Kung, M. C.; Oh, H.-S.; Wang, Y.; Kung, H. H. *Appl. Catal., A* **2002**, 232, 159.
- (22) Bond, G. C.; Thompson, D. T. *Gold Bull.* **2000**, 33, 41.
- (23) Yoon, B.; Haekkinen, H.; Landman, U.; Woerz, A. S.; Antonietti, J.-M.; Abbet, S.; Judai, K.; Heiz, U. *Science* **2005**, 307, 403.
- (24) Suh, Y.-W.; Kung, M. C.; Wang, Y.; Kung, H. H. *J. Am. Chem. Soc.* **2006**, 128, 2776-2777.
- (25) Zeidan, R. K.; Dufaud, V.; Davis, M. E. *J. Catal.* **2006**, 239, 299-306.
- (26) Zeidan, R. K.; Hwang, S.-J.; Davis, M. E. *Angew. Chem. Int. Ed.* **2006**, 45, 6332-6335.
- (27) Zeidan, R. K.; Davis, M. E. *J. Catal.* **2007**, 247, 379-382.
- (28) Machajewski, T. D.; Wong, C.-H. *Angew. Chem. Int. Ed.* **2000**, 39, 1352-1374.
- (29) Karlstrom, A.; Zhong, G.; Rader, C.; Larsen, N. A.; Heine, A.; Fuller, R.; List, B.; Tanaka, F.; Wilson, I. A.; Barbas III, C. F.; Lerner, R. A. *Proc. Natl. Acad. Sci. USA* **2000**, 97, 3878-3883.
- (30) Bass, J. D.; Solovyov, A.; Pascall, A. J.; Katz, A. *J. Am. Chem. Soc.* **2006**, 128, 3737-3747.
- (31) Defreese, J. L.; Hwang, S.-J.; Parra-Vasquez, A. N. G.; Katz, A. *J. Am. Chem. Soc.* **2006**, 128, 5687-5694.
- (32) Frey, P. A.; Hegeman, A. D., *Enzymatic Reaction Mechanisms*, Oxford University Press, New York, 2007, pp. 69-128.
- (33) Goodsell, D. S., *Bionanotechnology: Lessons from Nature*, Wiley-Liss, Hoboken, 2004, pp. 135-226.

- (34) Fersht, A., *Structure and Mechanism in Protein Science: A Guide to Enzyme Catalysis and Protein Folding*, W. H. Freeman and Company, New York, 1999.
- (35) Haruta, M. *Stud. Surf. Sci. Catal.* **2003**, 145, 31.
- (36) Meyer, R.; Lemire, C.; Shaikhutdinov; Freund, H. *J. Gold Bull.* **2004**, 37, 72.
- (37) Hutchings, G. *Gold Bull.* **1996**, 29, 123.
- (38) Haruta, M.; Tsubota, S.; Kobayashi, T.; Kageyama, H.; Genet, M.; Delmon, B. *J. Catal.* **1993**, 144, 175.
- (39) Zanella, R.; Giorgio, S.; Shin, C.-H.; Henry, C. R.; Louis, C. *J. Catal.* **2004**, 222, 357.
- (40) Grisel, R. J. H.; Weststrate, K.-J.; Gluhoi, A.; Nieuwenhuys, B. E. *Gold Bull.* **2002**, 35, 39.
- (41) Guczi, L.; Horvath, D.; Pastel, Z.; Toth, L.; Horvath, Z. E.; Karacs, A. *J. Phys. Chem. B.* **2000**, 104, 3183.
- (42) Choudhary, T. V.; Sivadinarayana, C.; Chusuei, C. C.; Datye, A. K.; Fackler Jr., J. P.; Goodman, D. W. *J. Catal.* **2002**, 207, 247.
- (43) Mavrikakis, M.; Stoltze, P.; Nørskov, J. K. *Catal. Lett.* **2000**, 64, 101-106.
- (44) Xu, Y.; Mavrikakis, M. *J. Phys. Chem. B* **2003**, 107, 9298-9307.
- (45) Finch, R. M.; Hodge, N. A.; Hutchings, G. H.; Meagher, A.; Pankhurst, Q.A.; Siddiqui, M. R. H.; Wagner, F. E.; Whyman, R. *Phys. Chem. Chem. Phys.* **1999**, 1, 485.
- (46) Hodge, N. A.; Kiely, C. J.; Whyman, R.; Siddiqui, M. R. H.; Hutchings, G. J.; Pankhurst, Q. A.; Wagner, F. E.; Rajaram, R. R.; Golunski, S. E. *Catal. Today* **2002**, 72, 133.
- (47) Park, D.; Lee, J. S. *J. Catal.* **1999**, 186, 1.
- (48) Oh, H.-S.; Yang, J. H.; Costello, C. K.; Wang, Y. M.; Bare, S. R.; Kung, H. H.; Kung, M. C. *J. Catal.* **2002**, 210, 375-386.
- (49) Liu, H.; Kozlov, A. I.; Kozlova, A. P.; Shido, T.; Iwasawa, Y. *Phys. Chem. Chem. Phys.*, **1999**, 1, 2851-2860.
- (50) Liu, H.; Kozlov, A. I.; Kozlova, A. P.; Shido, T.; Asakura, K.; Iwasawa, Y. *J. Catal.* **1999**, 185, 252-264.
- (51) Olea, M.; Kunitake, M.; Shido, T.; Iwasawa, Y. *Phys. Chem. Chem. Phys.*, **2001**, 3, 627-631.

- (52) Boccuzzi, F.; Chiorino, A.; Manzoli, M.; Lu, P.; Akita, T.; Ichikawa, S.; Haruta, M. *J. Catal.* **2001**, 202, 256.
- (53) Haruta, M. *Cattech* **2002**, 6, 102.
- (54) Stigter, D.; Alonso, D. O. V.; Dill, K. A. *Proc. Natl. Acad. Sci. USA* **1991**, 88, 4176-4180.
- (55) Mehler, E. L.; Fuxreiter, M.; Simon, I.; Garcia-Moreno, B. *Proteins: Struc. Funct. Gen.* **2002**, 48, 283-292.
- (56) Juffer, A. H.; Vogel, H. J. *Proteins: Struc. Funct. Gen.* **2000**, 41, 554-567.
- (57) Urry, D. W.; Peng, S. Q.; Parker, T. M. *Biopolymers*, **1992**, 32, 373-379.
- (58) Matthew, J. B.; Gurd, F. R. N. *Meth. Enzym.* **1986**, 130, 413-436.
- (59) Matthew, J. B.; Gurd, F. R. N. *Meth. Enzym.* **1986**, 130, 437-453.
- (60) Sharp, K. A.; Hong B. *Annu. Rev. Biophys. Biophys. Chem.* **1990**, 19, 301-332.
- (61) Urry, D. W.; Peng, S. Q.; Parker, T. M.; Gowda, D. C.; Harris, R. D. *Angew. Chem. Int. Ed. Engl.* **1993**, 32, 1440-1442.
- (62) Urry, D. W.; Gowda, D. C.; Peng, S. Q.; Parker, T. M.; Harris, R. D. *J. Am. Chem. Soc.* **1992**, 114, 8716-8717.
- (63) Urry, D. W. *Prog. Biophys. Molec. Biol.* **1992**, 57, 23-57.
- (64) Inoue, M. Yamada, H.; Yasukochi, T.; Kuroki, R.; Miki, T.; Horiuchi, T.; Imoto, T. *Biochemistry* **1992**, 31, 5545-5553.
- (65) Langsetmo, K.; Fuchs, J. A.; Woodward, C.; Sharp, K. A. *Biochemistry* **1991**, 7609-7614.
- (66) Langsetmo, K.; Fuchs, J. A.; Woodward, C. *Biochemistry* **1991**, 30, 7603-7609.
- (67) Blokzijl, W.; Engberts, J. B. F. N. *Angew. Chem. Int. Ed. Engl.* 1993, 32, 1545-1579.
- (68) Urry, D. W.; Peng, S. Q.; Hayes, L.; Jacgard, J.; Harris, R. D. *Biopolymers* **1990**, 30, 215-218.
- (69) McGrath, M. E.; Vásquez, J. R.; Craik, C. S.; Yang, A. S.; Honig, B.; Fletterick, R. J. *Biochemistry* **1992**, 31, 3059-3064.
- (70) Katchalsky, A. *J. Polym. Sci.* **1951**, 7, 393-412.

- (71) Harris, F.; Rice, S. A. *J. Phys. Chem.* **1954**, 58, 725-732.
- (72) Ottaviani, M. F.; Bossmann, S.; Turro, N. J.; Tomalia, D. A. *J. Am. Chem. Soc.* **1994**, 116, 661-671.
- (73) Ottaviani, M. F.; Montalti, F.; Turro, N. J.; Tomalia, D. A. *J. Phys. Chem. B* 1997, 101, 158-166.
- (74) Niu, Y.; Sun, L.; Crooks, R. M. *Macromolecules* **2003**, 36, 5725-5731.
- (75) Scott, R. W. J.; Wilson, O. M.; Crooks, R. M. *J. Phys. Chem. B* 2005, 109, 692-704.

Chapter 2

- (1) Yang, J. H., PhD Dissertation, Northwestern University (USA), June 2006.
- (2) Zetasizer Nano Series User Manual, Malvern Instruments Ltd., Worcestershire, 2003.
- (3) Levine, I. N. *Physical Chemistry*, 2nd Ed., McGraw Hill, New York, 1983, pp. 464-473.
- (4) Burchard, W. in *Laser Light Scattering in Biochemistry* (Eds.: Hardin, S. E.; Sattelle, D. B.; Bloomfield, V. A.), Royal Society of Chemistry, Cambridge, **1992**, pp. 3-22.
- (5) Chu, B. *Laser Light Scattering: Basic Principles and Practice*, 2nd Ed., Dover Publications, Mineola, 2007, pp. 93-136, 243-282.
- (6) Berne, B. J.; Pecora, R. *Dynamic Light Scattering : With Applications to Chemistry, Biology, and Physics*, Dover Publications, Mineola, 2000, pp. 10-23.
- (7) Sarin, V. K.; Kent, S. B. H.; Tam, J. P.; Merrifield, R. B. *Analytical Biochem.* **1981**, 117, 147-157.
- (8) Marken, F.; Neudeck, A.; Bond, A. M. in: *Electroanalytical Methods: Guide to Experiments and Applications* (Ed.: Scholz, F.), Springer, Berlin, 2002, pp. 51-97.
- (9) Kissinger, P. T.; Heineman, W. R. *J. Chem. Ed.* 1983, 60, 702-706.
- (10) Mabbott, G. A. *J. Chem. Ed.* 1983, 60, 697-702.
- (11) Evans, D. H.; O'Connell, K. M.; Petersen, R. A.; Kelly, M. J. *J. Chem. Ed.* 1983, 60, 290-293.
- (12) Maloy, J. T. *J. Chem. Ed.* 1983, 60, 285-289.

Chapter 3

- (1) Haruta, M.; Yamada, N.; Kobayashi, T.; Iijima, S. *J. Catal.* **1989**, 115, 301.
- (2) Bond, G. C.; Thompson, D. T. *Catal. Rev.. Sci. Eng.* **1999**, 41, 319.
- (3) Bond, G. C.; Thompson, D. T. *Gold Bull.* **2000**, 33, 41.
- (4) Boccuzzi, F.; Chiorino, A. *J. Phys. Chem. B* **2000**, 104, 5414.
- (5) Grunwald, J.-D.; Keener, C.; Wogerbauer, C.; Baiker, A. *J. Catal.* **1999**, 181, 223.
- (6) Boccuzzi, F.; Chiorino, A.; Manzoli, M.; Lu, P.; Akita, T.; Ichikawa, S.; Haruta, M. *J. Catal.* **2001**, 202, 256.
- (7) Date, M.; Ichihashi, Y.; Yamashita, T.; Chiorino, A.; Boccuzzi, F.; Haruta, M. *Catal. Today* **2002**, 72, 89.
- (8) Wolf, A.; Schüth, F. *Appl. Catal. A: General* **2002**, 226, 1.
- (9) Park, E. D.; Lee, J. S. *J. Catal.* **1999**, 186, 1.
- (10) Zanella, R.; Giorgio, S.; Shin, C.-H.; Henry, C. R.; Louis, C. *J. Catal.* **2004**, 222, 357.
- (11) Valden, M.; Lai, X.; Goodman, D. W. *Science* **1998**, 281, 1647.
- (12) Chen, M. S.; Goodman, D. W. *Science* **2004**, 306, 5694.
- (13) Fierro-Gonzalez, J. C.; Gates, B. C. *J. Phys. Chem B* **2004**, 108, 16999.
- (14) Guzman, J.; Kuba, S.; Fierro-Gonzalez, J. C.; Gates, B. C. *Catal. Lett.* **2004**, 95, 77.
- (15) Costello, C. K.; Kung, M. C.; Oh, H.-S.; Wang, Y.; Kung, H. H. *Appl. Catal. A: General* **2002**, 232, 159.
- (16) Daté, M.; Okumura, M.; Tsubota, S.; Haruta, M. *Angew. Chem. Int. Ed.* **2004**, 43, 2129.
- (17) Costello, C. K.; Yang, J. H.; Law, H.-Y.; Wang, Y.; Lin, J.-N.; Marks, L. D.; Kung, M. C.; Kung, H. H. *Appl. Catal. A: General* **2003**, 243, 15.
- (18) Tsubota, S.; Cunningham, D. A. H.; Bando, Y.; Haruta, M. *Stud. Surf. Sci. Catal.* **1995**, 91, 227.
- (19) Costello, C. K.; Guzman, J.; Yang, J. H.; Wang, Y. M.; Kung, M. C.; Gates, B. C.; Kung, H. H. *J. Phys. Chem. B* **2004**, 108, 12529.

- (20) Schumacher, B.; Plzak, V.; Kinne, M.; Behm, R. J. *Catal. Lett.* **2003**, 89, 109.
- (21) Kung, M. C.; Costello, C. K.; Kung, H. H. *Catalysis* **2004**, 17, 152.
- (22) Frenkel, A. I.; Hils, C. W.; Nuzzo, R. G. *J. Phys. Chem. B* **2001**, 105, 12689.
- (23) Yang, J. H.; Henao, J. D.; Costello, C. K.; Kung, M. C.; Kung, H. H.; Miller, J. T.; Kropf, A. J.; Regalbuto, J. R.; Bore, M. T.; Pham, H. N.; Datye, A. K.; Laeger, J. D.; Kharas, K. *Appl. Catal. A* **2005**, 291, 73.
- (24) Schwartz, V.; Mullins, D. R.; Yan, W.; Chen, B.; Dai, S.; Overbury, S. H. *J. Phys. Chem. B* **2004**, 108, 15782.
- (25) Boccuzzi, F.; Tsubota, S.; Haruta, M. *J. Electron Spectrosc. Relat. Phenom.* **1993**, 64/65, 241.
- (26) McIntosh, D.; Ozin, G. A. *Inorg. Chem.* **1977**, 16, 51.
- (27) Boccuzzi, F.; Chiorino, A.; Manzoli, M. *Surf. Sci.* **2002**, 502-503, 513.

Chapter 4

- (1) Haruta, M.; Yamada, N.; Kobayashi, T.; Iijima, S. *J. Catal.* 1989, 115, 301.
- (2) Boccuzzi, F.; Chiorino, A. *J. Phys. Chem. B* 2000, 104, 5414.
- (3) Boccuzzi, F.; Chiorino, A.; Manzoli, M. *Surf. Sci.* 2002, 502-503, 513.
- (4) Haruta, M. *CATTECH* 2002, 6, 102.
- (5) Kung, H. H.; Kung, M. C.; Costello, C. K. *J. Catal.* 2003, 216, 425.
- (6) Daté, M.; Okumura, M.; Tsubota, S.; Haruta, M. *Angew. Chem., Int. Ed.* 2004, 43, 2129.
- (7) Costello, C. K.; Yang, J. H.; Law, H. Y.; Wang, Y.; Lin, J.-N.; Marks, L. D.; Kung, M. C.; Kung, H. H. *Appl. Catal., A* 2003, 243, 15.
- (8) Costello, C. K.; Kung, M. C.; Oh, H.-S.; Wang, Y.; Kung, H. H. *Appl. Catal., A* 2002, 232, 159.
- (9) Sanchez-Castillo, M. A.; Couto, C.; Kim, W. B.; Dumesic, J. A. *Angew. Chem., Int. Ed.* 2004, 43, 1140.

- (10) Haruta, M. *Catal. Today* 1997, 36, 153.
- (11) Oh, H.-S.; Yang, J. H.; Costello, C. K.; Wang, Y.; Bare, S. R.; Kung, H. H.; Kung, M. C. *J. Catal.* 2002, 210, 375.
- (12) Valden, M.; Lai, X.; Goodman, D. W. *Science* 1998, 281, 1647.
- (13) Chen, M. S.; Goodman, D. W. *Science* 2004, 306, 252.
- (14) Mavrikakis, M.; Stoltze, P.; Nørskov, J. K. *Catal. Lett.* 2000, 64, 101.
- (15) Xu, Y.; Mavrikakis, M. *J. Phys. Chem. B* 2003, 107, 9298.
- (16) Bond, G. C.; Thompson, D. T. *Gold Bull.* 2000, 33, 41.
- (17) Fu, Q.; Saltsburg, H.; Flytzani-Stephanopoulos, M. *Science* 2003, 301, 935.
- (18) Davis, R. J. *Science* 2003, 301, 926.
- (19) Guzman, J.; Gates, B. C. *J. Am. Chem. Soc.* 2004, 126, 2672.
- (20) Yoon, B.; Haekkinen, H.; Landman, U.; Woerz, A. S.; Antonietti, J.-M.; Abbet, S.; Judai, K.; Heiz, U. *Science* 2005, 307, 403.
- (21) Yang, J. H.; Henao, J. D.; Raphulu, M. C.; Wang, Y.-M.; Caputo, T.; Groszek, A. J.; Kung, M. C.; Scurrrell, M. S.; Miller, J. T.; Kung, H. H. *J. Phys. Chem. B* 2005, 109, 10319.
- (22) Shiga, A.; Haruta, M. *Appl. Catal., A* 2005, 291, 6.
- (23) Remediakis, I. N.; Lopez, N.; Nørskov, J. K. *Appl. Catal., A* 2005, 291, 13.
- (24) Molina, L. M.; Hammer, B. *Appl. Catal., A* 2005, 291, 21.
- (25) Okumura, M.; Kitagawa, Y.; Haruta, M.; Yamaguchi, K. *Appl. Catal., A* 2005, 291, 37.
- (26) Liu, H.; Kozlov, A. I.; Kozlova, A. P.; Shido, T.; Iwasawa, Y. *Phys. Chem. Chem. Phys.* 1999, 1, 2851.
- (27) Olea, M.; Kunitake, M.; Shido, T.; Iwasawa, Y. *Phys. Chem. Chem. Phys.* 2001, 3, 627.
- (28) Olea, M.; Iwasawa, Y. *Appl. Catal., A* 2004, 275, 35.
- (29) Carrettin, S.; Concepcio'n, P.; Corma, A.; Lo'pez Nieto, J. M.; Puentes, V. F. *Angew. Chem., Int. Ed.* 2004, 43, 2538.
- (30) Guzman, J.; Corma, A. *Chem. Commun.* 2005, 743.

- (31) Guzman, J.; Carrettin, S.; Corma, A. *J. Am. Chem. Soc.* 2005, 127, 3286.
- (32) Liu, H.; Kozlov, A. I.; Kozlova, A. P.; Shido, T.; Asakura, K.; Iwasawa, Y. *J. Catal.* 1999, 185, 252.
- (33) Shubina, T. E.; Hartnig, C.; Koper, M. T. M. *Phys. Chem. Chem. Phys.* 2004, 6, 4215.
- (34) Boccuzzi, F.; Chiorino, A.; Tsubota, S.; Haruta, M. *J. Phys. Chem.* 1996, 100, 3625.
- (35) Grunwaldt, J.-D.; Maciejewski, M.; Becker, O. S.; Fabrizioli, P.; Baiker, A. *J. Catal.* 1999, 186, 458.
- (36) Boccuzzi, F.; Chiorino, A.; Manzoli, M.; Lu, P.; Akita, T.; Ichikawa, S.; Haruta, M. *J. Catal.* 2001, 202, 256.
- (37) Jia, J.; Kondo, J. N.; Domen, K.; Tamaru, K. *J. Phys. Chem. B* 2001, 105, 3017.
- (38) Boccuzzi, F.; Chiorino, A.; Manzoli, M. *Surf. Sci.* 2000, 454-456, 942.
- (39) Calla, J. T.; Davis, R. J. *J. Phys. Chem. B* 2005, 109, 2307.
- (40) Boccuzzi, F.; Tsubota, S.; Haruta, M. *J. Electron Spectrosc. Relat. Phenom.* 1993, 64/65, 241.
- (41) Lemire, C.; Meyer, R.; Shaikhutdinov, S. K.; Freund, H. J. *Surf. Sci.* 2004, 552, 27.

Chapter 5

- (1) Suh, Y-W.; Kung, M. C.; Wang, Y.; Kung, H. H. *J. Am. Chem. Soc.* **2006**, 128, 2776-2777.
- (2) Katz, A.; Davis, M. E. *Nature* **2000**, 403, 286-289.

Chapter 6

- (1) Goodsell, D. S., *Bionanotechnology: Lessons from Nature*, Wiley-Liss, Hoboken, 2004, pp. 135-226.
- (2) Vögtle, F., *Supramolecular Chemistry: an Introduction*, Wiley, Chichester, 1991, pp. 129-169.
- (3) Kung, H. H.; Kung, M. C. *Appl. Catal. A* **2003**, 246, 193-196.

- (4) Kung, H. H.; Kung, M. C. *Catal. Today* **2004**, 97, 219-224.
- (5) Sundaresan, V.; Abrol, R. *Protein Sci.* **2002**, 11, 1330-1339.
- (6) Fersht, A., *Structure and Mechanism in Protein Science: A Guide to Enzyme Catalysis and Protein Folding*, W. H. Freeman and Company, New York, 1999.
- (7) Kappler, M. H. *Prog. Bioorg. Chem.* **1973**, 2, 55-133.
- (8) Richards, F. M. *Ann. Rev. Biophys. Bioeng.* **1977**, 6, 151-176.
- (9) R. J. Farrauto and C. H. Bartholomew, *Fundamentals of Industrial Catalytic Processes*, Chapman & Hall, New York, 1997, pp. 341-666.
- (10) Bhatia, S. *Zeolite Catalysis: Principles and Applications*, CRC Press, Boca Raton, 1990, pp. 75-170.
- (11) Gates, B. C. *Chem. Rev.* **1995**, 95, 511-522.
- (12) Thomas, J. M.; Raja, R. *Chem. Comm.* **2001**, 675-687.
- (13) Corma, A.; Iborra, S. in *Fine Chemicals through Heterogeneous Catalysis* (Eds.: Sheldon, R. A.; van Bekkum, H), Wiley-VCH, Weinheim, pp. 309-326.
- (14) (a) Lane, G. S.; Modica, F. S.; Miller, J. T. *J. Catal.* **1991**, 129, 145-158. (b) Hong, S. B.; Mielczarski, E.; Davis, M. E. *J. Catal.* **1992**, 134, 349-358. (c) Mielczarski, E.; Hong, S. B.; Davis, R. J.; Davis, M. E. *J. Catal.* **1992**, 134, 359-369. (d) Besoukhanova, C.; Guidot, J.; Barthomeuf, D.; Breyse, M.; Bernard, J. R. *J. Chem. Soc. Faraday Trans.* **1981**, 77, 1595-1604. (e) Tauster, S. J.; Steger, J. J. *J. Catal.* 1990, 125, 387-389.
- (15) Hutchings, G. J. in *Surface Chemistry and Catalysis* (Eds.: Carley, A. F.; Davies, P. R.; Hutchings, G. J.; Spencer, M. S.), Kluwer Academic, New York, 2002, pp. 241-274.
- (16) (a) Scott, R. W. J.; Wilson, O. M.; Crooks, R. M. *J. Phys. Chem. B* **2005**, 109, 692-704. (b) Scott, R. W. J.; Datye, A. K.; Crooks, R. M. *J. Am. Chem. Soc.* **2003**, 125, 3708-3709. (c) Scott, R. W. J.; Wilson, O. M.; Oh, S.-K.; Kenik, E. A.; Crooks, R. M. *J. Am. Chem. Soc.* 2004, 126, 15583-15591.
- (17) (a) Chung, Y.-M.; Rhee, H.-K. *Catal. Lett.* 2003, 85, 159-164. (b) Lang, H.; May, R. A.; Iversen, B. L.; Chandler, B. D. *J. Am. Chem. Soc.* **2003**, 125, 14832-14836. (c) Esumi, K.; Suzuki, A.; Yamahira, A.; Torigoe, K. *Langmuir* **2000**, 16, 2604-2608.
- (18) (a) Kang, Y.; Taton, T. A. *Angew. Chem. Int. Ed.* **2005**, 44, 409-412. (b) Sanji, T.; Ogawa, Y.; Nakatsuka, Y.; Tanaka, M.; Sakurai, H. *Chem. Lett.* **2003**, 32, 980-981. (c) Liu, S.; Weaver, J. V. M.; Save, M.; Armes, S. P. *Langmuir* **2002**, 18, 8350-8357.

- (19) (a) Kralmer, M.; Pérignon, N.; Haag, R.; Marty, J.-D.; Thomann, R.; Lauth-de Viguerie, N.; Mingotaud, C. *Macromolecules* **2005**, 38, 8308-8315. (b) Grohn, F.; Bauer, B. J.; Akpalu, Y. A.; Jackson, C. L.; Amis, E. J. *Macromolecules* **2000**, 33, 6042-6050.
- (20) (a) Martino, A.; Yamanaka, S. A.; Kawola, J. S.; Loy, D. A. *Chem. Mater.* **1997**, 9, 423-429. (b) Zarur, A. J.; Ying, J. Y. *Nature*, **2000**, 403, 65-67.
- (21) Huang, B.; Tomalia, D. A. *J. Luminescence* **2005**, 111, 215-223.
- (22) Boyen, H.-G.; Kästle, G.; Zürn, K.; Herzog, T.; Weigl, F.; Ziemann, P.; Mayer, O.; Jerome, C.; Möller, M.; Spatz, J. P.; Garnier, M. G.; Oelhafen, P. *Adv. Funct. Mater.* **2003**, 13, 359-364.
- (23) (a) Huo, Q.; Liu, J.; Wang, L.-Q.; Jiang, Y.; Lambert, T. N.; Fang, E.; *J. Am. Chem. Soc.* **2006**, 128, 6447-6453. (b) Qiang, L. L.; Fan, Q.-L.; Ma, Z.; Zheng, Z.; Wang, Y.-Y.; Zhang, G.-W.; Huang, W. *Chem. Lett.* **2005**, 34, 1164-1165.
- (24) (a) Amir, R. J.; Pessah, N.; Shamis, M.; Shabat, D. *Angew. Chem. Int. Ed.* **2003**, 42, 4494-4499. (b) de Groot, F. M. H.; Albrecht, C.; Koekkoek, R.; Beusker, P. H.; Scheeren, H. W. *Angew. Chem. Int. Ed.* **2003**, 42, 4490-4494. (c) Rösler, A.; Vandermeulen, G. W. M.; Klok, H.-A. *Adv. Drug Delivery Rev.* **2001**, 53, 95-108. (d) Soppimath, K. S.; Tan, D. C.-W.; Yang, Y.-Y. *Adv. Mater.* **2005**, 17, 318-323.
- (25) Suh, Y.-W.; Kung, M. C.; Wang, Y.; Kung, H. H. *J. Am. Chem. Soc.* **2006**, 128, 2776-2777.
- (26) Sarin, V. K.; Kent, S. B. H.; Tam, J. P.; Merrifield, R. B. *Anal. Biochem.* **1981**, 117, 147-157.
- (27) Ressler, T. *J. Synchrotron Rad.* **1998**, 5, 118-122.
- (28) Hönes, G.; Koeber, K.; Kreuzbichler, I.; Neu-Becker, U.; Schwager, B.; Swoboda, G. in *Gmelin Handbook of Inorganic and Organometallic Chemistry*, 8th Ed, System Number 62, Supplement Volume B1 (Eds.: Hönes, G.; Huisl, W.; Keim, R.; Schwager, B.), Springer-Verlag, Berlin, 1992, pp.213-330.
- (29) Baes Jr., C. F.; Mesmer, R. E., *Hydrolysis of Cations*, Wiley, New York, 1976, pp. 279-286.
- (30) Robb, W. *Inorg. Chem.* **1967**, 2, 382-386.
- (31) Carlsson, L.; Lundgren, G. *Acta Chem. Scand.* **1967**, 21, 819.
- (32) Dubinskii, V. I.; Shul'man, V. M.; Peshchevitskii, B. I. *Russ. J. Inorg. Chem.* **1968**, 13, 27-28.

- (33) Peshchevitskii, B. I.; Belevantsev, V. I.; Kurbatova, N. V. *Russ. J. Inorg. Chem.* **1971**, 16, 1007-1009.
- (34) Puddephatt, R. J., *The Chemistry of Gold*, Elsevier, New York, 1978, pp. 179-242.
- (35) Mason, W. R.; Gray, H. B. *J. Am. Chem. Soc.* **1968**, 90, 5721-5729.
- (36) Mason, W. R.; Gray, H. B. *Inorg. Chem.* **1968**, 7, 55-58.
- (37) Gray, H. B.; Ballhausen, C. J. *J. Am. Chem. Soc.* **1963**, 85, 260-265.
- (38) Isci, H.; Mason, E. R. *Inorg. Chem.* **1983**, 22, 2266-2272.
- (39) Shriver, D.; Atkins, P., *Inorganic Chemistry*, 3rd Ed., W. H. Freeman and Company, New York, 1999, pp. 437-465.
- (40) Lever, A. P. *Inorganic Electronic Spectroscopy*, 2nd Ed., Elsevier, Amsterdam, 1984, pp. 203-375.
- (41) Peck, J. A.; Tait, C. D.; Swanson, B. I.; Brown Jr., G. E. *Geochim. Cosmochim. Acta* **1991**, 55, 671-676.
- (42) Belevantsev, V. I.; Kolonin, G. R.; Ryakhovskaya, S. K. *Russ. J. Inorg. Chem.* **1972**, 17, 1303-1306.
- (43) Gangopadhyay, A. K.; Chakravorty, A. *J. Chem. Phys.* **1961**, 35, 2206-2209.
- (44) Marken, F.; Neudeck, A.; Bond, A. M. in *Electroanalytical Methods: Guide to Experiments and Applications* (Ed.: Scholz, F.), Springer, Berlin, **2002**, pp. 51-97.
- (45) Zhu, S.; Gorski, W.; Powell, D. R.; Walmsley, J.A. *Inorg. Chem.* **2006**, 45, 2688-2694.
- (46) Kulakovskaya, S. I.; Levchenko, L. A.; Kulikov, A. V.; Sadkov, A. P.; Shestakov, A. F.; Pichugina, D. A. *Russ. J. Electrochem.* **2007**, 43, 92-104.
- (47) Ottaviani, M. F.; Montalti, F.; Romanelli, M.; Turro, N. J.; Tomalia, D. A. *J. Phys. Chem.* **1996**, 100, 11033-11042.
- (48) Ottaviani, M. F.; Montalti, F.; Turro, N. J.; Tomalia, D. A. *J. Phys. Chem. B* **1997**, 101, 158-166.
- (49) Zhao, M.; Sun, L.; Crooks, R. M. *J. Am. Chem. Soc.* **1998**, 120, 4877-4878.
- (50) Scott, R. W. J.; Wilson, O. M.; Crooks, R. M. *J. Phys. Chem. B* **2005**, 109, 692-704.

- (51) Smith, R. M.; Martell, A. E. *Critical Stability Constants Vol 2: Amines*, Plenum Press, New York, 1975, pp. 1-142.
- (52) Alner, D. J.; Lansbury, R. C.; Smeeth, A. G. *J. Chem. Soc. (A)* **1968**, 417-421.
- (53) Cox, M. C.; Everett, D. H.; Landsman, D. A.; Munn, R. J. *J. Chem. Soc. (B)* **1968**, 1373-1379.
- (54) Christensen, J. J.; Izatt, R. M.; Wrathall, D. P.; Hansen, L. D. *J. Chem. Soc. (A)* **1969**, 1212-1223.
- (55) Hansen, L. D.; Temer, D. J. *Inorg. Chem.* **1971**, 10, 1439-1442.
- (56) Katchalsky, A. *J. Polym. Sci.* **1951**, 7, 393-412.
- (57) Harris, F. E.; Rice, S. A. *J. Phys. Chem.* **1954**, 58, 725-732.
- (58) Sharp, K. A.; Hoing, B. *Annu. Rev. Biophys. Biophys. Chem.* **1990**, 19, 301-332.
- (59) Tanford, C. in *Advances in Protein Chemistry Vol. 17* (Ed.: Anson, M. L.), Academic Press, New York, **1962**, pp. 69-165.
- (60) (a) McGrath, M. E.; Vásquez, J. R.; Craik, C. S.; Yang, A. S.; Honing, B.; Fletterick, R. J. *Biochemistry* **1992**, 31, 3059-3064. (b) Kokesh, F. C.; Westheimer, F. H. *J. Am. Chem. Soc.* **1971**, 93, 7270-7274.
- (61) Urry, D. W.; Peng, S. Q.; Parker, T. M.; Gowda, D. C.; Harris, R. D. *Angew. Chem. Int. Ed. Engl.* **1993**, 32, 1440-1442.
- (62) (a) Frey, P. A.; Hegeman, A. D., *Enzymatic Reaction Mechanisms*, Oxford University Press, New York, 2007, pp. 69-128. (b) Frey, P. A.; Kokesh, F. C.; Westheimer, F. H. *J. Am. Chem. Soc.* **1971**, 93, 7266-7269. (c) Highbarger, L. A.; Gerlt, J. A.; Kenyon, G. L. *Biochemistry*, **1996**, 35, 41-46.
- (63) Farges, F.; Sharps, J. A.; Brown Jr., G. E. *Geochim. Cosmochim. Acta* **1993**, 57, 1243-2152.
- (64) Vaarkamp, M; Koningsberger, D. C. in *Handbook of Heterogeneous Catalysis, Vol. 2* (Eds.: Ertl, G.; Knözinger, H.; Weitkamp, J.), VCH, Weinheim, **1997**, pp. 475-493.
- (65) Crozier, E. D.; Rehr, J. J.; Ingalls, R. in *X-ray Absorption: Principles, applications, techniques of EXAFS, SEXAFS and XANES* (Eds.: Koningsberger, D. C.; Prins, R.), Wiley, New York, **1988**, pp. 373-442.
- (66) Langsetmo, K.; Fuchs, J. A.; Woodward, C. *Biochemistry*, **1991**, 30, 7603-7609.

- (67) Langsetmo, K.; Fuchs, J. A.; Woodward, C.; Sharp, K. A. *Biochemistry*, **1991**, 30, 7609-7614.
- (68) Karlstrom, A.; Zhong, G.; Rader, C.; Larsen, N. A.; Heine, A.; Fuller, R.; List, B.; Tanaka, F.; Wilson, I. A.; Barbas III, C. F.; Lerner, R. A. *Proc. Natl. Acad. Sci.* **2000**, 97, 3878-3883.
- (69) Inoue, M.; Yamada, H.; Yasukochi, T.; Kuroki, R.; Miki, T.; Horiuchi, T.; Imoto, I. *Biochemistry*, **1992**, 31, 5545-5553.

Chapter 7

- (1) Oxford, S. M.; Henao, J. D.; Yang, J. H.; Kung, M. C.; Kung, H. H. *Submitted*.